

Tokamak plasma edge studies by microwave short-pulse reflectometry and backscattering

Thèse N° 9515

Présentée le 16 août 2019

à la Faculté des sciences de base
SPC - Physique du Tokamak TCV
Programme doctoral en physique

pour l'obtention du grade de Docteur ès Sciences

par

Pedro Andres MOLINA CABRERA

Acceptée sur proposition du jury

Prof. C. Hébert, présidente du jury
Dr. S. Coda, Dr. L. Porte, directeurs de thèse
Dr T. Rhodes, rapporteur
Dr P. Hennequin, rapporteuse
Dr A. Merle, rapporteur

2019

Abstract

Moving towards an increased understanding of the dynamic processes in the edge of tokamak plasmas requires continuous innovation in diagnostic capabilities, pushing the envelope of both spatial and temporal resolutions. Plasma density and rotation, and their respective fluctuations, are essential quantities for tokamak physics studies. The present dissertation describes the design, development, and first results of two new dedicated diagnostics in the TCV tokamak: a heterodyne continuous-wave Doppler backscattering (DBS) system and a short-pulse reflectometer (SPR). Both of these diagnostics use a flexible quasi-optical launcher antenna and a pair of universal polarizers allowing flexible coupling to either O or X mode and programmable polarization changes during the shot. This flexibility allows both instruments to measure plasmas with edge densities inside a $0.8\text{--}7 \times 10^{19} \text{ m}^{-3}$ range.

DBS is an active diagnostic technique that allows the study of electron density turbulence via the scattering of a millimeter-wave (mmw) beam launched at oblique incidence to a cutoff layer. This technique has been implemented using a fast arbitrary waveform generator (AWG) as the main oscillator and commercial vector network analyzer extension modules as the main mm-wave hardware. It allows sweepable single frequency operation featuring an I/Q mixer to analyze the heterodyne signal. Also, an innovative multi-frequency approach has been demonstrated. It leverages on the flexibility of the AWG source by feeding a bi-frequency signal to a x6 varactor multiplier producing a 7-frequency output that is directly measured with a fast digital sampler in the receiver. Furthermore, a pair of fast polarizers have been used to measure the magnetic-field pitch angle in the edge of the plasma by monitoring the backscattered signal power as the probing beam output linear polarization angle is varied at constant ellipticity. Ray-tracing simulations reveal an accessible k_{\perp} range between $3\text{--}16 \text{ cm}^{-1}$ with a resolution of $2\text{--}4 \text{ cm}^{-1}$. Perpendicular rotation velocity estimates compare well against ExB plasma poloidal rotation estimates from charge exchange recombination spectroscopy.

In microwave reflectometry, the electron density can be inferred from the round-trip group-delay of EM waves reflected at perpendicular incidence from a plasma cutoff. Short pulse reflectometry (SPR) consists of sending broadband mmw pulses ($\sim 1\text{ ns}$) and measuring their round-trip group-delay using precise timing systems. This thesis describes the realization of a novel approach to SPR producing 0.7 ns pulses in the V-band using low-frequency pulses from an AWG and x6 varactor multipliers. The design offers unique flexibility regarding pulse output frequency and repetition rate, which allows the instrument to overcome traditional SPR spatial sampling limitations while reducing hardware complexity. In order to measure the group-delay of short pulses, both a traditional analog and a novel digital sampling technique have been explored. A group-delay resolution of under 17 ps in average has been achieved with both approaches. The direct sampling technique has the added advantage of measuring reflected pulse amplitude and width. Histograms of group-delay data show interesting qualitative changes from L to H-mode plasmas. Frequency spectra of group-delay data allow the identification of macroscopic density fluctuations as well as edge quasi-coherent modes. Lastly, density profiles have been measured with microsecond time resolution, effectively increasing the temporal resolution of edge density measurements in TCV by a factor of 10^3 .

Keywords: tokamak, plasma physics, plasma diagnostics, diagnostic development, pulse reflectometry, Doppler backscattering, turbulence diagnostics, magnetic confinement fusion, data analysis, inverse problems, arbitrary waveform generator, ray-tracing.

Abstract

Le bord d'un plasma thermonucléaire comme celle du soleil est un environnement très dynamique et chaotique montrant une grande gamme d'échelles spatiales et temporelles. Pour mieux comprendre les lois fondamentales de ces processus, la physique expérimentale doit toujours se réinventer et repousser les limites de la précision et de la rapidité des mesures. Cette thèse décrit la conception, la construction et les premiers résultats de deux nouveaux diagnostics dans le tokamak TCV de la famille de la réflectométrie. Le premier est un réflectomètre à rétrodiffusion Doppler et le second est un réflectomètre à profil d'impulsion courte (~ 1 ns). Les deux diagnostics utilisent une antenne quasi-optique et deux polariseurs universels qui permettent de changer la polarisation du faisceau entre les modes O et X, et ceci même pendant une décharge.

La réflectométrie Doppler à rétrodiffusion permet d'étudier la turbulence électronique par la diffusion d'une onde électromagnétique émise avec un angle oblique contre une couche de coupure. Cette technique a été mise en œuvre en utilisant un générateur d'ondes arbitraires comme oscillateur central et des modules d'extension d'analyseurs vectoriels du marché comme des circuits de radio fréquence. Le diagnostic permet de fonctionner avec une seule fréquence de sortie pouvant être modifiée dans le temps en utilisant un mélangeur I / Q pour analyser le signal hétérodyne. En plus de ce mode de fonctionnement habituel, un nouveau mode de production à plusieurs fréquences a été attesté. Ce mode utilise le générateur arbitraire pour générer jusqu'à 7 fréquences grâce à l'intermodulation d'un signal bifréquenciel envoyé à un diode varicap. De plus, en utilisant les polariseurs, de nouvelles expériences ont démontré la capacité de la réflectométrie à mesurer l'angle du champ magnétique au bord du plasma. Ceci a été réalisé en changeant l'angle de polarisation linéaire, en maintenant l'ellipticité constante et en mesurant la puissance du signal rétrodiffusé. En utilisant des calculs de «ray tracing», nous montrons que l'instrument permet de mesurer des longueurs d'onde comprises entre $k_{\perp} 3\text{--}16 \text{ cm}^{-1}$ avec une résolution de $2\text{--}4 \text{ cm}^{-1}$. Les vitesses de rotation des turbulences coïncident dans la marge d'incertitude avec la vitesse $E \times B$ mesurée par des méthodes spectroscopiques.

En réflectométrie, la densité de profil d'un plasma peut être mesurée par le retard de groupe des ondes électromagnétiques qui rebondissent sur une couche de coupure. La réflectométrie par impulsions courtes consiste à envoyer des impulsions de ~ 1 ns et à mesurer le retard de groupe avec des chronomètres de haute précision. Notre thèse décrit une nouvelle façon de concevoir ce type de réflectomètres en utilisant des impulsions de basse fréquence provenant d'un générateur d'ondes arbitraires et en multipliant leur fréquence dans une diode varicap. Cette approche offre une flexibilité unique en permettant la création de n'importe quelle fréquence à tout taux de répétition. Nous avons mesuré le retard de groupe de ces impulsions grâce à deux méthodes: la méthode traditionnelle utilisant des circuits analogiques et l'échantillonnage numérique direct. Cette dernière méthode novatrice permet non seulement de connaître le temps de vol, mais également l'amplitude et l'épaisseur temporelle des impulsions réfléchies par le plasma. Une résolution de 17 ps en moyenne a été obtenue sur la bande V (50-75 GHz) avec les deux techniques. Les histogrammes de ces retards de groupe montrent des changements

dans la dynamique des fluctuations de densité dans le plasma, en particulier des changements fondamentaux entre les modes de confinement bas et élevé (modes L / H). De plus, le spectre de fréquence du retard de groupe montre plusieurs modes d'oscillation dans le plasma : des modes macroscopiques, comme les «dents de scie», et des modes quasi-cohérents au bord des modes H. Bien que dans une plage spatiale plus courte que le diagnostic de diffusion Thomson, les profils de densité ont été mesurés en quelque microsecondes, ce qui améliore la résolution temporelle des mesures de densité au TCV d'un facteur de mille. La flexibilité de polarisation permet de mesurer des plasmas avec des densités comprises entre $0.3\text{-}4.5 \times 10^{19} \text{ m}^{-3}$.

Mots-clés: tokamak, physique des plasmas, diagnostic des plasmas, réflectométrie par impulsions courtes, rétrodiffusion Doppler, diagnostic de la turbulence, fusion par confinement magnétique, analyse de données, problèmes d'inversion, générateur d'ondes arbitraires.

Dedicado a mis padres

Before God's footstool to confess
A poor soul knelt, and bowed his head;
"I failed," he cried. The Master said,
"Thou didst thy best - that is success!"
Anonymous. After John Wooden.

Contents

Cover page	i
Abstract	iii
Contents	ix
List of Figures	xiii
List of Tables	xvii
1 Introduction	1
1.1 Fusion energy in the 21st century	1
1.2 Nuclear Fusion reactors	4
1.3 The Tokamak Reactor	6
1.3.1 Tokamak plasma heating	8
1.3.2 Transport	10
1.3.3 Confinement regimes	11
1.3.4 ITER and challenges ahead	12
1.4 The TCV tokamak	13
1.4.1 TCV Heating systems	17
1.4.2 TCV diagnostics	19
1.5 This thesis	22
2 Principles of Reflectometry	23
2.1 Cold plasma wave theory	23

2.2	Spatial localization and beam refraction	27
2.2.1	WKB approximation	27
2.2.2	Airy width	28
2.2.3	Refraction and geometric optics	31
2.3	Measuring density profiles - $n_e(\rho_\psi)$	33
2.4	Measuring density fluctuations	37
2.4.1	Tokamak plasma turbulence: a brief summary	37
2.4.2	Fluctuation reflectometry	42
2.4.3	Doppler back-scattering	46
3	Doppler back-scattering diagnostic	51
3.1	Hardware set-up	52
3.1.1	Sweepable single frequency set-up	52
3.1.2	Multiple simultaneous frequency set-up	54
3.2	Data analysis approach	57
3.2.1	Ray tracing and PrefGeom	57
3.2.2	Power spectral density and Doppler shift estimates	61
3.2.3	v_\perp uncertainty estimates	65
3.3	Results and discussion	67
3.3.1	I-Q signals during plasma discharge	68
3.3.2	DBS-CXRS comparison	68
3.3.3	Comparing sweepable single with multi-frequency DBS set-ups . .	70
3.3.4	In-shot polarization rotation to infer B-field line pitch	71
3.4	Future perspectives	78
3.5	Summary	79
4	Review of Reflectometry techniques	81
4.1	Basic phase detection techniques	82
4.1.1	Homodyne and heterodyne techniques	82
4.2	Continuous wave techniques	85
4.2.1	Single swept frequency	85

4.2.2	Multiple frequency techniques	87
4.3	Pulsed wave techniques	88
4.3.1	Short pulse reflectometry	89
4.3.2	Ultra-short pulse reflectometry	92
4.4	Comparison criteria	95
4.4.1	Range resolution	95
4.4.2	Range precision	97
4.4.3	Spatial Sampling	99
4.4.4	Temporal Sampling	100
4.4.5	Turbulence effects	102
4.5	Summary	106
5	AWG-driven short pulse reflectometry	109
5.1	Hardware implementation	111
5.2	Timing circuits	114
5.2.1	Requirements	114
5.2.2	Traditional analog approach	115
5.2.3	Direct sampling approach	117
5.2.4	Comparing the two pulse-timing techniques	118
5.2.5	Pulse amplitude and width reflected from lossy static mirror	122
5.3	Results and discussions	122
5.3.1	Pulse amplitude and width reflected from L-mode plasmas	123
5.3.2	Group-delay statistics from L and H-mode plasmas	125
5.3.3	Frequency spectrum of group-delay data	128
5.3.4	Density profile measurement	134
5.3.5	Inter-ELM density fluctuations	142
5.4	Summary and future perspectives	154
5.5	Conclusions	156
A	Diagnostic launcher antenna system	159
A.1	Signal path	159

A.1.1	Thomas Keating quasi-optical coupling telescope	159
A.1.2	HE ₁₁ waveguide and miter-bend	162
A.1.3	Polarizer miter bends	163
A.1.4	Vacuum window	165
A.2	Quasi-optical launcher antenna	167
A.3	Protection from ECH stray power	169
Acknowledgements		173
Glossary		177
Bibliography		179
Curriculum Vitae		206

List of Figures

1-1	Tokamak sketch	7
1-2	Divertor configuration sketch	8
1-3	TCV schematic	14
1-4	TCV poloidal cross-section showing main coils	18
1-5	Thomson scattering, intereformeter, and Mirnov coils observation geometry	21
2-1	Geometrical sketch of O and X-mode polarizations	26
2-2	O and X-mode cutoffs during L-mode discharge 60572	26
2-3	O and X-mode cutoffs during H-mode discharge 62734	27
2-4	Airy-integral function approaching a cutoff	29
2-5	Airy widths in O and X-mode during L and H-mode discharges	30
2-6	Linear growth rate of common tokamak instabilities over k_{\perp} spatial length.	39
2-7	DBS principle of operation	48
3-1	Single frequency DBS block diagram	52
3-2	Multiple-frequency DBS block diagram	55
3-3	Multiple-frequency receiver IF power spectral density spectrum	56
3-4	PrefGeom 3-point ray-tracing sample results	59
3-5	k_{\perp} accessibility map for shot 59534	61
3-6	Power spectral density of the DBS signal showing a regular Gaussian function fit.	62

3-7	Power spectral density of the DBS signal showing a skewed Gaussian function fit.	63
3-8	IQ-balance check using data from shot 55455	68
3-9	Comparison between DBS perpendicular turbulence velocity estimates and CXRS v_{ExB} estimates	70
3-10	Multi-frequency DBS set-up validation: comparison against single-frequency DBS and CXRS	71
3-11	Definition of polarization ellipse α and β	72
3-12	Polarization α and β maps as a function of miter-bend polarizer angle for 60GHz.	73
3-13	Theoretical wave coupling to both O and X-mode waves as a function of shot time while polarization angle α is made to vary keeping β constant.	74
3-14	Spectrogram of raw DBS data during shot 59679 as the beam's polarization angle α is made to vary keeping β constant.	75
3-15	DBS signal power evolution over time as the polarization axis angle is rotated.	76
4-1	Homo and heterodyne detection schemes	82
4-2	Sketch of an I/Q mixer	84
4-3	Principle of operation of a continuous-wave frequency modulation reflectometer	86
4-4	Principle of operation of an amplitude-modulated continuous-wave reflectometer	88
4-5	Principle of operation of short pulse reflectometer	89
4-6	Hardware implementation of a traditional short-pulse reflectometer	90
4-7	Pulse dispersion of pulses of varying width in O-mode polarization using a typical L-mode density profile	92
4-8	Principle of operation of an ultra-short pulse reflectometer	93
4-9	Hardware implementation of an ultra-short pulse reflectometer	94

4-10	Effects of profile varying bandwidth smoothing and spatial sampling in density profile reconstruction	97
4-11	Illustration of the effect of noise in the pulse envelope in range precision .	98
5-1	AWG-driven short pulse reflectometer schematic diagram	112
5-2	WR-15 zero-bias Schottky diode data demonstrating that Gaussian pulses of 650 – 750ns FWHM may be created by an AWG driving x6 VDI varactor multipliers.	113
5-3	SPC-150NX timing system block-diagram	115
5-4	Sample Gaussian fit of direct digital sampling data.	117
5-5	Comparing total group-delay uncertainty of analog and digital sampling techniques including 10dB power variations	121
5-6	Histograms Raw	126
5-7	Comparing FIR and SPR data showing signs of a macroscopic sawtooth oscillation	129
5-8	Comparing Mirnov coil and SPR group delay PSD showing signs of a quasi-coherent mode during the H-mode phase of shot 61834.	130
5-9	Comparing Mirnov coil and SPR data that feature signs of a GAM oscillation in the edge of shot 61626.	131
5-10	SPR PSD during ELM-free H-mode shot 62632 showing a rich variety of modes in the edge of the confined plasma.	133
5-11	Density profile evolution during a L-H mode transition using O-mode polarization	137
5-12	Density profile evolution during L-H mode transition using O-mode polarization in shot 61337	139
5-13	Density profile evolution during plasma startup in shot 60928 using X-mode polarization.	142
5-14	SPR data in X-mode polarization before ELM in shot 60929	145
5-15	Alternative diagnostics of plasma position.	146

5-16	PSD of X-mode SPR data during ELM-free period of shot 60929 leading to the first ELM at 0.348	147
5-17	PSD of X-mode SPR group-delay data for frequency 59GHz at two instants between the ELM-free period leading to an ELM at 0.348.	148
5-18	SPR data in O-mode polarization before ELM in shot 62744	151
5-19	Zoomed-in O-mode ELM SPR data showing the sharp density gradient 100μs preceding an ELM crash.	152
5-20	PSD of O-mode SPR data during ELM-free period of shot 62744 leading to the first ELM at 0.74	152
5-21	PSD snap of O-mode SPR group-delay data for frequency 51GHz at two instants between the ELM-free period leading to an ELM at 0.74s.	153
A-1	3D schematic of the physical location of reflectometry hardware with respect to the launcher antenna and the TCV tokamak	160
A-2	Zoomed-in view of the waveguide path from reflectometry hardware to the launcher antenna	160
A-3	TK quasi-optical telescope featuring reflectometry and ECE horn antennas	162
A-4	Vacuum window properties	166
A-5	3D schematic of the diagnostic launcher	168
A-6	2D schematic of the diagnostic launcher showing specific dimensions and mirror focal lengths.	169

List of Tables

1.1	TCV figures of merit	15
1.2	TCV diagnostics overview including the two new contributions realized during this thesis	19
2.1	Cold-plasma magnetized plasma cutoffs and resonances	25
4.1	Comparing figures of merit: continuous-wave techniques	107
4.2	Comparing figures of merit: pulsed-wave techniques	108
5.1	Comparing group-delay precision of analog and digital timing techniques	120
5.2	Pulse peak amplitude and width evolution at power variation extremes against static mirror.	123
5.3	Pulse amplitude and width statistics during L-mode plasma	123
5.4	Basic moment analysis of raw group-delay data during shot 62633.	127
5.5	Comparing pulsed-wave reflectometry techniques with the newly developed AWG-driven SPR system.	154

Chapter 1

Introduction

1.1 Fusion energy in the 21st century

Nuclear fusion is the reaction that powers stars. Apart from the mysterious dark-energy, nuclear fusion is the most abundant reservoir of energy in the universe. It is also the main energy source sustaining life on our planet. Modern human civilization could not have flourished without the Sun's energy. From the discovery of fire over 500,000 years ago, humans have been using the sun's energy transformed into wind, heat, and food through photosynthesis. In spite of the large scientific and technological progress witnessed in the last 250 years since the industrial revolution, a recurring global challenge facing modern society continues to be the sustainable production of energy. With population growth estimates predicting 9 billion people by 2050 from about 7 billion today, humankind will need to drastically increase its energy production as billions of people in developing countries attempt to increase their standard of living and industrialize their societies.

Drawbacks related to the availability and negative environmental effects of fossil fuels started to become apparent during the first energy crisis for charcoal in 1630 [1]. In 2014, over 80% of the world's energy sources are still fossil in nature: oil, coal, and natural gas [2]. Their cost per kWh remains highly competitive even as global resources

are consumed at enormous rates. Nevertheless, there is a large hidden economic cost to society when fossil fuels are burned. With global CO₂ emissions of 31.6Gt in 2012, negative effects on net agricultural productivity, human health, and increased property damage risk from natural disasters amount to implicit subsidies to fossil fuel companies in the order of 800 billion per year [3]. The complex economic and geopolitical inertia surrounding our heavy dependence on fossil fuels does not permit an immediate shift of energy production and use away from fossil fuels. The recent *gilets jaunes* protests in France are a very good example of the social consequences of suddenly lifting diesel and petrol subsidies.

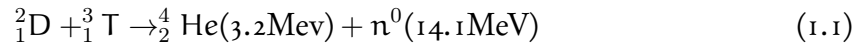
The 2013 Fifth Assessment report of the Intergovernmental Panel on Climate Change (IPCC) has highlighted the scientific consensus that “it is *extremely likely* that human influence has been the dominant cause of the observed warming since the mid-20th century” [4]. Their current models predict a global 1.5° increase in temperature for 2030-50 from pre-industrial levels if CO₂ emissions are substantially reduced and reach net zero by 2050. While the 1.5° increase is still believed to lead to important global changes, such as the disappearance of 70-90% of the Pacific coral reefs, a 2° increase could lead to much more deleterious consequences [5].

Securing the future global energy supply requires developing a diverse energy portfolio and improving the efficiency of energy use. Alternative sources of energy such as wind turbines and photovoltaics provide CO₂-free energy, albeit intermittently. Heavy reliance on this type of energy requires large and efficient storage solutions which are still in the research stage. A baseload power source that operates continuously in a reliable and predictable fashion is highly desirable to meet a minimum level of power demand.

Nuclear fission energy is a plausible solution. Fission has been an important part of the global baseload supply for over 50 years. However, serious safety concerns after repeated accidents leaving behind harmful radioactive pollutants in the environment have steered decision-makers away from fission. Fast breeder technology could provide fission fuel for many generations, but nuclear weapon proliferation risks have prevented the realization of such designs. While the technology exists and could do nothing but improve over time, the public anxiety has led to many countries, including Switzerland, to look

away from nuclear fission.

This manuscript describes research performed in the framework of magnetic-confinement nuclear fusion. Our current understanding of nature and technological prowess has brought our generation within reach of tapping into the Sun's power supply. Nuclear fusion has the potential to generate large amounts of steady, clean, safe, and nearly inexhaustible energy. The most accessible fusion reaction brings together deuterium and tritium (isotopes of hydrogen) nuclei to produce inert, non-toxic, helium nuclei and neutrons:



Deuterium can be found in large quantities in nature: one part in 5000 of hydrogen in seawater is Deuterium. Tritium cannot be found in nature since it has a short radioactive half-life of 12.3 years. It can, however, be produced from widely-available lithium through a reaction with a neutron which can conveniently come from the fusion reaction in equation 1.1. Lithium can also be found in sea-water: about 2 ions in 10 million in average. The fuels of the D-T reaction are then nearly inexhaustible, predicted to last for more than a million years [6, p. 3].

The energy of the D-T fusion reaction is found in the kinetic energy of its products: a helium atom and a neutron. The combined mass of the reactants is larger than the mass of the products. The difference in mass is transformed to energy via Einstein's equation $E = mc^2$. Energy densities are 150 thousand times that of coal/gas burning; therefore, much smaller quantities of fuel are required in comparison: a liter of seawater could produce as much energy as 300 liters of oil [6, p. 3] [7, p. 24]. The kinetic energy in the released neutrons can be used to heat liquids and rotate turbines. Unfortunately, these neutrons would eventually render the walls of the reactor radioactive. Nevertheless, wall materials can be chosen to lose their radioactivity in relatively short periods (50-500 years) compared to hundreds of thousands of years for fission-reactor long-term waste. Aneutronic fusion reactions do exist, but the D-T reaction has the highest reactivity at less extreme conditions.

1.2 Nuclear Fusion reactors

The problem with fusion is practical: it is very hard to do. The scientific and engineering challenges of lightning up a star on Earth are enormous. It has puzzled several generations of researchers from the most technologically advanced nations in the world since the early 1950s. The main problem is simple: both particles in the above D-T reaction are positively charged: the electrostatic (Coulomb) force acts to keep them far from each other. Only when this natural repulsion is overcome, and partly thanks to quantum tunneling, the strong nuclear force may allow fusion reactions to occur. One way to overcome this Coulomb force is to give the reactants large kinetic energy.

The fusion of light elements into heavier ones was achieved in 1932 by Mark Oliphant at Cavendish Laboratory in the University of Cambridge [8] by accelerating hydrogen isotopes and causing them to collide against solid targets. This method proved impractical for industrial energy production, however. More energy was required to make the fusion reactions than it gave in return. The ratio of the thermonuclear power produced over the heating power supplied is called Q . Even when $Q > 1$, the limited electrical and thermodynamic efficiencies of a power plant may make the reactor impractical.

Currently, the only fusion-powered device capable of producing more energy than it was given is the H-bomb. In this device, a nuclear fission explosion drives deuterium and tritium atoms to fuse by providing enormous X-ray pressures that both drive and confine the fusion reactions. The fusion bomb is the most powerful weapon ever conceived with yields above 2×10^7 TJ [9].

Instead of using particle beams or thermonuclear explosions, another approach is to heat a gas to large temperatures such as those found in the core of the Sun. At these temperatures, hydrogen enters the fourth state of matter: a plasma. To make a plasma, the temperature of a gas must be increased to levels where electrons have enough energy to free themselves from their host nuclei. The result is a macroscopically-neutral mixture of positively-charged nuclei and free negatively-charged electrons that exhibits collective behavior.

It became clear in the late 1950s [10], however, that not only temperature had to be

kept high but also that the fusion products had to be confined for a sufficiently long time. The ultimate ideal fusion reactor requirement is the so-called *ignition* condition [11] which requires that the heat produced by the helium particles in the fusion reaction (equation 1.1) solely keeps the reactants at an adequate temperature against the natural convective and radiative losses of the reactor. This ignition condition corresponds to a $Q=\infty$ and is quantitatively expressed in the so-called triple product.

$$nT\tau_E > 3 \times 10^{21} \text{m}^{-3} \text{keVs}$$

where n is the D/T particle density (assumed equal), T the D/T temperature and τ_E the energy confinement time. The conditions for ignition would be reached for $n = 10^{20} \text{m}^{-3}$, $T = 10 \text{keV}$, and $\tau_E = 3 \text{s}$. This 10keV temperature turns out to be about 10 times higher than those found in the core of the sun, a stunning: 116 million degrees.

The most promising approach to achieving this ignition condition, thus far, has been magnetic confinement fusion (MCF). A plasma is electrically conductive and reacts to electro-magnetic fields which can be used to control its trajectory and/or increase its temperature. MCF relies on the basic fact that charged particles gyrate around magnetic field lines according to the Lorentz force $\vec{F}_L = q\vec{v} \times \vec{B}$. Strong magnetic fields, a million times stronger than the Earth's magnetic field, are used in MCFs to confine these hot particles. The most promising MCF reactor designs to-date have been the tokamak and the stellarator. Both approaches use a toroidal magnetic field to confine the plasma, but they differ in the approach to generate optimal B-field shear to keep the particles away from the walls. The tokamak uses external coils and an internal current to achieve this shear, while the stellarator relies on a carefully-shaped set of coils. The tokamak will be the focus of this manuscript, and it is further explained below.

Although MCF reactors have been an active area of research for over 60 years, there are still many unsolved physical and engineering problems, mainly plasma-wall interaction, instability control, and anomalous transport. Because fusion is technically challenging, it is also very expensive. At the writing of this manuscript, it is far from being an economically competitive alternative to wind, solar, or fission energy. That being said, it

is currently transitioning from the research to the development stage. Generic economical models describing the development and deployment of new large technologies have been recently applied to MCF [12] concluding that while fusion is late to significantly contribute to carbon-free energy production by mid-century, it is not necessarily slow or expensive.

1.3 The Tokamak Reactor

Tokamak is a transliteration of a Russian word, an acronym for "Toroidal chamber with magnetic coils". Toroidal refers to the geometry resembling a wheel tube shape. Research on this type of magnetic confinement machine started in the Soviet Union in the 1950s with a letter written by O. A. Lavrent'ev [13] describing the idea of an electrostatic device capable of realizing controlled nuclear fusion energy. This letter inspired A. D. Sakharov and I. E. Tamm who worked out the initial theoretical feasibility in the early 1950s, at what is today the Kurchatov Institute in Moscow. By 1968, once vertical stabilization had been solved, the T-3 tokamak reported electron temperatures in the order of 1keV. Once confirmed by British scientists in 1969, the tokamak became the most widely researched magnetic-confinement machine in the world. To this day, it remains the leading candidate for the industrial production of fusion energy.

The tokamak is a very elegant modular machine. Its principle of operation is shown in figure 1-1 on the facing page. It uses a series of coils arranged along the toroidal direction (D-shaped coils in blue in figure 1-1) which generate a strong toroidal magnetic field inside the coils. Because these coils and hence the machine cannot be infinitely large, charged particles inevitably drift to the top and bottom of the tube due to changes in the magnetic-field strength. The tokamak deals with this problem by driving an electrical current in the plasma along the toroidal direction (green arrow in figure 1-1). This current naturally produces an additional magnetic field that wraps around it, which is called the *poloidal* field. The addition of both toroidal and poloidal fields gives rise to a curved helical field along the toroidal direction (shown in dark blue in figure 1-1) which averages out the particle drifts so that the motion of the particles around the torus can follow a

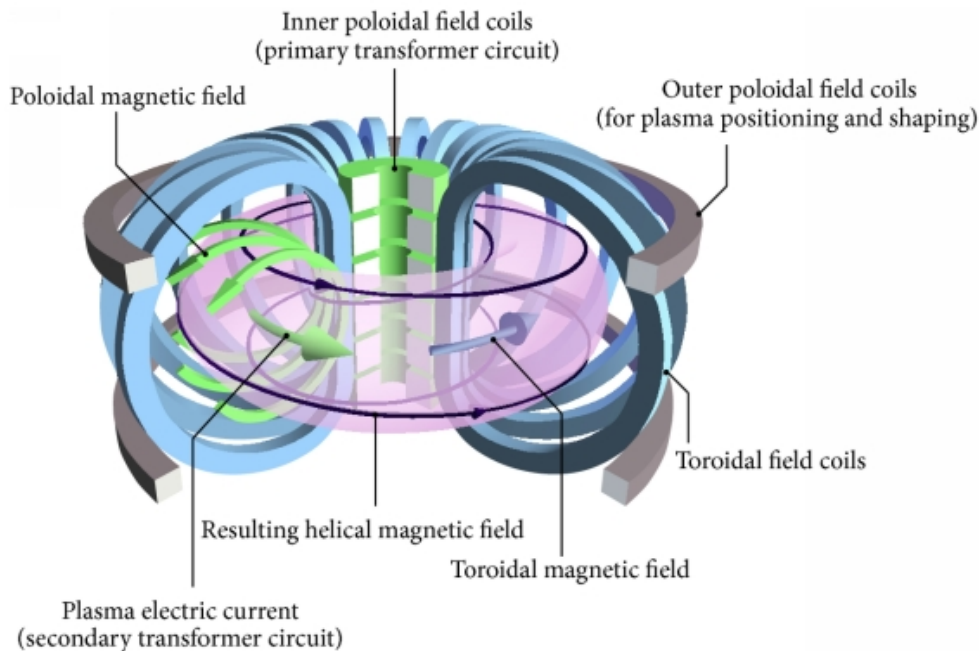


Figure 1-1: Tokamak sketch

regular pattern. Figure 1-1 also shows 2 conductors positioned on the top and bottom of the tokamak sketch. These coils create a vertical field that through the Lorentz force produces a radial force preventing high pressure plasmas from naturally bursting outwards in the radial direction towards the outer walls. These coils are also used to control the plasma's vertical position, shape, and stability [7, p. 277].

An important innovation that led to improved performance in the tokamak is the divertor configuration. Figure 1-2 on the following page below shows a schematic of a traditional 'X-point' divertor. It emerged in the 1980s as an efficient approach to reducing plasma-wall interaction. Regardless of the specific magnetic field geometry generated in the tokamak approach, there is a limited volume of plasma that is confined. The boundary of the confined plasma is called the separatrix or last-closed-flux-surface (LCFS). Beyond the LCFS, magnetic field lines touch the vessel walls leading to a plasma region featuring large changes in density and temperature in the so-called scrape-off-layer (SOL).

Before the divertor, all tokamaks used the *limiter* configuration where a protruding

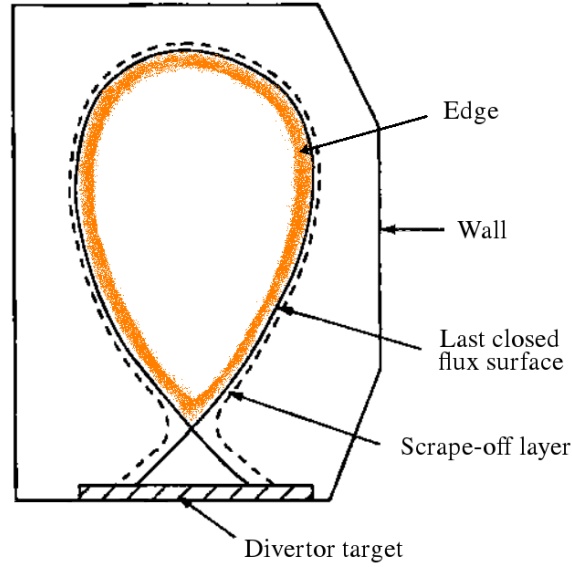


Figure 1-2: Divertor configuration and plasma edge. Adapted from Wesson [11].

conductor was made to interact directly with the edge of the confined plasma. Unfortunately, wall-material ions were easily sputtered from this limiter and entered the plasma. These *impurities* radiated away energy and diluted the confined plasma composition. The divertor approach modifies the magnetic field shape at the bottom of the plasma to converge into a 'X' point and drives the plasma to touch the walls at the bottom of the machine in specifically-designed divertor plates. The specific conditions (high neutral gas pressure) at these plates and the physical separation from the LCFS prevent wall material from easily polluting the confined plasma.

1.3.1 Tokamak plasma heating

The early success of the tokamak was in part due to the inherent heating power provided by the plasma current. Although plasmas are highly conductive charged gases, they feature a small electric resistance due to electron-ion collisions. When a current is passed through a resistor, Joule heating dissipates energy according to Joule's first law $P \propto I^2 R$. In a tokamak plasma it can be shown [7] that the Joule/Ohmic heating is proportional to $P_{\Omega} \propto \frac{I_p^2}{T_e^{3/2}}$. Thus, as the plasma temperature increases, the resistivity goes down along with the Joule heating power. Electron temperatures of a few keV can be reached, but Joule heating is not sufficient to reach reactor ignition conditions. Furthermore, plasma

stability limits the maximum current that can be run toroidally in a tokamak equilibrium [14]. In order to bring tokamak plasmas to ignition-relevant temperatures, several mega Watts of external power must be efficiently coupled. This is because, although once enough nuclear fusion reactions start to occur the fusion-product helium ion energy should contribute to self-heating of the plasma, radiation (Breemsthrallung) and heat convection power losses to the walls must be compensated by additional external heating before reaching ignition.

There are three major parallel efforts to provide this external power to tokamaks, namely: ion cyclotron resonance heating (ICRH), electron cyclotron resonance heating (ECRH), and neutral beam heating (NBH). The first approach consists of launching radio-frequency waves in the tens of mega Hertz which couple energy to the plasma ions through collisionless wave-particle interaction. These waves enter in resonance with ions undergoing cyclotron motion around magnetic field lines. Highly efficient and powerful sources of ICRH-RF power are inexpensive and readily available. ICRH waves, however, cannot propagate in vacuum and antenna structures must be very close to the edge of the plasma, leading to launcher plasma-edge interaction. In addition to the extreme thermal environment of the fusion plasma edge and risk of arcing, this interaction is enhanced by the intense RF fields around the launcher [15].

ECRH couples external power into the plasma via wave-particle interactions with the gyrating electrons in the magnetic field. Given the smaller mass of electrons compared to ions, these undergo cyclotron motion with much larger frequencies. Hence, the ECRH wave sources and antennas are markedly different. ECRH uses vacuum wave-tube generators called gyrotrons, which oscillate in the tens to hundreds of gigahertz. Fusion research has motivated the successful development of high-power gyrotron sources with surprisingly good electrical efficiency ($>50\%$) which can couple mega Watts of power with nearly full plasma absorption. Vacuum-compatible quasi-optical antenna systems allow the coupling of these waves to the plasma with minimum accessibility requirements and losses. Unfortunately, this heating mechanism couples external power exclusively to the plasma electrons, which then must exchange energy with the fusion-relevant ions via Coulomb collisions. ECRH waves can also be used to drive the plasma current [16] and

quench instabilities [17].

Another popular heating mechanism is neutral-beam injection (NBH). It consists of injecting a beam of high-energy neutral particles into the plasma. The energy of these neutral particles is usually above the 10keV required for ignition. These particles must be neutral so they can penetrate unencumbered the high magnetic fields of the tokamak periphery. Upon entering the confined plasma these neutral particles undergo charge-exchange or impact ionization with the background plasma and introduce a high-energy ion population. These hot ions then exchange energy with lower energy ions and electrons. Fusion research has also sparked much technological improvement in neutral beam sources which have reached neutral energies in the sub mega eV level. Neutral-beam injection also provides momentum and current to the plasma, which are highly welcome features in a burning tokamak plasma requiring currents in the 10s of mega Ampères [18].

1.3.2 Transport

The triple product figure of merit presented above shows that particles must have a sufficient density and temperature, as well as a large enough energy confinement time to achieve sufficient fusion reactions and produce energy in a continuous fashion. Transport studies attempt to understand the physical variables that control particle and energy confinement which have a direct effect on these three quantities. Such studies are of critical importance since they have a direct impact on predicting reactor performance and eventually its size and cost. In the case of a tokamak plasma, kinetic models have been developed that take into account the specific intricacies of magnetized plasma transport in the toroidal geometry. These go by the name of neoclassical transport theory. Excellent reviews have been written on the subject by Wesson [11, p. 150] and Freidberg [7, p. 449], for example. Unfortunately, particularly in low-confinement tokamak regimes, this neoclassical transport theories predict electron and ion confinement times up to two orders of magnitude longer than those measured experimentally [19]. It is believed that plasma turbulence is the major cause of this increased cross-field transport termed *anomalous* transport. Understanding transport is one of the outstanding problems in magnetic con-

finement fusion, just as a complete theory of turbulence remains an unsolved problem in classical physics.

1.3.3 Confinement regimes

Another break-through in tokamak research came in 1984 with the discovery of a high-confinement or ‘H-mode’ [20] regime. It was found that when a diverted tokamak plasma is heated with a sufficient amount of NBH power, it develops a transport barrier in the edge region (see figure 1-2 on page 8) leading to increased plasma density, temperature, and energy confinement. This improved confinement regime comes about thanks to the formation of an edge transport barrier created by sheared $E \times B$ flow that quenches fluctuations, reduces turbulent transport, and builds steep gradients at the edge. It was later found that external NBH power is not the only plasma heating approach that leads to H-mode: the transition occurs once a threshold amount of external power is reached via either NBH, ohmic, ICRH, and/or ECRH heating or a combination thereof. The dynamics of the transition are an active field of research; many features are not yet clarified [21]. It is believed a complex non-linear interplay between power, toroidal momentum, and poloidal flow balance is behind establishing and maintaining the transport barrier. Experimental efforts to characterize the transition require diagnostics with temporal resolution in the micro-second level. Access to density, temperature, electric-field, and poloidal-flow measurements as well as their respective fluctuations is required to further elucidate the driving forces at play. A problem with H-mode is the appearance of edge-localized modes (ELMs), which periodically release large amounts of energetic particles to the reactor walls. ELMs present a significant challenge to plasma-facing materials in ignition-relevant devices since they can release up to 20% of the stored plasma energy in under 0.5ms. Understanding H-mode is paramount since it has become the *recipe* to achieve the high tokamak performance.

Recently, other confinement regimes have been discovered which may prove more advantageous for reactor operation. *I-mode*, first transiently discovered in the ASDEX-Upgrade tokamak in 1995, features an edge energy transport barrier without an accompanying particle barrier [22]. H-mode-like energy confinement is achieved without ELMs.

Density profiles remain similar to L-mode, while a temperature pedestal (typical of H-mode) is seen. In the TCV tokamak, the negative triangularity plasma shape can be routinely created. As further addressed in section [1.4 on the facing page](#), it has been identified that electron energy confinement is significantly improved in this shape thanks to the weakening of Trapped Electron mode drift-wave turbulence. The DIII-D tokamak has recently demonstrated that a L-mode negative triangularity plasma can have H-mode like confinement [23] without ELMs. Studying the physics behind these alternative confinement regimes is key to operating tokamaks in the best possible conditions for steady-state operation. Studying these regimes can further elucidate the physics of H-mode or lead towards a yet better regime of operation for future reactors.

1.3.4 ITER and challenges ahead

The current record in fusion power generation is held by the Joint European Torus (JET) tokamak, which in 1997 using a D-T plasma recorded a fusion power output of 16MW against a heating input of 24MW. A Q of 0.67 was held for about 100ms during an ELM-free H-mode discharge [24]. The total electrical power input was in the order of 800MW, but the JET tokamak proved that substantial amounts of energy can be released from a thermonuclear tokamak plasma. The Japanese JT-60U [25] tokamak also achieved excellent confinement properties in pure Deuterium plasmas in 1998. If the fuel had been D-T, the plasma may have reached a Q factor of 1.25. Unfortunately, since the early 1990s no new large tokamaks have been built partly because of the large cost involved in building larger more capable machines than JET (already measuring over 9 meters across).

The next step in tokamak research is the International Thermonuclear Research Experiment, currently under construction in Cadarache, southern France. It is an international collaboration of seven entities: the European Union, India, Japan, China, Russia, South Korea, and the United States. Design began in 1987, and it is currently scheduled for first-plasma operation in late 2025. It has been designed to achieve a Q factor of 5 and possibly 10 using advanced high-pressure scenarios [18]. If successful, it would produce between 250 and 500MW of fusion power with 50MW of input power. It is also ex-

pected to maintain fusion-relevant plasma conditions continuously for up to 16 minutes. Tritium-producing blankets will be installed immediately behind the first wall to prove that tritium can be produced by the fusion plant directly from the neutrons of the D-T reaction. It is still considered an experimental reactor and no net electrical power will be sent to the grid. The project cost is currently estimated around 20 billion USD [26].

Many challenges remain ahead of the success of ITER. Beyond the engineering challenges of building the enormous vacuum vessel, state-of-the-art superconducting toroidal and vertical field coils and divertor heat-exhaust and pumping systems, there are still important plasma physics questions that require robust answers or educated guesses. Avoiding plasma instabilities that cause a rapid ($\sim 20 \mu\text{s}$) plasma disruption [27] has been highlighted as an important priority for ITER. Predictions of thermal, electromagnetic, and fast electron (runaways) loads have to be refined to low uncertainty levels. Schemes to avoid, predict, and/or mitigate these disruptions are also required. Furthermore, numerical simulations of the plasma conditions in ITER's SOL region are important to accurately predict the heat loads released onto the divertor plates of high-power ITER plasmas. ELM heat loads are of special concern.

Another important source of uncertainty remains further quantifying plasma transport in the edge barrier (figure 1-2 on page 8) or pedestal region of H-mode plasmas. The EPED model [28] has managed to successfully predict pedestal height and width based upon the destabilization of two fundamental MHD modes: peeling-ballooning and kinetic ballooning. Yet the role of impurity seeding [29], plasma shape [30, 31], external current drive, and heating mechanism remain areas of active research. These open research questions are the topic of intense research in fusion facilities world-wide. This manuscript details work performed to experimentally characterize the edge region of the TCV tokamak.

1.4 The TCV tokamak

The Swiss Plasma Center (SPC), previously called the Centre de Recherches en Physique des Plasmas (CRPP), is a research center located in Lausanne, Switzerland. Founded in

1961, it is the only research facility in Switzerland devoted to the study of thermonuclear plasmas. SPC's largest experimental facility is the TCV tokamak. TCV is a French acronym for *Tokamak à Configuration Variable*. It became operational in 1992. A 3D model of the machine can be seen in figure 1-3. The main technical specifications of TCV are summarized in table 1.1.

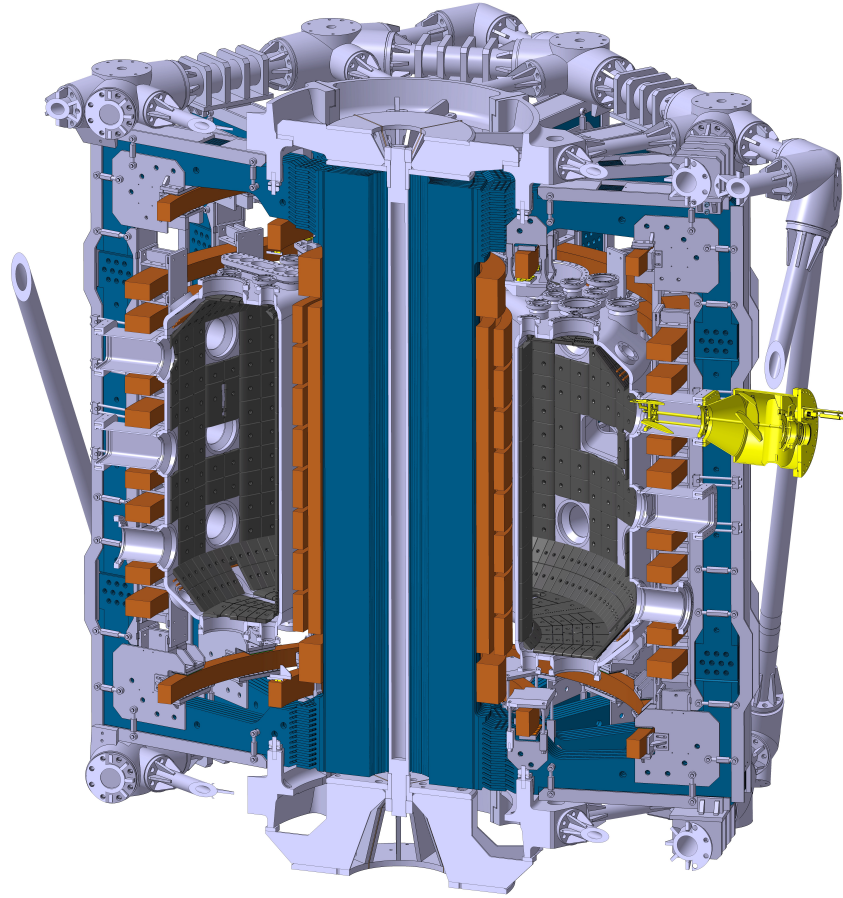


Figure 1-3: 3D model of the TCV tokamak courtesy of Matthieu Touissaint. Toroidal field coils are seen in blue and vertical/ohmic coils in orange. The diagnostic launcher heavily used in this thesis and further described in appendix A is shown in yellow.

TCV's schematic shows large toroidal field coils in dark blue which produce a toroidal field of up 1.54T with coil currents of over 70kA . What sets TCV apart from other tokamaks is both its elongated vacuum vessel and the large number of vertical field coils it possesses. The vacuum chamber is about 3 times as tall as it is wide. It boasts 16 independently powered poloidal field coils, shown in orange above and in greater detail in figure 1-4 on page 18. The combination of both features allows for extraordinary

Parameter	Symbol/Acronym	Value
Toroidal field	B_ϕ	$< 1.53\text{T}$
Plasma Current	I_P	$< 1.2\text{MA}$
Major plasma radius	R_o	0.88m
Minor plasma radius	a	0.25m
Elongation	κ	$0.9\text{-}2.8$
Triangularity	δ	$-0.6\text{ - }+0.9$
Electron cyclotron resonance heating	ECRH	$X_2 (82.7\text{GHz}) < 2.8\text{MW}$ $X_3 (113\text{GHz}) < 1.3\text{MW}$
Neutral beam heating	NBH	$(15\text{-}30\text{keV D}) < 1\text{MW}$ [32]
Plasma-facing material	R6650MX2	Carbon
Plasma density	n_e	$1\text{-}20 \times 10^{19} \text{ m}^{-3}$
Electron temperature	T_e	$1\text{keV}(\text{ohmic}) / 15\text{keV (ECH)}$ [33]
Ion temperature	T_i	$1\text{keV}(\text{ohmic}) / 3.5\text{keV (NBH)}$
Discharge duration typical/maximum		$2\text{s}/4\text{s (ECCD)}$ [16]

Table 1.1: TCV figures of merit as of early 2019

plasma shape flexibility. Plasma elongation (κ) and triangularity (δ) may range from $0.9 < \kappa < 2.8$ and $-0.6 < \delta < 0.9$. Elongation refers to stretching the plasma shape in the vertical over the horizontal dimension. Triangularity refers to how much the plasma resembles a capital D letter by stretching its horizontal dimension. A positive triangularity plasma has the point of the D on the low-field-side, vice versa for negative triangularity. Since both toroidal and vertical field coils are made of copper and not actively cooled, the discharge time is limited to 2 seconds due to Joule heat dissipation.

The evolution from circular to non-circular plasma cross-sections has led to important insights. Firstly, vertical elongation allows a higher toroidal plasma current (I_P) to run stably through the plasma. It scales as $I_P \propto (\kappa^2 + 1)/2$ [34]. A larger plasma toroidal current improves tokamak energy confinement as seen in empirical scaling laws [7, p.509]. Furthermore, vertical elongation allows for larger plasma β values. β is defined as the ratio of the volume averaged plasma pressure to the magnetic field pres-

sure in vacuum. A larger β improves the plasma triple product for a given toroidal field. The Troyon scaling law [14] (an important theoretical CRPP finding) is widely used to compute the ideal MHD stability β limit

$$\beta(\%) = C_T \frac{I_P(\text{MA})}{a(\text{m})B(\text{T})}$$

where C_T corresponds to the Troyon constant between 2-4 depending on plasma conditions. Hofmann et al. [34] provided the first experimental confirmation that the current limit in highly elongated plasmas follows the Troyon scaling up to $\kappa \sim 2.3$ after which it saturates as predicted by theory. Also, Reimerdes et al. [35] found that the ubiquitous central plasma sawtooth oscillation disappears in high elongation plasmas $\kappa > 2.2$. The decrease in sawtooth period and amplitude is linked to the predicted decrease in the central pressure limit of ideal internal kink mode.

Another noteworthy result from TCV's flexibility is the finding that in relatively low-confinement plasmas, the electron energy confinement time improves with decreasing triangularity [36]. In ECRH heated plasmas, only half of the EC power is required at a triangularity of -0.4 compared with +0.4 to obtain the same temperature profiles. Considerable theoretical and experimental effort has been invested in understanding this improved electron confinement. Marinoni et al. [37] found that negative triangularity is found to have a stabilizing influence on ion-scale micro-instabilities, specially on the trapped electron mode (TEM). The stabilization is argued to come as a result of the modification of the toroidal precessional drift of trapped particles caused by the negative triangularity.

Using correlation electron cyclotron emission diagnostics (CECE), Fontana et al. [38] found that the radial fluctuation amplitude and correlation lengths of temperature fluctuations are significantly smaller in negative triangularity plasmas. Using the tangential phase-contrast imaging diagnostic, Huang et al. [39] found that fluctuation amplitude, spectral index, and radial correlation length of radial density fluctuations are also smaller in negative triangularity plasmas. Although triangularity does not penetrate significantly

beyond $\rho_\psi \sim 0.8$, the reduction in density fluctuations extends deep in the core. Both of these studies were performed in ohmic and/or ECH heated L-mode plasmas. High performance fusion reactors are expected to operate in H-mode with the highest possible pedestal pressures. At such large densities, collisionality is expected to be large. Collisionality, defined as $\nu_{\text{eff}} = 0.1Rn_e Z_{\text{eff}}/T_e^2$, has the effect of damping the TEM instability drive. It has been observed that the difference between density fluctuations in positive and negative triangularity plasmas tends to become smaller with higher collisionality [39]. Merle et al. [30] (using the EPED model) have recently shown that negative triangularity plasma shapes result in smaller ELMy H-mode pedestal-top pressures than their positive triangularity counterparts. While this limits the stored energy, it also results in more benign ELMs, as has been seen experimentally.

Another advantage of TCV's flexibility is that it can explore exotic divertor magnetic field configurations. The snowflake divertor [40] is routinely realized in TCV. A snowflake H-mode [41] has also been demonstrated showing a reduced ELM frequency over a regular diverted plasma. Both of these interesting plasma shapes produced by TCV are shown in figure 1-4 along with its complete set of coils.

1.4.1 TCV Heating systems

Toroidal plasma currents of up to 1.2MA can be generated in TCV, allowing ohmic heating power between 0.2-1MW to be released into the plasma. Unfortunately, there are well-understood ideal magneto-hydrodynamic instabilities [14] that limit the maximum current that can be run through a particular plasma shape. In general, the edge safety factor q must remain above 2 to avoid the most restrictive external kink mode [7, p.405].

TCV also features a highly powerful and flexible ECRH system. At its peak, 2.8MW of 82.7GHz second harmonic (X2) and 1.3MW of 118GHz third harmonic (X3) power were available for heating and current drive. A grand total of over 4MW of power for plasmas with average volumes of 1.4m³ results in an ECRH power density of over 2.8MWm⁻³, which is unusually high and allows unique electron energy distribution [42], electron transport barriers [33], and electron-cyclotron current drive [16] studies. It uses modern transmission lines and 3D steerable quasi-optical launchers, one of which is de-

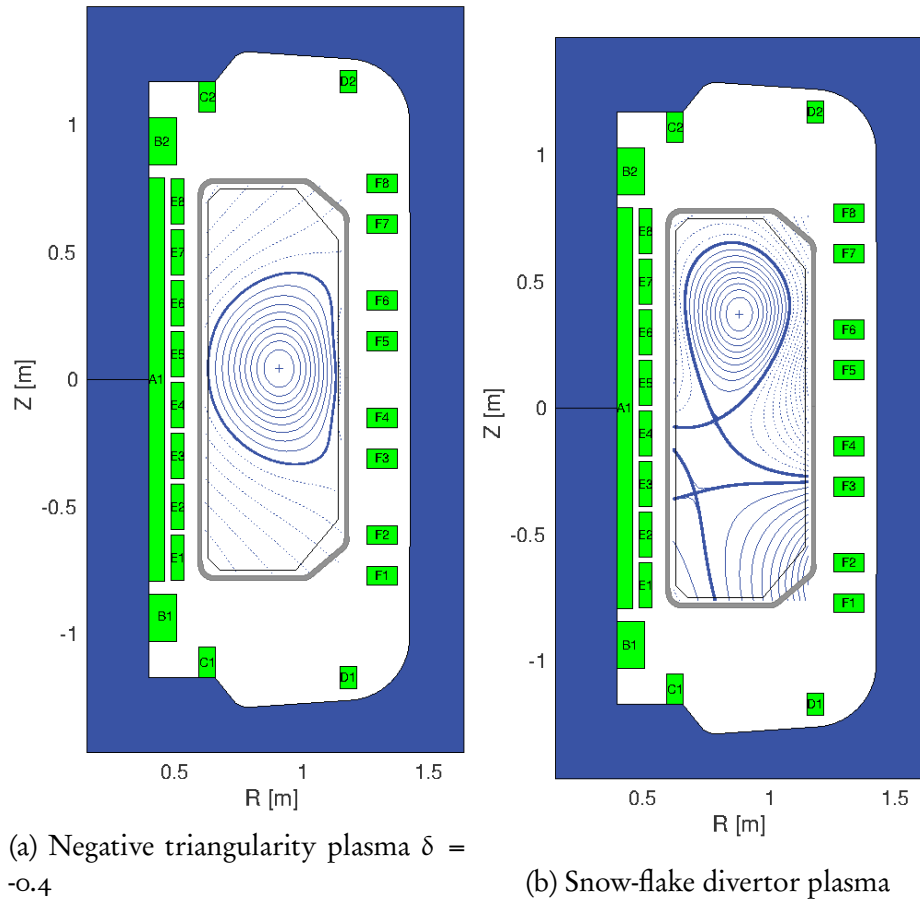


Figure 1-4: Poloidal cross-section of TCV showing its large number of coils permitting exotic plasma shapes: toroidal field coils (blue), the poloidal field coils (green - E and F), and ohmic field coils (green A to D)

scribed in detail in appendix [A on page 159](#). Upgrades are planned including the installation of two additional 1MW dual-frequency (X₂ and X₃) gyrotrons in the second half of 2019.

TCV was also recently fitted with a neutral beam heating system in 2015[32]. 1MW of a focused deuterium beam with 15-30keV energy is available for up to 2 seconds. Record ion temperatures of up to 3.5keV in TCV have been achieved in ELMy H-mode. Momentum injection provided by the neutral beam has also allowed toroidal rotation velocities of up to 160km/s. A second 1MW 50-60keV neutral beam is planned for 2020. The combined upgraded ECRH and NBH power could bring TCV's plasmas close to the β -limits in H-mode, which is a relevant research regime for ITER plasmas [32].

1.4.2 TCV diagnostics

With over 25 years of operation, TCV is a very well diagnosed tokamak. Table 1.2 attempts at highlighting the current diagnostics installed in TCV.

Name	Parameter	dR[cm]/No.points	dt
Thomson Scattering (TS)	T_e, n_e	0.6-1.7/89	16 ms
Interferometer (FIR)	$\int n_e dl$	2.8/14vl	50μs
Tangential phase contrast imaging (TPCI)	$\delta n_e(k_r)$	0.25	0.6-100μs
(CXRS) Charge Exchange Recombination Spectroscopy	v_θ, v_ϕ	0.3-1 4 × 40vl	60-90 ms
Fast Reciprocating probe (RPTCV)	T_e, n_e, ϕ_p, v_{id}	0.2	2-500μs
Wall-mounted Langmuir probes	T_e, n_e, ϕ_p	1.6/114	5 μs
Magnetic probes	$\frac{dB_\theta}{dt}$	203	4 μs
Electron Cyclotron Emission (ECE)	$T_e, \delta T_e$	2	0.1ms - 1μs
Compact Neutral Particle Analyzer (CNPA)	0.5-50keV neutrals	1vl: 15-30° view angle	2.5-0.01ms
Photodiodes (PD)	Line radiation 380-740nm	9vl	20μs
Foil Bolometers (BOLO)	$\int \frac{dP_{rad}}{dV} dl$ (2eV-2keV)	64vl	0.5ms
Ultraviolet bolometers (AXUV)	$\int \frac{dP_{UV-rad}}{dV} dl$ (1.2eV-6keV)	140vl	5μs
Soft X-rays (XTOMO)	$\int \frac{dP_{Brem}}{dV} dl$ (>1keV)	200vl	10μs
Soft X-ray counter (DMPX)	$\int \frac{dP_{Brem}}{dV} dl$ (3-30keV)	64vl	5 μs
Hard X-ray Tomographic Spectrometer (HXRS)	$\int \frac{dP_{Brem}}{dV} dl$ (10-200keV)	101vl	83 ns
Reflectometry	$n_e, \delta n_e(k_r)$	0.4-1	<2 μs
Doppler Backscattering	$v_\theta, \delta n_e (k_\theta), S(\vec{k}_\theta)$	0.4-1	<1 ms

Table 1.2: TCV diagnostics overview. These are roughly divided between active and passive by a double horizontal line. LOS stands for line of sight and highlights that these diagnostics have the ability to sample anywhere inside the LOS. ‘vl’ stands for view lines. The last two diagnostics are discussed in detail in this document.

In table 1.2 'Brem' stands for Bremsstrahlung radiation which is a German word that means breaking radiation. It refers to radiation emitted by accelerated electrons during collisions with electrons or ions. It is strongly dependent on plasma density and more weakly on electron temperature. It also linearly increases with a larger Z_{eff} . In table 1.2 'rad' refers to total radiation, and it is composed of both line radiation from excitation/recombination and Bremsstrahlung. It is beyond the scope of this introduction to describe the working principles of each of the above diagnostics. Only a few relevant diagnostics to this thesis will be briefly presented here.

Plasma density measurements play an essential role in the study and operation of tokamaks [43]. In TCV, electron density and temperature measurements from the plasma core to the LCFS are routinely available from the Thomson Scattering (TS) diagnostic with a radial resolution of about 0.6 – 1.7cm but only 60Hz temporal sampling. This diagnostic uses the incoherent Thomson scattering light from a powerful (1.5J) 1.06 μm wavelength Nd:YAG laser. Plasma electrons are accelerated in the laser electric field and emit radiation at the same frequency of the incident wave. The strength and broadening of this scattered light allow measurement of electron density and temperature, respectively. Further details on the working principles can be found here [44]. Figure 1-5a on the facing page shows the location of the main laser line and the view lines where the TS samples density and temperature.

Plasma density measurements may also be obtained from the far infrared interferometer diagnostic (FIR). It uses 14 parallel CH_2F_2 laser (184.3 μm) vertical chords separated by about 2.8cm. Interferometry measures the line-integrated plasma density through each chord by measuring the phase difference with respect to a reference beam. It uses Mach-Zehnder heterodyne detection to access this phase difference [45]. FIR is an integral part of TCV's plasma start-up and control. The FIR view lines are shown in figure 1-5b on the next page below.

The magnetic probes measure the time derivative of the poloidal magnetic flux in over 200 passive coils positioned symmetrically around the machine as shown in figure 1-5c on the facing page. There are 6 toroidal arrays of 17 probes each covering the low-field side top, mid, and bottom. The high-field side contains 8 probes on top, mid, and

bottom. These toroidal arrays allow the identification of toroidal (or 'n') mode numbers. There are also 4 poloidal arrays with 38 probes each in sectors 3, 7, 11, and 15 each separated by 90 degrees. These may allow in some cases the identification of poloidal ('m') mode numbers. The geometry of the poloidal arrays is shown in figure 1-5c along with the vertical location of the toroidal arrays.

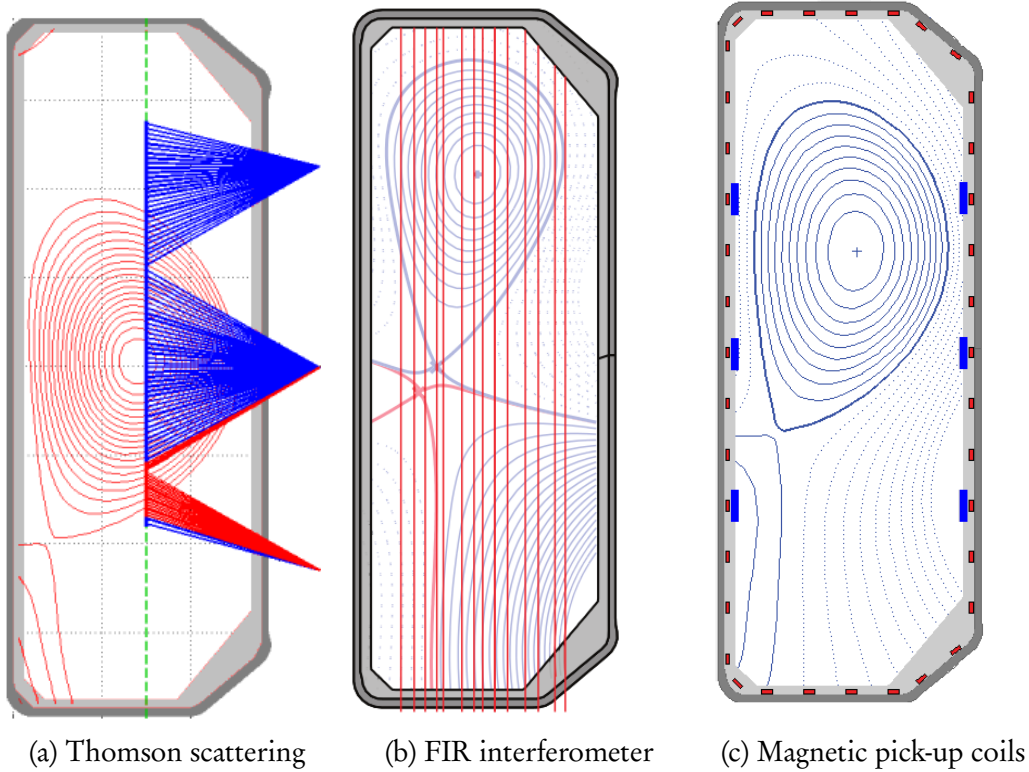


Figure 1-5: 2D poloidal cross-section geometry and sampling locations of TCV diagnostics used in this thesis.

Another diagnostic used in the following discussion is a D_α photodiode (PD). This is a PN-junction semiconductor diode where incident light is transformed into electric current via the photoelectric effect. TCV's D_α PD features a filter at 656.3nm which permits only Balmer alpha (H/D_α) line radiation to generate an electric signal. This radiation results from the collisional excitation of neutral hydrogen or deuterium atoms when these interact with the plasma. Much of this radiation is emitted in the edge since plasma temperatures are low and neutral hydrogen/deuterium atoms can be found [11, p. 537]. According to Owen et al. [46], using models for D_α emission and transport, the intensity of the D_α signal can indicate the plasma environment where the radiation

occurs and the plasma fluxes towards the reactor walls. It is mostly used in this thesis as a qualitative signature of the occurrence of ELM instabilities which generate spikes in this signal due to large amounts of hot plasma being expelled towards the divertor region following the instability. It is important to carefully interpret the D_α signal as pointed out by Zohm [47] since as explained above it can depend both on particle fluxes and divertor conditions: with a fully detached divertor, the D_α signal would no longer be a sound ELM sensor. TCV's D_α photodiode signal is acquired at 10kHz and is installed on top of the vessel looking vertically down from top to bottom.

1.5 This thesis

Acting as a bridge between disparate core and SOL plasmas, the *edge* region (see figure 1-2 on page 8) has been long known to play a key role in overall confinement. Electron transport in the edge region of L-mode plasmas has been recently found by Sauter et al. [48] to directly respond to changes in plasma current, input power, and triangularity in strong contrast to the rest of the profile ($\rho_V = 0 - 0.8$) which remains *stiff* (fitted with the same scale-lengths). There is a pressing need to further quantify experimentally plasma quantities such as density, temperature, potential, and flow in the edge region with increased temporal and spatial resolution.

As shown in table 1.2 on page 19, two new edge diagnostics have been added to the diagnostic list during this PhD thesis. The main motivation has been to improve the temporal and spatial resolution of plasma edge density and rotation measurements in TCV. The principles of reflectometry and Doppler backscattering (DBS) will be addressed in the theory chapter 2 on the facing page below. The design, implementation, and first results of TCV's DBS diagnostic are presented in chapter 3 on page 51. A literature review of various reflectometry techniques including short and ultra-short pulse reflectometry is presented in chapter 4 on page 81. The conclusions from the latter motivate the design and implementation of TCV's short-pulse reflectometer (SPR) diagnostic presented in chapter 5 on page 109. A first-order study of SPR data during ELMy H-mode shots is presented in section 5.3.5 on page 142.

Chapter 2

Principles of Reflectometry

2.1 Cold plasma wave theory

In order to understand the theoretical basis of the reflectometry technique, the propagation of electromagnetic waves in a cold plasma is briefly addressed. Details on derivations can be found in [49] [ch.2], [50] [ch.6], [51] [ch.4], and [43]. Starting with Maxwell's equations, the curl of Faraday's equation leads to the wave equation:

$$\nabla \times (\nabla \times \vec{E}) = -\mu_0 \frac{\partial \vec{j}}{\partial t} - \frac{1}{c^2} \frac{\partial^2 \vec{E}}{\partial t^2} \quad (2.1)$$

The plasma properties enter into the above equation through the current density term; it can be assumed proportional to the electric field through a *conductivity* $\bar{\sigma}$ tensor. This tensor is found by linearizing the second moment of the Boltzmann-Vlasov equation (the momentum equation) for both ions and electrons in a cold ($T=0$) magnetized two-fluid plasma model [50] (ch.6). Assuming that the perturbed system is *uniform* and *stationary*, Fourier decomposition leads to:

$$\vec{j}_{\omega,\vec{k}} = \vec{\bar{\sigma}}_{\omega,\vec{k}} \cdot \vec{E}_{\omega,\vec{k}} = \sum_{\alpha} q_{\alpha} n_{\alpha 0} \vec{u}_{\alpha 1} \quad (2.2)$$

$$-\vec{k} \times (\vec{k} \times \vec{E}_{\omega,\vec{k}}) = i\omega\mu_0 \vec{\bar{\sigma}} \cdot \vec{E}_{\omega,\vec{k}} + \frac{\omega^2}{c^2} \vec{E}_{\omega,\vec{k}} \quad (2.3)$$

$$-\frac{c^2}{\omega^2} \vec{k} \times (\vec{k} \times \vec{E}) = \vec{\bar{\epsilon}} \cdot \vec{E} \quad (2.4)$$

$$\left(N^2 \left[\frac{\vec{k}\vec{k}}{k^2} - \vec{1} \right] + \vec{\bar{\epsilon}} \right) \cdot \vec{E} = 0 \quad (2.5)$$

where N is the refractive index ($N^2 = \frac{k^2 c^2}{\omega^2} = \frac{c^2}{v_{ph}^2}$), \vec{k} is the wave-vector, $\vec{\bar{\epsilon}}$ is the dielectric tensor $\vec{\bar{\epsilon}} = \frac{i\vec{\bar{\sigma}}}{\epsilon_0 \omega} + \vec{1}$ (representing the plasma relative permittivity). Dyadic notation has been used in 2.5 to represent the double \vec{k} cross product. The left hand side term on the last equation above is a *dispersion relation* that characterizes the dynamics of the wave-vector at a given frequency in the plasma. Assuming that the wave-vector is perpendicular to the magnetic field, two solutions to equation 2.5 are found: the ordinary (O) and extraordinary (X) modes with refractive indexes:

$$N_{OM}^2(E_1 \parallel B_0) = 1 - \frac{\omega_{p,e}^2}{\omega^2} \quad (2.6)$$

$$N_{XM}^2(E_1 \perp B_0) = \frac{(\omega^2 - \omega_R^2)(\omega^2 - \omega_L^2)}{(\omega^2 - \omega_{UH}^2)(\omega^2 - \omega_{LH}^2)} \quad (2.7)$$

where $\omega_{R,L,UH,LH}$ are defined in table 2.1 below. The *reflectometer* diagnostic uses the fact that, for certain frequencies, the plasma's refractive index can vanish: a so-called *cutoff*. At this point $N^2 = 0 \rightarrow \frac{\omega}{k} \approx \infty (k \rightarrow 0, \omega \neq 0)$ and the wavelength of the wave becomes essentially infinite: a decaying exponential function. Thus, the wave energy is **reflected**. At the other extreme where the refractive index approaches infinity, a *resonance* is encountered. Upon reaching a resonance, the wave may change oscillation modes and/or be absorbed. Table 2.1 below summarizes both cutoffs and resonances of O and X modes. In this table, $\Omega_{e,i} = q_{e,i} B / m_{e,i}$ is the cyclotron frequency.

Figure 2-1 illustrates the polarization geometry of these two solutions. In the O-mode polarization, electrons accelerated in the field E_1 do not feel the presence of the

Mode	Cut-off	Resonance
O-mode	Electron Plasma Frequency	
	$\omega^2 = \omega_{pe}^2 = \frac{n_e e^2}{\epsilon_0 m_e}$	
X-mode	R and L frequencies	Hybrid resonances
	$\omega_{R,L} \cong \frac{1}{2} \left(\sqrt{\Omega_e^2 + 4\omega_{pe}^2} \pm \Omega_e \right) \quad \omega_{LH}^2 = \Omega_e \Omega_i \frac{1 + \frac{m_e}{m_i} \left(\frac{\Omega_e}{\omega_p} \right)^2}{1 + \left(\frac{\Omega_e}{\omega_p} \right)^2}$	
	$\omega_{UH}^2 \simeq \omega_{pe}^2 + \Omega_e^2$	

Table 2.1: Cut-offs and resonances of plasma waves in perpendicular incidence to a cold magnetized plasma.

background magnetic field since they do not feel the Lorentz force. Table 2.1 shows that for this reason the O-mode cutoff frequency is only a function of the electron density. On the other hand, in X-mode the cutoffs depend on both the electron density and the magnetic field. Note that the X-mode as shown in figure 2-1b on the next page is not perfectly transverse electro-magnetic (TEM) as the O-mode, since it allows both x and y components of E_1 . This is true inside the plasma. In order to couple this wave into the plasma, however, a perfect TEM is required for vacuum propagation in which case E_1 needs to be perfectly aligned with the x-axis in figure 2-1 [49].

Figure 2-2 and 2-3 illustrate the cold-plasma resonances (except the LH resonance which lies below 1GHz) and cutoffs for both O and X-modes for typical L and H-mode discharges in TCV. Density profiles were obtained from smoothing TS data. The figures also include the first three harmonics of the cyclotron frequency and horizontal dashed lines showing the electron-cyclotron heating frequencies in TCV for second (X_2 at 82.7GHz) and third-harmonic ECH heating (X_3 at 118GHz).

These figures reveal important information regarding the best frequency band to sample typical TCV plasmas. It shows that a good portion of the density profile may be sampled by U-band(40-60GHz) or V-band(50-75GHz) reflectometers if the polarization can be made to vary between O and X-mode. The U-band seems ideally suited to sam-

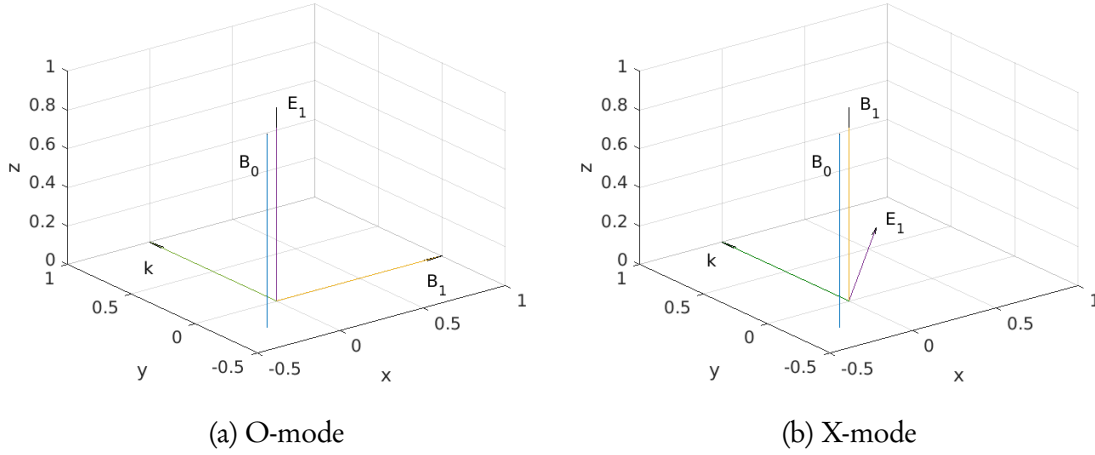


Figure 2-1: Polarization geometry (subscript '1') of both solutions to the cold-plasma dispersion relation along with propagation direction (k) and background magnetic field B_0

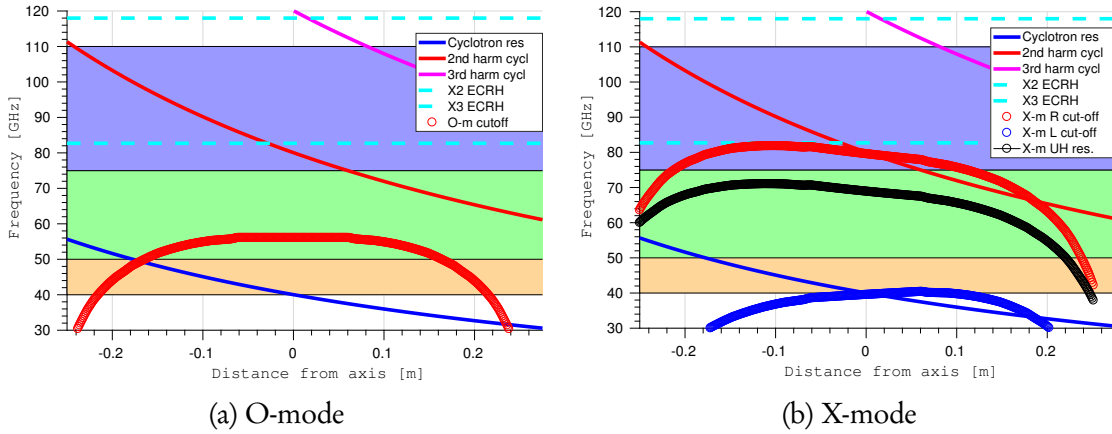


Figure 2-2: Cut-offs and resonance during typical L-mode shot 60572 at 0.85s. U, V, and W mm-wave bands are shown in yellow, green, and violet.

ple L-mode plasmas in both modes. Yet, in H-mode, the X-mode polarization would only access the bottom of the pedestal. V-band misses the bottom of the profile in L-mode plasmas, but it has the potential to access both the bottom and top of the H-mode pedestal by switching between X and O-mode polarization. W-band (75-110GHz) may be of interest exclusively if the waves could be launched from the high-field side.

Thermal corrections to the cold-plasma cutoffs presented here become important only for electron temperatures exceeding 5keV [49, pg.96]. Temperatures of up to 17keV can be achieved with large quantities of ECRH heating in TCV [33], but during the

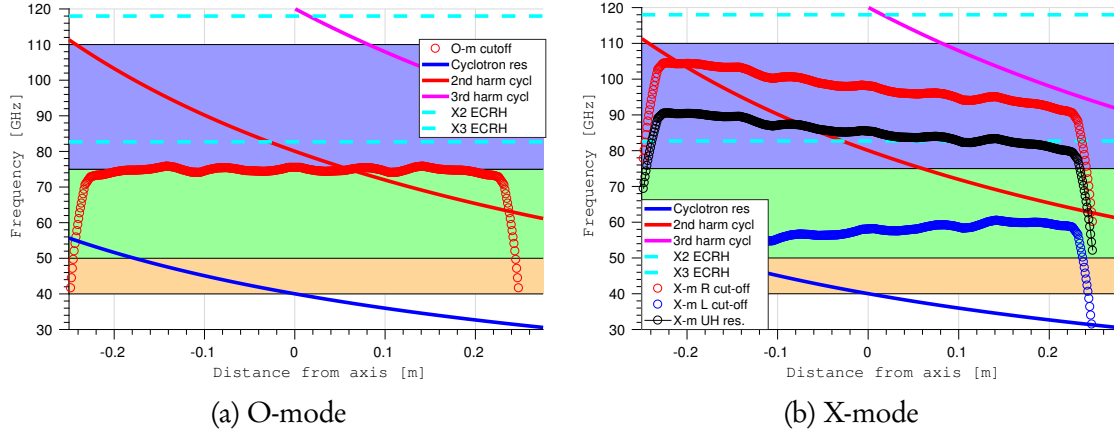


Figure 2-3: Cut-offs and resonance during typical H-mode shot 62734 at 1.2s. U, V, and W mm-wave bands are shown in yellow, green, and violet.

typical TCV ohmic H-mode shot 62734, for example, they reach only about 1.5keV. The cold-plasma approximation presented above is used henceforth.

2.2 Spatial localization and beam refraction

2.2.1 WKB approximation

The Wentzel-Kramers-Brillouin (WKB) method allows one to solve the wave equation 2.4 in inhomogeneous media under the assumption that these inhomogeneities are gradual compared to the sampling vacuum wavelength. Assuming the propagation of a beam in a one-dimensional plasma featuring inhomogeneities along the direction of travel, equation 2.4 can be cast in the form of a Helmholtz equation ([49, ch.2.8]).

$$\left[\frac{d^2}{dx^2} + \frac{\omega^2}{c^2} \epsilon_r(x, t) \right] E(x, t) = 0 \quad (2.8)$$

Taking an *ansatz* for the electric field solution $E(x, t) = E_0 e^{i[\vec{k}(x)x - \omega t]} = E_0 e^{i[\phi(x) - \omega t]}$ into the above equation yields.

$$i \frac{d^2 \phi(x)}{dx^2} - \left(\frac{d\phi(x)}{dx} \right)^2 + k^2(x) = 0 \quad (2.9)$$

Where $k^2 = \frac{\omega^2}{v_{ph}^2} = \omega^2 \epsilon_r \epsilon_0 \mu_0$. In a *smoothly varying* plasma, the $d^2 \phi(x)/dx^2$ term

is expected to be small and negligible with respect to $k^2(x)$. That would imply that $d\phi(x)/dx = \pm k(x)$ and thus that $d^2\phi(x)/dx^2 = \pm dk(x)/dx$. Replacing the latter in the above equation and integrating yields:

$$\frac{d\phi(x)}{dx} = k(x) \sqrt{1 \pm i \frac{1}{k^2(x)} \frac{dk(x)}{dx}} \approx k(x) + i \frac{1}{2} \frac{1}{k(x)} \frac{dk(x)}{dx} \quad (2.10)$$

$$\phi(x) = \pm \int_0^x k(x') dx' + i \ln \left(\sqrt{\frac{k(x)}{k(0)}} \right) \quad (2.11)$$

Equation 2.11 connects a measurable phase difference with plasma conditions through the above definition of \vec{k} from the dispersion relation 2.5. This approximation is valid as long as the starting assumption holds, namely $\frac{d^2\phi(x)}{dx^2} \ll k^2(x)$.

2.2.2 Airy width

Unfortunately, near the cutoff layer, as the refractive index rapidly approaches zero, the WKB approximation breaks down. If it is assumed that at the cutoff region the refractive index goes towards 0 in a linear fashion, it was shown by Ginzburg [52] that the round-trip phase-shift can be expressed in a WKB-like form:

$$\Phi_{\text{round trip}} = 2 \int_0^{x_c} \vec{k}(x') dx' - \frac{\pi}{2} \quad (2.12)$$

where $x = x_c$ the cutoff point. The factor of two indicates the round-trip to the reflection point. This result is derived by changing variables in the Helmholtz equation to arrive at Stokes equation whose solutions are Airy integral functions. The asymptotic versions of these integrals were matched to the WKB solution away from the cutoff. Figure 2-4 shows the shape of these Airy functions near the cutoff. The FWHM of the last maximum of $\text{Ai}^2(\zeta)$ gives the spatial localization of the reflecting layer. By reversing the change of variables performed to arrive at the Stokes equation, the spatial width of this region can be found to be:

$$\Delta x \approx \frac{1.6}{\left[\left(\frac{\omega}{c} \right)^2 \frac{d(N^2)}{dx} \Big|_{x=x_c} \right]^{1/3}} \quad (2.13)$$

which for O-mode simplifies to $\Delta x_{OM} \approx \frac{1.6}{\left[\left(\frac{\omega}{c} \right)^2 \frac{1}{L_n} \right]^{1/3}}$ where $L_n = n_e / (dn_e/dx)$ is the gradient scale length of the density profile at the cutoff point. It can be seen from the latter that a steep density profile at the cutoff point results in highly localized measurements, while the opposite occurs for flat density-profile gradients. Reflectometry is, therefore, ideally suited to resolve steeply-varying density profiles, such as those found in the edge and pedestal regions of a tokamak. However, it is also precisely where large gradients occur that the WKB approximation can break down. As shown in [49, p. 89] and by the magenta line in figure 2-5 on the following page, WKB holds inside the pedestal region of H-mode plasmas but truly breaks down in the SOL region as the density rapidly drops to zero.

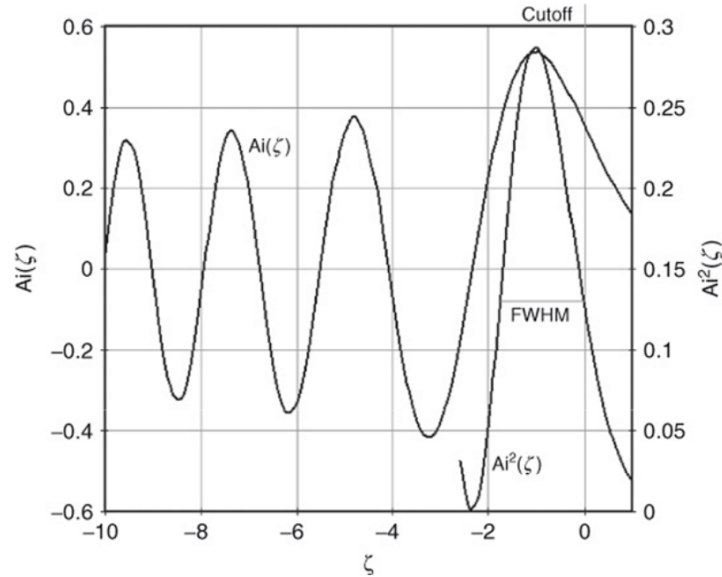


Figure 2-4: The Airy-integral function $Ai(\zeta)$ representing the \vec{E} -field of a wave approaching a cutoff at $\zeta = 0$. Taken from figure 3.17 in [49, p. 90]. $\zeta = d/dx(k^2)^{1/3}(x - x_c)$

Figure 2-5 on the next page plots the Airy widths for both modes in TCV shots 60572(LM) and 62632(HM). This figure shows that the reflection layer extent translates

into \sim cm resolution in O-mode and sub-cm resolution in X-mode. X-mode polarization allows for better localization given that the refractive index depends both on the density and magnetic field: the refractive index gradient approaching the cutoff can be larger than in O-mode. Both polarizations provide sub-cm localization in regions near the edge, particularly in the H-mode pedestal in figure 2-5 b. The WKB validity condition for O-mode can be analytically expressed as $kL_n \gg 1$. The value of kL_n is also plotted on the same (right-hand) axis as the Airy width in figure 2-5 to illustrate that, in O-mode, the WKB approximation is valid in the confined plasma edge.

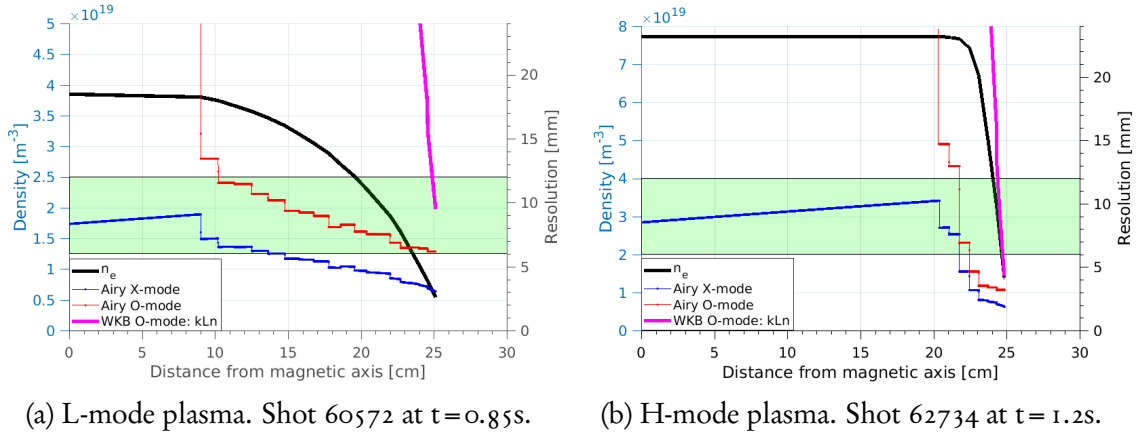


Figure 2-5: Airy width for both X and O modes inside L and H mode plasmas. The resolution range of the TS diagnostic, 0.6-1.2cm, is illustrated via a green transparent rectangle.

Figure 2-5 shows that the O-mode polarization cannot sample flat density profiles featured towards the core of both L and H-mode plasmas. This is because the cutoff depends entirely on the density. Conversely, the X-mode polarization is still able to resolve the density profiles due to its dependence on the magnetic field which is constantly varying in a tokamak. Figure 2-5 shows that the X-mode Airy width remains competitive with the TS diagnostic inside the core of TCV plasmas.

The O-mode polarization is also unable to sample hollow density profiles. The X-mode may allow sampling of hollow profiles as long as the increase in magnetic field is larger than the decrease in density profile, albeit at reduced resolution. Strongly hollow core profiles are observed when high quantities of ECRH powers are coupled to the core of TCV plasmas in so-called *pump-out* discharges [53].

2.2.3 Refraction and geometric optics

Tokamak plasma geometry is not one-dimensional. The plasma properties change both parallel and perpendicular to the beam's propagation direction. Such inhomogeneities, as in the classical case of Snell's law, cause refraction and thus steer the probing beam's direction of propagation. This refraction can be quantified assuming that inhomogeneities remain gradual compared to the wavelength, invoking again the WKB approximation. Equation 2.4 can be written in three dimensions:

$$[\nabla^2 + k^2(\vec{r}, t)] \vec{E}(\vec{r}, t) = 0 \quad (2.14)$$

Assuming a trial solution, we obtain:

$$\begin{aligned} \vec{E}(\vec{r}, t) &= \vec{E}_o(\vec{r}) \exp i[k_0 S(\vec{r}) - \omega t] \\ \nabla^2 \vec{E}_o + \left[\frac{k^2}{k_0^2} - (\vec{\nabla} S) \cdot (\vec{\nabla} S) \right] k_0^2 \vec{E}_o &= 0 \end{aligned}$$

where k_0 is the vacuum wavenumber and the function $S(\vec{r})$ is called the *eikonal* function (from Greek, for image [54, p. 316]). Because $k_0 S(\vec{r})$ contains the periodic spatial variation of the trial solution, a set of wavefronts are defined by 2π increments of $k_0 S$. Since by definition the refractive index $N^2 = \frac{c^2}{v_{ph}^2} = \frac{k^2}{k_0^2}$, and neglecting the $\nabla^2 \vec{E}_o$ term on the basis of the WKB approximation, the above equation becomes:

$$\vec{\nabla} S \cdot \vec{\nabla} S = |\nabla S|^2 = N^2 \quad (2.15)$$

$$\nabla S = N(\vec{r}) \hat{s}(\vec{r}) \quad (2.16)$$

where the unit vector \hat{s} is perpendicular to the wavefront and parallel to the direction of motion. The wave's refraction can thus be studied with this approach during propagation in inhomogeneous media along a single ray path. This approach is thus called *ray-tracing* or *geometric optics* approximation. Unfortunately, it cannot formally

provide details regarding the evolution of the width of a beam, for example. It is useful when the characteristic system size and dimensions of interest are much larger than the wavelength. The function S can be eliminated from the above equation through vector identities [54, pg318] to obtain the ray tracing equation:

$$\frac{d}{ds}(N\hat{s}) = \nabla N \quad (2.17)$$

This first order ordinary differential equation allows one to describe the path of a ray given an initial direction \hat{s}_0 and a refractive index map defined in two or three dimensions. Careful modeling of the beam's refraction is important in reflectometry since the cutoff can be encountered deep inside the plasma. Depending on the specific approach to reflectometry either at near-perpendicular incidence or at an angle to the cutoff layer, ray tracing is a first-order calculation that is vital to planning experiments. Quantifying refraction is particularly important in tokamaks such as TCV with their rich variety of plasma shapes. Figure 2-7 on page 48 shows an example of quantifying refraction by solving equation 2.17 above in a 2D geometry where the plasma density varies along the horizontal dimension.

Unfortunately, since the equations derived above treat the beam as a single ray, interference and diffraction effects are not taken into account [55]. Diffraction effects can become important where the beam's width $W \sim \sqrt{\lambda L}$ where L is the inhomogeneity scale length of the medium. In the SOL and pedestal regions of H-mode plasmas, diffraction may become important. Parabolic equation, complex-eikonal, or beam-tracing methods [55] can be used to quantify these effects. Their description is beyond the scope of this thesis, but the implementation of such methods should be pursued in earnest by future reflectometry efforts in TCV. Since tokamak plasmas are highly turbulent media, the beam can also undergo scattering on the way towards and/or at the cutoff layer. Further details are presented in section 2.4 on page 37

2.3 Measuring density profiles - $n_e(\rho_\psi)$

In reflectometry, the electron plasma density can be inferred from the round-trip group-delay of waves reflected from a plasma cutoff. The previous section derived a relationship between phase and wave-number within the WKB approximation. The refractive index of both X and O-mode waves was derived from the cold-plasma dispersion relationship above. In the case of OM, the group-delay defined as $v_g = \partial\phi/\partial\omega$ becomes:

$$\phi_{OM} = \frac{2}{c} \int_{x_e}^{x_c} \sqrt{\omega^2 - \omega_p^2(x)} - \frac{\pi}{2} \quad (2.18)$$

$$\frac{\partial\phi_{OM}}{\partial\omega} = \frac{2\omega}{c} \int_{x_e}^{x_c} \frac{dx}{\sqrt{\omega^2 - \omega_p^2(x)}} \quad (2.19)$$

where x_e refers to the distance between the antenna and the plasma edge and x_c refers to the cutoff position with respect to the antenna. Equation 2.19 shows that reflectometry in plasmas is fundamentally different from conventional radar. The group-delay of pulses in reflectometry is not only a function of the location of the target (or the cutoff layer in this case) but also of the plasma conditions to and from this point. In radar applications, the refractive index of air can be assumed to be constant all along the path; therefore, the group-delay is directly proportional to the distance to the target. A change of variables in equation 2.19 [56, p. 147] above leads to:

$$\text{if } \lambda = \frac{2\pi c}{\omega} \text{ and } \lambda_p = \frac{2\pi c}{\omega_p} \quad (2.20)$$

$$\frac{d\phi}{d\omega} = 2 \int_{\lambda_e}^{\infty} \left(\frac{dx_c}{cd\lambda_p} \right) \frac{\lambda_p d\lambda_p}{\sqrt{\lambda_p^2 - \lambda^2}} \quad (2.21)$$

It turns out that equation 2.21 has the same form as the projection of a radial function over a number of parallel chords if we let $\partial\phi/\partial\omega \rightarrow F(y)$, $\frac{dx_c}{cd\lambda_p} \rightarrow f(r)$, $\lambda \rightarrow y$, and $\lambda_p \rightarrow r$. Such integral functions can be transformed into a radial function by applying the so-called Abel transform:

$$F(y) = 2 \int_y^\infty f(r) \frac{r dr}{\sqrt{r^2 - y^2}} \rightarrow f(r) = -\frac{1}{\pi} \int_r^\infty \frac{dF}{dy} \frac{dy}{\sqrt{y^2 - r^2}} \quad (2.22)$$

$$\frac{\partial \phi}{\partial \omega} \rightarrow x_c(\omega) = a - \frac{c}{\pi} \int_0^\omega \frac{\partial \phi}{\partial \omega'} \frac{d\omega'}{\sqrt{\omega^2 - \omega'^2}} \quad (2.23)$$

Thus the location of the reflection point at a given cutoff frequency ω can be localized if $\partial \phi / \partial \omega$ (group-delay) is measured for many smaller frequencies, starting from zero. Practically, however, it is not possible to launch waves from zero frequency all the way up to the U/V bands. Thus, the group-delay curve for frequencies below 40 or 50GHz must be obtained from other measurements or from educated guesses. In TCV, the TS diagnostic can provide a reliable initialization of the profile, but the different sampling times of the two diagnostics could pose problems. Another option is to extrapolate from the lowest frequency point to the edge of the plasma, in which case a certain SOL density profile must be assumed [57]. Recent measurements of the SOL density profiles performed with the fast reciprocating probe diagnostic in TCV permit accurate estimations of these $\partial \phi / \partial \omega$ profiles [58] as further developed practically in section 5.3.4 on page 136.

In X-mode there is no analytical inversion formula such as the Abel transform to convert measured group delays over frequency to cutoff location over frequency. Numerical inversion is required [59]. The most widely used algorithm was proposed by Bottolier-Curtet and Ichchenko in 1987 [60]. There are modern alternatives recently published by Shelukhin et al. [61] and Morales et al. [62], but the well-established Bottolier approach is presented here as a first order effort with a simpler implementation. It consists of estimating the successive cutoff radial locations in an iterative process that uses measured phase differences between adjacent frequencies:

$$R(i+1) = R(i) + \frac{\frac{c}{2} \frac{(\phi_{i+1} - \phi_i)}{2\pi} - S_n(i+1)}{\frac{F(i+1)}{2} N(R(i), F(i+1))} \quad (2.24)$$

$$S_n(i+1) = F(i+1) \int_{R_{Ref.}}^{R(i)} N(r, F(i+1)) dr - F(i) \int_{R_{Ref.}}^{R(i)} N(r, F(i)) dr \quad (2.25)$$

$$N_{XM} = \sqrt{\frac{(\omega^2 - \omega_R^2)(\omega^2 - \omega_L^2)}{(\omega^2 - \omega_{UH}^2)(\omega^2 - \omega_{LH}^2)}} \quad (2.26)$$

where R is the distance to the cutoff layer along the beam path, and F stands for frequency. The quantity $S_n(i+1)$ can be geometrically interpreted as the difference between the area under the curve of the refractive index over distance from the cutoff between two adjacent frequencies [60]. In successive iterations, it is important to let $S_n(i+1) = (S_n(i+1) - S_n(i))/2$ in order to damp numerical instabilities that can arise due to noise in the phase measurements or changes in the location of the first frequency cutoff. It is important to note that the Bottolier-Curtet algorithm uses experimental data in the form of a phase difference $(\phi_{i+1} - \phi_i)$ between two frequencies and not the group-delay as the Abel transform in the O-mode in equation 2.23 on the preceding page above.

Once the $i+1$ cutoff point is found, precise knowledge of the background magnetic field is required to solve for $N(R(i+1), F(i+1)) = 0$ in order to obtain the density at point $R(i+1)$. The background vacuum toroidal field of the tokamak can be taken as a first approximation. If the equilibrium reconstruction is available, it can contribute with a precise knowledge of the poloidal field. The latter can be up to 20% of the vacuum toroidal field in the edge of tokamak plasmas, which contributes with a 2% correction to the vacuum toroidal field. Diamagnetic or paramagnetic effects further accentuate this difference towards the plasma core.

Inverting X-mode profiles also requires profile-initialization inputs. First, the shape of the refractive index from a *reference* point up to the first cutoff is required for all frequencies. This implies the assumption of particular density and magnetic field profiles. Second, the location of the first cutoff R_1 must be known from other measurements or from assumed density and magnetic field profiles. Fortunately, in the exclusive case of

X-mode, at the plasma-wall interface with the density approaching zero, the cutoff frequency (R cutoff above) corresponds to the cyclotron frequency. In the low-field-side vessel edge of TCV, the cyclotron frequency is about 33 GHz. Thus, it is practically possible to measure group-delays all the way down to the plasma-wall interface. However, the large, sub-cm, changes in density profile in the SOL lead to violation of the WKB approximation (equation 2.11) and can also violate Ginzburg's assumption that N^2 is linear at the cutoff (see discussion before equation 2.12). This is made worse by the longer wavelengths of lower frequencies which can span a significant fraction of the SOL density profile. Nonetheless, SOL density-profile reflectometers have been built [63].

Another concern in the SOL is that the R cutoff is found in close proximity to the UH resonance (see figures 2-2b on page 26 and 2-3b on page 27). Tunneling can occur, which would lead to absorption of the launched wave and/or mode conversion. It was calculated by Schubert [64], that for densities of $2 \times 10^{16} \text{m}^{-3}$, up to 20% of the waves' energy may be lost to the resonance. This calculation was done for the ASDEX Upgrade tokamak, with a toroidal field of 3.1 T on axis. It remains a valid order-of-magnitude estimate for TCV. Tunneling can thus be a concern if group-delay measurements are attempted in TCV's SOL where densities could be found in the order of 10^{16}m^{-3} . However, TCV's typical LCFS densities are much above that, in the order of $\sim 1 \times 10^{18}$. Hence, no significant power loss due to tunneling into the UH resonance is expected when sampling the pedestal region in TCV in X-mode polarization.

In summary, the radial density profile of an inhomogeneous plasma can be inferred from measurements of the group-delay or phase difference between frequencies that encounter cutoffs at relevant plasma locations. There are many experimental approaches to measuring these group-delays, further addressed in chapter 4. Accurate measurement of these group-delays and phases requires that the wavevector must be normal to the reflection layer. Since the plasma shape and launching angle can vary significantly, especially with the shaping flexibility of TCV, the incidence angle must be carefully chosen. The changing refractive index with density/magnetic field introduces beam refraction, which can be quantified via the geometric optics method presented above. Details of the practical aspects of implementing this calculation can be found in section 3.2.1.

2.4 Measuring density fluctuations

The previous section addressed the potential of reflectometry to infer the density profile from the round-trip group-delay and/or phase measurements over frequency. Reflectometry has also been employed to measure density fluctuations. Experimental characterization of the physical processes that bring about plasma fluctuations holds great importance in fusion research. Plasma turbulence has been hypothesized to be the main driver of anomalous transport [19].

Turbulence is naturally difficult to characterize given its large spectrum of spatial and temporal scales. Tokamak plasma turbulence can be characterized in terms of wavenumber spectra in the perpendicular (radial and poloidal) and parallel (\sim toroidal) directions with respect to the magnetic field. Reflectometry has been used to access the radial and poloidal spectra by aiming the outgoing beam at normal and non-normal incidence to the cutoff region and sampling the zeroth order reflection and the higher-order scattered power, respectively.

Although careful interpretation of experimental results by reflectometry requires advanced modeling, there exist regimes where long-wavelength radial density fluctuations can be measured simply through changes in the phase of reflected waves. Extracting quantitative information about the underlying micro-turbulence from the fluctuating reflectometer signal is an active field of research. Before delving into how reflectometers respond to density fluctuations, a brief description of the current theoretical basis of tokamak plasma turbulence is due.

2.4.1 Tokamak plasma turbulence: a brief summary

A tokamak plasma is designed to be a place where extremes: temperatures larger than the core of the sun (1×10^7 °K) are maintained less than a meter away from solid walls ($< 1 \times 10^3$ °K). Plasma densities in the order of 10^{20}m^{-3} in the core are maintained less than a meter away from plasma densities of 10^{16}m^{-3} in the far-SOL past the wall-shadow region [58]. In fluid mechanics, turbulence arises from instabilities when large Reynolds numbers are present [65, p. 1-10]. A fluid flow with excessive kinetic energy, when made

unstable, resorts to chaotic, non-linear, multi-scale changes to its properties to enhance the rate of energy and momentum exchange with its surroundings. In a tokamak plasma, the large pressure and current gradients constitute a large source of energy, ready to be dissipated through various instabilities involving both ion and electron spatial and temporal scales.

Tokamak plasma instabilities can be mainly divided into macro and micro instabilities. Macroscopic instabilities are mainly driven by energy in either the pressure gradients or the tokamak toroidal current and can be attributed to identifiable (single-fluid) MHD modes. These relatively large instabilities cause observable changes to the density profile; some of these feature scale lengths comparable to the plasma size. Reflectometry techniques that recover the density profiles with time resolution better than above a few milliseconds (see section 4.4 on page 95) are able to reveal the dynamics of these macro-modes [66]. Even though a few questions remain, most of these macroscopic instabilities have been characterized as either ideal or resistive MHD modes [11, p. 311-348]. Experimental techniques have been developed to avoid the onset of such instabilities or to quench them using ECRH, for example [67].

Microscopic instabilities are much more difficult to experimentally characterize and model numerically. The physics behind the onset, drive, and damping of micro-instabilities is an active field of research. These are called micro because they involve spatial scales 10^2 - 10^3 times smaller than large MHD modes. They are usually much smaller than the characteristic plasma size. Their frequency is far lower than the ion and electron plasma and cyclotron frequencies, and thus well below reflectometry probing frequencies. Microscopic instabilities can have many drives and fluctuating quantities; they have been classified by their fluctuating quantities (electrostatic and electromagnetic), instability nature (interchange, drift-wave, Alfvénic modes), and even whether they primarily involve trapped (banana orbit) or passing particles [68, p. 40-50]. It is possible to derive dispersion relations within certain limits but in the extreme tokamak environment there are various types of micro-instabilities with varying amounts of growth rates and mutual non-linear interactions.

Drift-wave turbulence

The most universal type of instability often cited to dominate the tokamak confined plasma is the drift-wave instability. The reader is referred to excellent physical descriptions of the drift wave turbulence process found in [69], [68, p. 40-50], and [70, p. 29-36]. There are four main types of drift-wave micro-instabilities in tokamak plasmas: Trapped Ion Modes (TIM), toroidal Ion Temperature Gradient (T-ITG), Trapped Electron Modes (TEM), and Electron Temperature Gradient (ETG) - three of which are shown in figure 2-6 (taken from figure 2.5 in [70, p. 34]).

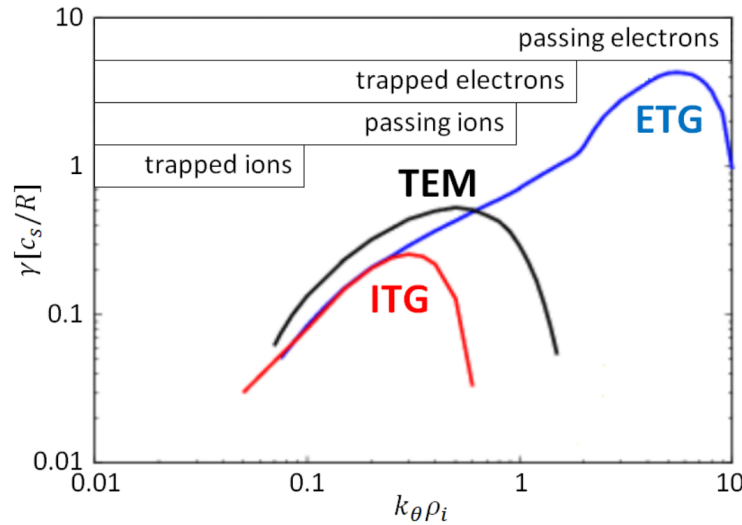


Figure 2-6: Linear growth rate γ over poloidal scale length $k_\theta \rho_i \sim k_\perp \rho_i$ featuring the most relevant tokamak drift-wave-type microinstabilities. $\rho_i = v_{th,i}/\Omega_i$ is the ion Larmor radius.

All of the instabilities shown in figure 2-6 are electrostatic in nature and do not perturb the magnetic field. There is empirical evidence that transport in the confined edge region is mostly caused by electrostatic turbulence [19], although close enough to the plasma boundary the resistive ballooning modes start playing an important role (non-ideal MHD modes [71]).

The toroidal ITG instability occurs because of the steep ion temperature gradients found between the core and SOL plasmas. In the low-field side region of the torus, a poloidal pressure perturbation can be amplified by the interplay between local $E \times B$ drifts and the vertical ∇B ion drift velocity. An E field is naturally created between

regions of high and low ion density. The $E \times B$ drift that results convects hot core plasma radially outwards towards regions of high density concentration creating *hot* and *cold* spots. The higher temperatures lead to faster ∇B drifts and further growth of the density perturbations. The mechanism requires $\nabla T_i \cdot \nabla B > 0$ and is therefore not seen on the high-field side. The radial wave number and oscillation frequency of toroidal ITGs is typically about:

$$\langle k_{\perp} \rangle \rho_i \simeq 0.1 - 1 \text{ peaked at } \sim 0.4$$

$$\omega_{\text{T-ITG}} \sim \omega_{*i} = \frac{k_{\theta} \rho_i v_{\text{th},i}}{L_n} = \frac{(m/r) v_{\text{th},i}^2}{\Omega_i L_n}$$

where $\rho_i = v_{\text{th},i}/\Omega_i$ is the ion Larmor radius, $L_n = \frac{n}{dn/dr}$ is the density gradient length, ω_* is the ion diamagnetic drift frequency, and the ion thermal velocity is $v_{\text{th},i} \equiv T_i/m_i$. Using ion temperature measurements from CXRS and assuming a typically-large poloidal mode number of about 16 (see [72, p. 17-27]) allows a rough estimate of the ITG k_{\perp} spectra extending between $k_{\perp} \sim 1.3\text{-}8 \text{ cm}^{-1}$ in a typical TCV discharge (i.e. 42636). The peak $k_{\perp, \text{peak}}$ is approximately $\sim 3.3\text{-}3.9 \text{ cm}^{-1}$ from edge to core while $\omega_{\text{T-ITG}}$ lies between 30-180kHz.

Trapped Electron modes are driven unstable by the combined effect of the precession drift resonance of trapped electrons and the electron temperature gradient on the low-field side of the torus. The precession effect occurs due to vertical drift experienced by electrons as they undergo neoclassical banana orbits in the poloidal plane. The drift results in net toroidal motion. The mode driver is a net toroidal drift *velocity* that enters in resonance with ITG perturbations. Growth rates for this mode are found to significantly differ from the ITG case, yet oscillation frequencies remain rather close. The TEM frequency is limited by the electron bounce frequency defined as [73]:

$$\omega_{be} = \frac{\sqrt{\epsilon} v_{the}}{q R_o}$$

$$\omega_{tTEM} \sim \omega_{*e} = \frac{k_{\theta} \rho_s c_s}{L_n} = \frac{k_{\theta} c_s^2}{\Omega_i L_n}$$

where c_s is the ion acoustic speed defined as $c_s^2 = k_b T_e / m_i$. For the same typical shot parameters, bounce frequencies are found to be a few MHz while the ω_{*e} is found between 60 and 400 KHz, just slightly higher than the ITG frequencies. Since ion and electron diamagnetic velocities are in the same order of magnitude, the peak TEM wavelength is found close to that of ITG: a few ion Larmor radii [72, p. 17-27]. The lower k_{\perp} ITG limit can be thus maintained for TEMs, but their higher limit must be larger than ITG given the small electron scales involved. Assuming a $\langle k_{\perp} \rangle \rho_i \simeq 0.2-2$ gives k_{\perp} spectra extending between $k_{\perp} \sim 1.3-20 \text{ cm}^{-1}$.

Electron-temperature gradient (ETG) modes feature very short wavelengths as seen in figure 2-6 on page 39. They can have large growth rates but are expected to have a significant impact exclusively on electron transport. Since the mmw reflectometry and scattering systems described below cannot access these scales, they will not be further discussed.

The scale lengths discussed above refer to the poloidal direction. Radial wavelengths are not expected to be the same, but they are expected to be of same order of magnitude given the circularly-symmetric nature of drift-wave eddies [69]. Toroidal wavelengths (along magnetic field lines) tend to be much longer because particle motion along field lines is much faster than across them. Since experimental verification of these wavelengths with reflectometry would require several antennas along the toroidal direction, parallel wavelengths will not be discussed in the frame of the first dedicated reflectometer system in TCV.

The so-called 'mixing-length' limit gives an indication of the density perturbation level of drift-wave turbulence [74]:

$$\frac{\delta n}{n} = \frac{1}{\langle k_{r,\theta} \rangle L_n}$$

This estimate gives about 10% for the edge and 1% for plasmas near the core of TCV. Carreras [19, pg. 1294] discusses evidence of core density fluctuations being indeed 1% or lower, and edge density fluctuations reaching values as high as 20-60%.

Zonal flows

Another important character in the intricate play of fusion plasma turbulence are zonal flows (ZFs). These are turbulence-generated poloidal plasma flows radially localized to a magnetic surface. The term *zonal* is inspired in latitudinal quasi-two-dimensional large-scale atmospheric and oceanic flows [75]. These modes enjoy great importance in fusion research because they moderate drift-wave turbulence via shearing of turbulent eddies and acting as an energy sink [76]. ZFs are rigid flow oscillations with an axisymmetric mode structure ($m=n=0$) and with a spectrum of radial wavelengths limited by $\sqrt{a\rho_i} > \lambda_{\rho, ZF} > \rho_i$, which in the typical TCV shot corresponds to about $\lambda_{\rho, ZF} \sim 0.1-2$ cm or $k_\rho \sim 3-63$ cm⁻¹. There are two main forms of ZFs: a low frequency branch ($f \sim 0$) and a high frequency oscillation at the geodesic acoustic mode frequency $\omega_{GAM} = \frac{\sqrt{2}c_s}{R_0}$. For typical parameters, the GAM frequency above corresponds to about 40-80kHz. In general, this GAM frequency is usually broadband due to the nature of turbulence. In TCV, GAM signatures have been identified in multiple diagnostics [77], lately being observed by Langmuir probes in the SOL [78]. Further details on the physics of tokamak zonal flows can be found in Diamond et al. [75]

2.4.2 Fluctuation reflectometry

The most widely used approach to characterize density fluctuations with reflectometers is to launch a microwave beam perpendicular to a cutoff layer and detect the reflected wave phase fluctuations. Early researchers attributed fluctuations in phase directly to density fluctuations at the cutoff. However, wave propagation to and back from a cutoff

layer featuring the broad spatial and temporal spectrum of plasma turbulence shown above makes the interpretation of reflectometry measurements quite complex [43].

One-dimensional picture

To get an intuitive feeling for the reflectometer's response to density fluctuations, it is useful to start with the most simplistic models. The 1D picture is valid only when fluctuations propagating perpendicular to the magnetic field have wavelengths and characteristic scale lengths much longer than the beam's width and wavelength $\lambda_{f\perp} \gg w, \lambda_0$. This approach ignores important effects such as diffraction and interference which will be further addressed below. In the extreme case where the radial wavelength of fluctuations is also much longer than the probing wavelength $\lambda_{f\rho_\psi} \gg \lambda_0$, the reflected waves would effectively observe a moving reflecting layer. In such cases, the phase fluctuations can be directly connected to radial fluctuations of the reflection layer to a first order approximation when fluctuation levels are small:

$$\delta n_e = \frac{\partial n_e}{\partial r} \delta r \quad (2.27)$$

$$\delta \phi = 2k_o \delta r = 2k_o \left(\frac{\partial n_e}{\partial r} \right)^{-1} \delta n_e \quad (2.28)$$

$$\delta \phi = 2k_o L_n \frac{\delta n_e}{n_e} \quad (2.29)$$

Given that probing wavelengths in TCV are in the order of 0.4-1cm (O-mode), only macroscopic instabilities in the 10s of cm could lead to such simple relationships between measured phase and density fluctuations. A less extreme yet still highly simplified picture assumes that the plasma's refractive index varies smoothly along the direction of the beam propagation. The 1D WKB approach discussed above can then be applied. Using the cold-plasma dispersion relationship in O-mode (equation 2.5), phase fluctuations due to density fluctuations can be quantified as follows [49, p. 98]:

$$\delta k(r) = \frac{\partial k}{\partial n_e} \delta n_e(r) \quad (2.30)$$

$$\frac{\partial k}{\partial n_e} = -\frac{\omega}{c} \frac{1}{2n_c \sqrt{1 - n_e/n_c}} \quad (2.31)$$

$$\delta \phi(r) = -\frac{\omega}{c} \int_{r_e}^{r_c} \frac{\delta n_e(r)}{n_c \sqrt{1 - n_e/n_c}} dr \quad (2.32)$$

where equation 2.12 was used to arrive at equation 2.32. It relies on the approximation that the refractive index decreases linearly towards zero at the cutoff location. Equation 2.32 shows that, within the WKB approximation, phase fluctuations at the receiver are a round-trip integral function of density fluctuations to the cutoff layer. The denominator in the latter integral does, however, give a higher weight to density fluctuations near/at the cutoff layer. Within Ginzburg's assumption, equation 2.32 can be considered valid for radial fluctuations with scale lengths longer than the Airy width (eq. 2.13). As seen above in figure 2-5, the Airy width stands at 0.3-1.2cm, which is in the same order of magnitude as ITG and TEM drift-wave turbulence discussed in section 2.4.1 above. Thus, especially concerning TEM and ETG turbulence, Ginzburg's assumption of a linear refractive index at the cutoff layer is not valid and equation 2.32 does not apply. It can, however, be perfectly valid during macroscopic MHD modes.

Considering the effects of perturbations smaller than the last Airy lobe requires a more complete treatment of the wave equation. Mazzucato and Nazikian [79] took a more formal approach applicable in the general case of scattering near a cutoff. Using a linearization of the relative permittivity tensor in the presence of small density perturbations (Born approximation), it was confirmed that the backscattered field is strongly enhanced near the cutoff for the cases $\lambda_{f\rho_\psi} \gg \lambda_0$. The X-mode is found to provide superior localization. However, smaller fluctuation scale-lengths $\lambda_{f\rho_\psi} < \lambda_0$ result in scattering away from the cutoff and uncertainty in the localization of the measured density fluctuations. Assuming a sampling frequency of 60GHz, corresponding to a vacuum wavelength of 5mm, this implies that $k_{f\rho_\psi} \ll 12.5\text{cm}^{-1}$. Thus, the reflectometer could (assuming a factor of 1/5 substituting the \ll symbol) sample the lower end of ITG and

TEM turbulence which feature scale lengths from 1.3cm^{-1} as presented in section 2.4.1 above.

The full wave equation in 1D was solved by Bretz [74]. In addition to confirming that long fluctuation wavelengths dominate measured phase fluctuations, it was found that any sufficiently strong radially propagating fluctuations along the beam's path that obey the Bragg back-scattering resonance condition $k_f = 2k_i \approx 2N(x)k_0$ can also significantly affect the measured phase. Thus, when density fluctuations in the beam path approach $\lambda_f \rightarrow \lambda_0$, localizing the phase fluctuations measured becomes challenging. Solving the full-wave 1D equation [74] also showed that density correlation length measurements based on probing adjacent plasma cutoffs with different frequencies cannot produce correlation lengths less than 4-8 times the vacuum wavelength.

Two-dimensional effects

Unfortunately, 1D models were largely unable to explain large experimental variations in amplitude and sharp increases in phase called phase run-away [80]. Even for large wavelength radial fluctuations, proper consideration of 2D wave-effects such as diffraction and far-field interference is vital in interpreting practical reflectometry signals in tokamaks [6, p. 143] [81]. This is because fluctuations propagating perpendicular to the main B-field (pseudo-poloidal) can be significant and feature a range of wavelengths that include $\lambda_{f\perp} \sim \lambda_0$. These fluctuations cause chaotic interference patterns in the detectors outside the plasma, which can lead to recording statistical properties that are not those of broadband turbulence. 2D arrays of detectors could be used (at the expense of higher accessibility demands) in a technique called *imaging* reflectometry [6, p. 149].

Conway et al. [81, 82] used reflections against a two-dimensional distorted mirror to study the effects of two-dimensional fluctuations of varying strength and wavenumber. Experiments were compared with numerical simulations using the physical-optics model for far-field backscattered power. This model assumes the plasma cutoff as an infinitely thin layer, thus not taking into account the Airy widths above nor the filamentary radial transport observed in the SOL of tokamaks [83]. Nonetheless, good agreement was found with data from tokamak experiments fitting values for the k_\perp fluctuation level and

spectral width in reasonable ranges. Both phase and amplitude information was required to reconstruct information regarding poloidal fluctuations. An important conclusion of these investigations is that the symmetry between incident and reflected power (normal incidence alignment of probing beam into the cutoff layer) is paramount to the stability of power and phase signals. Asymmetries of even 1° may severely complicate the analysis [84].

2D full-wave [85] codes have also been developed in the Born approximation limit to account for interference, diffraction, and scattering. These codes generally require long computing times and careful interpretation. Narrow antenna patterns are found more resilient against poloidal fluctuations and better able to resolve radial fluctuation levels. These codes arrive at a similar conclusion that 2D effects cannot be ignored and that careful quantitative interpretation of fluctuation reflectometry signals requires synthetic diagnostic modeling in the presence of realistic turbulence.

Nonetheless, there is strong evidence that in carefully-aligned conditions taking refraction into account, macroscopic MHD modes and/or Alfvén eigenmodes can be studied in the phase frequency spectrum of reflectometers [66]. This is because the large radial perturbations caused by these modes outweigh the effect of background broadband poloidal turbulence and the 1D picture shown above becomes valid.

2.4.3 Doppler back-scattering

Reflectometry has also been used in the scattering configuration where instead of sampling the zeroth order specular reflection from a cutoff, a higher order scattering term is measured instead. The earliest use of reflectometry in tokamaks was to detect small-scale density fluctuations through microwave scattering [86]. Doppler reflectometry [87] or Doppler back-scattering (DBS) is a relatively new technique used to measure the dynamics of poloidal fluctuations: poloidal flow velocities and wavenumber spectrum.

DBS deliberately chooses the beam's line-of-sight to be non-perpendicular to the cutoff layer and relies on scattered power from density fluctuations perpendicular to the B-field (almost poloidal in tokamaks). Launching a mmw-beam at an oblique angle to the cutoff surface allows the enhanced E-field amplitude near a plasma cutoff to localize

the scattered power to where the refractive index reaches a minimum: the beam turning point. The scattering process relies on the presence of density fluctuations at this turning point and selects the probed fluctuation wavenumber according to the Bragg condition [6, p. 82]:

$$\vec{k}_f = \vec{k}_s - \vec{k}_i \quad (2.33)$$

$$\vec{k}_f = -2\vec{k}_i \quad (2.34)$$

where ‘f’ refers to fluctuation, ‘i’ to incident, and ‘s’ to scattered. Figure 2-7 illustrates the principle of operation of DBS. It uses a linear density profile going from $3 \times 10^{19} \text{m}^{-3}$ (cutoff density for frequency 50GHz in O-mode polarization) to zero density from 1m to 1.5m in the horizontal scale. A sample mmw-beam incident at a 30° from the horizontal is seen to find a *turning* point at about $N_{\min}^2 = 0.5$. This illustrates that the DBS beam does not necessarily reach the cutoff. The figure also illustrates that the beam undergoes refraction inside the variable N^2 plasma. In order to quantify this refraction, the ray-tracing equation presented above can be used. Once the ray’s path has been computed past the turning point, the results of the numerical procedure can be used to infer the sampled k_\perp from the Bragg condition $k_{\perp f} = -2k_i = -2k_0 N_{\min}$. Figure 2-7 shows that the same antenna that transmits the beam can be used to sample the first order back-scattered power. This is called the monostatic configuration. In a slab geometry, the above Bragg condition 2.34 simplifies to $k_f = 2k_i \sin(\theta_s)$.

If the fluctuations are moving with velocity \vec{v} with respect to the laboratory frame, the scattered radiation will be Doppler shifted by $\Delta\omega = \vec{v} \cdot \vec{k}$. If the wave-vector of the incident beam is perpendicular to the main magnetic field at the turning point (which requires a small toroidal tilt of the antenna in tokamaks [88]) the Doppler shift can be approximated to $\Delta\omega \cong v_\perp k_\perp$.

This is a valid approximation given that, in tokamaks, $k_\perp \gg k_\parallel$ [89] because of the much larger particle mobility along B-field lines. Additionally, $k_{\rho\psi}$ fluctuations do not contribute since at the beam turning point, the incident k_i beam lies on the flux surface

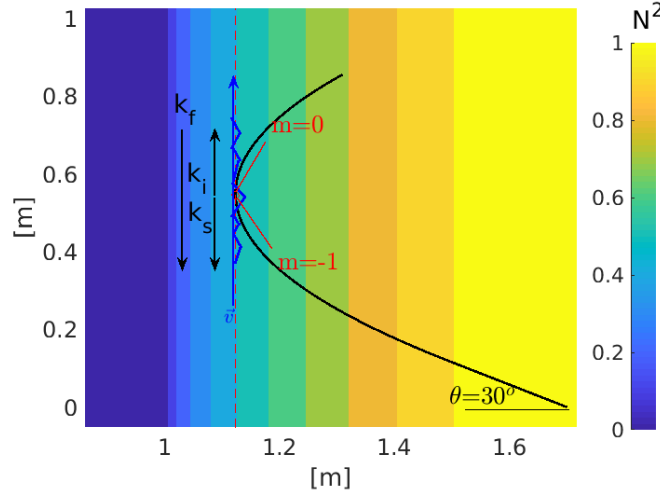


Figure 2-7: Principle of operation of a monostatic Doppler back-scattering diagnostic. Ray-tracing is used to calculate the refraction of an O-mode wave in a linear density profile growing from 0 to $3 \cdot 10^{19} \text{ m}^{-3}$ from 1.5 to 1.0 m along the horizontal axis.

perpendicular to the radial dimension. This perpendicular rotation velocity of electron turbulence v_{\perp} is the sum of the phase velocity of turbulence and a background plasma component, i. e.: $v_{\perp} = v_{\text{phase}} + v_{\text{ExB}}$. In cases where the latter is found to dominate, the E_r profiles may also be obtained from the measured Doppler shifts.

DBS could also be used to study the statistical temporal dynamics and energy spectrum of turbulence. In low turbulence level conditions (linear regime in [90]), the scattered wave amplitude can be linearly linked with the turbulence level at the probed k_{\perp} [91]. While it is experimentally challenging to ensure the same plasma volume is probed with different k_i (at different incidence angles), experimental wavenumber spectra represent highly valuable avenues to validate theoretical modeling. Quantitative results, however, require the use of advanced synthetic diagnostics to carefully evaluate the diagnostic's response [92].

k_{\perp} ranges between 3 and 15 cm^{-1} are usually attainable [89], [93], [94], [95]. The lower limit ensures that the antenna does not sample a mixture of the $m=-1$ and $m=0$ in figure 2-7. The higher limit is usually a consequence of SNR issues because tokamak plasma turbulence follows decaying power laws with increasing k_{\perp} . Yet k_{\perp} s up to 20 cm^{-1} have been reported [96]. The k_{\perp} resolution of DBS (Δk_{\perp}) is a function of the beam's width

at the cutoff. Analytic formulas exist [97], the simplest of which lets the resolution be inversely proportional to the width $\Delta k_{\perp} = \sqrt{2} \frac{\lambda}{w}$ in the absence of plasma curvature. This resolution can also be estimated via numerical simulations. It has been empirically shown by Conway et al. [98] that ‘3-point’ ray-tracing (where one ray represents the beam’s center and the other two describe the Gaussian-beam envelope 1/e amplitude points) offers a reasonably robust estimate of Δk_{\perp} wavenumber and $\Delta \rho_{\psi}$ localization resolutions of DBS.

Chapter 3

Doppler back-scattering diagnostic

Doppler back-scattering (DBS) is an active diagnostic technique that allows the study of electron density turbulence via the scattering of an electromagnetic beam launched at oblique incidence to a cut-off layer [89], [93], [95]. This technique takes advantage of the enhanced E-field amplitude near a plasma cut-off (refractive index $\rightarrow 0$) and the presence of a broad wave-number spectrum of electron density fluctuations to efficiently scatter these mm-waves. By measuring the Doppler shift and power of the scattered radiation, the perpendicular velocity and wave number spectrum of density fluctuations can, respectively, be inferred. The diagnostic principles have been covered in detail in section 2.4.3 above.

This chapter describes the hardware set-up, data-analysis techniques, and results of the first in-house DBS implementation on TCV. Prototype microwave reflectometers and DBS systems had been tested in TCV in the past, on loan from collaborators from the University of Stuttgart (Germany), Forschungszentrum Jülich (Germany), and the Laboratoire de Physique des Plasmas of Ecole Polytechnique Palaiseau (France) [77]. However, the DBS system described here is the first effort to build a *dedicated* DBS diagnostic for TCV with long-term exploitation goals in mind. The DBS diagnostic presented below uses TCV's quasi-optical diagnostic launcher system. A detailed description of this antenna can be found in appendix A.

3.1 Hardware set-up

TCV's DBS diagnostic is capable of swept single and multi-channel frequency operation through two interchangeable setups as described below.

3.1.1 Sweeable single frequency set-up

The first, more conventional set-up consists of a V-band (50-75GHz) heterodyne transmitter/receiver. Figure 3-1 shows a schematic diagram. At the core sits a commercial off-the-shelf transceiver vector network analyzer (VNA) extension module from Virginia Diodes (VDI). This extension module was originally designed to extend VNA frequency ranges above 40GHz into the V-band. This module is used in SPC to study material properties at high frequencies. The RF circuitry inside the Tx/Rx module is identical to the RF hardware found in most reflectometry systems. This section explains the external hardware required to extract backscattered signal amplitude and phase, as well as heterodyne Doppler shifts.

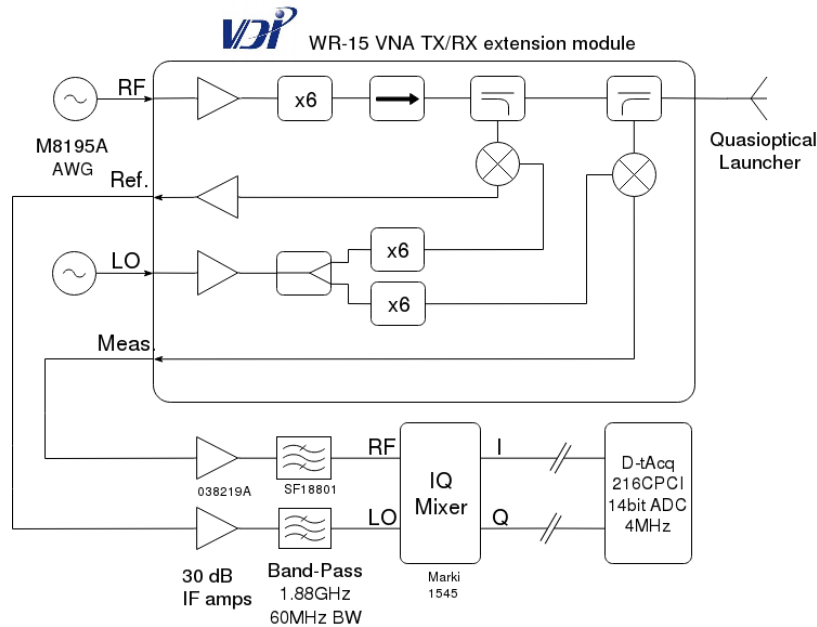


Figure 3-1: Block diagram of the sweepable single-frequency DBS implementation in TCV.

To launch waves inside the V band, mW-level sinusoidal signals in the range 8.33-

12.5GHz are fed to the RF port of the TX/RX VDI module, wherein their frequency is multiplied by a factor of 6 by built-in varactor multipliers. To generate these low-frequency sinusoids, a fast arbitrary waveform generator (AWG Keysight M8195A) with 25GHz analog bandwidth is used. The output power in the V-band ranges between 6 and 10dBm. Inside the VDI module, about -30dB of the transmitted power is coupled to a subharmonic mixer and mixed with a continuous-wave local oscillator (LO) input. This LO signal is also obtained by multiplying a second AWG channel input in the 8.33-12.5GHz range. The resulting LO has a frequency difference with respect to the RF that results in an intermediate-frequency (IF) output in the 5MHz-3GHz range. The output of mixing the probing signal with the LO appears at the *reference* output, while the signal resulting from mixing the reflected (or back-scattered) power with the same LO appears in the *measure* output port. The relatively large IF frequency of 1.88GHz was chosen to ensure minimal interference from spurious signals present in the tokamak's electromagnetic environment and to minimize the $1/f$ noise contribution.

In order to separate amplitude and phase in the measured heterodyne signal, hardware quadrature detection is used in the form of an I/Q mixer (Marki Microwave model 1545). Inside this mixer the reference signal is split into two, one phase shifted by 90° , and both mixed with the measured signal in two separate balanced mixers [6][pg. 56]. The output consists of an *in-phase* I signal and the *quadrature* Q, from which a phasor $P = I + iQ$ can be defined [6][pg. 55]. Given that the power available in the reference and measure ports is often under -25dBm and that the I/Q mixer requires +10dBm and ~0dBm in the LO and RF ports respectively, broadband IF amplifiers (0.01-3GHz, 34dB gain, Fairview Microwave model SLNA-030-34-14) and narrow bandpass filters (1.88GHz center frequency, 60MHz bandwidth, Fairview Microwave model SF18801) are used to condition power and reject spurious signals (coaxial cable pick-up and LO bleedthrough). I/Q amplitude deviation and quadrature phase deviation are under 0.2dB and 3degrees, respectively. In order to protect the integrity of I/Q signals from the harsh electromagnetic environment in the TCV tokamak hall, the IF-amplifier, band-pass filters (BPF), and I/Q mixer hardware were installed next to the VDI Tx/Rx extension module. Also, the entire fixture was enclosed in a 2mm thick aluminum shielding box (bottom right in

figure A-2). It is important to minimize the distance the Ref. and Meas. signals travel in coaxial cables, which although properly terminated were found sensitive to pick-up. This noise may be attributed to potentials generated due to the impedance mismatch (imbalance) between the coaxial cables' central conductor and shield in the presence of changing E fields [99]. The I/Q signals are routed from the DBS box to the digitizer ($\sim 2\text{m}$) through shielded twisted pair cables which are balanced and hence resilient against changing E fields. The I/Q signals are then sampled by a 14-bit differential ADC (D-tAcq model 216CPCI) at 4MHz. The ADC contains an internal 5MHz low-pass filter, which is used to reject LO bleed-through from the I/Q mixer and sample only Doppler shifts expected to be a few MHz at most. The ADC output is stored in the MDSplus TCV database.

3.1.2 Multiple simultaneous frequency set-up

A novel hardware set-up has been demonstrated for the production and detection of multiple simultaneous frequencies. Different frequencies allow the measurement of a DBS signal at several radial locations simultaneously. The radial evolution of fast events can thus be studied in detail. In addition, if the k_{\perp} sampled can be made similar across the radial dimension with careful plasma shaping (as seen below in figure 3-5), fast measurements of the radial evolution of k_{\perp} fluctuations can be tracked. Furthermore, a multiple-frequency system can allow radial correlation DBS studies [100]. The ability to vary the frequency spacing of the multi-frequency outputs is particularly welcome in radial correlation DBS studies.

Leveraging the multi-tone capabilities of the fast AWG, a novel approach to multi-channel DBS has been demonstrated. Conventional multi-channel DBS systems use a comb frequency generator (non-linear transmission lines), a frequency multiplier, and a fixed set of filters in a heterodyne receiver [101][102]. The newly proposed method consists of creating a double frequency spectrum with the AWG, feeding this signal into the varactor multiplier inside the VDI Tx/Rx module, down-converting the backscattered power with a mixer, and sampling the entire output spectrum with a fast oscilloscope as shown in figure 3-2. A separate receiver (Rx) module is used for detection instead of the

Tx/Rx module above because the Rx module features a larger IF bandwidth from 5MHz to 11GHz.

It is well known [103] that the nonlinear response of frequency multipliers implies the generation of all frequency products of the form $nf_1 + mf_2$ (where n and m are integers) to a double frequency input. Therefore, if a two-tone input composed of f_1 and f_2 is fed into the x6 varactor multipliers, their output would consist of $6f_1$, $6f_2$, and also (at least) 5 other intermodulation products in between, namely: $5f_1 + 1f_2$, $4f_1 + 2f_2$, $3f_1 + 3f_2$, $2f_1 + 4f_2$, $1f_1 + 5f_2$. The separation between these products corresponds to the initial frequency difference $f_1 - f_2$. Seven frequencies can thus be sent into the plasma. The distance between the first two tones can be easily changed and is only limited by the maximum IF bandwidth of the receiver. A fast (Lecroy Wavemaster 813Zi-B) 8-bit oscilloscope with 13GHz analog bandwidth (40GSa/s) is used to directly sample the IF output of the receiver mixer in figure 3-2. It is interesting to note that given the variable gain available in the scope input, no IF amplification was required to sample Doppler shifts with SNR $\sim 20-30$ dB.

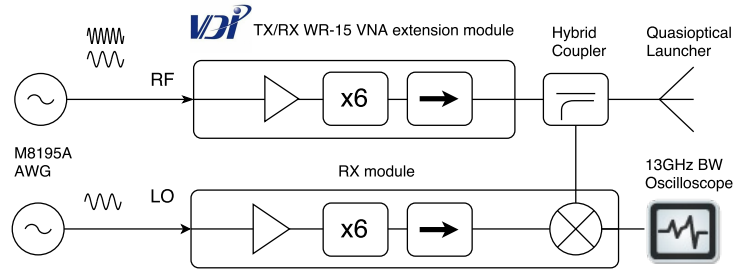


Figure 3-2: Block diagram of the multi-channel DBS setup.

Figure 3-3 shows the full IF power spectral density (PSD) spectrum recorded with the set-up in figure 3-2 at 40Gsa/s for 0.4ms at time 0.7s in shot 59551. The two-tone input comprised $f_1 = 8.33$ GHz and $f_2 = 9.33$ GHz, which produces 50 and 56GHz as x6 multiplication products and 5 intermodulation products in-between as explained above. The LO input was 8.325GHz, which resulted in an IF frequency of 50MHz for f_1 and 6.05GHz for f_2 as can be seen in figure 3-3. It is important to note the presence of other strong frequency terms in the spectra in figure 3-3. These were not the focus of the analysis but are likely useful intermodulation terms above and below $6f_2$ and $6f_1$,

respectively.

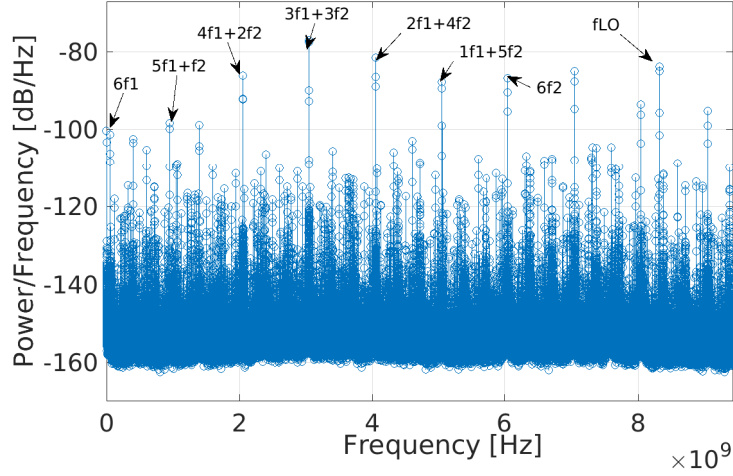


Figure 3-3: Raw IF PSD spectra recorded by the fast scope showing the main multiplication and intermodulation terms. Doppler shifts were recorded with this spectra during shot 59551, see section 3.3

This new approach to multi-channel DBS has both advantages and disadvantages. Firstly, the non-linear-transmission-lines (NLTL) of comb-frequency generators [101] [102] are not required. Furthermore, the fixed filter banks in the receiver are all replaced by the fast scope which records the Doppler shifts of each frequency simultaneously. Perhaps the strongest asset is that the multi-frequency output can change arbitrarily to best fit specific plasma conditions, conceivably inside the shot. Section 3.3 shows that both this multiple-frequency technique and the more conventional single-frequency swept technique give identical results. Furthermore, it shows that the frequency spacing of the multiple-frequency output can be changed at will. Radial correlation DBS studies [100] can benefit greatly from this flexibility by investigating various radial correlation lengths inside the shot.

A disadvantage of the current approach is that the plasma could be sampled for a maximum of $\sim 0.7\text{ms}$ given the limited scope memory at 32Mb. Multiple triggering may allow sampling of up to $8 \times 250\mu\text{s}$ instants during a shot, which remains impractical for routine measurements. This limitation can be overcome by data-acquisition solutions that feature memories of several 10s of gigabytes (Guzik ADP7000 for example), which would allow sampling the entire TCV discharge with varying frequency spacing inside

the shot. Another limitation is that the power dependence on frequency follows a near-parabolic curve. This could be a limitation for studies of relative fluctuation levels and k-spectrum, but it does not affect the determination of Doppler shifts and plasma rotation. Either an in-vessel power calibration and/or E-H tuners [101] can be used in the future to allow such studies. The next section presents sample spectra measured in a plasma and how these can be used to measure turbulence rotation velocities and energy spectra.

3.2 Data analysis approach

3.2.1 Ray tracing and PrefGeom

In order to correctly interpret the effective location and scattering wave number of the backscattered signal, it is imperative to model the trajectory of the microwave beam towards the turning point where the scattering takes place. It has been empirically shown by Conway et al. [98] that ‘3-point’ ray-tracing (where one ray represents the beam’s center and the other two describe the Gaussian-beam envelope 1/e amplitude points) offers a reasonably robust estimate of the fundamental Δk_{\perp} wavenumber and Δr localization resolutions of DBS.

Ray-tracing solves the wave equation within the framework of geometric optics making use of the WKB approximation explained in detail in chapter 2. Ray-tracing evolves each ray independently. A 2D ray-tracing routine called *PrefGeom* built in-house by C.A. de Meijere in 2013 using MATLABTM has been expanded to plan and interpret DBS experiments. It firstly propagates a Gaussian beam through vacuum using Gaussian-beam complex q-parameter formalism [49][pg.185] from the mouth of the HE11 waveguide through the four mirrors of the launcher. Once the beam reaches the last mirror, it is launched into an empty TCV vessel as a first approximation to show the beam propagation in vacuum. Figure 3-4 shows the launcher geometry and the vacuum beam envelope in red. The cut-off layer is also shown in red (i.e. for 65GHz in fig 3-4) at discrete poloidal launching angles spanning the entire poloidal range of the launcher. The cold-plasma dis-

persion relation for O/X mode waves is used to define this cut-off layer by evaluating the points where the refractive index (N) goes from positive to negative. Computing N requires both density and magnetic field information. The magnetic equilibrium is obtained from the LIUQE [104] reconstruction. The density profile of the confined plasma is taken from TCV's Thomson scattering (TS) diagnostic. Given the large inhomogeneities inherent to the instantaneous nature of TS, a cubic spline fit over the radial (ρ_ψ) dimension is performed on the raw TS data.

The scrape-off-layer (SOL) density profile is either obtained from TS when available or approximated based on recent fast-reciprocating-probe measurements [58]. The near SOL region (ρ_ψ 1.0-1.025) profile in L-mode plasmas is approximated with an exponential decay function of constant $\lambda_n = (|\nabla n_e|/n_e)^{-1}$ 1.5cm and 3cm in shots with core line average densities below and above $6 \cdot 10^{19} \text{m}^{-3}$, respectively. For the far SOL region (ρ_ψ 1.025-1.06 or beyond), in L-mode the exponential decay constant is 3cm regardless of density. In H-mode, the near and far SOL decay lengths used are 0.5 and 1cm, respectively, based on average measurements [105]. The SOL region is extended up to the ρ_ψ that matches the outer-gap width calculated with the LIUQE reconstruction. The latter is defined as the distance between the outer-most point (low-field side) of the last closed flux surface (LCFS) and the vessel wall. This outer-gap width effectively defines the SOL radial extent observed by the launcher. Vessel volume beyond this point is termed the wall shadow [106] and is considered to have much lower densities than the SOL. Beam refraction caused by this region is negligible because of both its significantly lower density and the short distances the beam passes through it. TCV's Psi-Toolbox suite [107] is used to combine both density and magnetic profiles in 2D cylindrical R-Z geometry.

Figure 3-4 shows the 3-point ray-tracing starting positions at the edge of the SOL region. The ray-tracing equation used by PrefGeom is $\frac{d}{ds}(N\hat{s}) = \nabla N$ [54], where \hat{s} is a unit vector whose direction is perpendicular to the wavefront. It is solved in 2D by MATLAB's ode45 solver. The initial direction of the central ray is defined by the launcher's poloidal angle. The top and bottom rays' locations and angles of divergence are defined by the local width and radius of curvature of an ideal Gaussian beam. At each point

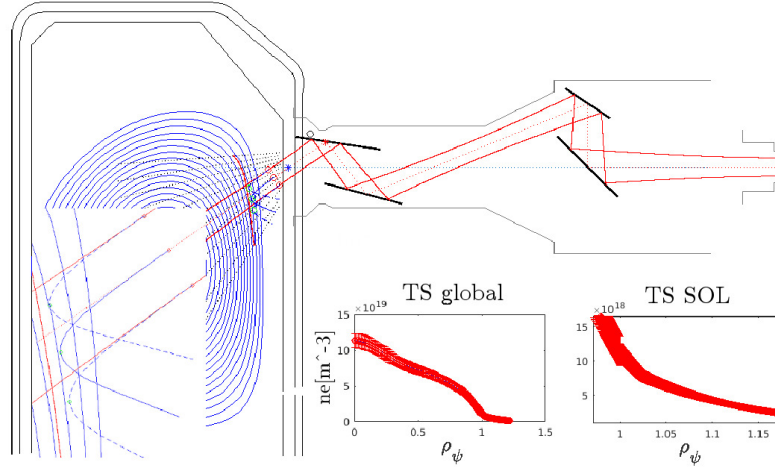


Figure 3-4: PrefGeom 2D 3-point ray-tracing output for shot 59534 at 1.0s, 65GHz, and X-mode polarization. A closeup of the beam trajectory approaching the turning point is shown in the bottom left corner for clarity. Confined plasma and SOL density profiles are shown for reference in the bottom right corner.

in each beam's trajectory, the refractive index is computed. When the refractive index reaches a minimum (shown with green circles in figure 3-4), the scattering wavenumber k_\perp is estimated using $k_\perp = 2 N_{\min} k_o$ [108]. Figure 3-5 shows a k-accessibility map for a negative triangularity L-mode TCV plasma, which provides near slab-like plasma cutoff layers.

Since the ray-tracing takes place in a purely poloidal 2D geometry, N_{\min} is not exactly N_\perp . As further explained by Honore [88], due to the small magnetic field pitch angle at the edge of tokamak plasmas, a purely poloidally oriented beam will not be perpendicular to the magnetic field at the turning point. The DBS beam must be slightly toroidally tilted usually 5 to 10 degrees in TCV. 2D ray-tracing cannot properly model the 3D trajectory of the beam. However, assuming a relatively deep cut-off location of the edge DBS system at $\rho_\psi = 0.85$ (roughly 3.7cm inside the confined plasma), a large toroidal angle of 10° , and an average 10cm separation between the antenna output and the plasma LCFS, the pseudo-toroidal displacement is about 2.5cm. This displacement is not very large: the focal width of the mmw beam at 50GHz is 2cm. The beam width at the turning-point can thus easily be larger than the pseudo-toroidal displacement caused by the slight toroidal angle. Therefore, if 2D 3-point ray tracing is used to compute errors in

radial location and k_{\perp} of DBS measurements, the 3D-induced changes would likely fall within these error bars. Also since pressure (the product of density and temperature) is a flux function, the turning-point location is not expected to be very different, specially at such small toroidal angles. Nonetheless, a 3D ray-tracing calculation is preferred in order to eliminate any systematic errors. It should be a priority for future exploitation of this diagnostic.

Figure 3-5 also shows the effects of different SOL profiles in determining the turning point localization and wavenumber. The so-called *exp* profile has been introduced above, and it is used by default. The *lin* profile refers to an unrealistic SOL profile that decreases linearly from $\rho = 1$ to zero at $\rho = 1.125$ regardless of the plasma conditions. For both of these, ray-tracing begins before entering the SOL (in the wall-shadow interface). The *vac* profile refers to treating the SOL as vacuum, propagating the beam using complex q parameters until reaching the LCFS, and starting the ray-tracing calculation just before (0.5mm) the interface.

Comparing results between linear and exponential SOL density profiles shows differences under 1cm^{-1} ($\sim 10\%$) inside $\rho_{\psi} < 1$. Uncertainties in k_{\perp} due to the finite width of the probing beam (from 3-point ray tracing) are usually found inside $\Delta k_{\perp} 2\text{-}4\text{cm}^{-1}$. Thus, the differences between both SOL profiles in k_{\perp} estimates lie well inside error bars. Localization differences between the two in ρ_{ψ} are much smaller, one order of magnitude below the ρ_{ψ} uncertainties from 3-point ray tracing $\sim 0.005\text{-}0.015$. However, the differences are much more significant when comparing both SOL profiles and the vacuum case. The differences in k_{\perp} estimates of turning points $\rho_{\psi} > 0.96$ are comparable to the 3-point Δk_{\perp} , with the vacuum case constantly underestimating the scattering wave-vector. For $k_{\perp} > 8\text{cm}^{-1}$, the vacuum estimates are significantly underestimated regardless of ρ_{ψ} . Turning-point localization discrepancies between the two SOL profiles and vacuum are not as pronounced, but they may become relevant (outside error bars) for $k_{\perp} > 10\text{cm}^{-1}$ and $\rho_{\psi} < 0.95$. It can be concluded from this figure that if the k_{\perp} measured is above 8cm^{-1} and/or has turning points above 0.95, the beam's refraction inside the SOL plays an important role in the accuracy of wavenumber estimates. While this results may be particular to TCV, it urges other ray-tracing codes to consider beam

refraction inside the SOL [94, 95]. It would be interesting to also study the effects of SOL density fluctuations and filaments on the k_{\perp} and ρ_{ψ} , but this is left for future work.

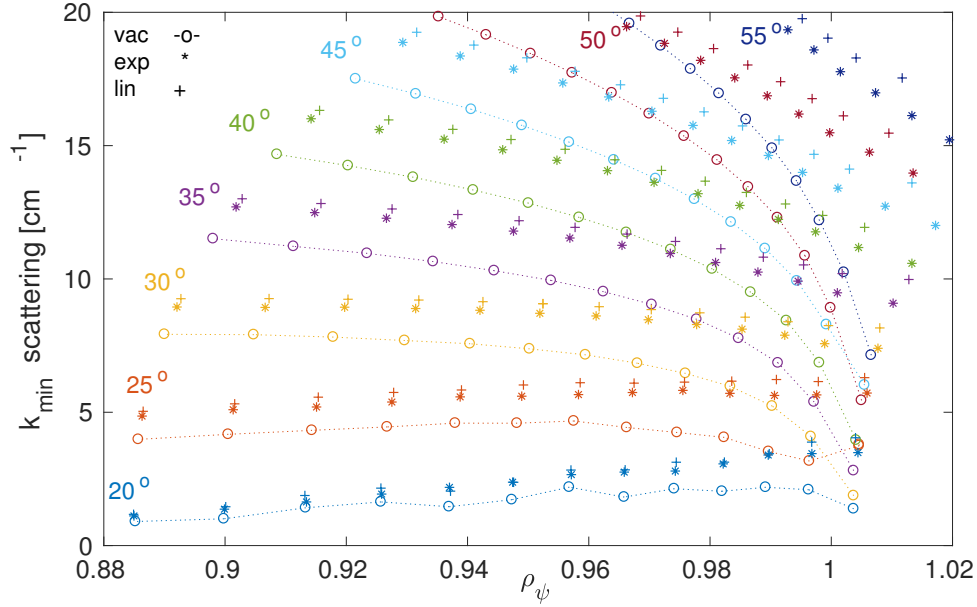


Figure 3-5: k_{\perp} accessibility map for shot 59534 at 1.0s varying the launcher’s poloidal angle between 56 and 20 degrees. The turning-point location depends on frequency going from 50 to 74GHz in steps of 2GHz. k_{\perp} and ρ_{ψ} uncertainties are found inside $2\text{-}4\text{cm}^{-1}$ and $0.005\text{-}0.015$, respectively, and are omitted above for clarity. The k_{\perp} axis extends up to 20cm^{-1} for illustrative purposes only. Useful signals are usually only measured up to $\sim 16\text{cm}^{-1}$.

3.2.2 Power spectral density and Doppler shift estimates

DBS can infer the poloidal rotation of electron turbulence by measuring the Doppler shift (f_D) of scattered signals. In order to extract this Doppler shift from the phasor defined by the I/Q signals or from the multi-frequency spectra in figure 3-3, a complex Power Spectral Density (PSD) estimate is obtained using the Welch method [109]. This method involves sectioning measurements and averaging modified periodograms of the sections, and it allows one to obtain a meaningful estimate of the PSD from finite Fourier Transforms [110]. Figure 3-6 shows a PSD estimate of I/Q data acquired during shot 55455 at 1 second. Data acquired for 1ms at 4MHz is split into 8 segments and finite Fourier Transforms of each segment are averaged. Each segment features 50% overlap-

ping. A Hanning window is used to avoid spectral leakage. The normalized standard error is equal to $\sqrt{\frac{11}{18N}}$ where N (equal to 8 in figure 3-6 for example) is the number of segments used in the Welch average. The factor of $11/18$ appears thanks to the 50% overlapping chosen [109].

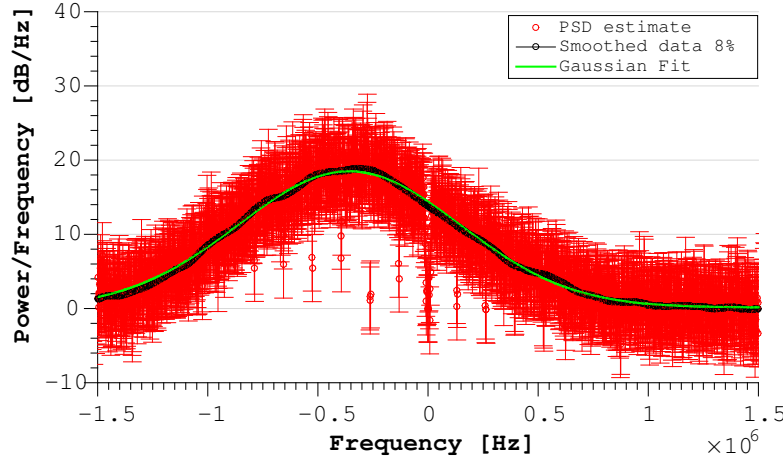


Figure 3-6: PSD estimate and f_D fits. Shot 55455 at 1.0s.

Although many precautions were taken against electromagnetic pickup, the PSD measured before the plasma discharge features numerous frequency-localized components under 1MHz. The PSD also features a strong DC component which naturally occurs from mixing Ref. and Meas. signals with different phases. A background PSD is therefore taken at -0.2 seconds before the shot and subtracted from all PSD estimates throughout the shot to eliminate signals that certainly do not originate in the plasma. Figure 3-6 shows the PSD estimate of I/Q data acquired during shot 55455 at 1.0 seconds. In order to extract the Doppler shift, a Gaussian function is then fit to the PSD estimate. Due to the removed background noise and DC offset, as well as the naturally large variance seen throughout the PSD estimate, it was necessary to smooth the data before successfully fitting a Gaussian that was centered around the observed Doppler shift. The rigid LOESS method[111], a generalization of the robust locally weighted regression method, has been chosen through MATLAB's built-in *smooth* function. This method smooths data by using weighted least squares second order polynomial fits to data in a defined neighborhood around each point. The robust option assigns zero weight to data

outside six mean absolute deviations, which helps to neglect the background outliers seen in figure 3-6. In this particular case 8% of the available data points were taken into account as the neighborhood about each smoothed point.

A Gaussian function is then fit to the smoothed data to find the horizontal offset that gives f_D . After smoothing, fits are found to have R^2 above 0.98, in general. In order to estimate the appropriate error in the estimate of f_D from the fit to the smoothed data, the 95% confidence interval errors are multiplied by the square-root of the number of neighborhood points taken for smoothing. Without smoothing, the fits have much poorer coefficients of determination and may miss the peak of the spectrum altogether. However, it must be acknowledged that the arbitrary amount of smoothing has an effect on the fit's final uncertainty. Nonetheless, f_D uncertainties are found in the range 0.05-0.2MHz, which is quite reasonable by visual inspection of figures 3-6 and 3-7.

Occasionally, the Gaussian function is found not to be a good fit to the data with R^2 coefficients under 0.9. An alternative fit model is to use a scaled skewed normal (SN) distribution function [112] as shown in figure 3-7.

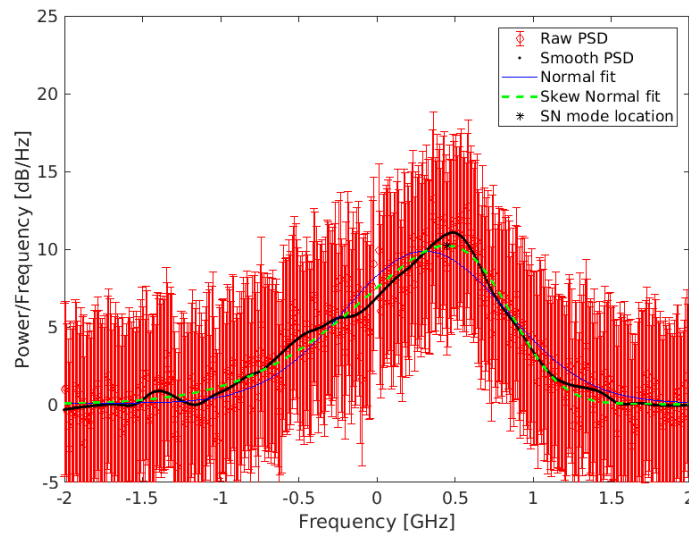


Figure 3-7: PSD estimate and f_D fits. Shot 59555 at 0.7s. $k_{\perp} = 5.4 \pm 4 \text{ cm}^{-1}$. $\rho_{\psi} = 0.967 \pm 0.002$.

$$\text{PDF} = \frac{2}{\omega\sqrt{2\pi}} e^{-\frac{(x-\xi)^2}{2\omega^2}} \int_{-\infty}^{\alpha\left(\frac{x-\xi}{\omega}\right)} e^{-t^2} dt \quad (3.1)$$

where ξ is the location parameter, ω is the scale parameter, and α is the slant parameter that allows asymmetry in the PDF. The normal distribution function is recovered when α is equal to zero. The integral in equation 3.1 above is estimated using MATLAB's *normcdf* function. Figure 3-7 shows both a generic Gaussian (Normal) and the SN fit and how the SN fit better estimates the peak of the Doppler shift. In order to estimate Doppler shift, the location of the maximum in the SN fit is found using accurate analytic estimates of the SN distribution's *mode*. Recall that the mode of a distribution is the value that appears most often. In the case of the DBS spectra, the peak Doppler shift corresponds to the SN mode instead of the mean. In the case of a regular normal distribution, the mean and the mode are the same. However, in the case of the SN distribution, the mode has been analytically estimated to be [112]:

$$\text{Mode} = \xi + \omega m_o(\alpha) \quad (3.2)$$

$$\text{where } m_o(\alpha) \approx \mu_z - \frac{\gamma_1 \sigma_z}{2} - \frac{\text{sgn}(\alpha)}{2} \exp\left(-\frac{2\pi}{|\alpha|}\right) \quad (3.3)$$

$$\text{where } \mu_z = \sqrt{\frac{2}{\pi}} \delta, \sigma_z = \sqrt{1 - \mu_z^2} \text{ and } \gamma_1 = \frac{4-\pi}{2} \frac{(\delta\sqrt{2/\pi})^3}{(1-2\delta^2/\pi)^{3/2}}$$

In order to estimate the uncertainty in the mode, the standard error propagation formula is applied to the mode formula above. The uncertainty in each fit parameter is obtained from the fit's 95% confidence interval estimates.

The physical interpretation behind the need to fit DBS spectra with a skewed normal distribution is unclear. The relatively large beam width in TCV could result in sampling regions with opposite rotation directions and hence a weak Doppler shift in the opposite frequency. Also, forward scattered power that is reflected against the reactor walls could cause further scattering power that returns into the antenna with a markedly different Doppler shift.

3.2.3 v_{\perp} uncertainty estimates

There are several factors that contribute to the uncertainty of measurements of the turbulence $v_{\perp} = 2\pi f_D/k_{\perp}$ velocity. These can be divided into intrinsic and extrinsic to the DBS technique. There are three inherent uncertainties in the DBS technique. Firstly, given the finite size of the mmw-beam, there are a wavenumber Δk_{\perp} and a turning point radial $\Delta \rho_{\psi}$ resolutions. Both of these can be determined via 3-point ray-tracing as explained above. Δk_{\perp} is usually found in the $2\text{-}4\text{cm}^{-1}$ range and $\Delta \rho_{\psi}$ inside $0.005\text{-}0.015$. The 3-point ray-tracing calculation is required for every frequency and plasma condition to properly estimate the influence in the v_{\perp} error. The last inherent DBS uncertainty comes from uncertainty in the Doppler shift measured Δf_D . This is found through the 95% confidence interval of the fits (either normal or skewed normal) to the measured Doppler-shifted spectrum. Δf_D is usually found in the range $50\text{-}200\text{kHz}$. Both the Δk_{\perp} resolution and the Δf_D enter into the calculation of the Δv_{\perp} via the standard error propagation formula. As can be seen in figures [3-9 on page 70](#) and [3-10 on page 71](#), the Δv_{\perp} can range from $0.2\text{-}10\text{km/s}$. In order to reduce this uncertainty, the beam width at the turning point can be reduced by further focusing the optics of the launcher.

There are also experimental uncertainties external to the DBS diagnostic that have a direct effect on the k_{\perp} and ρ_{ψ} estimates. These can be divided into density and magnetic profile uncertainties. Density profile uncertainty comes directly from the TS density profile error bars which are about 10% in magnitude in the plasma edge.

This n_e magnitude error comes from two main sources: background subtraction and Raman calibration uncertainties. The TS emission spectrum is measured by 3 polychromator filter bands in TCV's TS system. Look-up table interpolation is used to interpret the polychromator output into a value of density. The background subtraction uncertainty arises from the fact that these polychromators measure the TS emission lines and also background Bremsstrahlung radiation which adds uncertainty to the look-up interpolation. There is also uncertainty in the TS absolute calibration which uses Raman scattering from molecular nitrogen gas filling the TCV vessel. Drifts in the relative alignment of the laser beams and detection optics may cause changes to this absolute calibration. Further details can be found in [\[44, ch. 3.4\]](#).

Uncertainty in the density profile affects the accuracy of the ray-tracing k_{\perp} and ρ_{ψ} estimate. In order to estimate the effect, of - for example a 10% TS magnitude error, the density profile is artificially changed to 110% and 90% and k_{\perp} and ρ_{ψ} are computed on each to estimate the TS-driven Δk and $\Delta \rho_{\psi}$. In order to keep the TS uncertainties separate from the inherent uncertainty of the DBS technique, average TS-driven error bars have been plotted separately for reference in figures 3-9 and 3-10. These figures show that the TS-driven uncertainty can be up to 0.006 in ρ_{ψ} but only 0.2 cm⁻¹ in k_{\perp} (which has a negligible effect on v_{\perp}) in shot 59555 further addressed in section 3.3.

The position (ρ_{ψ}) uncertainty for each TS point, and hence position uncertainty for the radial spline fit used as input to the ray-tracing routine, depends on the LIUQE magnetic reconstruction used to map the TS viewing locations to ρ_{ψ} . A good TS calibration is assumed ignoring ρ_{ψ} uncertainty arising due to laser horizontal position and fiber viewing angle changes. LIUQE uses magnetic probe experimental measurements to solve the Grad-Shafranov equation. The accuracy of the reconstruction is considered best in the plasma edge region given the close proximity of the probes to the LCFS. However, many factors can affect the LIUQE reconstruction's accuracy. The magnetic probes are sensitive to currents coming from the external coils, vacuum vessel, plasma current density, and plasma position. A covariance analysis by Dellaferrera [113] has recently evaluated the accuracy of the LIUQE regression subject to multiple error sources. This study ignores the effects of kinetic measurements of electron and ion density and temperature profiles in the functional form of the current density profile, which can introduce additional uncertainty on TS- ρ_{ψ} . Yet, it is the latest and most up-to-date effort of quantifying LIUQE reconstruction errors. The plasma radial and vertical positions have been assigned a maximum uncertainty of 0.1cm and 0.3cm, respectively, during a L-mode shot 56000 at $t = 1s$ [113, p.10-15]. The larger vertical 0.3cm uncertainty translates into a ρ_{ψ} error of 0.004 along the TS viewing line at $\rho_{\psi} = 0.95$. Assuming that this plasma position error affects equally all TS data points, LIUQE plasma position uncertainties translate into a DBS turning-point ρ_{ψ} uncertainty of ~ 0.004 . This LIUQE-driven uncertainty is also included in figures 3-9 and 3-10 for reference. Covariance error analysis is, unfortunately, not currently available in H-mode.

Beyond TS density profile position errors, plasma vertical and horizontal position errors also affect the computed k_{\perp} and ρ_{ψ} since the intersection point between the mmw beam and the plasma is then uncertain. In order to estimate this error, the plasma position can be artificially moved. This requires advanced privileges controlling the LIUQE output. Instead, the launching position of the diagnostic launcher beam is artificially changed in the PrefGeom raytracing routine by the amounts given by Dellaferrera above. Using the same reference shot and time, it is found that the LIUQE plasma position errors result in a shift of turning point k_{\perp} and ρ_{ψ} of 0.23cm^{-1} and 0.0004 , respectively. These are both an order of magnitude under finite-beam error contributions determined via 3-point ray-tracing. Thus, LIUQE plasma position errors have a negligible effect on k_{\perp} and ρ_{ψ} uncertainty. Recall, however, that LIUQE vertical position errors have a direct effect on the localization of the TS profile as shown above.

Lastly, errors introduced by the uncertainty in the position of the launcher's poloidal angle of 0.2° are assumed negligible. To check this assumption, the launcher poloidal angle was changed by 0.3° resulting in an indeed negligible k_{perp} and ρ_{ψ} of change of 0.12cm^{-1} and 0.0003 , respectively. In conclusion, the DBS v_{\perp} estimate is subject to a large number of intrinsic and extrinsic error sources. These have been separated in figures [3-9 on page 70](#) and [3-10 on page 71](#) to illustrate the diagnostic limitations separately from uncertainties in TS density magnitude and the LIUQE magnetic reconstruction.

3.3 Results and discussion

Assuming typical magnetic field values in TCV, the V band DBS system presented here may sample densities in the range 3 to 7 (O-mode) and 0.8 to 4 (X-mode) $\times 10^{19} \text{ m}^{-3}$ which cover a large range of TCV's operational density space. The average SNR of the DBS signal is usually 20dB and may fluctuate between 10 and 40dB depending on shot conditions and k_{\perp} . Doppler shifts are often found under 0.75MHz in L-mode and may reach 1.5MHz in H-mode. The full-width at half max of the spectrum is usually 0.5-1MHz. Doppler shift uncertainties are usually found in the 50-200kHz range.

3.3.1 I-Q signals during plasma discharge

The single-frequency DBS I/Q data from TCV discharge 55455 is presented here to check I/Q signal integrity. With a launcher poloidal angle of 57° , the turning point is found at ρ_ψ 0.94 with a k_\perp of 6.2cm^{-1} . The Doppler shift recorded is red-shifted by about 400kHz as shown in figure 3-6 on page 62. Figure 3-8a depicts about 20 μs of raw I/Q data and shows that the I signal leads the Q by approximately 90deg. Specifically, the phase between these two signals is calculated to be 89.8deg over a 5ms period by taking the inverse cosine of their normalized dot product. The I/Q phasor circle is plotted in figure 3-8b and shows very good I/Q balance.

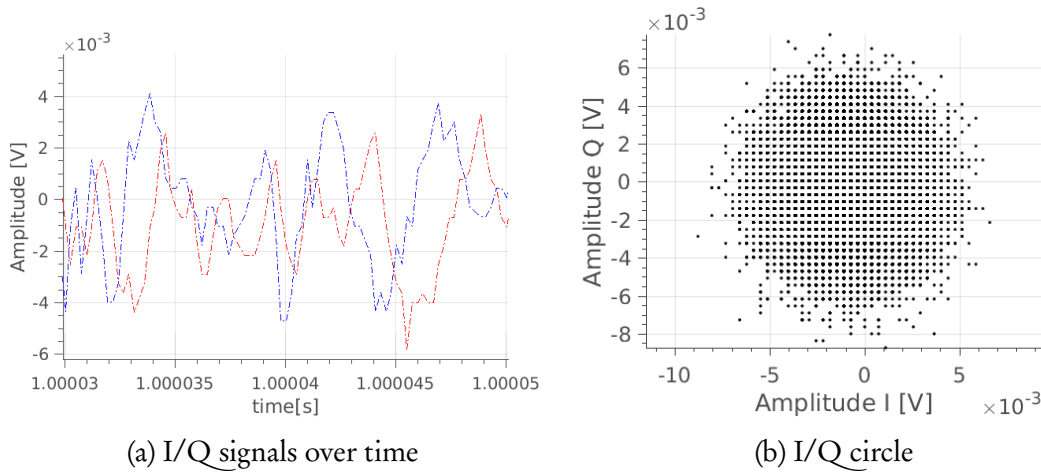


Figure 3-8: I(blue) and Q(red) signals acquired during shot 55455 at about 1.0s. No filtering is applied.

3.3.2 DBS-CXRS comparison

Single-frequency DBS turbulence v_\perp rotation estimates are compared with ExB poloidal rotation measurements from the charge-exchange recombination spectroscopy (CXRS) diagnostic in figure 3-9. Positive velocity in this figure refers to the electron diamagnetic drift direction, vertically upwards in figure 3-4. It should be noted that both diagnostics measure different quantities at different positions: CXRS lines of sight are at the plasma equator while the DBS beam, coming from an upper-lateral launcher, enters the plasma at a poloidal angle of $\sim 40^\circ$. Note that poloidal plasma rotation is not a flux quantity.

Yet, poloidal velocity estimates from both diagnostics have been historically shown to have relatively good agreement [87]. It is interesting to compare their order of magnitude, rotation direction, and radial profile since the turbulence rotation is expected to be dominated by ExB rotation in the edge of tokamaks [89].

The TCV CXRS diagnostic measures charge-exchange recombination emission from fully ionized Carbon impurities (C^{+6}) directly in front of a diagnostic neutral beam injector which supplies high velocity neutral particles for the reaction. C^{+6} density, temperature, and velocity are measured in the toroidal and poloidal directions with two spectroscopic cameras for each. In order to access the radial electric field, the radial force balance equation is used [114, eq.4.22]:

$$E_r = \frac{1}{n_\alpha q_\alpha} \frac{\partial p_\alpha}{\partial r} - u_{\alpha,\theta} B_\phi + u_{\alpha,\phi} B_\theta$$

where θ and ϕ refer to the poloidal and toroidal directions, and α refers to the Carbon impurity measured. The magnetic field components are obtained from the LIUQE reconstruction. The rest of the quantities are directly measured by the CXRS system [114, p. 57]. Many variables can affect the uncertainty of impurity density, temperature, and velocity: intrinsic photon statistics, noise in the instruments, and fit errors. Refer to Marini's PhD thesis for more details [114, ch. 2]. Velocity uncertainties in ideal background conditions can reach less than 1 km/s while the accuracy on both the temperature and density regularly attain levels under 10% and 15%, respectively. The standard error propagation formula is used to arrive at the error bars included in figure 3-9. Note that the CXRS curve in this figure is a spline fit of individual v_{ExB} estimates over ρ_ψ .

Figure 3-9 shows that the L-mode discharge 59555 features reasonably good agreement between DBS and CXRS. In the ohmic H-mode shot 59558, agreement is still good but lies almost outside error-bars for the outermost two points. Beyond the expected discrepancy regarding sampling position, the agreement can also be affected by many experimental factors. Firstly, the 20ms instantaneous stair-case sweeping of single-channel DBS frequencies samples the plasma differently than the time-integrated multi-channel

35ms averages in CXRS. Differences between measurements of ExB poloidal rotation via CXRS and turbulence perpendicular velocity via DBS can also be attributed to the phase velocity of turbulent density fluctuations relative to the plasma bulk. It is interesting to note that both discharges are ohmic and the difference has the same sign in both discharges.

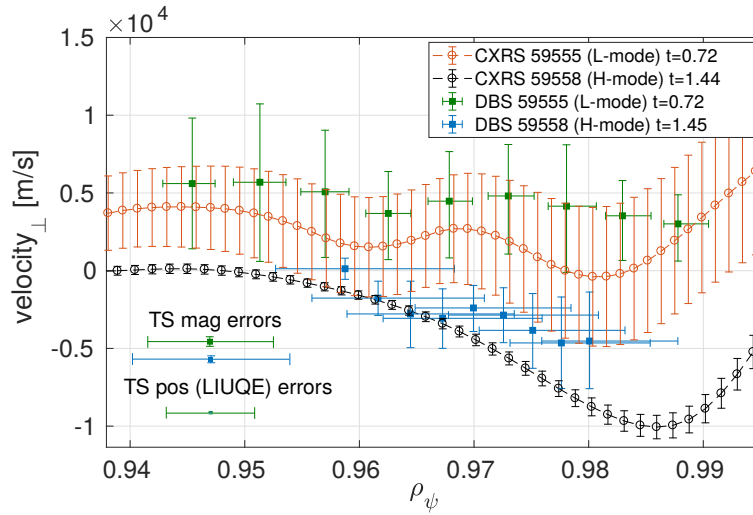


Figure 3-9: Comparing DBS perpendicular turbulence velocity estimates with a radial spline fit of CXRS $v_{E\text{XB}}$ estimates in L-mode (59555, k_{\perp} 5-5.8 cm^{-1}) and H-mode (59558, k_{\perp} 6.5-7.5 cm^{-1}) discharges. The average TS contribution to $\Delta\rho_{\psi}$ and Δv are shown decoupled from the inherent DBS uncertainties for illustrative purposes.

3.3.3 Comparing sweepable single with multi-frequency DBS setups

Figure 3-10 shows the velocity estimates of three identical shots at time 0.7s where the frequency spacing between the inputs was varied between 0.5, 1, and 2GHz resulting in seven output frequencies between 50-53, 50-56, and 50-62GHz, respectively. Figure 3-10 shows that the different estimates agree with each other and with the frequency-swept DBS using conventional I/Q detection.

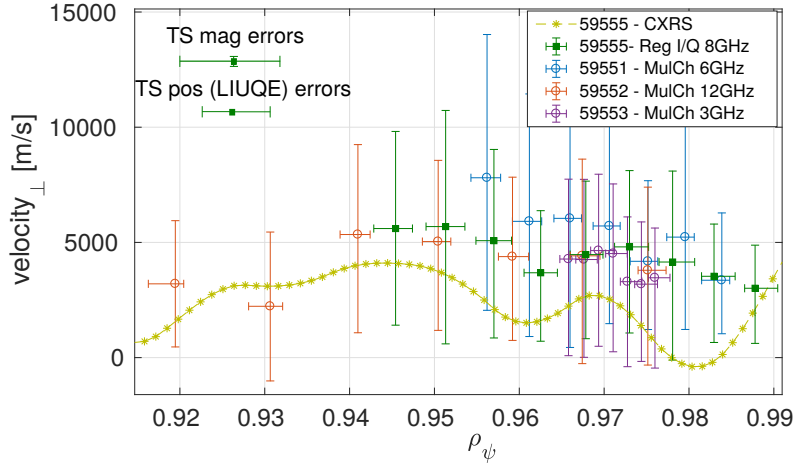


Figure 3-10: AWG-driven multi-channel DBS validation during similar shot conditions 59551-55 at 0.7s. $k_{\perp} = 4.5\text{-}6.0 \text{ cm}^{-1}$. CXRS traces as shown in figure 3-9 are included without error-bars for clarity.

3.3.4 In-shot polarization rotation to infer B-field line pitch

The pair of fast HE₁₁ polarizer miter bends presented in appendix A have been used to change the inclination angle of the polarization ellipse α while keeping a constant elliptical polarization angle β in search of an independent measurement of the magnetic field-line pitch. As summarized by Felici [115, p. 2], the polarization angle α is defined as the orientation of the main axis of the polarization ellipse with respect to the laboratory horizontal (Ex in figure 3-11). The *elliptical* polarization angle β is defined as the arctangent of the ratio of minor to major axis of the ellipse. Its sign defines the polarization direction: right or left handed. Both of these angles are limited to $\pm 90^\circ$. For example, a perfectly linearly polarized wave with an electric field oscillating in the horizontal axis lab frame has an α and β of 0 and 0, respectively. A perfectly right-handed (rotating clock-wise as observed from a location facing the direction of propagation) circularly polarized wave has $\beta = 45^\circ$; α cannot be defined in that case. A more complete definition can be found in Born's textbook [116].

The ideal α and β to obtain a perfect coupling to either X or O mode can be calculated by matching the launching beam wavevector and polarization to the plasma's LCFS magnetic field based on a trustworthy magnetic reconstruction. If the plasma conditions

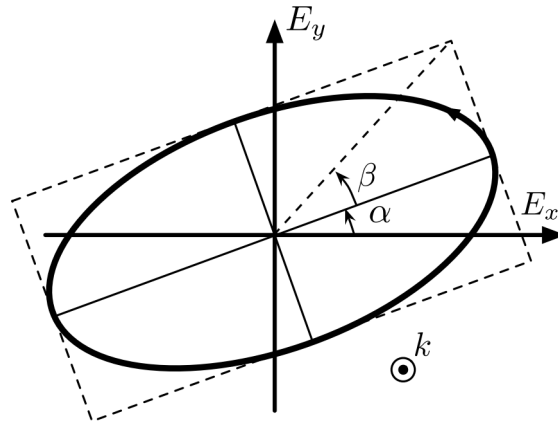


Figure 3-11: Electric field trajectory of an right circularly polarized wave propagating out of the page. This figure shows the definitions of the polarization ellipse angles α and β . Taken from [115]

are stable, the coupling of the launched wave to either X or O mode at the plasma LCFS can be made to change by varying α while keeping β constant. If both the effective α and the power of the DBS signal during the shot are examined, a measurement of the magnetic field pitch angle at the edge of the plasma is possible. Such innovative measurement is demonstrated here for the first time in a tokamak plasma. The plasma edge magnetic field pitch angle is defined as the arc-tangent of the ratio of the poloidal to the toroidal magnetic field at the LCFS: $\gamma = \arctan(B_\theta/B_\phi)$ at $\rho_\psi = 1.0$.

A few conditions must be met for this measurement to be possible. The α angle is measured with respect to the horizontal lab-frame [115], to which the edge B-field line usually has an inclination between $\gamma = 5 - 15$ degrees. Ideally, the X or O-mode cut-off to be sampled would be located in close proximity to the LCFS. This would minimize power variations caused by changing plasma conditions between the LCFS and the cut-off location, which may induce spurious power variations. Also, preferably, the cut-off of the opposite mode to be scanned should be found further separated in ρ_ψ from the LCFS and/or scatter at a larger k_\perp , so that backscattered power from the main mode (cut-off closer to the LCFS) is significantly larger and a clear coupling maximum can be found.

Figure 3-15 shows the evolution of both α and β angles during shot 59679. The encoder output of both linear and elliptical miter bend polarizer angles is mapped onto

α and β maps for each time step over the shot. These maps are generated for the 60GHz output frequency used in shot 59679 using the ECPOL[115] software package and are shown in figure 3-12. Figures 3-15 and 3-12 show that the effective α changes between +20 and -40 degrees while β can be made to remain between -5 and -6 degrees, aiming for an ideal -5.493 degrees for X-mode best coupling at a chosen toroidal angle of 0 degrees based on the LIUQE magnetic reconstruction. The best coupling to the X-mode wave into the main plasma (and then towards the scattering point expected at $\rho_\psi 0.97 \pm 0.01$) should occur when the probing beam's α hits a perfect 90° to the LCFS B-field line. Figure 3-13 shows the theoretical coupling to both X and O-mode given the effective polarization achieved by the fast polarizers through the shot time. This figure shows that the maximum coupling to a pure X-mode is expected by LIUQE to be found just before 1s when α reaches 81.43° .

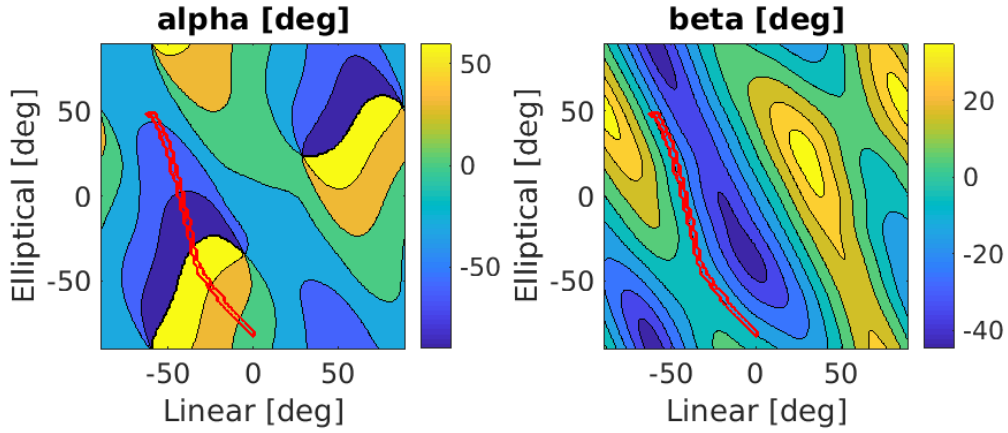


Figure 3-12: Polarization maps as a function of polarizer unit angle for 60GHz. The trajectory during shot 59679 is shown

The DBS signal power-spectral density evolution over the shot time is shown in the spectrogram in figure 3-14. This spectrogram was evaluated using 20ms time windows and the Welch algorithm presented above. It would seem from the raw spectra that the signal encounters a maximum towards 1.2s. It is likely that beyond 1s, the diagnostic is measuring a mixture of X and O-mode scattered power as seen theoretically in figure 3-13, yet the spectra does not show two separate peaks. Between $t=0.7$ and 1.6s, a Gaussian function is enough to fit the Doppler shifted PSD spectra with a R^2 above 0.985. The

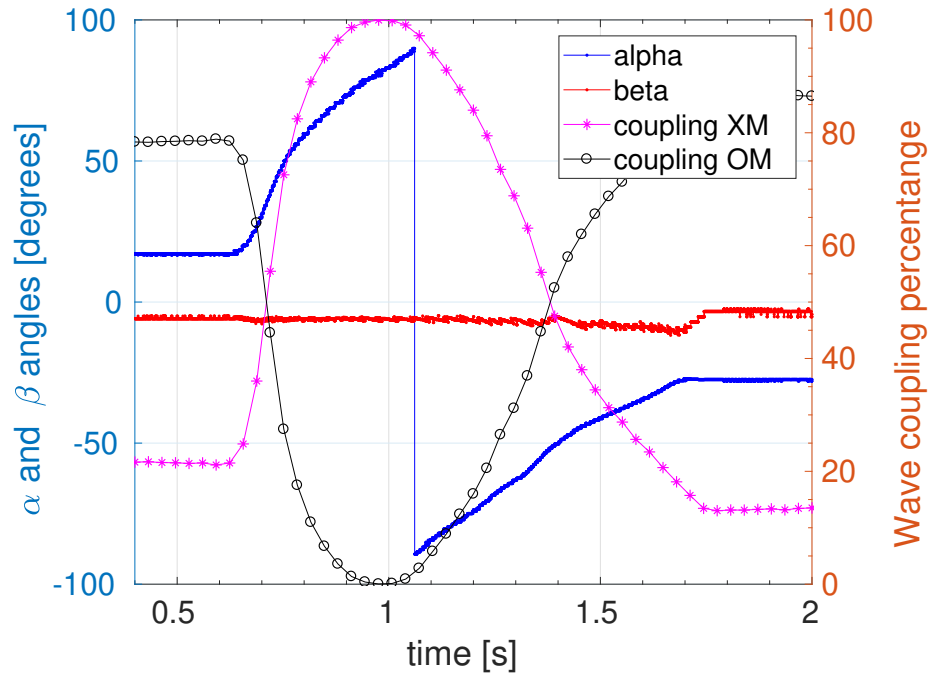


Figure 3-13: Theoretical wave coupling to both O and X-mode waves as a function of shot time while polarization angle α is made to vary keeping β constant.

standard deviation of the raw data also shows an increased signal scatter at around 1.2s.

However, the DBS signal power is best estimated by integrating the area under the Gaussian or SN fits to the smooth PSD spectra as described in section 3.2. Figure 3-15 shows the DBS power over the shot time estimating the area under the PSD fits with trapezoidal integration. The error bars in this estimate of power come from the 95% confidence intervals of the PSD fits. The recorded power is unfortunately noisy and features variations in the order of the error bars. This is probably due to plasma vertical oscillations through the shot which reached up to 6mm in the vertical ‘z’ axis dimension. Smoothing is done again on the DBS power estimates (20%) and a parabola $a - ((b * (x - c))^2)$ is fit to the points between 0.85 and 1.15s around the apparent peak at about 1s. The peak power is thus found at time 1.02 ± 0.01 where the alpha angle was 84.5 ± 3 , shown by the dark green line in figure 3-15. The error in the time location of the peak power is taken from the 95% confidence interval in the parabola fit for the constant c above. The parabola fit is done to the smooth power curve; the adjusted R^2 is 0.98. It must be admitted that the DBS power estimates are noisy and that the smoothing prior

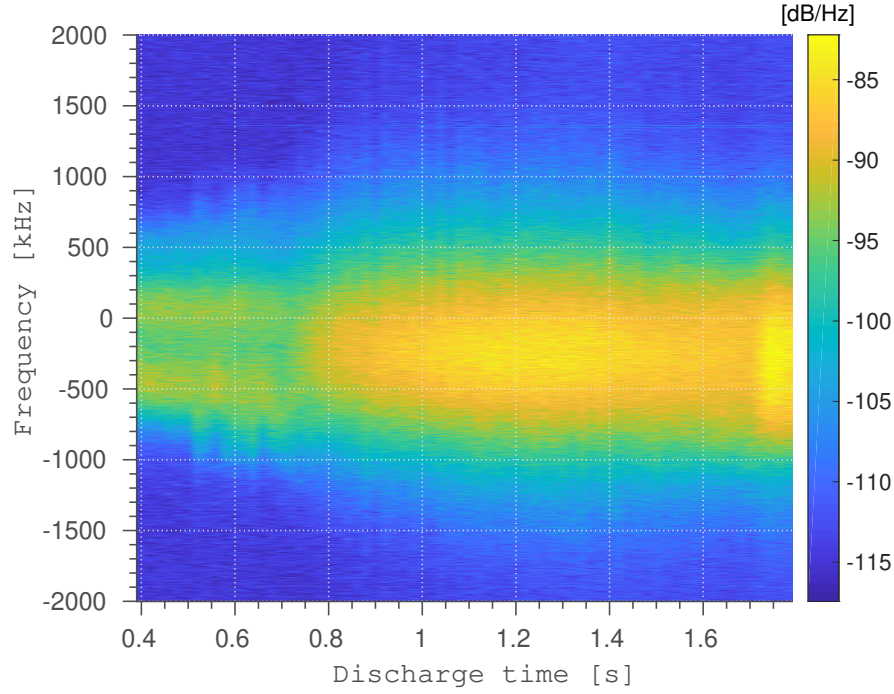


Figure 3-14: Spectrogram of raw DBS data during shot 59679 as the beam’s polarization angle α is made to vary keeping β constant. 20ms time windows for each PSD estimate are taken.

to the parabola fit has the potential to underestimate the error. However, the estimate is in the right order of magnitude at the very least and provides a lower bound to an error that could be as large as 10° from visual inspection of figure 3-15. It is not clear why the DBS signal power does not decrease rapidly after 1s as in the theoretical coupling figure 3-13.

The best X-mode coupling α estimate agrees within uncertainty with the LIUQE suggestion of $81.43 \pm 0.4^\circ$ (at $t \sim 0.98$ s shown in light green in figure 3-15). The LIUQE field pitch uncertainty was estimated assuming that the largest contribution to the error in the field-line pitch at the LCFS is the reconstruction of the plasma position. Del-la-ferrera’s [113] covariance analysis (introduced in section 3.2.3 on page 65) results for L-mode shot 56000 are invoked: the LIUQE plasma axis position can feature errors of 0.3cm in the vertical and 0.1cm in the radial dimension. These errors are multiplied by a factor of two to obtain an upper boundary. The error in the poloidal field can be found by multiplying the local gradient of the poloidal field at the scattering location by the

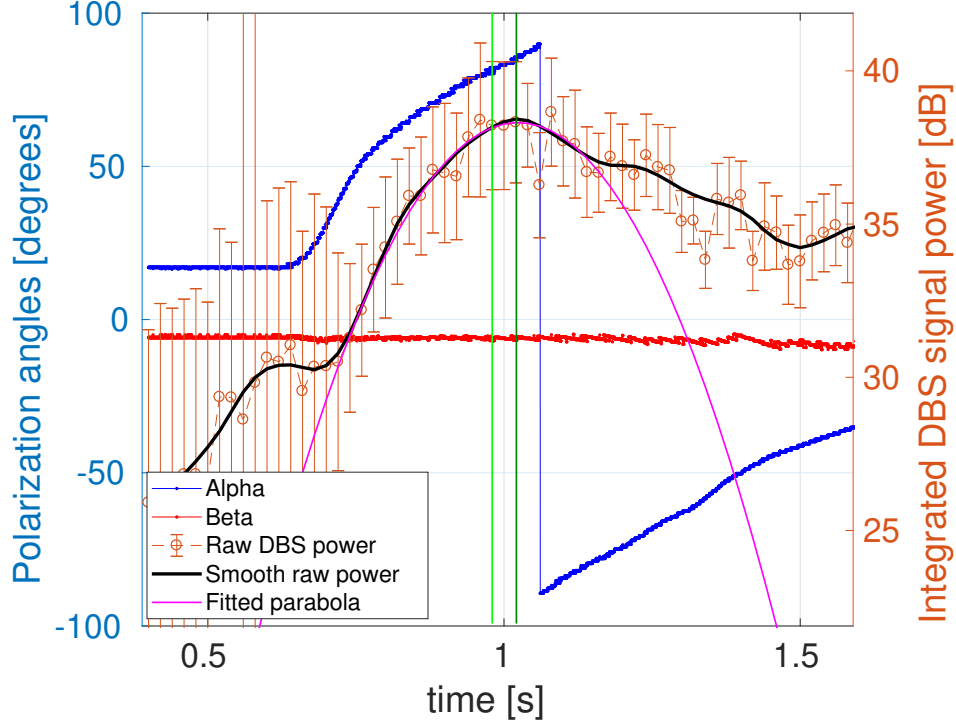


Figure 3-15: DBS signal power evolution over changing polarization axis inclination (α) angle: i.e. coupling into X/O-mode. 20ms time windows are taken for each PSD estimate, which leads to a 20ms DBS power signal. Shot 59679. Output frequency was 60GHz. Poloidal and toroidal angles are 18 and 0 degrees respectively. X-mode turning point at $\rho = 0.97 \pm 0.01$ with $k_{\perp} = 8.2 \pm 2 \text{ cm}^{-1}$. O-mode turning point expected at $\rho = 0.89 \pm 0.01$ with $k_{\perp} = 10.5 \pm 2 \text{ cm}^{-1}$. Dark green vertical line shows the peak integrated DBS signal power and the light green shows the LIUQE estimate of where such peak *should* have happened.

amplitude of the displacement, namely $\Delta B_{\theta} = \partial B_{\theta} / \partial s \cdot ds$ where s refers to the direction of the sampling beam, ds refers to the displacement error due to LIUQE defined as $ds = \sqrt{dz^2 + dR^2}$. dz and dR are given by Dellaferrera above. $\partial B_{\theta} / \partial s$ is found by inquiring B_{θ} in the LIUQE magnetic reconstruction at two locations along the beam's path ' s ' separated by 1mm. The error propagation formula is then used to estimate the error in the field pitch angle assuming no error in the toroidal field.

It is rightly acknowledged that this is a very rough estimate of the error in the field-line pitch. A covariance analysis focusing exclusively on the variations of the LCFS location and LCFS poloidal field contribution would be a more convincing approach. It is intuitively expected that given the proximity of the Mirnov coils to the LCFS that

the LIUQE regression's results are accurate at the LCFS. Future work should attempt to better point out LIUQE's field line pitch uncertainty at the LCFS, making use of covariance analysis and regressions including kinetic density and temperature profiles.

It can be concluded that the current lower-bound experimental uncertainty of $\pm 3^\circ$ must decrease by at least an order of magnitude to make this method practically relevant. In order to realize the polarization changes shown in figure 3-12, the elliptical and linear miter-bend polarizer stages moved by 128° and 62° , respectively, in about one second. Considering the peak-torque of 12 Nm of the RD-150 stepper motor drivers, the units could have theoretically achieved such trajectory in less than 100ms, which would have contributed to a 10x narrower parabola and less uncertainty in the peak coupling. Unfortunately, permanent increased mechanical torque in the elliptical unit due to friction between the mirror and the miter-bend casing prevented such faster trajectories to be realized due to driver overheating. A repair is foreseen as of this writing. Another potential contributor to a smaller uncertainty could be the shortening of the α range used to find the maximum coupling. Figure 3-15 fits the DBS power only inside $\alpha \pm 70^\circ$ (36° for the elliptical and 12° for the linear units), which could have been theoretically achieved in about 50ms. Additionally, both motors could be programmed to turn continuously at carefully synchronized rates that perform an α scan at constant β during predetermined sections of a revolution. Such approach would avoid the (de)acceleration stages where the largest torque in the trajectory is found.

The α, β trajectory could also be optimized to move out of good alignment symmetrically around the maximum. Figure 3-13 shows that the X-mode coupling increases rapidly between 0.6 and 0.8s, which is reproduced almost perfectly by the spectra in figure 3-14. However, as the O-mode coupling starts increasing again, there's a more gradual mixing of both modes (compounded by vertical plasma oscillations) as the polarization moves away from ideal X-mode. Future trajectories could focus on a faster and more symmetric exploration of the peak power.

Finally, a stronger DBS signal could also have contributed to reducing the uncertainty. A larger SNR could be achieved by introducing a non-zero toroidal angle and aligning the wave-vector of the beam as perpendicular as possible to the field line based

on the LIUQE field pitch estimates. The toroidal angle was chosen at 0° in this discharge because the PrefGeom ray-tracing routine is currently 2D and cannot model a beam with a non-zero toroidal angle. Lastly, a plasma under active vertical position control could have also contributed to a cleaner parabola and less uncertainty. Further experiments are planned once the elliptical fast polarizer unit is repaired.

3.4 Future perspectives

DBS has been operated in TCV from late October 2016 to April 2018 in the configuration presented here. Over two hundred shots are awaiting active analysis. Section 3.3 presented first results aiming at measuring poloidal rotation just inside the LCFS of TCV L-mode plasmas. Information regarding v_\perp modulation by geodesic acoustic modes awaits careful analysis. Additionally, this DBS diagnostic has the potential to study the turbulence energy spectrum by making use of the highly steerable launcher antenna and/or TCV's vertical plasma position flexibility. Shots 59532-59540 were devoted to measuring the energy spectrum of turbulence by varying the launcher's poloidal angle in both O and X-mode polarizations during positive and negative triangularity shots. These discharges could not be analyzed due to time constraints. These energy-spectrum studies can be a powerful tool to validate gyro-kinetic simulations through the use of DBS synthetic diagnostics [92]. The latter must include the response of the diagnostic launcher antenna to different probing angles by taking into account beam diffraction effects in backscattered power re-entering the last mirror of the launcher.

Furthermore, the DBS hardware presented above is identical to that of a continuous-wave heterodyne fluctuation reflectometer. The only difference between the two diagnostics is the effective macroscopic angle between the probing beam and the normal to the cutoff surface, which can easily be changed with the flexible launcher antenna available. Fluctuation reflectometers have the potential to characterize density fluctuations by measuring the phase of I/Q signals. MHD modes and density fluctuation levels may be inferred; however, long wavelength and relatively low fluctuation levels are required to extract quantitative information as addressed in chapter 2. Research campaigns search-

ing for the I-mode confinement regime [22] in TCV have made use of the DBS diagnostic in this mode of operation to search for a quasi-coherent mode in the edge ($\sim 200\text{kHz}$ in Alcator C-mod). Unfortunately, the I-mode has not yet been unequivocally identified in TCV, and the amplitude and phase spectra at perpendicular incidence have shown no evidence of such quasi-coherent modes.

Lastly, as shown in appendix A, the launcher antenna is shared with a correlation ECE diagnostic. If the O-mode cut-off location can be matched with a ECE sampling volume, both diagnostics can be combined to measure the statistical properties of density and temperature fluctuations simultaneously. Coherence and cross-phase of amplitude and phase between fluctuation reflectometry (dn) and ECE (dT) data have the demonstrated potential to reveal important information regarding turbulence drives [117] and to provide a direct validation of linear and non-linear gyro-kinetic simulations. The only hardware requirement is to have the same acquisition system measure the two signals, which is straightforward with the single frequency 16-channel D-tACQ system.

3.5 Summary

The present chapter presents the newly-installed V-band heterodyne DBS diagnostic in the TCV tokamak. The diagnostic can be uniquely configured for both sweepable single and multi-channel operation and is coupled to a flexible steerable quasi-optical launcher with in-shot adjustable polarization stages. It may reach densities between $0.8\text{--}7 \times 10^{19} \text{ m}^{-3}$. The accessible k_{\perp} range has been determined as $3\text{--}16 \pm 2\text{--}4 \text{ cm}^{-1}$ using 2D 3-point ray-tracing. The first results show perpendicular rotation velocities of electron turbulence in agreement with ExB poloidal rotation estimates from the CXRS diagnostic. Innovative experiments demonstrate a new approach to generating and detecting multiple simultaneous frequencies using a digital AWG and direct sampling. Furthermore, the magnetic-field line pitch angle at the edge was estimated by rotating the polarization axis orientation of the probing beam while maintaining a constant ellipticity, demonstrating unique O/X-mode coupling capabilities during the shot made possible by fast HET polarizers.

Unfortunately, the DBS diagnostic relies on experimental density and magnetic equilibrium reconstructions to determine the scattering location and probed k_{\perp} . Thus, although the DBS diagnostic may be sampled at 4MHz and used to explore sub-ms changes in Doppler shift, robust estimates of any quantity are intrinsically dependent on TS sampling intervals currently no shorter than 16ms. In contrast, the rapid E_r changes during L-H mode transitions occur over sub-millisecond scales [87]. A short pulse profile reflectometer diagnostic was built during this thesis to overcome this 16ms limitation and make full use of the DBS diagnostic capabilities. This diagnostic is presented in chapter 5 on page 109.

Chapter 4

Review of Reflectometry techniques

In TCV, electron density measurements from the plasma core to the last closed flux surface (LCFS) are routinely available from the Thomson Scattering (TS) diagnostic with a spatial resolution between 6-17mm but only 60Hz temporal sampling. Microwave reflectometry has been identified as a strong candidate for complementary measurements at the edge of confined plasmas given its high spatial (sub cm) and temporal (μ s) resolutions. Increasing the temporal resolution of edge density measurements could be decisive in revealing the dynamics of confinement regime transitions and fast pedestal events such as edge-localized modes (ELMs).

In reflectometry, the plasma electron density profile can be inferred from the round-trip group-delay of EM waves reflected from a plasma cut-off as described in [section 2.3 on page 33](#). If the group-delay is measured over a sufficiently large number of frequencies covering a portion of the tokamak radial profile, an Abel inversion (O-mode) recovers the density profile as a function of distance from the antenna. The current chapter begins by reviewing the practical approaches to measuring $\partial\phi/\partial\omega(\omega)$ and how pulse reflectometry fits in the big picture. A number of excellent reviews on the subject of reflectometry exist, e.g., Laviron [59], Mazzucato [43], Doyle [118]. The ideas presented here attempt to bring these reviews together and include modern pulsed reflectometry achievements. Before addressing the different implementations, the basic homodyne and heterodyne phase detection architectures are briefly introduced.

4.1 Basic phase detection techniques

4.1.1 Homodyne and heterodyne techniques

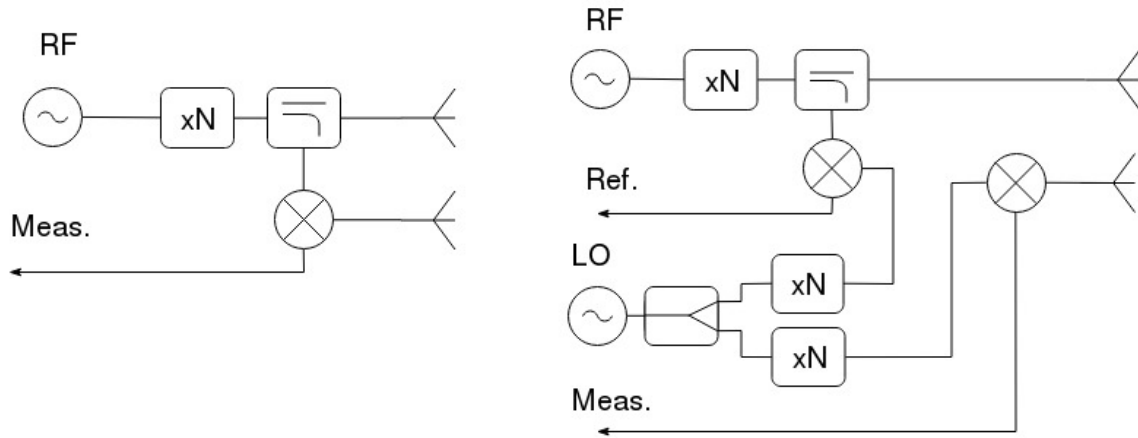


Figure 4-1: Homo and heterodyne continuous-wave reflectometer implementations

In order to practically measure a phase difference, both homodyne and heterodyne approaches have been used. Figure 4-1 [43] shows a simplified sketch of these two approaches. Both designs make use of relatively low frequency oscillators and frequency multipliers. This is the most common modern approach to generating reflectometry-relevant frequencies in U/V/W bands. The VDI modules used in this thesis, for example, require inputs within 8.33-12.5GHz and employ varactor multipliers (x6) to generate frequencies in the 50-75GHz range. Both designs also feature microwave mixers shown by the round X symbol. This symbol implies that mixer output consist of the product of their inputs. In practice, these are realized by coupling the input signals into non-linear or time-varying elements (diodes or transistors) to achieve frequency conversion producing a large variety of harmonics and products of the input signals. Their principle of operation is further addressed in Pozar [103][ch.13.5]. The homodyne reflectometer signal can be expressed as follows:

$$S_{\text{out}} = A_1 \cos((\omega_{\text{RF}} \times N)t) = A_1 \cos(\omega_0 t) \quad (4.1)$$

$$S_{\text{Refl}} = a(t) \cos(\omega_0 t + \phi(t)) \quad (4.2)$$

$$S_{\text{Meas.}} = a(t) \cos(\omega_0 t + \phi(t)) \cdot B \cos(\omega_0 t) \quad (4.3)$$

$$= \frac{a(t)B}{2} \cdot [\cos(2\omega_0 t + \phi(t)) + \cos(-\phi(t))] \quad (4.4)$$

$$S_{\text{Meas.} + \text{LPF}} = \frac{a(t)B}{2} \cdot \cos(\phi(t)) \quad (4.5)$$

As can be seen in the final equation above, after low pass filtering (LPF), the relatively simple hardware of the homodyne reflectometer allows the measurement of the phase change induced by the probing beam's round-trip to and from the cut-off layer. Unfortunately, the time-dependent reflected signal amplitude is also present in the final signal. Conway et al. [81] show how a hybrid tee and matched detectors can be used to separate amplitude and phase in the homodyne approach. Also, the digital complex demodulation method (CDM) [43][pg.2211] can be used during analysis to separate the signal's phase. Unfortunately, homodyne systems do suffer from increased 1/f noise compared with heterodyne approaches [43] since the beating frequency measurements are done about 0 frequency. Also, the sign of the phase difference and possible Doppler shifts cannot be distinguished unless the CDM technique is used in the analysis.

The heterodyne approach improves on these issues by making use of a separate local oscillator (LO) signal to measure amplitude and phase changes at an intermediate frequency (IF) at the expense of increased hardware complexity. The IF frequency brings measurements further away from DC and as long as the IF frequency is not too large (<20GHz), low noise amplifiers and SMA filter technology allow good signal quality. The heterodyne reflectometer signal can be expressed as:

$$S_{\text{out}} = A_1 \cos((\omega_{\text{RF}} \times N)t) = A_1 \cos(\omega_0 t) \quad (4.6)$$

$$S_{\text{Ref.}} = A_1 \cos(\omega_0 t) \cdot B_1 \cos((\omega_{\text{LO}} \times N)t) \quad (4.7)$$

$$= A_1 B_1 \cos(\omega_0 t) \cos(\omega_1 t) \quad (4.8)$$

$$= \frac{A_1 B_1}{2} (\cos((\omega_0 + \omega_1)t) + \cos((\omega_0 - \omega_1)t)) \quad (4.9)$$

$$S_{\text{Ref.} + \text{LPF}} = \frac{A_1 B_1}{2} \cos((\omega_0 - \omega_1)t) \quad (4.10)$$

$$= \frac{A_1 B_1}{2} \cos(\omega_{\text{IF}} t) \quad (4.11)$$

$$S_{\text{Ref.}} = a(t) \cos(\omega_0 t + \phi(t)) \quad (4.12)$$

$$S_{\text{Meas.}} = a(t) \cos(\omega_0 t + \phi(t)) \cdot B_1 \cos(\omega_1 t) \quad (4.13)$$

$$= \frac{a(t) B_1}{2} \cdot [\cos((\omega_0 + \omega_1)t + \phi(t)) + \cos((\omega_0 - \omega_1)t + \phi(t))] \quad (4.14)$$

$$S_{\text{Meas.} + \text{LPF}} = \frac{a(t) B_1}{2} \cdot \cos(\omega_{\text{IF}} t + \phi(t)) \quad (4.15)$$

where ω_{IF} is the intermediate frequency corresponding to the difference between the RF and LO (xN) frequencies. The filtered Ref. and Meas. are then connected to an I/Q mixer to extract amplitude and phase. The schematic of an I/Q mixer is shown in figure 4-2 below [6][pg.56].

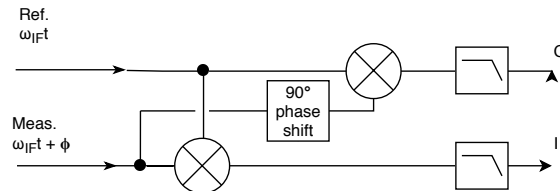


Figure 4-2: Circuitry inside the so-called I/Q mixer.

$$S_{I+LPF} = \frac{a(t)A_1B_1^2}{4} \cos(\phi(t)) \quad (4.16)$$

$$S_{Q+LPF} = \frac{a(t)A_1B_1^2}{4} \cos(\phi(t) + 90^\circ) = \frac{a(t)A_1B_1^2}{4} \sin(\phi(t)) \quad (4.17)$$

which can immediately be identified as a complex number: $P = I + iQ$, from which amplitude and phase can be easily calculated.

4.2 Continuous wave techniques

4.2.1 Single swept frequency

The continuous-wave frequency modulation technique (CWFM) is the most widespread reflectometry technique in fusion plasmas [119]. It is actively used in the world's largest tokamaks: DIII-D[120], JET, ASDEX-U [121], among others. It consists of launching a single frequency into the plasma and measuring a phase difference between the launched and reflected waves. If the launched frequency is rapidly swept, the phase also evolves in time giving rise to a beating frequency.

$$\tau_g = \frac{\partial \phi}{\partial \omega} \cong \frac{d\phi/dt}{d\omega/dt} \quad (4.18)$$

CWFM reflectometers measure the $d\phi/dt$ beating frequency and given a well-known, stable, frequency sweeping rate, the group delay can be inferred. Figure 4-3 shows a sketch of the CWFM approach along with the time evolution of its probing signal.

Beyond the technical approach to measuring the phase evolution, CWFM systems can also be divided in two main groups: broad-band and narrow-band. The former consists of using a transmitter whose frequency can be varied over a few tens of GHz so that entire portions of the profile can be recovered in a single sweep. In early CWFM reflectometers, the mm-wave source was a backward-wave oscillator (BWO) [59]. These are vacuum tubes where electrons interact with a slow-wave structure. Output powers

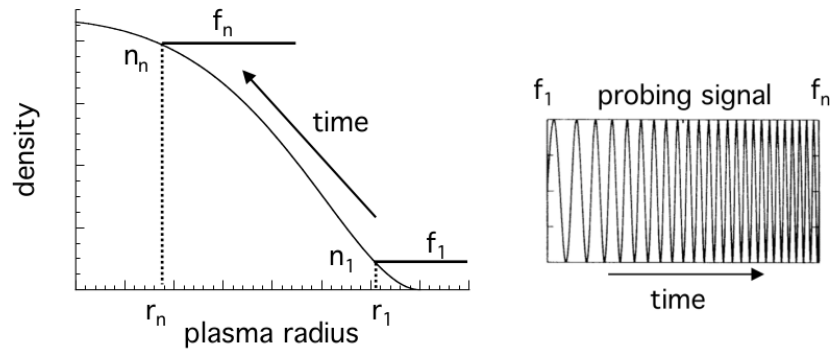


Figure 4-3: Principle of operation of continuous-wave frequency modulation technique. Adapted from [59]

in the 100s of mW are possible up to 140GHz. Unfortunately, BWOs could be made to sweep through an entire band in a time only as fast as a few milliseconds, which turns out to be problematic in a plasma due to MHD modes and micro-instabilities that evolve over faster time scales and induce errors in the beating frequency. In the late 90s, voltage-controlled oscillators (VCOs) became available in frequencies below 20GHz [122]. VCOs in combination with active frequency multipliers can be made to reach into the mm-wave ranges. At the core of VCOs are LC-tank oscillators which can be made to change frequency by varying the voltage across varactor diodes. Frequency sweeping through an entire band can be achieved in μs time scales [121], offering increased resilience against density fluctuations.

The other CWFM approach consists of launching individual frequencies that are locally varied by a few 100s of MHz such that the group delay from a particular cutoff layer can be found at each location independently [123]. This technique requires separate oscillators for each data point, which complicates hardware if a detailed profile is required. Interpolation between the group delays of each frequency is required and can lead to fictitious profiles if the separation is too large [118]. Gunn diodes [59], also known as transferred-electron devices (TED), have been used by this approach. These are semiconductor devices that feature negative differential resistance in their IV curve. Mounted inside a RF resonator, these can be made unstable and oscillate in the microwave range. Their range of tunability is limited to about 10% of the central frequency.

4.2.2 Multiple frequency techniques

The round trip group delay can also be measured by launching multiple frequencies simultaneously. This is the approach taken by double frequency and amplitude-modulation (AM) techniques. These techniques are currently being used in the edge region of TJ-II, and have been used in the defunct PBX-M [124], TFTR, and W-7AS [125] machines. In the double-frequency technique, two separate frequencies are launched simultaneously through the same antenna. If the phase difference of each frequency is measured separately in the receiver, the group delay can be approximated as:

$$\tau_g = \frac{\partial \phi}{\partial \omega} \cong \frac{\Delta \phi_1 - \Delta \phi_2}{\omega_1 - \omega_2} = \frac{\Delta \phi_{1-2}}{\Delta \omega_{1-2}} \quad (4.19)$$

$$(4.20)$$

Alternatively, the amplitude of the outgoing wave can be modulated at a frequency much lower than the carrier.

$$S_{\text{out}} = A(1 + m \cos(\omega_m t)) \cos(\omega_0 t) \quad (4.21)$$

$$= A \left[\cos(\omega_0 t) + \frac{m}{2} \cos((\omega_0 + \omega_m)t) + \frac{m}{2} \cos((\omega_0 - \omega_m)t) \right] \quad (4.22)$$

The frequency spectrum and time evolution of this signal is sketched in figure 4-4.

The group delay in this case is given by:

$$\tau_g = \frac{\partial \phi}{\partial \omega} \cong \frac{\phi_{f+fm} - \phi_{f-fm}}{\omega_{f+fm} - \omega_{f-fm}} = \frac{\Delta \phi}{\omega_m} \quad (4.23)$$

The amplitude modulation is usually achieved via a semiconductor PIN diode: a diode with a large undoped intrinsic semiconductor region. These PIN diodes have large resistances in the 100s of k Ω when not biased. When directly biased, their resistance drops below 1 Ω . Their internal packaging and parasitic capacitances can limit their low-

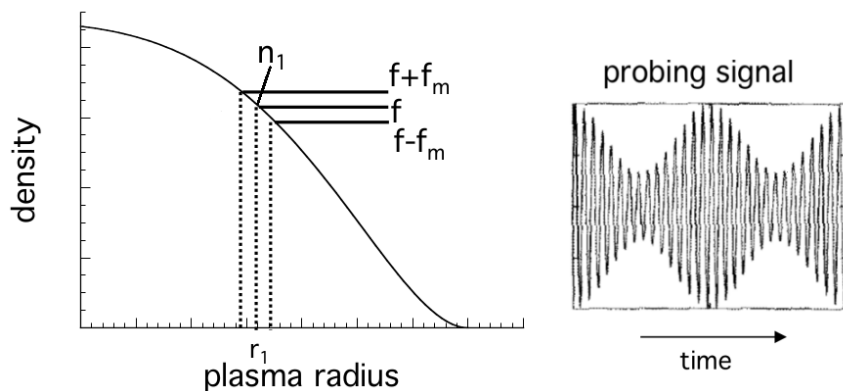


Figure 4-4: Sketch of waveform and spectra of the continuous wave amplitude-modulation technique (CWAM). Adapted from [59]

frequency performance, but for frequencies in the hundreds of MHz and above these pose no problems [126, p. 44].

The distance between both frequency terms (or its modulation frequency) is usually chosen in the order of 100-400MHz. This value corresponds roughly to the correlation length of turbulence, which allows this technique to average out the effects of density fluctuations. Since both frequencies are affected equally by turbulence, their phase difference is a better estimate of the average group-delay. Once this phase difference is measured at a given frequency, either both individual frequencies or the AM carrier frequency is swept in order to allow measurements of the group delay curve vs frequency. The practical implementation of both double-frequency and amplitude modulated reflectometers is presented in [43], [124], [125]; their implementation details are beyond the scope of this text.

4.3 Pulsed wave techniques

Another, less explored, approach to reflectometry consists of measuring the round-trip group delay of a time-localized microwave pulse. This approach is closest to conventional long-range radar, and it is arguably the most direct way of measuring $\partial\phi/\partial\omega$. The quantity being measured is directly the pulse envelope group delay or time-of-flight. Given the inverse relationship between time and frequency $\Delta f\Delta t = 1$, time-localized pulses

send a relatively large spectrum into the plasma when compared with the localized spectra of continuous-wave techniques. Hence these have been called *broadband* techniques [59]. Two main technological approaches have been realized so far: short and ultra-short pulse reflectometry.

4.3.1 Short pulse reflectometry

Short pulse reflectometry (SPR), also called moderate-pulse or pulse-radar, has been implemented by Shevchenko et al. [127], Heijnen et al. [126] (RTP and TEXTOR), and Tokuzawa et al. [128](LHD) in the nineties but none are operational today. SPR sends a 1-10 ns microwave pulse with a carrier frequency that encounters a cutoff and measures the pulse round-trip group delay with a precise chronometer. The frequency dependence of this quantity is obtained by launching sequential pulses with different carrier frequencies. Figure 4-5 below shows a sketch of the principle of the technique.

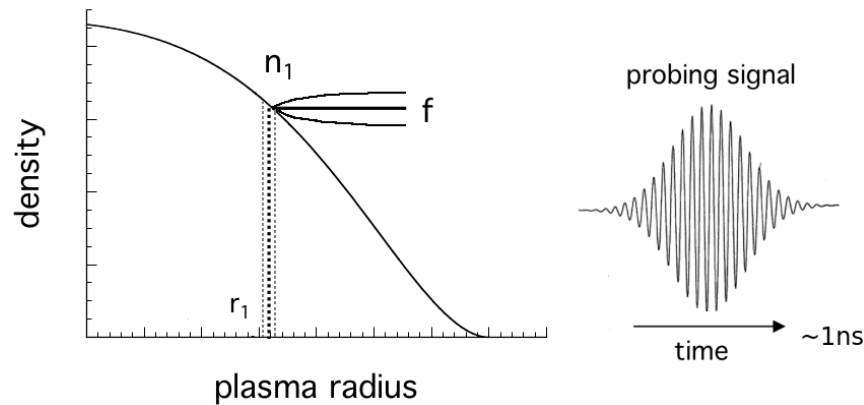


Figure 4-5: Conceptual sketch of short-pulse reflectometry featuring the time evolution of the sampling signal. Adapted from [59]

The technical realization of short-pulse reflectometry is shown in figure 4-6. It shows the approach taken by the RTP and TEXTOR pulsed reflectometers [126]. Several oscillators are combined in either a passive combiner or an active multiplexer (single pole, four throw SPFT) and their output is converted into a nanosecond pulse by a high-speed semiconductor PIN diode switch. These PIN diodes are driven by pulse generators in the 1-10 ns range. The shortest pulse obtained with this technique was 700 ps achieved

by the RTP group [126, p. 43] driving a PIN switch with bipolar pulses, at the expense of 7dB insertion losses. Four and ten channel versions of this instrument have been conceived [129, 130].

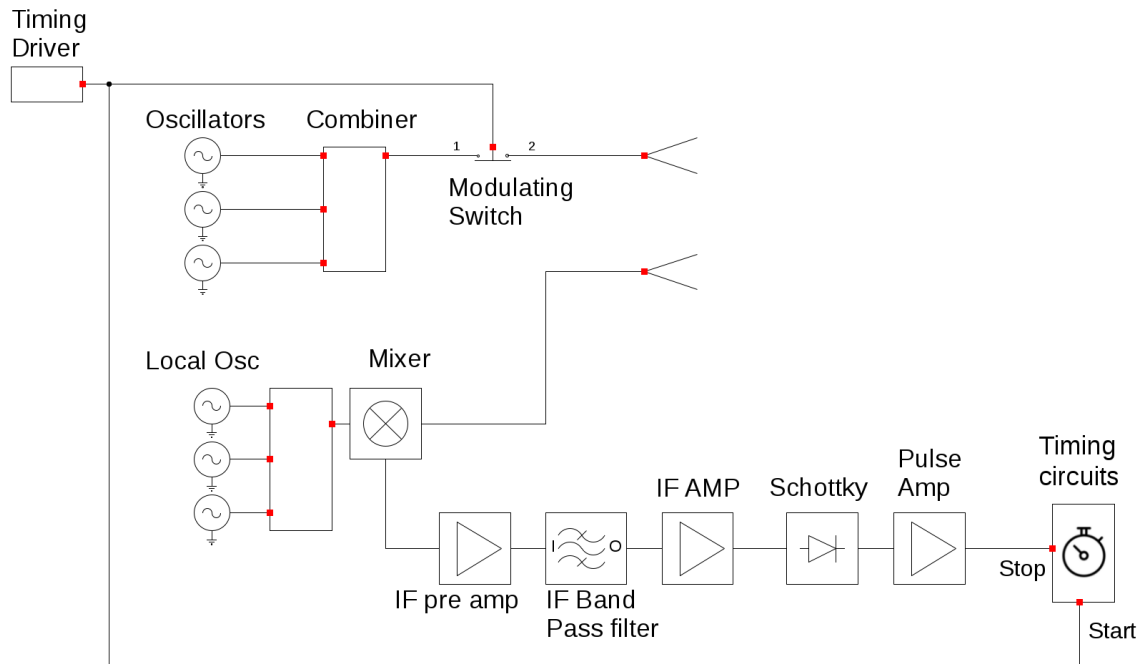


Figure 4-6: Short-pulse reflectometer block diagram. Based on the RTP design in Heijnen’s PhD thesis [126, p. 41]

The receiver in figure 4-6 uses heterodyne detection for added $1/f$ noise immunity. The intermediate frequency is usually below 20GHz, which allows filtering, amplification, and detection with relatively accessible components. Taking Gaussian pulses of about 1ns FWHM, the frequency spectrum launched into the plasma is also a Gaussian pulse of 1GHz FWHM. Thus, the IF filters must have a width of about 1-2GHz. The filter function should be a Gaussian to avoid ringing [126, p. 27-32]. After detection with a Schottky diode, which extracts the Gaussian envelope, the pulse is fed into timing circuits. Unfortunately, the Schottky detector extracts only the amplitude of the reflected pulse: heterodyne phase information is lost in this implementation. The timing circuits are discussed in detail in section 5.2 below.

Short pulse dispersion by smooth profile slopes

The 1GHz bandwidth of a 1ns pulse has raised concerns regarding pulse distortion by density fluctuations [118] and its effects on group-delay measurements. Heijnen presented an approach [126][ch.2] to study pulse distortion by smooth density profiles in the absence of small density fluctuations. This approach is applied here to study whether short pulses experience significant pulse dispersion by common TCV density profiles. The approach consists of taking the pulse frequency spectrum of a Gaussian pulse and evolving the phase of each frequency component of the Gaussian via Ginzburg's exact solution to the round-trip phase within the WKB approximation (presented in section 2.2.1). Then, an inverse Fourier transform can be used to recover the reflected pulse shape in the time-domain as follows:

$$S_{\text{out}}(t) = \frac{\alpha}{\sigma\sqrt{2\pi}} e^{\left(\frac{-t^2}{2\sigma^2}\right)} \cos(\omega_c t) \quad (4.24)$$

$$\tilde{S}_{\text{out}}(\omega) = \alpha \cdot e^{\left(\frac{-\sigma^2}{2}(\omega - \omega_c)^2\right)} \quad (4.25)$$

$$S_{\text{Ref.}}(t) = \frac{\alpha}{2\pi} \int_{-\infty}^{\infty} e^{\left(\frac{-\sigma^2}{2}(\omega - \omega_c)^2\right)} e^{(-i\phi(\omega))} e^{(i\omega t)} d\omega \quad (4.26)$$

where $\phi_{\text{round-trip}}(\omega) = 2 \int_{x_c}^{x_e} \vec{k}(x') dx' - \frac{\pi}{2}$ and the dispersion relationship for O or X-mode can be used to express $k(x')$ as a function of ω to solve the above equation as appropriate.

Figure 4-7 shows the results of applying the above calculations to O-mode reflectometry during shot 46735 assuming a quadratic profile. The figure shows that pulse dispersion is not a concern for pulses of 1ns except when these approach the plasma core. This result can be interpreted as various frequency components of the pulse reflecting from significantly different portions of the profile. Recall from chapter 2 that Airy widths were also found to increase when reflecting from flat portions of the profile in O-mode as seen in figure 2-5a.

Turning a potential drawback around, measuring pulse dispersion carries information about the plasma density gradient. Pulses under 0.5ns can be broadened by the local

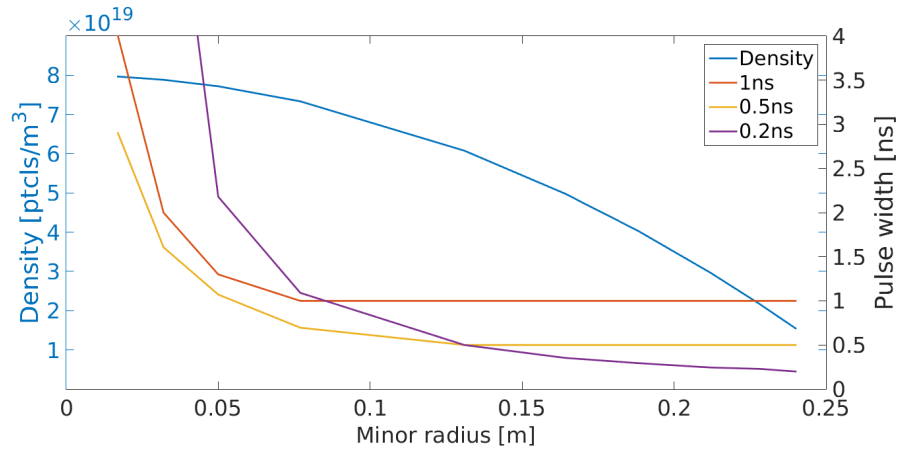


Figure 4-7: Pulse dispersion of pulses of varying width. Shot No.46735 core and edge densities of 8 and $1 \cdot 10^{19} \text{ m}^{-3}$ are used in a L-mode-like quadratic profile

plasma slope at the cut-off point as seen in figure 4-7. Hacquin et al.[131] have suggested dispersion could yield both the group delay and the slope of the density profile at the cut-off layer. The 0.2ns pulse in figure 4-7 is indeed seen to widen as the profile slope becomes flatter.

4.3.2 Ultra-short pulse reflectometry

Ultra-short pulse reflectometry (USPR) consists of using the wide frequency spectrum of a picosecond-range pulse to probe a large portion of the plasma density profile with a single pulse. It was pioneered by Domier [132] (CCT, SSPX) and various Japanese groups: Kubota(Gamma-10) [133], Tokuzawa(LHD) [134], and Takahiro(Hyper-1) [135]. Figure 4-8 below shows a sketch of the waveform launched by the USPR technique.

Figure 4-8 shows the waveform that results from *chirping* a 23ps FWHM, -2.2V peak pulse through a 0.5m-long R-band (WR-430) waveguide[134]. A 23 ps FWHM Gaussian pulse will correspond to a Gaussian centered at zero frequency with a spectral FWHM width of 43.5 GHz. The raw pulse, however, is not directly launched into the plasma. The usual approach is to chirp the pulse using a rectangular waveguide with a low frequency cut-off near the middle of the pulse's broad spectrum. The chirping process filters out low-frequency components and prepares the signal to enter mm-wave mixers and amplifiers that condition the output signal. The chirping process can be modeled by

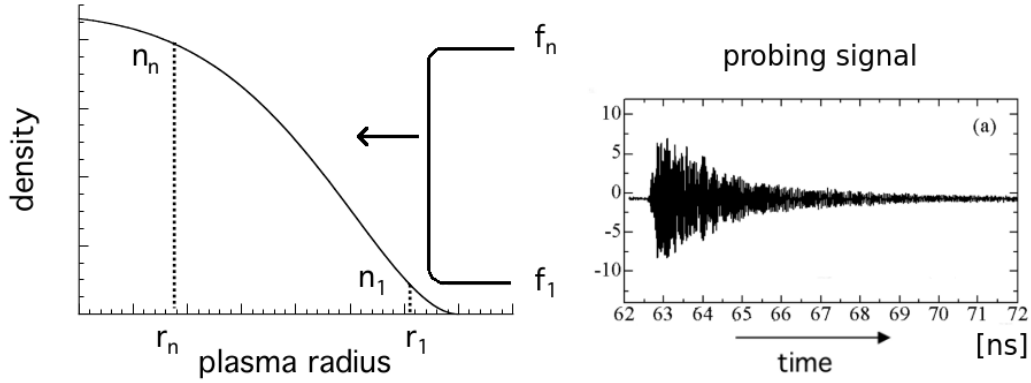


Figure 4-8: Conceptual sketch of ultra-short-pulse reflectometry featuring the time evolution of the sampling signal.

considering the dispersion relationship inside a rectangular waveguide (see [103, p. 110-114]):

$$k = \frac{1}{c} \sqrt{\omega^2 - \omega_{\text{cut-off}}^2} \quad (4.27)$$

$$\omega_{\text{cut-off}} = c \sqrt{\left(\frac{m\pi}{a}\right)^2 + \left(\frac{n\pi}{b}\right)^2} \quad (4.28)$$

Modeling the dispersion process inside the waveguide is important to optimize the duration and power of the chirp output as a function of waveguide cutoff and length [136]. Figure 4-9 shows the LHD USPR reflectometer. Some USPR implementations [135] use a step-recovery circuit to generate pulses down to 65ps. Another approach to generate even shorter pulses is to take the derivative of a very fast decaying signal as shown in figure 4-9. A 14ps fall-time signal is firstly generated with a non-linear transmission line and an impulse-forming network can be used to take its derivative. The result is a 23ps negative-polarity Gaussian pulse with a spectrum of about 43GHz FWHM.

Figure 4-9 shows that the spectrum coming out of the ultra-short pulse does not necessarily limit the instrument's highest output frequency [137]. After broad-band amplification, the spectrum is divided into high and low frequency branches. The high-frequency branch, above 25GHz, is frequency doubled into the V band (50-75), while

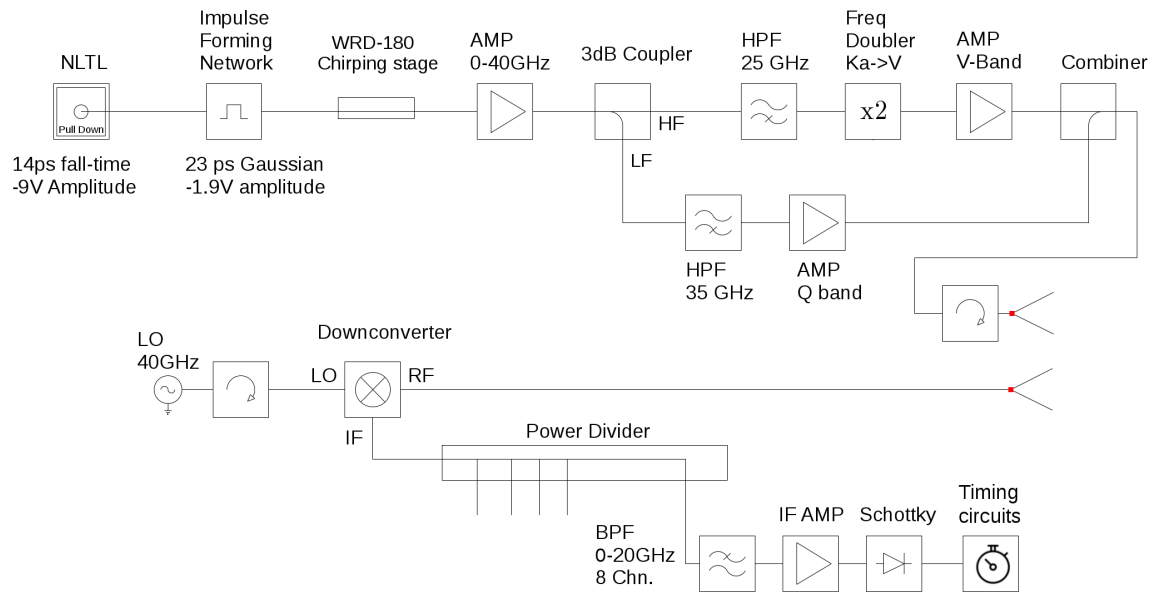


Figure 4-9: Ultra-short pulse reflectometer block diagram. Based on Tokuzawa's LHD design [134]

the low-frequency branch simply focuses on amplifying the input spectra above 35GHz. The result is an output spectrum with frequencies between 35-75GHz. This branching is required to bring the broad spectra into higher frequencies and also ensures that the power distribution over frequency is somewhat constant.

The receiver in figure 4-9 bears strong resemblance to ECE radiometers. It consists of a heterodyne stage where the reflected frequencies are first down-converted into an intermediate frequency and then individually detected through a filter bank. In this case, the local oscillator frequency is designed to receive the reflected spectra in the U band 40-60GHz. The power divider distributes the returning chirp into band-pass filters (BPF) which become single group-delay data-points. The output of each BPF is then amplified and fed into a Schottky diode detector as in the SPR receiver above. The latter extracts the pulse envelope function and provides a trigger signal to the timing circuits further addressed in section 5.2 on page 114.

4.4 Comparison criteria

The current section builds on comparison criteria presented by Doyle et al. [118], Lavi-ron et al. [59], and Mazzucato [43] to include pulsed-wave techniques and introduce the motivations behind building an AWG-driven short pulse reflectometer. Five comparison criteria are briefly introduced and used to semi-quantitatively compare the different approaches to reflectometry.

4.4.1 Range resolution

To find the location of a given object, a civil or military pulsed-radar launches a time-localized EM wave and records the time between launching and receiving the wave. The distance to the target, also called the *range*, can be found from simple algebra as $R = c t_d/2$ where c is the speed of light in vacuum (very close to the speed of light in air) and t_d is the time delay between launching and receiving the pulse. Range resolution refers to the ability of a ranging system to resolve two closely-spaced points. If a pulse is launched towards two closely spaced targets, two separate echos from each target can be resolved if the time light travels between these echos is greater than the pulse duration. Otherwise, the reflections from both targets can interfere resulting in either a pulse shape variation or a single pulse for both targets. Range resolution is then related to the pulse duration as follows [138, ch.1]: $\Delta R_{res} = \frac{cW}{2}$ where W is the pulse full width at half maximum (FWHM) duration. This resolution is independent of the hardware choice. The inverse relationship between time and frequency can be used to derive the range resolution of continuous wave radars [118, Sec 5.a]: $\Delta R_{res} = \frac{c}{2\Delta B}$, where ΔB corresponds to frequency bandwidth.

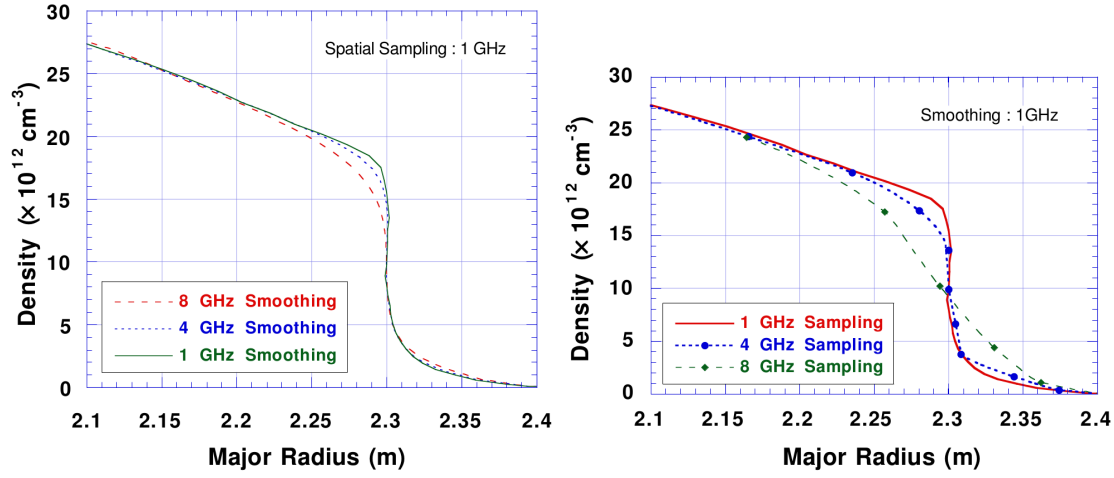
Range resolution is an important parameter in reflectometry because it indicates how well the diagnostic can deal with spurious reflections in the transmission lines. These may arise from miter bends, protection filters, or vacuum windows, which as seen in section A.1.4, can feature changing reflection coefficients as a function of frequency. Usually, spurious reflections have power levels 15-40dB below the main plasma reflections [139]. However, if the reflectometer is not able to identify these during calibration,

the profile reconstruction may be compromised. In pulsed reflectometry false reflections are easy to filter out since they appear at a different time window than the main plasma reflection, as long as the pulse is sufficiently short. The usual nanosecond pulse durations of SPR systems feature an 5-10cm range resolutions. In CWFM reflectometry, spurious reflections at different distances give rise to additional frequency components in the beat frequency spectrum [49]. Spectral filtering techniques [140] or the pulse-compression technique [139] can be used to account for these during calibration.

In multiple-frequency CW systems, spurious reflections present a serious concern. Since the frequency difference chosen is usually about $\sim 100\text{MHz}$, their range resolution is at least an order of magnitude below CWFM and/or pulsed techniques. Hartfuss shows mathematically how [49, Sec 8.3.5], without exact knowledge of the distance to each reflection and its contributing amplitude, it is impossible to separate spurious contributions to the differential phase from plasma reflections. Multiple-frequency CW systems benefit greatly from separate transmission and reception waveguides (bi-static).

A large bandwidth, however, does not necessarily mean better resolution at the cut-off in fusion plasmas because the refractive index changes as the wave approaches the cut-off. Also, the cut-off is a function of frequency, thus not every frequency component of a broadband signal bounces back from the same target as in regular radar. As illustrated in figure 4-7, in pulsed reflectometry, very short pulses of $\sim 0.2\text{ns}$ duration can lead to pulse dispersion since the large pulse spectrum reflects from significantly different locations. In broad-band CW reflectometry, the effective bandwidth is not the total frequency sweep bandwidth but the *smoothing* bandwidth chosen in the analysis. Choosing an overly-large smoothing bandwidth could lead to smearing errors in the reconstructed profile in sections featuring sharp changes as seen in figure 4-10a [118, Sec5.b].

Figure 4-10a highlights the importance of optimizing the bandwidth to avoid smearing the profile shape. It also highlights a powerful advantage of CWFM systems: flexible post-shot bandwidth. Within beating frequency digitization limits, broadband CWFM systems can adapt their effective bandwidth to reveal interesting profile structures. Small bandwidths can be used to resolve steep density gradients or sharp structures, while large bandwidths can be used in portions with little structure.



(a) Varying smoothing with fixed sampling (b) Varying sampling with fixed smoothing

Figure 4-10: Profile changes as a function of changing smoothing bandwidths and distance between spatial sampling points. Taken from Doyle et al. [118]

4.4.2 Range precision

Noise is present in any form of measurement system. Some authors refer to this limitation as range accuracy [138][141][59]. Accuracy refers to the closeness of a measured value to its true value, and it may be the combination of both systematic (or trueness) and random (or precision) errors. Given that fundamental spatial limitations in a well-calibrated reflectometer may come about exclusively due to random errors, the term *precision* is used here. In pulsed-wave systems, noise is present on the Gaussian pulse envelope that is fed to timing systems. Fluctuations in this envelope can cause timing errors in the chronometer hardware. Figure 4-11 illustrates this fact. Assuming a Gaussian pulse shape ($V(t) = V_0 e^{-\frac{t^2}{2\sigma^2}}$) is locked at 50% of its amplitude, the range precision can be shown to be [126][app.1]:

$$\Delta t = \frac{\Delta V}{\partial V / \partial t} = \frac{\Delta V}{-\frac{t}{\sigma^2} V_0 e^{-\frac{t^2}{2\sigma^2}}} \quad (4.29)$$

$$\Delta t = \frac{W}{2 \ln(2) \sqrt{\text{SNR}}} \quad (4.30)$$

$$\Delta R_{\text{prec}} = \frac{cW}{4 \ln(2) \sqrt{\text{SNR}}} \quad (4.31)$$

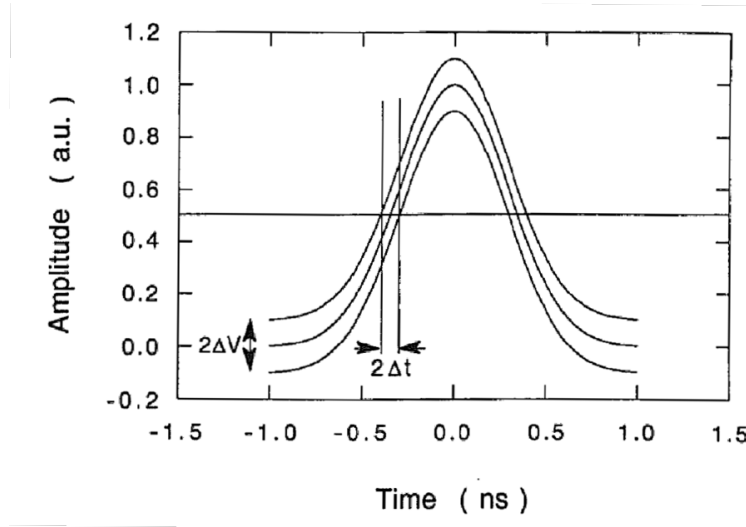


Figure 4-11: Source of pulse radar range precision errors. Taken from Heijnen [126]

where W is the FWHM $W = \sqrt{8 \ln(2)}\sigma$, and SNR is the signal to noise power ratio. Range precision depends on the signal-to-noise ratio, but it also depends on the pulse duration. A narrower pulse will have a sharper rise time, leading to a better range precision. Equation 4.31 also shows that a good SNR can make range precision smaller than range resolution ($\Delta R_{\text{res}} = \frac{cW}{2}$). The Δt seen above is called the timing precision. A SNR of about 200 ($\sim 23\text{dB}$) is required to let the timing precision of 1ns pulses reach 70ps, which allows sub-cm range precisions. This Δt must be matched by the inherent precision of pulse timing hardware shown in figures 4-6 and 4-9 to achieve this sub-cm performance.

In continuous-wave systems, range precision is expressed in terms of the bandwidth ΔB as given by Doyle et al. [118, Sec 5.a]: $\Delta R_{\text{prec}} = \frac{c}{2\Delta B\sqrt{\text{SNR}}}$. In the case of broad-band single frequency fast sweeping systems, ΔB corresponds to the smoothing bandwidth chosen in the analysis (see figure 4-10). The small bandwidth in CWAM systems can, in terms of range precision, be compensated by a large SNR. Both range resolution and range precision are fundamental figures of merit for radar systems. They highlight the fact that two parameters control the performance of a reflectometer regardless of the technique used: bandwidth and SNR.

4.4.3 Spatial Sampling

Spatial sampling refers to the effective number of group-delay values measured which are then used to recover the density profile. Spatial sampling limits the minimum spatial profile structures that can be recovered. The maximum wavenumber which can be measured without aliasing (Nyquist) is [118, Sec.5c] $k_{\max} = \frac{\pi}{\delta x}$ where δx is the spacing between group-delay data points. Ideally, the shortest possible δx is favored.

While short-pulse reflectometers feature broad local bandwidths, all practical realizations have been globally narrow-band: gaps between the carrier frequencies were larger than the pulse bandwidth. Both the START [129] and RTP [126] prototypes featured only 4 channels each with frequency steps of 14GHz and 4GHz, respectively. Traditional SPR systems required dedicated oscillators at both the transmitter and receiver stages for each sampling point; thus, featuring a large number of sampling points increases complexity rapidly as seen in the TEXTOR SPR system [130]. In USPR systems, the spatial resolution is limited by the number of channels in the filter bank receiver in figure 4-9, as it is determined by the frequency steps between them. In the LHD-USPR system [142], featuring 10 channels, the distance between frequencies varies between 1 and 2 GHz. The SSPX system, featuring 24 channels (reduced from the original 48 [137]), the distance between filters goes down to 1.3GHz steps.

In TCV, a 1GHz spacing between sampling points would correspond to 2mm resolution in the plasma edge of L-mode plasma (50-51GHz X-mode probing in shot 60572 at 0.85s, cutoffs seen in figure 2-2) and 0.3mm resolution in the plasma edge of an H-mode plasma (50-51GHz O-mode probing in shot 62734 at 1.2s, cutoffs seen in figure 2-3). Such spatial sampling is already very good. The 2mm L-mode resolution is a factor of 3 better than the finest TS spacing of 6mm and at least a factor of 2 less than the Airy width (figure 2-5). It can be safely concluded that, in TCV, 1GHz steps in spatial sampling are highly competitive and already go beyond fundamental reflectometry sampling limits. 3GHz steps may be sufficient to remain competitive with TS and stay clear of Airy width ambiguity.

Spatial sampling in broad-band frequency swept continuous-wave techniques is flexible and depends upon the choice of the smoothing bandwidths during analysis. The

smoothing bandwidth and spatial sampling are interrelated [118]. In broadband CWFM systems, algorithms are in place to iterate between smoothing bandwidths until the maximum spatial information is recovered. While smoothing bandwidths under 1GHz would hardly be justified in TCV, it must be recognized that the freedom of choosing post-experiment is an undeniable strength of CWFM systems as highlighted by figure 4-10 on page 97. Narrow-band CWFM systems suffer from the same problem as pulsed-wave systems where each new group-delay point involves a new transmitter oscillator and receiver channel. Large gaps should be avoided and lack of spatial sampling freedom is certainly a weakness compared with broad-band swept CWFM systems. Not having enough spatial resolution could have drastic effects on the shape of the profile as shown in figure 4-10b.

Multiple frequency systems can measure group-delays with arbitrarily fine spatial sampling depending on phase digitization limits and the particular frequency sweep curve chosen. The frequency sweep sometimes includes flat portions to measure phase fluctuations for a few ms [125]. In other implementations, the sweep is constant and can take less than 1ms [124]. Thus, multiple-frequency techniques can be made to feature arbitrarily small spatial sampling depending on design choices and hardware constraints. If the SNR is good throughout the sweep, this method does not require smoothing over portions of the group-delay curve as in CWFM systems. This method can, however, make use of a similar optimization algorithm as CWFM systems if phase measurements allow sufficiently fine group-delay data to be recorded in each sweep.

4.4.4 Temporal Sampling

The main motivation behind building a reflectometer in TCV is the interest in increasing the temporal resolution of the TS diagnostic currently at 60Hz per profile. All reflectometry techniques investigated above can recover density profiles. Using the Nyquist argument, the maximum frequency that a system can sample without aliasing is given by $f_{\max} \leq \frac{f_{\text{sampling}}}{2}$. The time resolution of density profile measurements is limited by the fact the group-delay must be acquired for a large range of frequencies before the Abel inversion can return useful profiles. The USPR technique is fundamentally the fastest technique. In USPR, the chirped pulse launches a large frequency spectrum in a single

pulse. The receiver bank then measures group-delays from all frequencies simultaneously after receiving the broadband reflection from the plasma. The time resolution of this technique is then only dependent on the maximum ultra-short pulse repetition rate of the pulse generators and potentially on how fast timing circuits accept new pulses. In SPR, the pulse carrier frequency must be changed to measure successively the group delay curve over frequency. Thus, it is fundamentally slower than USPR, yet the ultimate temporal sampling depends on the pulse repetition rate.

In pulsed-wave reflectometry, the concept of unambiguous range can present a practical limitation to pulse repetition rates [141, ch.1]. In radar applications, once a pulse is transmitted, there must be a time delay before sending the next pulse while the system listens for a return echo. If the echo of the first pulse takes longer than the time between pulses, this echo could be interpreted as a reflection due to the second pulse. Thus, the pulse repetition rate is limited by the time it takes a pulse to do the round-trip to and from the cutoff. In TCV, the distance between the reflectometry hardware and the plasma is in the order of 9 meters depending on plasma conditions (see appendix A). This limits the unambiguous pulse repetition rate to about 16MHz. This is a serious limitation in practical radar implementations where various moving targets need to be tracked. However, in fusion plasma experiments, all transmission-line reflections are static and can be seen during calibration. Pulse interleaving is possible within the limitations of the timing hardware. Assuming a safe distance of 10ns between pulses, interleaving should allow for pulse repetition rates of up to 100MHz. This fundamental limit does not apply to CW systems.

All CW reflectometry techniques need to gather group-delay information by sequentially sampling different cutoff layers through a frequency sweep. The temporal resolution is then limited by how fast this sweep can occur. It became clear in the early days of CWFM that frequency sweeps had to be faster than a few ms in order to avoid the deleterious effects of large MHD modes on the measured phase [59]. Increasing the speed of the sweep brought about improvements in the stability of the beating frequency measurements at the expense of higher digitizer speed demands. The question of how fast

is fast enough for CWFM systems will be addressed below when discussing the effects of micro-turbulence. Multiple-frequency systems do not need to sweep very fast since their frequency separation averages the effects of fluctuations. Arguably, their frequency sweeps cannot be faster than the correlation time of turbulence, otherwise the phase difference cannot be a meaningful average.

This section can be concluded by presenting the best temporal sampling periods on record for each technique. Short-pulse radar systems have been able to recover profiles in up to $2\mu\text{s}$ [130] intervals. Ultra-short pulse, limited by pulse-generator repetition rates, achieved up to $10\mu\text{s}$ per profile [142]. Broad-band CWFM systems are currently limited by the sweeping rates of state-of-the-art VCOs at $1\mu\text{s}$ per profile with $0.25\mu\text{s}$ dead-time between sweeps [121]. Multiple-frequency systems feature slow sweeps with a record 1ms per profile [124].

4.4.5 Turbulence effects

The density profile of thermonuclear plasmas is far from smooth. Section 2.4.1 on page 37 addressed the types of micro-instabilities present in a tokamak plasma. There are both radial and poloidal fluctuations which span a large range of temporal and spatial scales. Laviron [59] succinctly compares a cutoff in a tokamak plasma with a lumpy surface made of small sub-reflectors. Conway [81] shows that modeling the reflection surface as a rippled conducting surface can lead to strong reflected power modulations depending on the fluctuation scale lengths. This power fluctuation effects affect all reflectometry techniques, attenuating the reflected beam by as much as -45dB . Section 2.4 on page 37 outlined how reflectometers have been used in specular and back-scattering configurations to obtain various degrees of information about density fluctuations. This section, however, presents how each density profile reflectometer implementation responds to the highly turbulent conditions found specially in the edge of fusion plasmas.

In order to access the average profile, turbulence effects can be partly eliminated using two main approaches [118]. First, performing measurements fast enough so that the spurious effects of turbulence are partially or totally eliminated. This is the approach in pulsed reflectometry and fast broadband CWFM. The second approach is to use two

or more frequencies that are separated by a turbulence correlation length, allowing direct extraction of the group delay by averaging-out the effect of turbulence. This is the approach used by CWAM and double-frequency systems.

In pulsed-wave techniques, either short or ultra-short, pulse propagation through the plasma to and from a cutoff takes only a few nanoseconds. During this time, the plasma can be truly considered to be *frozen*. Turbulent time-scales are found in the 10s of micro-seconds, safely away from the pulse-propagation time-scale. The USPR technique is particularly attractive since it measures the entire group-delay curve in a single pulse. Practical limitations in pulse generators and receiver timing hardware may limit the pulse repetition rate to hundreds of kHz, yet each USPR pulse gives a perfectly static snapshot of the density profile. In the case of SPR systems, each pulse group-delay measurement benefits from sampling a truly frozen plasma. If the pulse repetition rate is fast enough, statistics on the density fluctuations can potentially be extracted from the group-delay data. Unfortunately, SPR systems need to send and receive several pulses sequentially before reconstructing an entire profile with a good number of group-delays. The plasma could potentially have evolved within this time frame. Regardless, even if the plasma does evolve during the frequency scan, temporal averaging over each frequency can be used to access density profiles in the ms scales.

Pulsed-wave systems also feature the unique advantage of inherently performing time domain discrimination if focusing exclusively on the cut-off reflection. As presented by Bretz[74] and in section 2.4 on page 37, the mm-wave beam can encounter Bragg resonances on its way to the cut-off. While the amplitude is expected to be much smaller than the cut-off reflection, in the case of CWFM systems these situations can lead to errors in determining the beating frequency that cannot be removed via calibration before the experiment. Multiple-frequency systems would also measure an ambiguous mixture of Bragg resonances and cut-off phase contributions that can adversely affect the group-delay determination. Pulsed-wave systems, on the other hand, benefit from being able to focus exclusively on reflections in close-proximity to the cutoff. If the Bragg reflection occurs at a sufficient distance from the cutoff - which in the inhomogeneous plasma could well be less than the range resolution - both reflections can be separated. Other-

wise, the pulse shape can be distorted and ignored by smart timing hardware. Cohen et al. [143] show that measuring the time difference between Bragg and cut-off reflections could provide information on the radial wavelength of the fluctuations producing the scattering if the density profile gradient is known.

SPR systems do suffer from an inherent weakness when used in turbulent plasmas: their cm range resolution using 1GHz local bandwidths responds in uncertain ways to the presence of turbulence at the cutoff. Both the level of fluctuations and the slope of the density profile can affect the group delay. Section 4.3.1 on page 91 showed that, given a smooth density profile, 1ns pulses do not exhibit dispersion in the edge. Yet, this study did not - and arguably cannot within the WKB approximation - include realistic 2D density fluctuations. Shevchenko studied the effects of turbulence in short-pulse reflectometry through 1D theoretical models (full-wave with $\delta n/n < 1\%$) [144] and experiments (T-11M [127] and START [145] tokamaks). His theoretical studies concluded that there is an asymmetric overall slowing-down effect caused by either positive or negative perturbations in different degrees. The dependence of the error on the fluctuation levels was found to be linear. Unfortunately, Shevchenko's model [144] assumed tokamak turbulence consisted only of radially propagating density perturbations. As addressed in section 2.4.1 on page 37, modern tokamak density fluctuation theories and experimental findings highlight a wide range of poloidal and radial dimensions but do not indicate the presence of propagating radial fluctuations with the exception of SOL filaments, zonal flows, and avalanches.

Experimentally, it has been found by both Shevchenko[145] and Heijnen[126][pg.72] that the group-delay scatter (or jitter) increases significantly (by factors between 4 and 10) when reflections come from a plasma relative to when they come from a flat mirror. No information was given as to whether this increased scatter was due to SNR changes, the response of their timing hardware to changing reflection powers or pulse widths, and/or the radial fluctuations of the cut-off position. Heijnen reported that the distribution of the scatter was Gaussian, which disagrees with the modeling results of Shevchenko [144] predicting a skewed distribution due to the asymmetric slow-down effect of radially propagating density perturbations. Experimentally, it was also discovered that focusing the

beam pattern at the cutoff led to a factor of 2 decrease in the scatter [145]. Therefore, while the plasma seems to increase the scatter of group-delay values, the large time resolution achieved by SPR systems (5-10MHz) can be compromised to obtain average profiles in the ms scale. Cohen et al. [143] demonstrated as a proof-of-principle that pulsed wave techniques have the potential of recovering O and X-mode density profiles with good precision with up to 40% $\delta n/n$ fluctuation levels.

Continuous wave techniques are also affected by turbulence. Broadband CWFM is fundamentally the most sensitive technique since many plasma processes can affect the phase difference between launched and reference wave. Firstly, radially propagating filaments can induce Doppler shifts that can be misinterpreted as large changes in the profile. Secondly, as presented above, if any Bragg resonances are encountered towards the cut-off, the measured phase can be affected in unpredictable ways that cannot be compensated by calibration. Also, if there are slight antenna misalignments, poloidal density fluctuations rotating with the bulk plasma can induce Doppler shifts. This misalignments are the reason behind the highly documented *phase run-away* problem [80]. Early CWFM reflectometers, which used BWOs, swept the frequency relatively slowly and took 1-5ms to recover a profile. These systems had serious problems with reliability during turbulent discharges (L-mode) [59, Sec4.4] [146], due to the effects of macroscopic MHD modes and microturbulence. Modern CWFM systems use much faster sweeping rates at 1 μ s per sweep [121]. However, the question of how fast is fast enough does not have a clear answer in literature. CWFM proponents have argued that frequency sweeps of 100 μ s [118], 20 μ s [66], and 1 μ s today [121] are all fast enough that the plasma is effectively 'frozen' during the sweep.

Based on the Nyquist estimates, 1 μ s sweeps could only consider the plasma to be *frozen* only if fluctuation time-scales were limited to bandwidths under 500kHz. This is safely away from MHD and Alfvén-eigenmode frequencies under 200kHz. Yet, estimates of TEM drift-wave turbulence in TCV (section 2.4.1 on page 37) point at temporal scales up to 400kHz. Hence, the bandwidth may just be enough. In TCV, the TPCI diagnostic has measured significant radial fluctuations up to \sim 200kHz [147][pg.52] in L-mode plasmas. Micro-instability drives can change depending on plasma conditions and heating

mechanism. However, these fluctuations are also broadband and the amount of energy in the fast scales may be too small to truly make a difference in the profiles. Gyrokinetic simulations coupled with 2D synthetic diagnostics have the potential to properly address these limits in a wide range of plasma conditions. One could safely define an upper limit to ion-driven fluctuation time scales (ITG) at the ion cyclotron frequency. In TCV, Ω_{ci} sits at about 20MHz. However, it must be noted that sweeping the frequency faster did make the CWFM technique much more reliable. The fast sampling available also allows plenty of room for temporal averaging. Varela [119] presents a good summary of all the different approaches taken to filter and smooth the fast-changing beating signals recorded in the ASDEX-U tokamak CWFM reflectometer.

CWAM/double-frequency systems are fundamentally the best suited for average range measurements in a turbulent plasma. If the frequency spacing can be made to correspond to a turbulence correlation length, turbulence affects both frequencies equally. When taking the phase difference between both frequencies, any changes induced by turbulence are canceled out. However, in flexible machines like TCV, turbulence spatio-temporal scales can vary widely with plasma shape and heating mechanism. Also, given that turbulence drives are not constant over the plasma radius, these scales are expected to change radially. Nonetheless, reliability above 80% has been reported[124].

4.5 Summary

The above discussion may be succinctly summarized by tables 4.1 and 4.2. While this table does not compare all techniques on an equal footing, given that certain techniques have had over 35 years of development while others were implemented in a single machine before the 1990s, it attempts to highlight their strengths and weaknesses in a single place.

The broadband CWFM with flexible range resolution, precision, and spatial sampling and with μ s temporal resolution is certainly the most advanced and powerful reflectometry technique studied. While highly sensitive to plasma events affecting the phase, the speed of the broadband frequency sweeps approaches the Nyquist frequency of density

<i>Criteria</i>	Broad. CWFM	Nar. CWFM	AM/Double Freq
Range Resolution	Var BW	0.2GHz = 75cm [123]	0.2GHz = 75cm [124]
Spurious Reflections	Calibrate out	Calibrate out	Requires bi-static antenna
Range Precision	Var BW	f(SNR)	f(SNR)
Spatial Sampling	Variable post-shot smoothing	Fixed Ch.# 3-10GHz gap	Flexible
Temporal Sampling	1.25 μ s [121]	0.5ms	1-10ms [124] [125]
Effects of turbulence	Highly sensitive μ s sweep helps	Highly sensitive but localized sweep	Averages out

Table 4.1: Comparing CW reflectometry techniques

fluctuations. As discussed in section 4.4.1 and 4.10, range resolution is indirectly proportional to the bandwidth. Thus, the CWFM technique can increase its range resolution with a larger smoothing bandwidth at the expense of smearing over portions of the profile. Yet, the flexibility to choose this smoothing bandwidth in post-shot analysis -depending on the shot density gradient lengths - is an undeniable strength that depends on careful iterative analysis to ensure its validity.

Double-frequency/CWAM systems feature flexible spatial sampling and have the unique strength of strong resilience against turbulence. Their temporal sampling limits are design choices which can be easily increased with current hardware. Unfortunately, their poor range resolution limits these systems to using bi-static antennas, which may not be available in future devices with limited access.

Pulsed-wave techniques have been much less explored. This is probably because of the high SNR required to measure pulse group-delays with sufficient precision and the difficulty procuring such precise chronometer hardware. Furthermore, the open question of the effects of 2D density fluctuations on pulse group-delay and dispersion implies a level of risk in the implementation of such diagnostics as robust density profile systems. However, their unique ability to sample truly frozen plasmas and filter spurious reflections away from the cut-off is unmatched. Their temporal resolution can potentially match and exceed their CWFM counterparts.

<i>Criteria</i>	Trad SPR	USPR
Range Resolution	1ns pulse = 15cm	60ps = 0.9cm
Spurious Reflections	Time-domain filtering	Time-domain filtering
Range Precision	70ps = 1cm	80ps = 2.4cm
Spatial Sampling	Fixed Ch# 4GHz gap [126]	Fixed Ch# 1-2GHz gap [137]
Temporal Sampling	0.5μs per profile 0.05μs PRR[130]	10ns per profile 10μs PRR[128]
Effects of Turbulence	Group-delay skewed pulse dispersion possible	Resilient up to dn/n 40% [143]

Table 4.2: Comparing pulsed-wave reflectometry techniques. PRR refers to pulse repetition rate

As discussed above, the best pulsed wave technique in terms of temporal sampling is USPR. Unfortunately, at the beginning of this thesis, the company that manufactured ultra-short pulse sources, Picosecond Pulse Labs, had been acquired by Agilent, which no longer makes pulse generators under 100ps. Thus, the focus shifted to SPR techniques. Modern arbitrary waveform generators (AWG) with analog bandwidths in the 10s of GHz were identified as potentially game-changing. An AWG-generated pulse can be either up-converted or frequency multiplied into the V-band. The AWG allows freedom of output pulse frequency, duration, repetition rate, and envelope function. A multi-channel AWG can also be used to generate a LO signal to down-convert the V-band reflected pulses into a fixed IF frequency as done in traditional SPR implementations (see figure 4-6). Thus, an AWG-driven SPR reflectometer can overcome the spatial sampling, fixed range resolution, and temporal sampling limitations of previous implementations. Furthermore, modern sensitive microwave hardware and timing electronics have the potential to improve signal to noise ratio and hence range precision. The next chapter presents the implementation and first results of such an innovative SPR implementation.

Chapter 5

AWG-driven short pulse reflectometry

In the Tokamak à Configuration Variable (TCV) ($a=0.25\text{m}$, $R=0.89\text{m}$, $B_T=1.4\text{T}$), electron density measurements from the plasma core to the last closed flux surface (LCFS) are routinely available from the Thomson Scattering (TS) diagnostic with a spatial resolution between 6-17mm but only 60Hz temporal sampling. Microwave reflectometry has been identified as a strong candidate for complementary measurements at the edge of confined plasmas given its high spatial (sub cm) and temporal (μs) resolutions. Increasing the temporal resolution of edge density measurements could be decisive in revealing the dynamics of confinement regime transitions and fast pedestal events such as edge-localized modes (ELMs). In microwave reflectometry, the plasma electron density can be inferred from measurements of the round-trip group-delay of EM waves reflected from a plasma cut-off over a number of frequencies. Short pulse reflectometry (SPR) consists of sending broadband microwave pulses ($\sim 1\text{ns}$) with a defined carrier frequency and measuring their round-trip group-delay using precise chronometers.

SPR is a uniquely attractive approach to reflectometry. Firstly, assuming negligible absorption and weak dispersion, the group-delay of a pulse with a defined carrier frequency can be measured directly. This is in contrast with continuous-wave frequency modulation (CW-FM) techniques where the linearity of frequency sweeps is vital to measure accurate group-delays [121]. Secondly, pulse propagation through the plasma occurs in the ns-scale, at least 2 orders of magnitude under turbulence time scales expected in the sub- μs scale: the plasma can be considered to be *frozen* during pulse propagation. Lastly,

given the time-domain nature of SPR measurements, spurious reflections in waveguides, vacuum windows, and in-plasma coherent back-scattering are naturally separated from the plasma cut-off reflection allowing easy filtering.

SPR does also feature unique technical challenges. SPR prototypes were successfully demonstrated by Shevchenko et al. [127], Heijnen et al. [126], and Tokuzawa et al. [148] in the nineties but none are operational today. SPR was traditionally implemented by combining a discrete number of fixed frequency oscillators, sending sequential ns-scale pulses of increasing frequency, and measuring the round-trip group delays using analog pulse-detection systems. The fixed oscillator frequencies entailed unavoidable frequency gaps of 4-14GHz, which represented an important spatial sampling limitation over CW-FM systems [118]. Every data point in the reconstructed profile required at least one separate oscillator, thus, increasing the number of points in the reconstructed profile meant a linear increase in hardware complexity. Furthermore, pulses were created by fast semiconductor (PIN) switches which featured insertion losses at the 7dB level and relatively short lifetimes. Lastly, sub-cm group-delay precisions require the procurement of accurate pulse timing hardware which are complex on themselves but also require high input pulse SNRs above 25dB as seen in section 4.4.

The frequency signature of the SPR signal presents unique challenges and opportunities. Pulse envelope dispersion and distortion have been alluded to by many authors [118, 149] and studied theoretically [143, 150], but, prior to this thesis, have not been directly measured. Heijnen [126, p. 29] showed that, within the WKB approximation, pulses of durations above 0.5ns should not feature pulse dispersion when sampling smooth quadratic density profiles. This result was later confirmed by full-wave 1D simulations in a wider range of profile shapes by Hacquin et al. [150]. Pulse dispersion/distortion has the potential of reducing the accuracy of group-delay measurements, as further addressed in section 5.3.1. However, if the pulse output width can be varied and the reflected pulse width measured, pulse dispersion can provide information on the slope of the group-delay curve. This measurements can be used to initialize the profile without the need of other diagnostics [150]. Furthermore, direct sampling of distorted pulses can provide direct evidence of particular density fluctuations: away and close to

the cutoff layer in the form of Bragg resonances or wave-trapping, respectively [143, 151].

Nearly 15 years after the last SPR publication [148], advances in digital electronics and mm-wave hardware have allowed limitations regarding spatial sampling and range resolution to be surmounted while increasing range precision by a factor of 4. This chapter presents how a fast (65GSa/s, 25GHz analog bandwidth), multi-channel, arbitrary waveform generator (AWG) and a $\times 6$ varactor multiplier can bring about flexibility in pulse carrier frequency, width, and repetition frequency. 25-point density profiles can be thus reconstructed with sub-cm spatial resolution and μ s temporal sampling comparable with established continuous-wave reflectometry techniques [121]. Equally importantly, little work has been published [144] connecting short-pulse group-delay fluctuations with density fluctuations and establishing the potential of the technique as a fluctuation diagnostic.

This chapter begins by presenting the hardware implementation in section 5.1. It proceeds by presenting and comparing two approaches to measure pulse group-delays in section 5.2. First data and preliminary results are presented in section 5.3.

5.1 Hardware implementation

Figure 5-1 shows both transmitter and receiver stages of TCV's SPR. The transmitter section produces pulses of 650-750ps full-width-at-half-max (FWHM) of arbitrary frequency inside the V-band (50-75GHz) by using 1-2s, 8.33-12.5GHz carrier, pulses from the Keysight M8195A AWG fed into a $\times 6$ varactor multiplier [152]. This frequency multiplier is found inside a transmitter/receiver (TX/RX) commercial off-the-shelf vector network analyzer (VNA) extension module built by Virginia Diodes Inc (VDI). Only the transmitter portion of the module is used and sketched in figure 5-1. The varactor multiplier has a non-linear response to input pulses leading to varying degrees of pulse compression and amplitude saturation. Nonetheless, thanks to the unique flexibility of fast AWGs, Gaussian output envelopes can be created by carefully controlling input pulse amplitude, duration, and phase. Figure 5-2 shows the envelopes of pulses of 650-750ps FWHM over the V-band measured with a fast zero-bias Schottky diode detector (>6 GHz

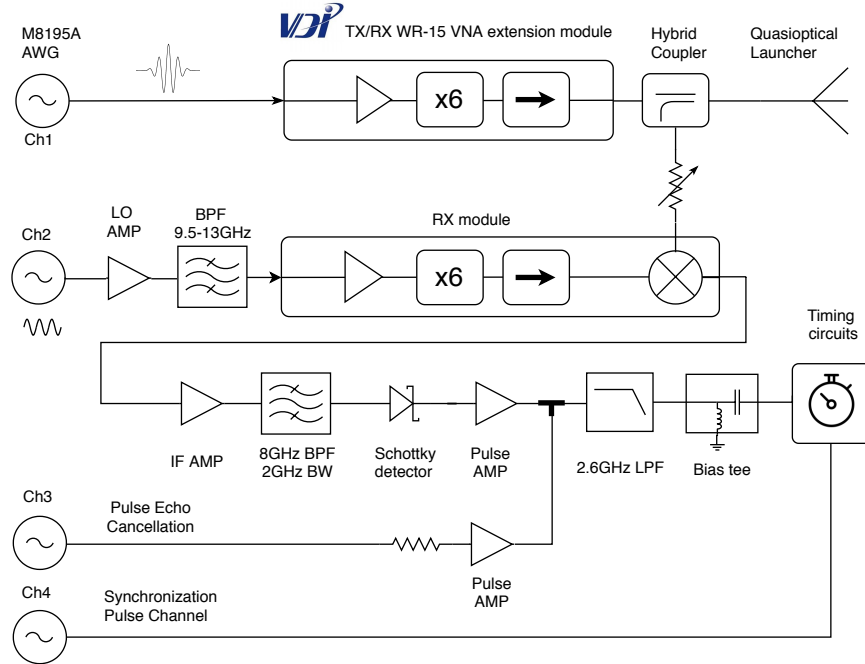


Figure 5-1: AWG-driven SPR schematic diagram

bandwidth WR15, OR4 1-16 from VDI) directly at the output of the varactor multiplier. The internal memory of the AWG allows launching up to 273 unique pulses at 16MHz repetition rate, which once played are looped inside a discharge. Sequencing capabilities, making use of the external memory, may allow over 10^6 unique pulses.

All integer frequencies in the V-band have been tested to provide output powers between -5 and -8dBm based on the sensitivity curves of the WR-15 diode. Figure 5-2 normalizes all pulse peak amplitudes and stacks them vertically for clarity purposes. The Tx pulses are transmitted to the plasma via TCV's diagnostic launcher. It consists of a quasi-optical telescope, 6.5m of low-loss 65.3mm HE₁₁ waveguide, a pair of fast miter-bend polarizers in HE₁₁ waveguide, and a quasi-optical launcher antenna [153]. The telescope assembly was recently upgraded by replacing the smooth-walled U-band horn by a V-band corrugated Gaussian horn designed and built by Thomas Keating Ltd. Transmission-line insertion losses (IL) amount to ~7.5dB. These were directly measured using a time-domain-gated (TDG) vector-network analyzer (VNA). This figure does not include losses in the launcher antenna, which, based on Gaussian beam truncation due to mirror size, should theoretically remain under 0.3dB at 50GHz. Round-trip beam

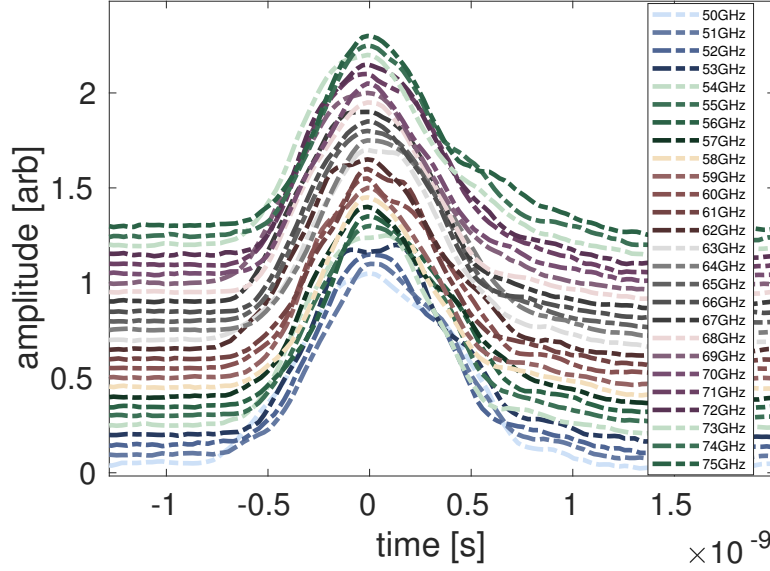


Figure 5-2: WR-15 zero-bias Schottky diode data demonstrating that Gaussian pulses of 650 – 750ns FWHM may be created by an AWG driving x6 VDI varactor multipliers. Pulse peak amplitudes, which vary between -5 and -8dBm are normalized and stacked vertically for clarity purposes.

expansion and non-normal incidence at the cut-off layer may give rise to larger losses, independent of plasma reflection coefficients. The entire waveguide system is about 8.6m long. Thus, in order to avoid pulse ambiguity, pulses must be spaced by about 57ns which fixes the maximum unambiguous pulse repetition rate at 17.5MHz. Pulse interleaving could potentially be used given that the cut-off location ranges can be easily predicted. Assuming a safe distance of 10ns between pulses, interleaving could allow for pulse repetition rates of up to 100MHz. Pulse interleaving is not demonstrated in this dissertation.

The receiver stage uses heterodyne detection for added sensitivity. Reflected pulses are coupled to a WR-15 VDI RX (receiver) module via a broadband directional hybrid coupler. A sensitive (0.1dB flatness) variable waveguide attenuator (STA-60dB-WR-15-D1 from Sage Millimeter) is used to limit the incoming power to avoid receiver saturation. The signal is then mixed with a local oscillator (LO). This LO is produced by multiplying a continuous 8.33-12.5GHz signal provided by a second AWG channel synchronized with the pulse channel. Given that this signal may contain analog distortions of up to

-30dBc, it is first amplified (18dB gain, 2.2dB NF, FMAM1027) and then band-pass filtered (9.5-13GHz BPG7817A) to ensure a pure and strong LO is provided to the mixer. The resulting intermediate-frequency (IF) output was chosen at 8GHz, the largest frequency that permits receiving 0.5ns pulses inside the 10GHz mixer bandwidth limit. The IF pulse output is firstly amplified by a broadband (8-12GHz), low noise (2.2dB NF), high gain (38dB) amplifier (SLNA-120-38-22-SMA). The signal is then band-pass filtered at 8GHz (2GHz bandwidth BPF5620A) to remove the LO-bleed through and spurious mixer frequencies. This IF band-pass filter has a boxcar shape with -3dB and -30dB points at 6.91/9.14 and 6.75/9.31GHz, respectively. Since the outgoing pulse widths are 750 ± 50 ps, the reflected pulse FWHM bandwidth is expected at 1.4 ± 0.1 GHz, comfortably inside the passband. The filter allows detecting pulses of widths above 500ps with various amounts of ringing due to its aggressive (50MHz/decade) boxcar shape.

The filtered pulse is then fed into a fast Schottky detector (302A from Krytar), which extracts the pulse envelope. Lastly, the pulse envelope is amplified by a low-noise (2.5dB NF) pulse amplifier (9kHz-3GHz SLNA-030-32-30-SMA). The amplified pulse is then low-pass-filtered (DC to 2.6GHz LPF8132A) to reduce noise as much as possible. A bias tee (Inmet 64671 8810SMF2-26) is used to reduce small DC offset voltages from the pulse amplifier to zero. The filtered pulse envelope is then sent to the timing circuits further described below. Figure 5-1 also shows AWG channels 3 and 4 producing pulse echo cancellation and synchronization signals. Their role is explained in section 5.2.2 below. A SMA T is used to couple the pulse echo cancellation with the reflected signal. All amplifiers and filters were procured from Fairview and UIY Microwave, respectively.

5.2 Timing circuits

5.2.1 Requirements

Assuming the outer 20% of the confined TCV plasma (~ 5 cm) to feature a parabolic density profile, reconstructing a 20 point density profile requires a 2.5mm range resolution. Such a resolution in vacuum corresponds to requiring the timing circuits to discern pulse

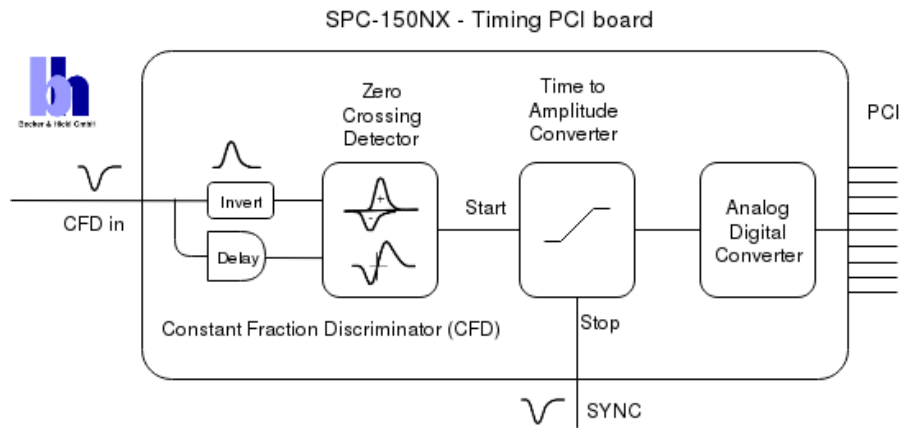


Figure 5-3: SPC-150NX schematic diagram[154]

round-trip group-delays with a 17ps maximum error. In order to obtain a 20-point profile measurement with a competitive [121] $1.25\mu\text{s}$ temporal resolution, a pulse repetition rate (PRR) of at least 16MHz is required. At these pulse repetition rates, the timing circuits should be capable of recording $32 \cdot 10^6$ group-delays to cover the full 2 seconds of the standard TCV discharge. As seen above in section 5.1, unambiguous pulse repetition rates with TCV's diagnostic launcher system comfortably allow for a 16MHz PRR. Pulse interleaving has the potential of enhancing the temporal resolution of a 20 point profile down to $0.2\mu\text{s}$.

5.2.2 Traditional analog approach

Traditionally, short and ultra-short pulse reflectometers have used a combination of a constant fraction discriminator (CFD), a time-to-amplitude converter (TAC), and an analog to digital converter (ADC) to measure group-delays. All these elements have been identified in the commercial SPC-150NX timing module from Becker and Hickl GmbH shown in figure 5-3[154]. These modules are primarily used in biochemistry photon counting applications to record fluorescence decay curves of organic dyes in solution.

Since the reflected power from the plasma can vary as a function of frequency and shot conditions, the CFD's function is to trigger the reception of a pulse irrespective of its incoming amplitude. This is achieved by splitting the incoming power into two channels: one that inverts and one that delays the pulse. These two are then recombined

resulting in a bipolar signal that gives an accurate pulse arrival event when it crosses a small variable voltage threshold called the *zero-crossing* level. After receiving a pulse, the CFD outputs a TTL signal that is fed into the *start* input of a TAC which also receives a *stop* (SYNC in figure 5-3) pulse directly from the AWG (Ch 4 in figure 5-1). The output voltage of the TAC is proportional to the time difference between the start and stop signals. This voltage is digitized by a 14bit ADC, which can distribute this time difference into channels of width down to 450fs. At this low channel width the temporal range of measurements is 1.5ns, which accommodates group-delays from targets up to 22cm apart in vacuum (well within the 5cm requirement). Altogether, the module is capable of recording time differences with an electrical time resolution of 1.6ps root-mean-square (RMS). In addition, the module may be operated at a count rate of up to 10MHz. It may acquire up to 2×10^6 events, which at 10MHz corresponds precisely to the 2-second standard TCV discharge duration. Unfortunately, given that the AWG-generated LO must be defined in multiples of 128 samples, the maximum pulse repetition rate achieved under 10MHz has been 8.33MHz, a factor of 2 under the 16MHz requirement.

Figure 5-1 shows an AWG channel acting as an echo cancellation channel. This signal is required to actively cancel reflections along the signal path to avoid premature triggering of the CFD. These spurious reflections come from the limited directivity of the hybrid coupler, reflection coefficients of waveguide filters [153], and, most importantly, from the vacuum window at the entrance of the launcher antenna. Reflections from the coupler and filters remain under -16dB, but the vacuum window reflections may be as large as -5dB as seen in appendix A. Since all these reflections are constant, the SPC-150Nx could have been programmed to simply ignore these. Unfortunately, modifying the internal electronics of a commercial product proved to be prohibitively expensive. Instead, all reflections along the line were firstly sampled for each discrete frequency using a fast oscilloscope (see section 5.2.3 below). The recorded traces were inverted, played back by the AWG, amplified, and time-shifted so they coincide with the reflections. Echo pulses of up to 1.2V are thus reduced to less than 100mV (well under the 200mV CFD walk limit). Imperfections in the cancellation technique do not affect

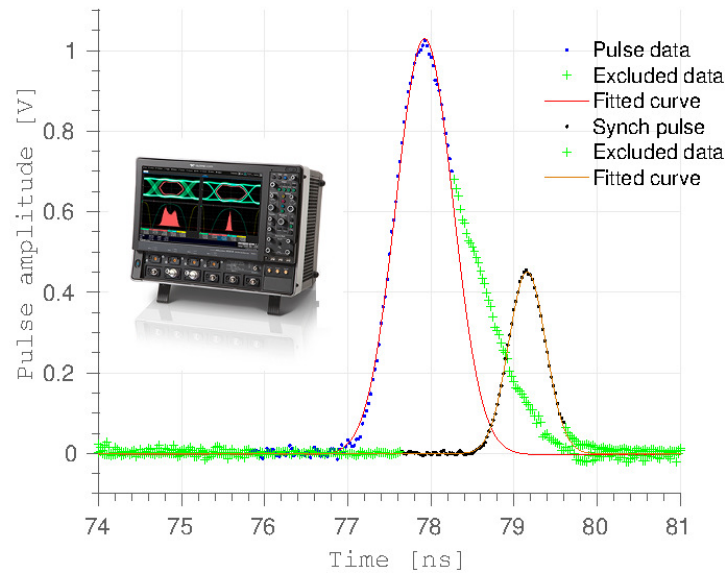


Figure 5-4: Sample least-squares fit of reflected and synchronization pulses. $R^2=0.998$.

the group-delay measurements since the signal travels at least 2m to and from the cutoff away from the vacuum window: over 10ns separate the two signals in time.

5.2.3 Direct sampling approach

A newly tested approach to quantifying group-delays is to directly sample the pulse envelope with a fast analog to digital converter (ADC). A fast (45GSa/s), 8-bit, 13GHz analog bandwidth oscilloscope (LeCroy 813Zi-B) is used for this purpose. A sample reflected pulse from the HE11 mirror is shown in figure 5-4. A Gaussian function is fit via least-squares. Unfortunately, the leftover Gaussian pulse power outside the IF filter pass-band produces ringing in the form of small-amplitude pulses which interfere and distort the right-hand side of the reflected pulse. Thus, the Gaussian fit ignores 70% of the right portion of the pulse. The synchronization pulse coming straight from the AWG is also shown; it is fit ignoring only the outer 20% of the right portion of the pulse. These rejection percentages were empirically chosen to maximize the number of points taken into account in the Gaussian fit, ignoring any departures from this functional form. IF filter ringing does not affect the performance of the analog SPC-150Nx circuits since only the pulse rising time is used by the CFD to trigger the TAC.

This approach has the immense advantage of storing the reflected pulses; future post-processing routines can re-interpret the data. Another advantage of this technique is that the fits return not only the time difference between input and SYNC pulses but also pulse envelope amplitude and width. Furthermore, this timing approach does not require active pulse cancellation. Characterizing the exact pulse amplitude and shape of these reflections in principle allows the unequivocal identification of the output pulse frequency. Lastly, the pulse repetition rate can reach 16.66MHz without pulse ambiguity.

However, this technique does feature a few drawbacks. Loading large ADC traces and fitting individual pulses to access group-delays requires more computing post-shot computing power. Yet, modern computers allow hundreds of fits within a few minutes. Perhaps the biggest disadvantage is the large memory requirement. At 45GSa/s, the limited oscilloscope memory of 32 mega samples allows a pulse train of only 0.7ms to be acquired. Multiple triggering may allow sampling of up to $8 \times 250\mu\text{s}$ instants during a shot. Nonetheless, such small sampling time remains impractical for routine density profile measurements. SPC has recently purchased a fast sampling system from Guzik (ADP7104 10-bit 32GSa/s) with a memory of up to 64GBytes. This sampling system, featuring a 10GHz analog bandwidth, will allow direct sampling of reflected pulses for over 1.5 seconds in the near future.

5.2.4 Comparing the two pulse-timing techniques

As outlined in section 5.2.1, the ultimate group-delay uncertainty is composed of three contributions: intrinsic hardware precision, random noise, and changing input pulse amplitude errors.

In the SPC-150Nx case, the first contribution comes from the intrinsic minimal electrical time resolution of the timing hardware at 1.6ps. In the direct sampling case, the intrinsic hardware errors come from the ADC clock jitter and/or from the limited sampling frequency. The sampling clock RMS jitter of the LeCroy 813Zi-B is 0.15ps for one channel and up to 0.33ps between channels. Another source of intrinsic hardware error may be the finite sampling period of the scope at a minimum of 22ps, although a good fit to the Gaussian envelope may achieve group-delay resolutions better than this sam-

pling interval [155]. To test this assertion, 166 pairs of 700ps FWHM Gaussian pulses were produced by the AWG and fed directly into two separate scope channels. The time difference between them was normally distributed with a SD of 1.15ps. Thus, both techniques feature intrinsic hardware errors under 1.6ps.

The second source of uncertainty comes from unavoidable thermal noise in the mixer and amplifiers, which translates into fluctuations in the pulse envelope fed to the timing circuits and into group-delay errors at constant input power. This contribution can be estimated by looking at the standard deviation (SD) of group-delay measurements against a static target. Irregularities in the output power of the AWG, the varactor multiplier, and the receiver mixer as well as non-flat transmission curves of filters and polarizers cause the effect of thermal noise to change with frequency. An HE₁₁-waveguide mirror at the entrance of the launcher antenna has been used to measure these changes. Reflections from this mirror take into account the response of all components except for the vacuum window and the launcher which are inaccessible when TCV is under vacuum. Simulating a plasma reflection coefficient (S_{11}) of -15dB using the variable attenuator in figure 5-1 with respect to a perfect mirror yields a mean SD of 8ps with the SPC-150NX module and 7ps with the direct sampling technique. The HE-11 waveguide mirror used in combination with the variable attenuator is henceforth called a lossy mirror target since it allows to study the response of the system to changing reflected powers (changing plasma S_{11}). Figure 5-5 shows how these SDs change over the V-band for a -15dB attenuation, corresponding to the lowest allowed amplitude of 200mVpk (see table 5.1). Group-delay data against this static mirror shows excellent agreement with the normal distribution.

The third source of uncertainty comes from changing input pulse power. In the SPC-150NX case, CFDs are meant to lock equally to pulses of varying amplitude, but they feature a non-zero variation in the locking time as a function of input pulse amplitude known as *time-slewing* or *CFD walk*. In the direct sampling case, since a Gaussian fit adapts specifically to the incoming amplitude, this approach should intuitively prove to be more resilient. However, the limited ADC resolution (8-bits) and fixed ADC gain in the presence of noise makes the fit of low-amplitude pulses less reliable. The adjusted

Pulse type	SPC-150Nx locking error [ps] 10^6 counts	Direct Sampling locking error [ps] 10^3 counts
<i>AWG clean</i> 500mVpk	1.6	1.15
Amp. change 500-35mVpk	8 ZC = 5mV	5 $R^2 = 0.985$
<i><mmw> noisy</i> 500mVpk -20dB SII	9	8
Amp. change 920-200mVpk -15/-25dB SII	13 ZC = 24mV	10 $R^2 = 0.985$
Total	17	14

Table 5.1: Comparing group-delay precisions of both analog and direct digital sampling timing techniques.

coefficient of determination R^2 is used to judge goodness of the Gaussian fit. Only pulses with $R^2 > 0.985$ are counted since allowing lower R^2 fits results in large group-delay variations above the 17ps requirement.

In order to quantify this walk error contribution, firstly, low-noise 700ps-FWHM Gaussian pulses from the AWG were used to characterize the fundamental walk response of each timing technique in the lowest possible noise conditions. The clean pulse peak amplitude was varied between 500 and 35mV. A CFD walk of up to 8ps was recorded with the SPC-150Nx using a zero-crossing (ZC) point [154] of 5mV. The direct sampling approach showed an equivalent walk of up to 5ps. Then, the lossy mirror target (HE₁₁ waveguide mirror in combination with the variable attenuator) was used to quantify walk errors including all circuit noise sources and power variations over the V-band. Peak pulse amplitude was varied between 920 and 200mV, simulating a 10dB power change in the plasma. Using a ZC point of 24mV, the SPC-150Nx walked by 13ps in average. The direct sampling walked by 10ps in average. Table 5.1 and figure 5-5 show how each timing technique responded to changing input amplitudes.

The total timing error is estimated by adding in quadrature all three error sources

presented above and results in a mean over frequency of 17ps for the SPC_{150-NX} and 14ps for the direct sampling technique. Figure 5-5 shows the individual error contributions (omitting the intrinsic hardware error, which is negligible) at discrete frequencies across the V-band. It is worth noting that the direct sampling approach allowed a larger amplitude change ($\Delta P = 12\text{dB}$) going from 920 down to 145mVpk to be counted with a walk of 12ps in average, resulting in total average error of 15ps - 2ps under the requirement. Unfortunately, frequencies 50, 64, and 73-75GHz did not provide a strong signal in the receiver and resulted in final errors much larger than the 17ps requirement. The power-level drop is localized in the Rx module since these frequencies were found to produce a good output signal in the diode tests shown in figure 5-2.

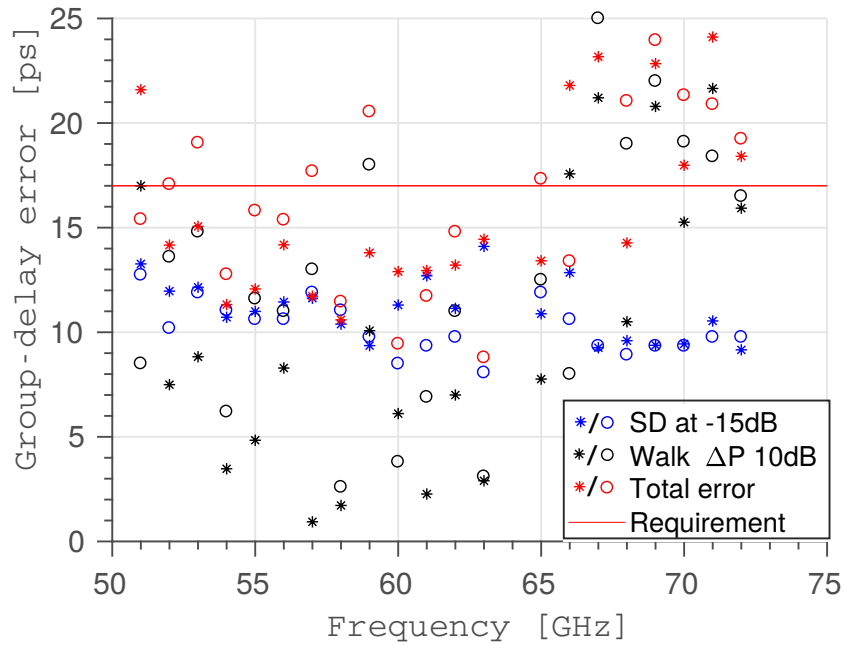


Figure 5-5: Realistic estimation of the total group-delay error of the SPC-150Nx (o) and direct sampling (*) techniques in the V-band considering 10dB power variations in reflected power.

Since triggering of pulses of amplitudes under 200mV would lead to unacceptably high CFD walk, the SPC-150Nx is programmed to ignore pulses under 200mVpk. The direct sampling technique stores all pulses regardless of incoming amplitude. However, the current fitting routine accepts only pulses fit with a $R^2 > 0.985$ which also limits amplitudes above 190mVpk. This threshold requires the launcher-plasma reflection coef-

ficient (S_{11}) of every pulse to be above -25dB so the it can be successfully counted. Note that turbulent plasma S_{11} may be as low as -45dB due to 2D-scattering [81], hence, it is expected that varying amounts of launched pulses may not be counted in the receiver depending on the plasma conditions and alignment at the cut-off layer (see section 5.3.1).

5.2.5 Pulse amplitude and width reflected from lossy static mirror

Direct sampling fits provide not only group-delays but also pulse envelope amplitude and width. Following the clean and noisy definitions in table 5.1, table 5.2 shows the amplitude and width evolution with power. Firstly, the amplitude estimates seem robust to power changes. Even in the presence of full-system noise, the amplitude SD stays under 1%. However, the width estimate seems to vary by as much as 4% in low-amplitude pulses. Pulse width is also seen to significantly decrease (beyond the SD) as the pulse amplitude is decreased when the full mmw system hardware is used. This may be due to the Schottky diode's impedance variations as it departs from the square-law region with high input power. Nonetheless, given the careful characterization of group-delay errors above, these power-driven pulse-width variations do not affect the group-delay accuracy as quantified. However, pulse width variations caused by pulse dispersion in the plasma can affect group-delay determination in a fashion not characterized in this study. In principle, the AWG's flexibility can be used to vary the launched pulse width, but such calibration has not been performed yet.

5.3 Results and discussions

Both timing techniques presented above have been used in plasma discharges. Comparing group delays between identical L-mode discharges 61831 and 62642 revealed that both techniques measured group-delay differences between pulses of carriers 51 and 58GHz within 6ps. Given the overly small sampling duration available in the current direct sampling implementation, the SPC-150Nx timing solution was the only practical option to extract physically useful group-delay data as shown in the section 5.3.2 on page 125. Before focusing entirely on SPC-150Nx group-delay results, the next section presents the

Amplitude		Width	
mean [mV]	SD [mV]	mean [ps]	SD [ps]
<i>AWG clean</i>			
500	1.2	717	3
35	1	696	35
<i><mmw> noisy</i>			
920	13	783	10
528	11	748	11
219	7	720	24

Table 5.2: Pulse peak amplitude and width evolution at power variation extremes against static mirror.

variations in pulse amplitude and width observed in the plasma with the direct sampling technique.

5.3.1 Pulse amplitude and width reflected from L-mode plasmas

The direct digital sampling technique was used to measure about 2700 pulses reflected from L-mode plasma 62642 with frequencies 51-57GHz. After fitting, about 65% of recorded pulses featured R^2 above 0.985, which added up to 250 pulses per frequency. Statistical analysis of these well-fit pulse amplitude and width is shown in table 5.3.

Quantity	mean	SD	max	min	skewness
Amplitude [mV]	550	220	1120	190	0.48
Width [ps]	780	70	1140	610	1.02

Table 5.3: Pulse peak amplitude and FWHM statistics during L-mode plasma 62650. Table presents averages of frequencies 51-57GHz for 333 μ s at 0.7s (ρ_ψ 0.9-0.83. $k_\perp < 50\text{m}^{-1}$).

Raw pulse amplitudes were found to vary strongly, between 1.2V and the noise floor at the mV level. Hence, raw power variations may easily exceed 40dB, in agreement with power modulations extremes estimated by Conway [81]. Fits with adjusted $R^2 > 0.985$ allow only pulses of Gaussian shape and amplitudes above 190mV to be meaningfully studied. Enforcing this double filter, average amplitudes in L-mode sat at an average 550mV with a SD of 220mV. Notice that the amplitude scatter in a L-mode plasma is

an order of magnitude above the amplitude scatter caused by noise in the mmw circuits presented in table 5.2.

Reflected pulse widths can also vary strongly. There are cases where the reflected pulse is not a single pulse. Considering only single-Gaussian reflections with $R^2 > 0.985$ fits that work only for single Gaussian pulses, pulse widths can range from 1.12ns down to 0.61ns showing experimental evidence of pulse dispersion [150]. The minimum pulse width of 610ps, safely away from fit uncertainty under 30ps, shows that the plasma can shrink the pulse width; this is an unexpected result. Considering that the average pulse amplitude recorded was 550mV, the average pulse width was expected at about 748 ± 11 ps from tests against a mirror. However, the average pulse width reflected from the plasma is found to be 780ps with a SD of 70ps. This SD is due solely to plasma-induced pulse width variations since pulse width changes due to pulse amplitude variations have been taken off the SD using the calibration data shown in table 5.2. The skewness of width changes is strongly positive, indicating a higher tendency of reflected pulses to feature a larger width than average.

Changing pulse widths affect the group-delay precision of both timing techniques. In the direct digital sampling approach, a good Gaussian fit should intuitively allow for an accurate determination of a group-delay if the dispersed pulse maintains a good Gaussian shape and amplitude. Also since amplitude, width, and group-delay are recorded, severely dispersed pulses can be safely discarded in averages attempting a density-profile reconstruction from group-delay data. Unfortunately, however, the analog SPC-150Nx module is currently blind to pulse width changes. Analog measurement of rising and falling edges is in principle possible [149]. The effect of varying pulse width on the SPC-150Nx group-delay precision has not been quantified. However, a first-order guess can add half of the standard deviation of pulse width measurements (70ps) to the group-delay uncertainty. Only one-half of this scatter is taken because only the rising portion of the pulse is used to trigger the pulse arrival in the CFD. The average L-mode plasma group-delay error then becomes 39ps by adding in quadrature 35ps and the 17ps error quantified above. No direct-sampling data was available from H-mode plasmas at the writing of this thesis, but dispersion is expected to be lower based on the observed reduced scatter of

group-delay data as shown in the section 5.3.2 below.

5.3.2 Group-delay statistics from L and H-mode plasmas

The data presented here onwards corresponds to group-delays measured with the SPC-150Nx analog timing module. When moving from the static mirror to the plasma target, the first observable feature was that the scatter of the raw group-delay data changed significantly as a function of plasma conditions. Three factors may affect these group-delay fluctuations: variations in returned pulse power, signal to noise (SNR) variations, and physical changes to the pulse group-delay or shape. As presented in section 5.2.2, electrical noise and CFD walk contribution at the allowed pulse amplitude ranges (10dB) can amount up to 17ps (in average) at power extremes. Tests against the HE11 mirror *during* a discharge revealed negligible increased electrical noise interference in the measurement: identical group-delays scatter was measured during and after a shot. Therefore, changes in the raw group-delay histograms for pulses at 58GHz beyond a normal distribution with a 14ps SD are due to plasma-driven changes to the group-delay and/or width. Figure 5-6 shows the normalized histograms of frequency 58GHz acquired for 100ms at 8.33MHz PRR against the HE11 mirror and during the L-mode and (ELM-free) H-mode phases of discharge 62633 (I_p 360kA, $\delta = +0.44$, $Z = 23$ cm, I_p driven H-mode). The maximum of the histograms has been shifted to an arbitrary zero group-delay so the shape of the individual distributions can be best compared. The O-mode polarization ensures that changes in group-delay are entirely due to fluctuations in the electron density.

Basic statistical moments of the raw group-delay data can be seen in table 5.4. L-mode plasmas show a 10-fold increase in the scatter versus a static mirror. Pulse width changes caused by dispersion in the plasma are not taken into account by the SPC-150Nx, but as presented in section 5.3.1 these may contribute to an increased scatter of up to 35ps. Altogether, a L-mode plasma does seem to feature group-delay fluctuations with a 2.5-fold increase all other contributions studied here.

H-mode plasmas show only a slight increase in group-delay scatter versus the mirror total error at 14ps (for 58GHz). The marked decrease in group-delay fluctuations is consistent with the well-known fact that density fluctuations are suppressed in the edge of H

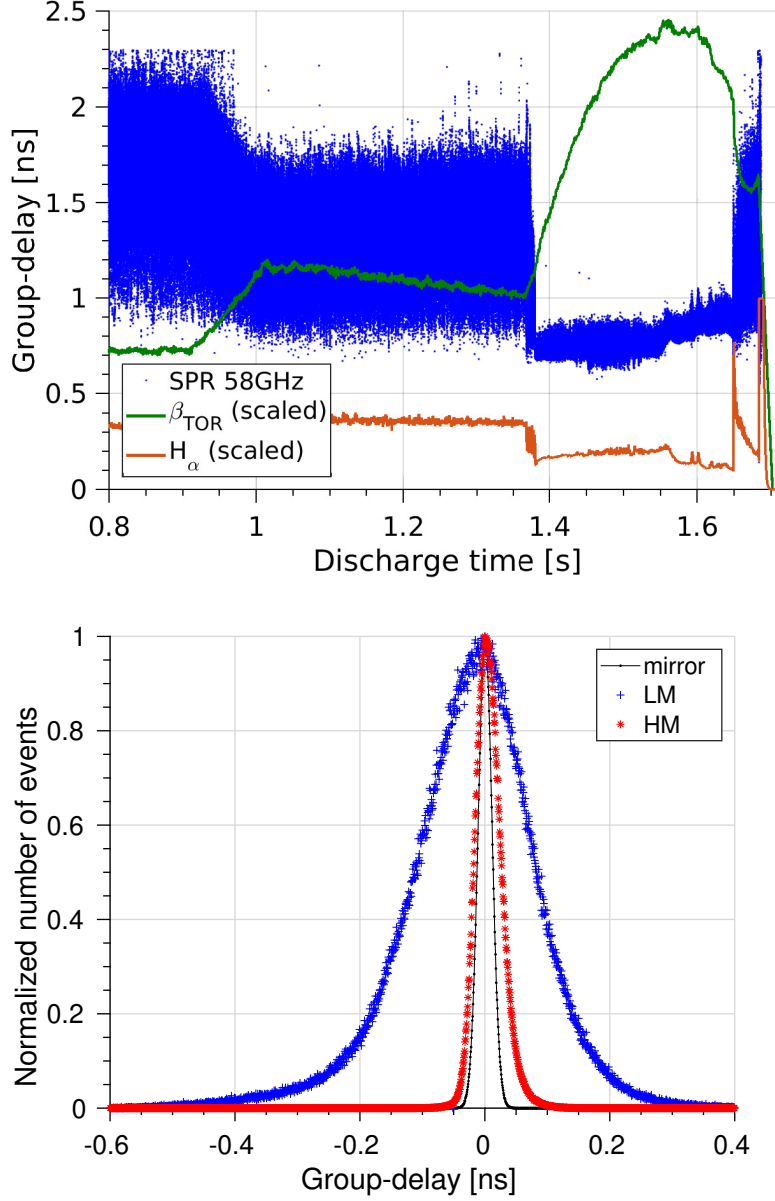


Figure 5-6: (a) Raw group-delay data for frequency 58GHz during shot 62633. (b) Histograms of group-delay data during L-mode (1.15-1.25s), and H-mode (1.4-1.5s) phases compared with against a mirror. Pulse return rates are 93 and 96% for L-mode and H-mode sections respectively. Cut-off location (ρ_{ψ}) and perpendicular wavenumber k_{\perp} were found to be 0.91 and 58m^{-1} during the L-mode and 0.99 and 23m^{-1} H-mode phases using the PrefGeom ray-tracing code.

Target	Stdev[ps]	Skewness	E. Kurtosis
Mirror -10dB	11.2	0.004	0.02
L-mode t = 1.15-1.25	109	-0.52	1.73
H-mode t = 1.4-1.5	22	0.65	1.95

Table 5.4: Basic moment analysis of raw group-delay data during shot 62633.

vs L-mode plasmas due to turbulence decorrelation by shear-flow. The reduction is also consistent with an increased density gradient in the H-mode density profile. Analytical formulas presented by Fanack et al. [156] show that the level of *phase* fluctuations of a single frequency CW reflectometer are not only proportional to the density fluctuation level but also to the square root of the density gradient length $\Delta\phi_{\max} \propto \delta n_0 \sqrt{L_n/k_f}$ (where $L_n = n_e/(dn_e/dr)$ and k_f is the fluctuation wavenumber). This analytical formula applies to large wavelength fluctuations ($k_f \ll k_o$) and small fluctuations where the *spatial* regime of Bragg scattering applies ($2k_{\text{Airy}} < k_f < 2k_o$ [156]). Note also that the increased gradients are less likely to cause pulse width dispersion, which may also reduce the group-delay scatter. The increased group-delay scatter in the plasma over the mirror has also been reported by Heijnen[126] (180ps) and Shevchenko[145] (147ps).

Skewness is also seen to change as a function of plasma conditions. It is seen to transition from negative to positive going from L to H-mode. The positive skewness indicates that group-delays are preferentially *delayed* by fluctuations in the plasma density. No skewness has been reported by previous publications. A theoretical full-wave 1D study[144] showed that radially-propagating density perturbations have the average effect of delaying the group-delays, consistent with the positive skewness reported here in H-mode plasmas. Since the cut-off location is $\rho_\psi = 0.99$, filamentary transport could be causing the positive skewness in agreement with Shevchenko [144]. At the moment, it is unknown why the skewness is negative in L-mode. During large group delay fluctuations such as macroscopic sawtooth oscillations (see section 5.3.3 below), the skewness is also negative. During this L-mode both a 230Hz and 3.8kHz modes can be observed in the low frequency ranges about 10dB above the noise floor.

Excess kurtosis is also seen in both L and H-mode quantifying that the group-delay statistics are beyond normal in both cases, suggesting possible burstiness. It can be expected that rich physics information could be extracted from these findings with the aid of synthetic modeling of pulse reflection in the presence of realistic tokamak plasma density fluctuations.

5.3.3 Frequency spectrum of group-delay data

Conventional continuous-wave fluctuation reflectometers have been able to unequivocally identify macroscopic MHD density fluctuations from the power spectral density (PSD) of phase variations [66]. Studying the PSD of SPR group-delay data has revealed a similar potential. As discussed in section 2.4.2, interpretation is straightforward when the perpendicular scale-lengths of the fluctuations are larger than the beam width at the cutoff ($\lambda_{f\perp} \gg w$), the radial scale-lengths are larger than the probing wavelength ($\lambda_{f\rho_\psi} \gg \lambda_0$), and when the alignment to the normal to the cutoff surface is under 1° . Assuming a 50GHz beam with a 2cm width at the cutoff (focal point for 50GHz beam launcher output - see appendix A), these requirements may roughly translate into $k_\perp \ll 3.14\text{cm}^{-1}$ and $k_{\rho_\psi} \ll 10.5\text{cm}^{-1}$. This stands in contrast to the DBS technique presented in chapter 3 which selects a particular $\lambda_{f\perp}$ by choosing a particular macroscopic angle to the cutoff layer inside the range $k_\perp = 3\text{--}15\text{cm}^{-1}$.

Sawtooth oscillations with a period of about 320Hz have been clearly observed as large variations in the group delays at a pulse carrier frequency of 66GHz during shot 60491, which found a cutoff at about $\rho_\psi = 0.76 \pm 0.01$. TCV's far-infrared interferometer chord number 4, measures line-integrated electron density along a vertical chord located at the same radial location as the reflectometry cut-off: $R=0.972\text{m}$. Figure 5-7 shows the raw data of both diagnostics showing clear signs of macroscopic sawtooth crashes at the same frequency. The signals feature a different time evolution over the sawtooth cycle. This can be expected because of the different nature of both measurements: local reflection at a given point (SPR) and vertical refractive-index integration through the plasma column at the same radial point (FIR).

Figure 5-7 also shows a power spectral density (PSD) estimate of the raw data shown

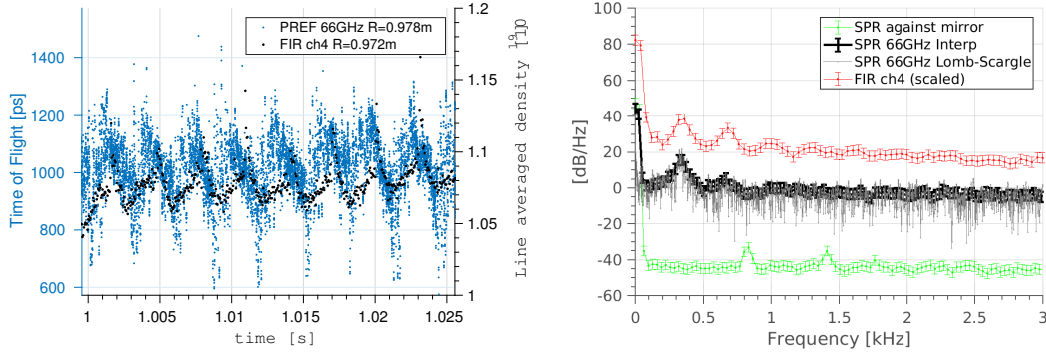


Figure 5-7: Comparison between FIR and SPR diagnostic data showing macroscopic sawtooth oscillation at about 330Hz. SPR frequency 66GHz, $\rho_\psi = 0.76 \pm 0.01$. $k_\perp < 124 \text{ m}^{-1}$. Pulse-return-rate 17%. FIR channel 4 vertically integrates across the plasma at $R=0.972$

in the left. SPR data against the HE-11 mirror is included for reference. It was taken during another discharge (60632) to include background noise in the PSD and features a pulse-return rate of 100%. The Welch algorithm is used to estimate the PSD since the time vector is uninterrupted. The FIR PSD uses data between 0.8 and 1.2 seconds to achieve a good frequency resolution given that FIR data is acquired at 20kHz only. The SPR data PSD takes a 25ms window at 1s. Unfortunately, pulse return rates are only 17%. In order to estimate the PSD, in first order, a simple interpolation approach is taken to use the Welch algorithm. The average effective sampling rate of a time window is used to linearly interpolate between missing SPR data. A more statistically correct approach is to use the Lomb-Scargle algorithm, which specializes in noisy unevenly-spaced data [157]. The built-in MATLAB *plomb* function is used to implement the Lomb-Scargle approach with a default oversampling rate of 4. Figure 5-7 shows that for low-frequency macroscopic modes, the simple interpolation method agrees in identifying the sawtooth frequency with the Lomb-Scargle technique. It is important to note that regardless of the PSD estimation algorithm, SPR data features fluctuations 40dB/Hz above the mirror/background case.

In addition to these low-frequency macroscopic modes, the PSD of group-delay data has shown evidence of a $\sim 40\text{kHz}$ quasi-coherent mode in the edge of NBH-heated ELM-free H-mode plasmas as shown in figure 5-8. In this case, given the improved alignment

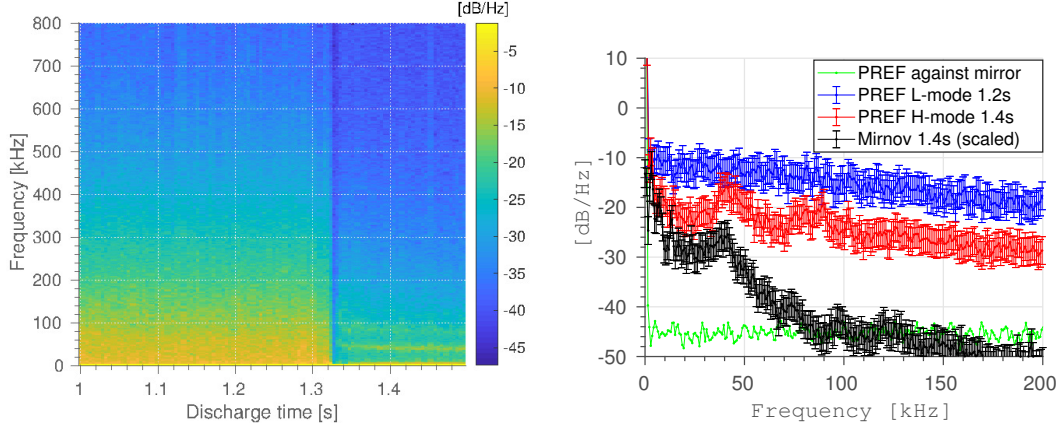


Figure 5-8: PSD of SPR group-delay data over L-H transition during shot 61834. Freq. 50GHz. $\rho_\psi = 0.95$. $k_\perp < 20 \text{ m}^{-1}$. Pulse-return-rate above 85%. Scaled PSD from Mirnov coil No.77 in sector 13.

at the cut-off layer ($k_\perp < 20 \text{ m}^{-1}$), the pulse success rate is 85%. Thus, simple linear interpolation is used for missing pulses. These modes have also been observed by TCV's magnetic pick-up coil arrays [158]. TCV's magnetic analysis routines [159, 160] have been used to identify a mixture of even toroidal mode numbers with dominant $n=0$ and $n=2$ propagating in the counter-current direction. Poloidal arrays hinted at a $m=1$ mode number.

Another interesting finding is the signature of Geodesic Acoustic modes (GAMs) [75] in the group-delay SPR PSD fluctuation data. Figure 5-9 shows a weak mode at about 25kHz, which motivated the search for the same mode in the Mirnov coils. The probing frequency was 58GHz which finds a cutoff at $\rho_\psi = 0.961$ with a $k_\perp = 38 \text{ m}^{-1}$ at 1.4s into discharge 61626. The pulse return rate was only 45%, which motivated the inclusion of the Lomb-Scargle PSD estimate. The latter shows that, although the interpolation technique shows a weak peak outside error bars, there is no unequivocal evidence of the presence of the 25kHz mode.

Figure 5-9 does show an unequivocal $\sim 6.5 \text{ kHz}$ mode in both the magnetics and SPR data. Since the $q=2$ surface is found at $\rho_\psi \sim 0.95$, it is believed that the strong 6.5kHz mode and its harmonics correspond to the signature of a magnetic island rotating in the background plasma flow. Toroidal mode analysis using the above-mentioned magnetic routines reveals a strong dominant $n=1$ character propagating in the co-current

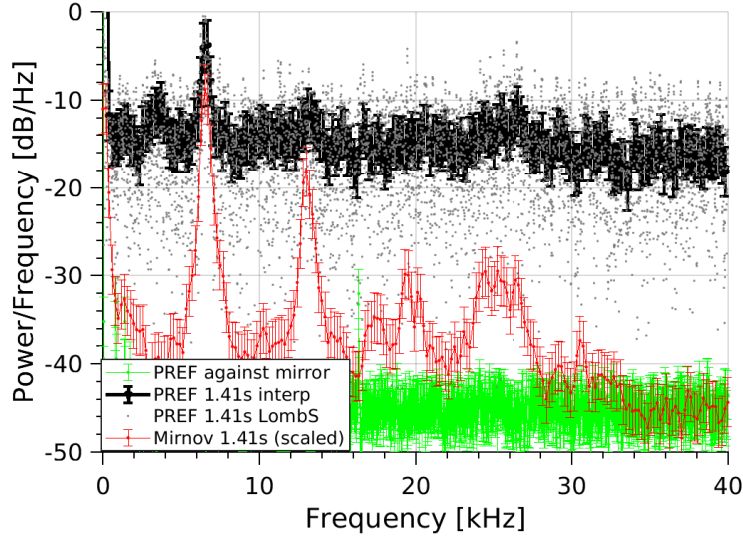


Figure 5-9: PSD of SPR group-delay data for rooms around 1.41s during L-mode shot 61626, believed to host GAMs. Freq. 58GHz, $\rho_\psi = 0.961$, $k_\perp 38 \pm 20 \text{ m}^{-1}$. Pulse-return-rate 45%. Scaled PSD from Mirnov coil No.77 in sector 13.

direction. Poloidal mode number analysis reveals a dominant $m=1$. The 25kHz mode has a strong dominant $n=0$ character, characteristic of zonal flows, but poloidal mode number analysis is not able to conclusively discern an m number. Previous studies have identified GAMs with amplitudes peaking at $\rho_\psi = 0.95$ with a $n=0$ and $m=2$ character, specifically for the magnetic component, as published by de Meijere et al. [161]. However, the density component is believed to be predominantly $m=1$ with a standing-wave pattern.

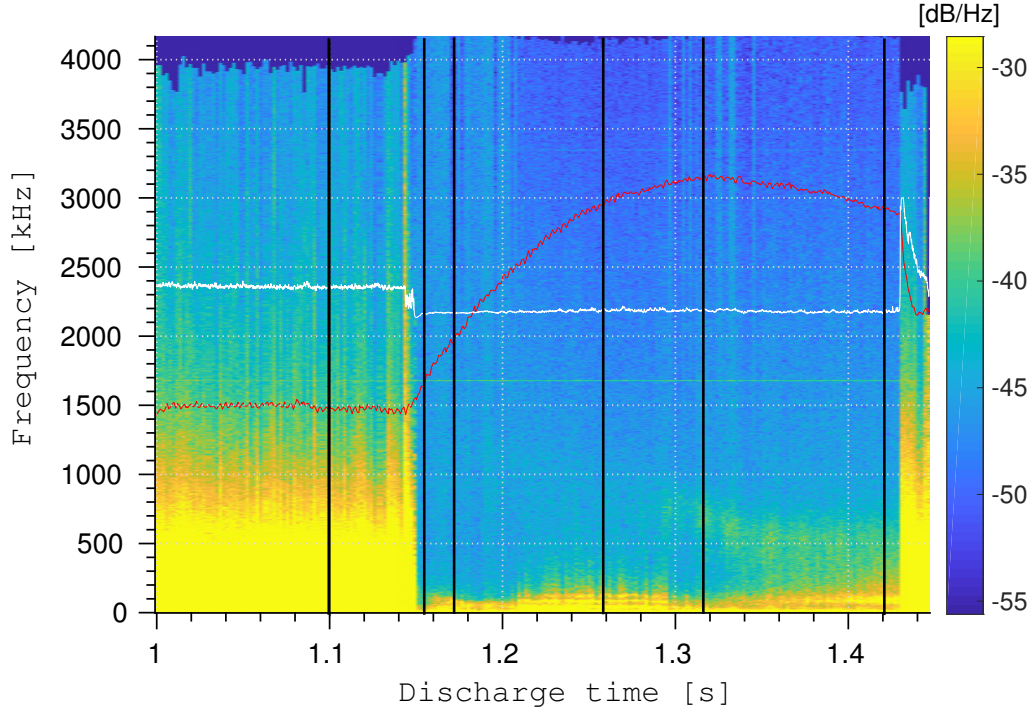
Lastly, a range of as yet unexplained oscillatory modes have been observed in SPR data during ohmic ELM-free H-modes. Figure 5-10 shows the PSD of SPR group delay data during shot 62632 over time featuring various dynamic changes to the pedestal density fluctuations. The white line is the scaled H_α signal. The red line is the LIUQE estimate of the beta toroidal. SPR pulse repetition rate was 8.33MHz, corresponding to a Nyquist fluctuation frequency of 4.16MHz. Pulse return rates average at about 98% during the H-mode phase of the shot, hence the Welch interpolation method is considered perfectly adequate to estimate PSD. Since the O-mode polarization was chosen, fluctuations correspond exclusively to density fluctuations above the diagnostic noise. The SPR output frequency was 58GHz finding a cutoff at $\rho_\psi = 0.879$ ($k_\perp = 47 \text{ m}^{-1}$) at

1.15s, $\rho_\psi = 0.989$ ($k_\perp = 48 \text{ m}^{-1}$) at 1.15s, $\rho_\psi = 0.994$ ($k_\perp \sim 20 \text{ m}^{-1}$) at 1.173s, $\rho_\psi = 0.993$ ($k_\perp \sim 15 \text{ m}^{-1}$) at 1.258s, $\rho_\psi = 0.993$ ($k_\perp \sim 150 \text{ m}^{-1}$) at 1.318s, and $\rho_\psi = 0.992$ ($k_\perp \sim 90 \text{ m}^{-1}$) at 1.421s. Without ELMs to control the particle inventory and flush out impurities, the core average plasma density increases from 4 to $14 \cdot 10^{19} \text{ m}^{-3}$ from the L-H transition at 1.15s to 1.42s. Plasma radiation measurements from bolometry inversions show a steady increase of confined-plasma radiation due to the accumulation of carbon impurities from TCV's wall.

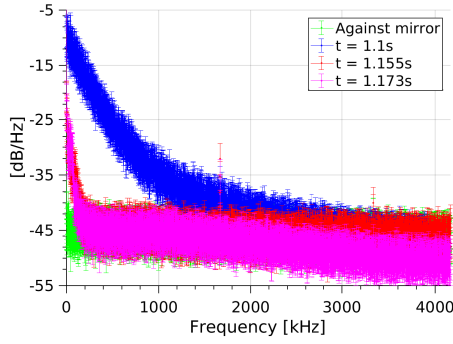
Figure 5-10 on the next page shows the signatures of at least three different types of density fluctuations. Figure 5-10b shows that L-mode plasmas feature fluctuations up to 2MHz above the noise floor. H-mode plasmas feature a very clear decrease of fluctuations that extend only up to about 250kHz. The right hand side of figure 5-10b shows that at 1.15s the H-mode group-delay oscillations remain flat over frequency while at 1.17s the spectra monotonically drops at higher frequencies. The PSD snap at 1.17s features increased fluctuations under 100kHz. Such behavior changes between 2 and 4MHz encourage the development of even faster diagnostics. Figure 5-10c shows that after 50ms in the ELM-free H-mode, a very clear 35kHz mode forms at roughly $\rho_\psi = 0.993$ featuring a harmonic at 80kHz. Unfortunately, the Mirnov coils do not show evidence of such a mode at this time. Once a maximum in toroidal beta is reached at around 1.3s, a very fast broadband quasi-coherent mode appears at around 800kHz and chirps down to 500kHz in 50ms: a snap at 1.316s is shown in figure 5-10d. As this broad-frequency oscillation drops in frequency, the beta is also seen to decrease. Figure 5-10e shows that another strong mode, less broadband than the chirping one above, begins to appear at 1.38s. At 1.421s, the frequency can be identified as about 80kHz. It is also interesting to note that in contrast with the early H-mode snap at 1.15s, the PSD shows oscillations above the noise floor up to 800kHz (seemingly remnants of the chirping mode in 5-10d).

While a formal physical interpretation of these oscillations is not provided at this time, these results highlight the importance of studying density fluctuations at increased sampling rates.

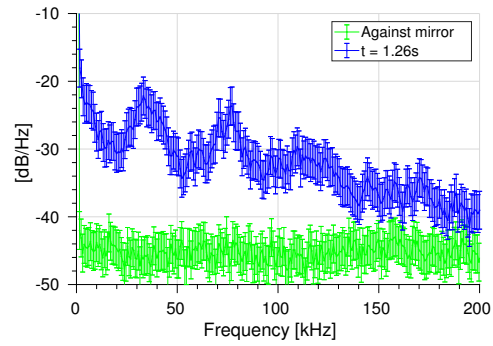
The quasi-coherent 40kHz mode seen in 5-10c seems to allow a steady increase of the beta toroidal until it is abruptly terminated at around 1.3s by the high-frequency less



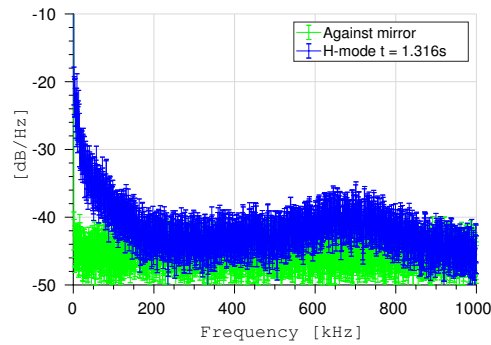
(a) Frequency spectrogram during shot 62632. 5ms windows. Red line is the scaled beta toroidal and the white line is the H_{α} signal. Black vertical lines correspond to the PSD snaps below.



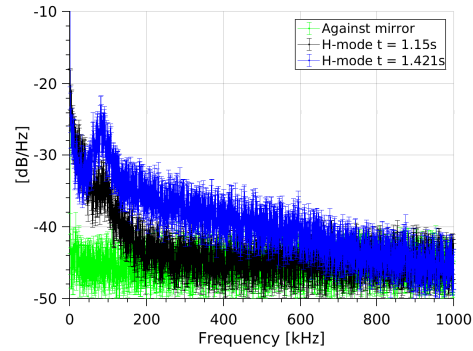
(b) L vs H-mode (ρ_{ψ} 0.879 and 0.989)



(c) H-mode 1.258s (ρ_{ψ} 0.993)



(d) H-mode 1.318s (ρ_{ψ} 0.993)



(e) H-mode 1.421s (ρ_{ψ} 0.992)

Figure 5-10: PSD of SPR group-delay data over ELM-free H-mode during shot 62632. Freq. 58GHz cutoff found at $\rho_{\psi} = 0.89\text{-}0.994$. $k_{\perp} < 150 \text{ m}^{-1}$. Pulse-return-rate $> 97\%$.

coherent 800kHz oscillation. This very high frequency broadband mode 5-10d seems temporally connected with the saturation of the beta toroidal, which is a measurement of the plasma stored energy. While this broadband quasi-coherent mode is not very strong, its frequency is remarkably high: a factor of 3 above the toroidal Alfvén-eigenmode frequencies which are some of the fastest coherent fluctuations observed in tokamaks. Also the back H-L transition seems to be preceded by the strengthening of the 800kHz mode in 5-10e. SPR stands as a useful experimental tool to further understand the fast phenomena in the pedestal.

5.3.4 Density profile measurement

Prior to attempting measurements of density profiles, individual frequencies are calibrated against the lossy-mirror target at the entrance of the launcher. Their individual group-delays are measured and then time-delayed so that all frequencies give the same group-delay within 1ps against the static target. This step is necessary to discard group-delay variations over frequency produced by the mm-wave and transmission-line hardware. The TAC/ADC linearity of the SPC-150Nx was confirmed by artificially delaying the synchronization pulse over the entire measurement range of 1.5ns. The last calibration step consists of applying a correction curve for the pulse group-delay changes through the vacuum window. The quartz interface acts as a Fabry-Perot interferometer with varying amounts of absorption and reflection over the V-band resulting in variable group-delays of as much as 30ps. These group-delay variations were quantified on an optical table using Gaussian beam antennas and TDG VNA measurements. These were later confirmed during a vacuum opening of TCV with a mirror installed inside the vessel facing the launcher antenna. The results of these calibrations are shown in appendix A on page 159.

Profile measurements require a plasma whose cutoff layers are normal to the beam's wave-vector over a good portion of the V-band range. TCV's plasma shape and vertical position flexibility allows for a given launcher poloidal angle to reach a good portion of the V-band frequencies at normal incidence, but the plasma and launcher angle must be carefully chosen. All profile reflectometers measure the group-delay curve over a range

of frequencies and then invert this curve into a density profile over distance from the antenna. Although the AWG has the flexibility of launching any arbitrary frequency into the plasma, the current calibrated approach takes steps of 1GHz as shown in figures [5-2 on page 113](#) and [5-5 on page 121](#). Thus, profiles of up to 20 points (taking into consideration reduced SNR in frequencies 50, 64, 73-75GHz) can be generated with SPR.

The universal polarizers presented in appendix [A on page 159](#) permit the adjusting of the output polarization to fit either O or X-mode at the LCFS. The unique flexibility of these polarizers allows one to couple above 90% of the output power for any B-field pitch angle at the edge of TCV plasmas over the V-band. Transmission can be over 99% at a given frequency but when optimizing for an entire range frequencies at the extremes of the band can feature couplings of only 90%. The 10% uncoupled power could be problematic when sampling in the O-mode polarization, since the X-mode cutoff can be found before the O-mode. Direct sampling of the reflected pulses has the advantage of directly showing the presence of such spurious opposite-polarization pulses. Nonetheless, the unique SNR requirements and time-domain nature of the pulse reflectometry technique that should make this spurious pulses undetectable. Firstly, given that a high SNR is required to detect a pulse, sub-degree perpendicular incidence is required at the cutoff. If the launcher angle is optimized for O-mode, the reflection for X-mode will suffer a reduced SNR because of misalignment. Most importantly, since the current analog SPC-150Nx timing module accepts pulses of only 200mV and above, it is extremely unlikely that the X-mode pulse triggers the timing circuits. However, if both the alignment is good and the power reflected high, it is possible that the O-mode pulse appears 'riding' on top of the X-mode weaker pulse, which can lead to uncertainty in the O-mode group-delay. This must be investigated in more detail through direct sampling. Lastly, it must be noted - for bigger machines than TCV - that since the two reflections are separated in time, if the displacement between the X and O mode cutoffs is separated by more than the range resolution ($700\text{ps} \rightarrow 11\text{cm}$ in vacuum), the two reflected pulses will not interfere with each other. Simple time domain discrimination should allow a clear separation.

Depending on the polarization of the probing beam, different approaches are taken

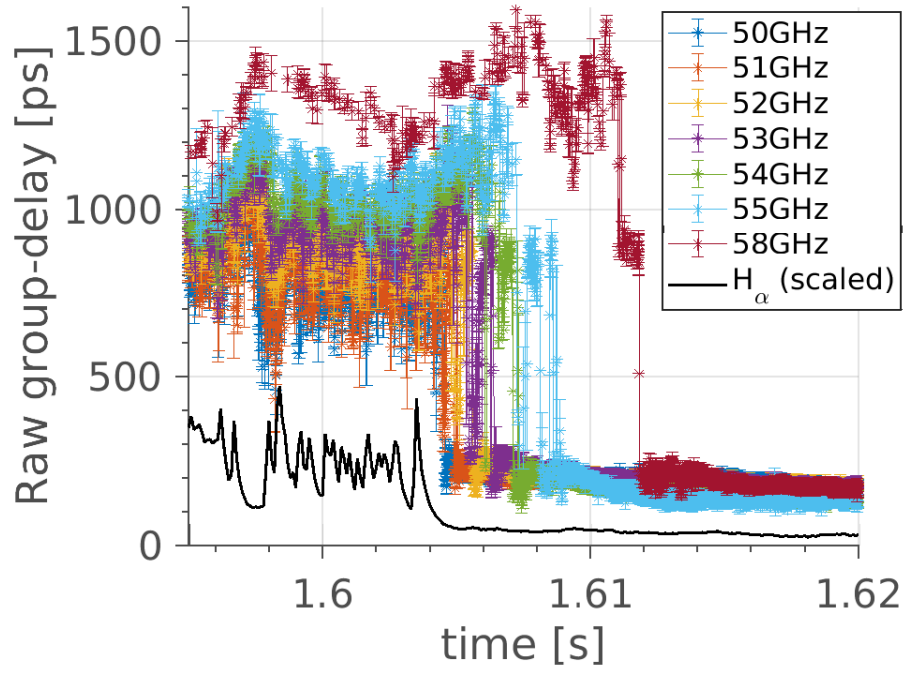
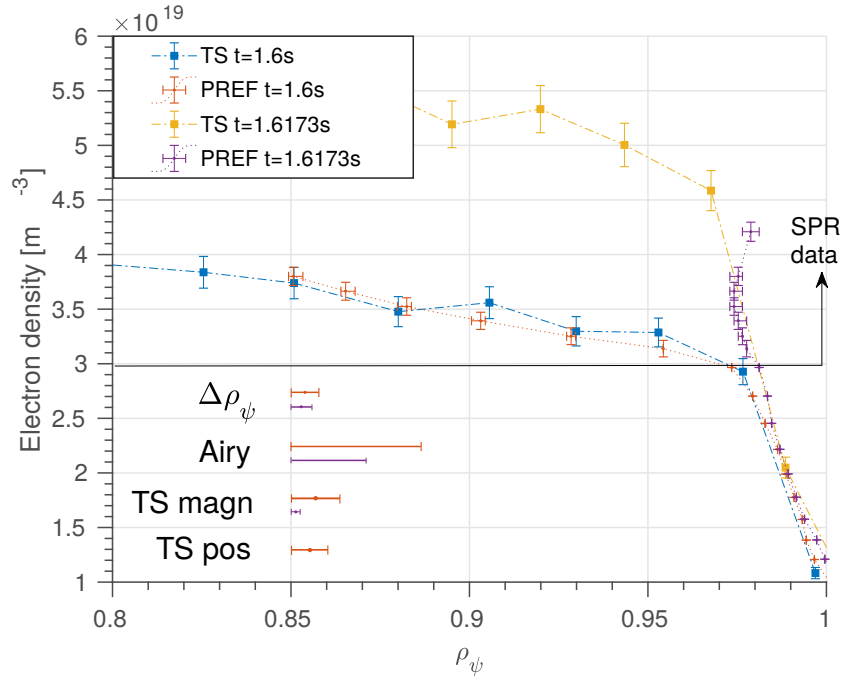
to invert the group-delay data as presented below.

O-mode density profiles

Once group-delays have been measured for a number of frequencies in the O-mode polarization, the well-known Abel transform can be applied to obtain a density profile (see [56] and section 2.3 on page 33).

Unfortunately, as addressed in the theory section 2.3 on page 33 O-mode density profile reconstructions require information regarding the $\partial\phi/\partial f$ curve below the lowest frequency (50GHz in our case). This curve must be obtained from other diagnostics and/or by assuming a particular model[57]. Group-delay initialization is obtained using the 2D ray-tracing routine PrefGeom. This code is presented in a recent publication [153] and in section 3.2.1 on page 57. It uses TS data inside the LCFS (and beyond when available) and features a realistic double-decaying exponential scrape-off-layer (SOL) density profile based on recent measurements [58]. The SOL profile extends out to the end of the far SOL where the vessel walls are first encountered. Vessel volume beyond this point is termed the wall shadow [106] and group-delay contributions from this region are ignored. PrefGeom is used to identify the cut-off frequency at the transition between the far SOL and the wall-shadow, usually between 15 and 25GHz in O-mode. Then, taking 20 steps from this frequency up to 50GHz, ray-tracing is performed to obtain the cut-off locations as a function of frequency. The Abel transform is then numerically inverted to find the group-delay curve between 15/25 and 50GHz. The advantage of this approach is that the curve is inferred from published average SOL density measurements and not models [57]. The disadvantage is that when the 50GHz cut-off is found inside the LCFS, the initialization $\partial\phi/\partial f$ curve is only available on the TS 60Hz period.

Figure 5-11 shows the raw SPR data and two density profiles during a L-H mode transition recorded with 7 frequencies during shot 61337. The group-delay data in 5-11 a and b was averaged over 8.75 μ s to produce each profile, which averages about 5 pulses in each frequency. Density information for $\rho_\psi > 0.975$ is inferred from TS. The density error bars in figure 5-11 b come from the finite width of the 70ops FWHM Gaussian pulse in the frequency domain: ~ 0.61 GHz SD. The ρ_ψ error bars come from

(a) Raw group-delay with $8.75\mu\text{s}$ averaging(b) Comparison with TS $8.75\mu\text{s}$ averaging**Figure 5-11:** Pulse reflectometer density profile during L-H-mode transition shot 61337.

the spread in the group delays (SD divided by the square-root of number of pulses taken in the average) added in quadrature with the 40ps hardware error including the first order

width dispersion correction presented in section 5.3.1.

The points that do not feature error bars in figure 5-11 b come from the initialization procedure described above and do not come from SPR measurements. There are many factors that affect the uncertainty of the initialization procedure both to the shape of the group-delay curve under the lowest frequency and to the location of the first reflection point. Figure 5-11 b shows a $\Delta\rho_\psi$ error that comes from the finite beam size at the cut-off and was estimated using 3-point ray-tracing [153]. The TS magnitude error at the lowest frequency cutoff point of 50GHz is found to be 3%. The density profile is then varied within this range to estimate the ρ_ψ error in the first cutoff location of the initialization. As shown in figure 5-11 b the TS magnitude error leads to $\Delta\rho_\psi \pm 0.006$ and 0.001 uncertainty in the location of the first frequency cutoff during L and H-mode, respectively. The TS position errors driven by the LIUQE vertical plasma position error of 3mm in L-mode inferred from covariance analysis [113] leads to an uncertainty of $\Delta\rho_\psi \pm 0.005$ in the TS profile radial position. Lastly, for reference, figure 5-11 b also shows the Airy width [49][pg.90] which is an estimate of the cut-off layer radial extent. The orange and violet colors refer to the L and H-mode instants, respectively.

Uncertainty in the density reconstruction due to the SOL density profiles has not been studied. Vianello et al. [58] provide ranges for each decaying exponential length as a function of flux expansion and core density. Varying these decaying lengths (by factors between 2 and 3 as seen in figure 6 in [58]) and the transition between near and far SOL will modify the shape of the group-delay curve under 50GHz. Changing this curve would have an effect on the ρ_ψ location of the first few reconstructed profile points. However, the ultimate location of the first reconstructed point would remain the same. Thus, in light of the large position uncertainty seen in figure 5-11 b, it can be conjectured that TS magnitude and position errors may dominate the ρ_ψ uncertainty of the first point. Additionally, it should be noted that as demonstrated by Varela et al. [57], the inversed density profile becomes less and less sensitive on the initial plasma profile shape as the frequency is increased. Nonetheless, exploring the effect of SOL density profiles and its fluctuations on the accuracy of the reconstruction remains an open question for future work.

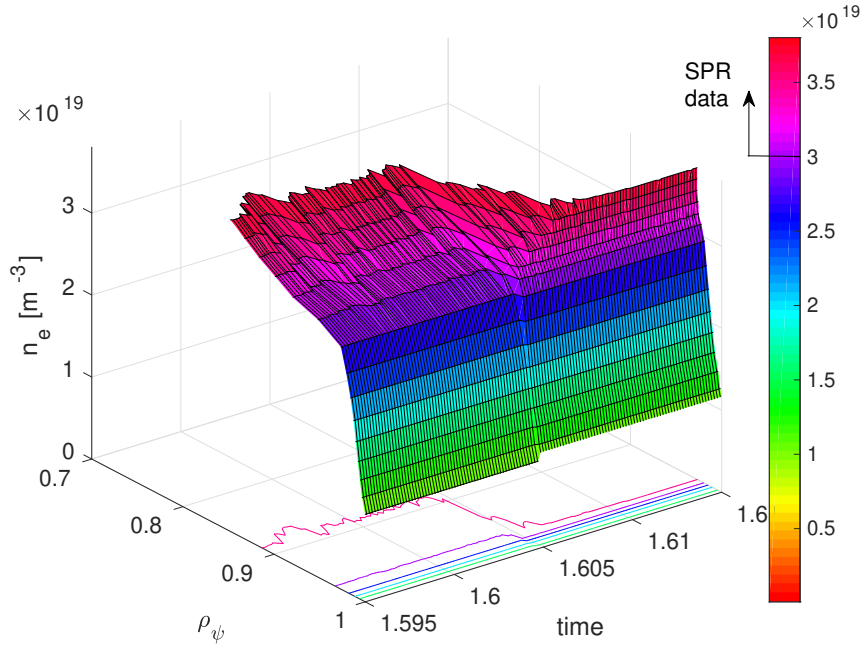


Figure 5-12: Density profile time evolution with 160 μ s averaging during shot 61337.

Figure 5-12 shows the density profile evolution during the L-H mode transition shown in the raw data of figure 5-11 a with a larger 160 μ s window. This was done to avoid having significant periods where profile data was missing because of drops in the pulse return rate. The averaging was also increased to reveal a clearer, smoother transition. The pulse return rate during the discharge time shown in figure 5-12 varied between 95 and 65%.

X-mode density profiles

As presented in section 2.3 on page 33, the Bottolier-Curtet algorithm [60] can be used to transform phase differences between frequencies into distances to a cut-off layer. Knowledge of the magnetic reconstruction allows this information to be transformed into density profile over ρ_ψ . Although it would be best to use an inversion algorithm that uses group-delay as an input, SPR group-delay measurements over frequency can be transformed into phase change over frequency through trapezoidal numerical integration.

$$\phi_{\omega_{i+1}} - \phi_{\omega_i} = \int_{\omega_i}^{\omega_{i+1}} \frac{\partial \phi}{\partial \omega} d\omega \quad (5.1)$$

$$\phi_{\omega_{i+1}} - \phi_{\omega_i} \cong (\omega_2 - \omega_1) \frac{\frac{\partial \phi}{\partial \omega_1} + \frac{\partial \phi}{\partial \omega_2}}{2} \quad (5.2)$$

The magnetic field is obtained from the LIUQE reconstruction inside the Psi-toolbox framework (see section 3.2.1 on page 57). Since it relies on various magnetic coil measurements, it is available at a maximum 0.1ms period. The Bottolier algorithm requires knowledge of the density profile under the first frequency cut-off layer. Unfortunately, since the current SPR implementation features frequencies in the V-band, it was not possible to use frequencies from 30GHz to find out experimentally the shape of the density profile under 50GHz. Instead, the measured TS density profile and the Vianello et al.[58] average SOL profile is used as in the O-mode inversion above. These profiles provide the shape of the refractive index and the position of the first cutoff layer.

Since the TS profiles are available only at 16ms intervals and given that SPR provides measurements of group-delays in the micro second level, a special initialization procedure is proposed. At the very instant of the TS measurement, PrefGeom is used to estimate the ideal group-delay for the lowest sampling frequency. Since precise magnetic reconstruction data and sound estimates of confined and SOL densities are available at that instant, the round-trip group-delay between the shadow and first-frequency cut-off is estimated as follows:

$$\frac{\partial \phi}{\partial \omega_i} = \tau_g(\omega_i) = 2 \int_{R_o}^{R_i} \frac{dr}{v(r)} = 2 \int_{R_o}^{R_i} \frac{N(r) dr}{c} \quad (5.3)$$

$$= 2 \int_{R_{\text{shadow}}}^{R_i} \frac{N_{X\text{-mode}}(r) dr}{c} \quad (5.4)$$

The measured first-frequency SPR group-delay is then scaled to fit the model above at the TS measurement instant. Any future changes to the measured lowest-frequency group-delay indicate a change to the integrated refractive index above. This change can be

due to changes to the magnetic reconstruction and/or the density profile. If the first measured group-delay has changed beyond the SPR uncertainty including dispersion effects at 40ps (corresponding to 6mm in vacuum), then the updated LIUQE reconstruction is firstly fed into PrefGeom to calculate an updated group-delay. If the new magnetic reconstruction cannot account for the change in group-delay, then the TS density profile is scaled iteratively until the modeled group-delay matches the measured group-delay within uncertainty. This approach allows the evolution of the first reflection point of SPR profiles to evolve inside the TS 16ms periods. Figure 5-13 shows an example of using this approach to infer the evolution of the density profile during the plasma startup phase of shot 60928. Figure 5-13b shows how this first reflection point moved using the above-mentioned approach between 0.2 and 0.217s in the discharge. Note that without knowledge of the physical location nor the profile shape of the next TS period, the algorithm arrives at excellent agreement with the TS sampling point at $t=0.21734$. Given the large averaging used to avoid excessive data points in this example, the SPR profiles look rather smooth in contrast with the TS profiles which include the fluctuations present at the sampling instant.

The error bars in figure 5-13c are calculated using the error propagation formula. Group-delay uncertainty (adding 40ps of experimental uncertainty in quadrature with the SD of group-delays in the averaging window) is transformed into phase difference uncertainty by error-propagation through the trapezoidal integration formula assuming exact frequency steps guaranteed by the exact pulse carrier frequency steps produced by the AWG. In the Bottolier-Curtet inversion procedure, the width of pulses in the frequency domain is taken as an additional source of uncertainty and propagated together with phase difference errors.

TS magnitude and position errors also affect the initialization position of X-mode profiles. The nearest point to the 50GHz cutoff at $t=0.2s$ is found at $\rho_{\psi} 0.954$ where a 4% error in n_e magnitude is equivalent to a 0.002 ρ_{ψ} position error. TS position errors due to LIUQE's 0.3cm vertical plasma position uncertainty leads to a 0.005 ρ_{ψ} error. These sources of error are shown in figure 5-13c decoupled from inherent SPR uncertainty for reference.

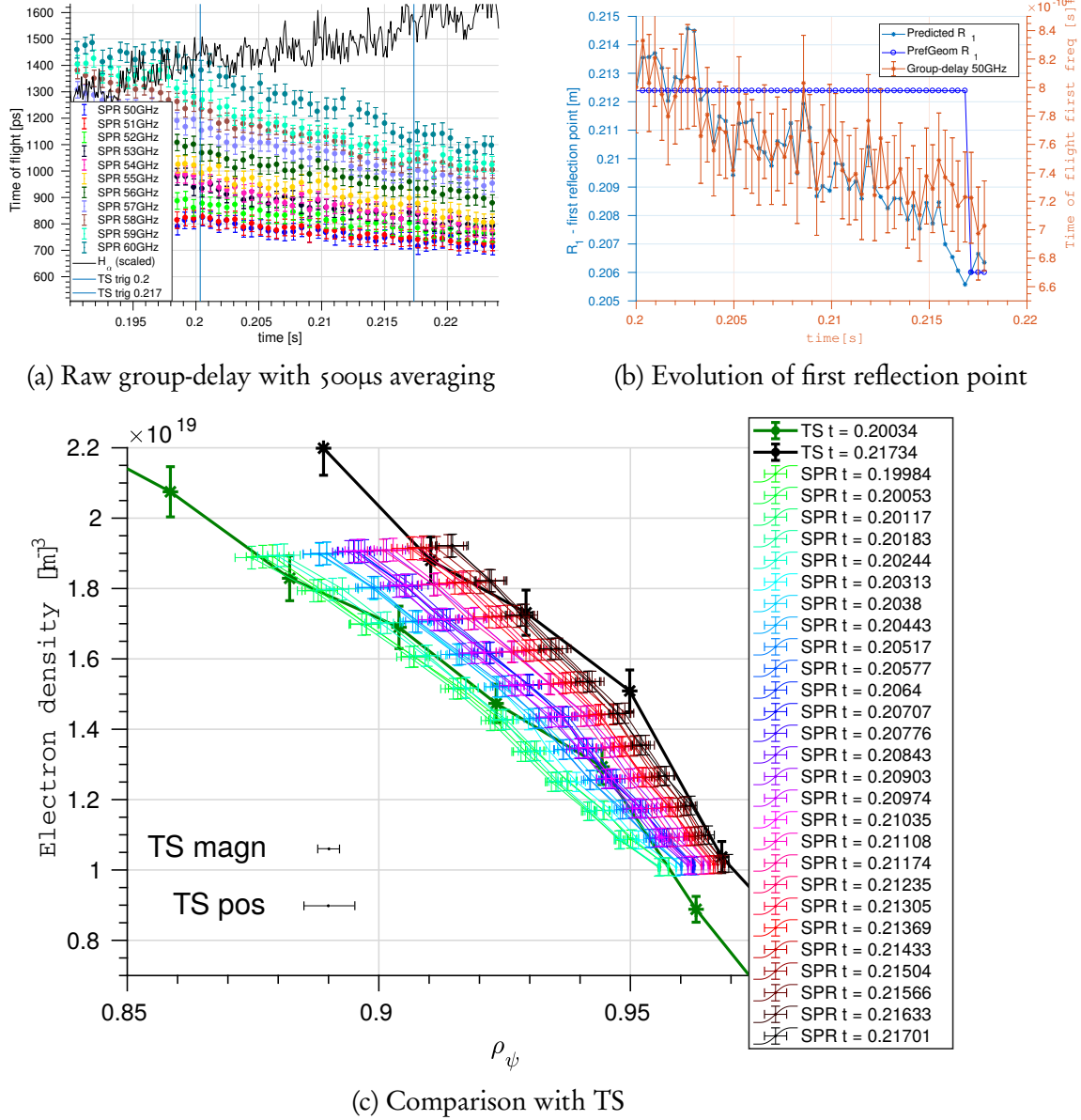


Figure 5-13: Pulse reflectometer density profile in X-mode polarization during starting phases of shot 60928.

5.3.5 Inter-ELM density fluctuations

This section reports on initial observations of density profiles and fluctuations on the ELM instability time scale. These are very preliminary and strictly phenomenological observations, presented primarily because they provide a tantalizing glimpse into the novel capabilities of this diagnostic and the new physics insight that it can be hoped to yield, particularly in conjunction with first-principles modeling.

ITER hopes to achieve its $Q=5$ and $Q=10$ goals through the successful sustainment of an quasi-steady ELMy H-mode. In H-mode, an edge localized transport barrier develops thanks to a sheared ExB flow that quenches turbulent fluctuations. The large density and temperature gradients created by this shear flow raise the pressure performance of the core plasma as if put on a ‘pedestal’. The location of this transport barrier has accordingly been termed the pedestal region. In TCV, it is usually contained inside $\rho_\psi = 0.94\text{--}1.0$.

Although micro-instabilities are quenched by the shear flow, the large pressure gradient in the pedestal can drive a large variety of MHD modes. The EPED model [28] is the leading candidate for predicting the key pedestal quantities, i.e., its width and height (pressure at the top of the pedestal). It has been validated across many tokamaks. It invokes two main groups of MHD instabilities [162]. The first are pressure driven (ideal ballooning modes), current driven (kink or peeling modes), or a combination thereof. The second is a kinetic ballooning mode (KBM). The EPED model, however, does not fully explain the rapid (\sim ms) development of the non-linear phase of the [163] edge localized mode (ELM) [47] instability. ELMs are of vital importance to maintaining a sustainable particle inventory in H-modes. They allow the H-mode energy and particle confinement performance to be quasi steady-state by flushing out impurities. In burning fusion plasmas, these are expected to flush out the helium ashes from large quantities of fusion reactions. However, this instability is also responsible for a rapid decrease of plasma energy and particle content by roughly 5-10% in sub-ms scales which poses particular challenges to plasma facing materials in the divertor region.

Experimentally, it is important to validate theoretical models by attempting to identify signatures of these modes [162] and/or to report on new experimental information to the theoretical community. In support of the ITER discharge design, it is also essential to study how the pedestal responds to changing experimental conditions such as fueling and plasma shape [31]. The inter-ELM density profiles and fluctuations have been studied with the AWG-driven SPR diagnostic. The following section will show preliminary SPR data taken during ohmic ELMy-H-mode discharges 60929 and 62632 with average density of about $6.0\text{--}7.0 \times 10^{19} \text{ m}^{-3}$ with a plasma top triangularity $\delta_{\text{up}} 0.2\text{--}0.25$.

X-mode polarization - ρ_ψ 0.995-0.982

In shot 60929, 11 frequencies between 50 and 65GHz were used to probe the plasma as shown in figure 5-14. The group-delays have been artificially separated vertically so they can be observed separately. Normally, during the H-mode they are found in very close proximity to each other as seen in figure 5-11a. All frequencies are well aligned ($k_\perp < 30\text{m}^{-1}$) and feature very good return rates during *quiet* portions of the H-mode. There are several interesting observations to be made. Firstly, the zoomed-in portion of the graph shows that, about 1ms before the ELM event, all SPR frequencies are either delayed, are accelerated, or start disappearing. This is accompanied by increased coherence in the Mirnov coil oscillation and a slight dip in the H_α signal. The simplest interpretation of missing SPR pulses is power loss due to scattering of the pulse. The SPC-150Nx module will ignore pulses of less than 200mV of amplitude. The timing module will also ignore pulses that appear outside the sampling window of 15ns; however, a large macroscopic motion of the cutoff is usually observed gradually over time: the cutoff layer is very unlikely to move several millimeters in sub micro second scales. Another possible explanation is that the pulses are being strongly dispersed by changes to the local slope of the plasma density. Since the pulse shape is not measured by the SPC-150Nx module, this information is lost. However, given the SPC-150Nx sampling range of 1.5ns, pulse dispersion leading to missing pulses must exceed 4ns, which was not observed in section 5.3.1 on page 123 where in (more turbulent) L-mode plasmas pulse dispersion was only about 80ps. Thus, power signal loss is the most likely candidate behind pulse return rate loss. It can be safely conjectured that a large m-mode number mode could be causing increased scattering. If that were the case, the mode is localized inside $\rho_\psi < 0.984$, which corresponds to the upper portion of the pedestal.

Another interesting fact is that the Mirnov coil shows a large magnetic oscillation during and immediately after the ELM, which is not found in the SPR data nor in the H_α signal. Magnetic reconstruction (LIUQE) calculated in the 0.1ms scale suggests oscillations in the order of millimeters in the z-axis during this post-ELM oscillation, shown in figure 5-15a. Also, the magnetic reconstruction reports a change in the plasma position in the order of 4mm between ELMs. SPR data does not seem to indicate such a large

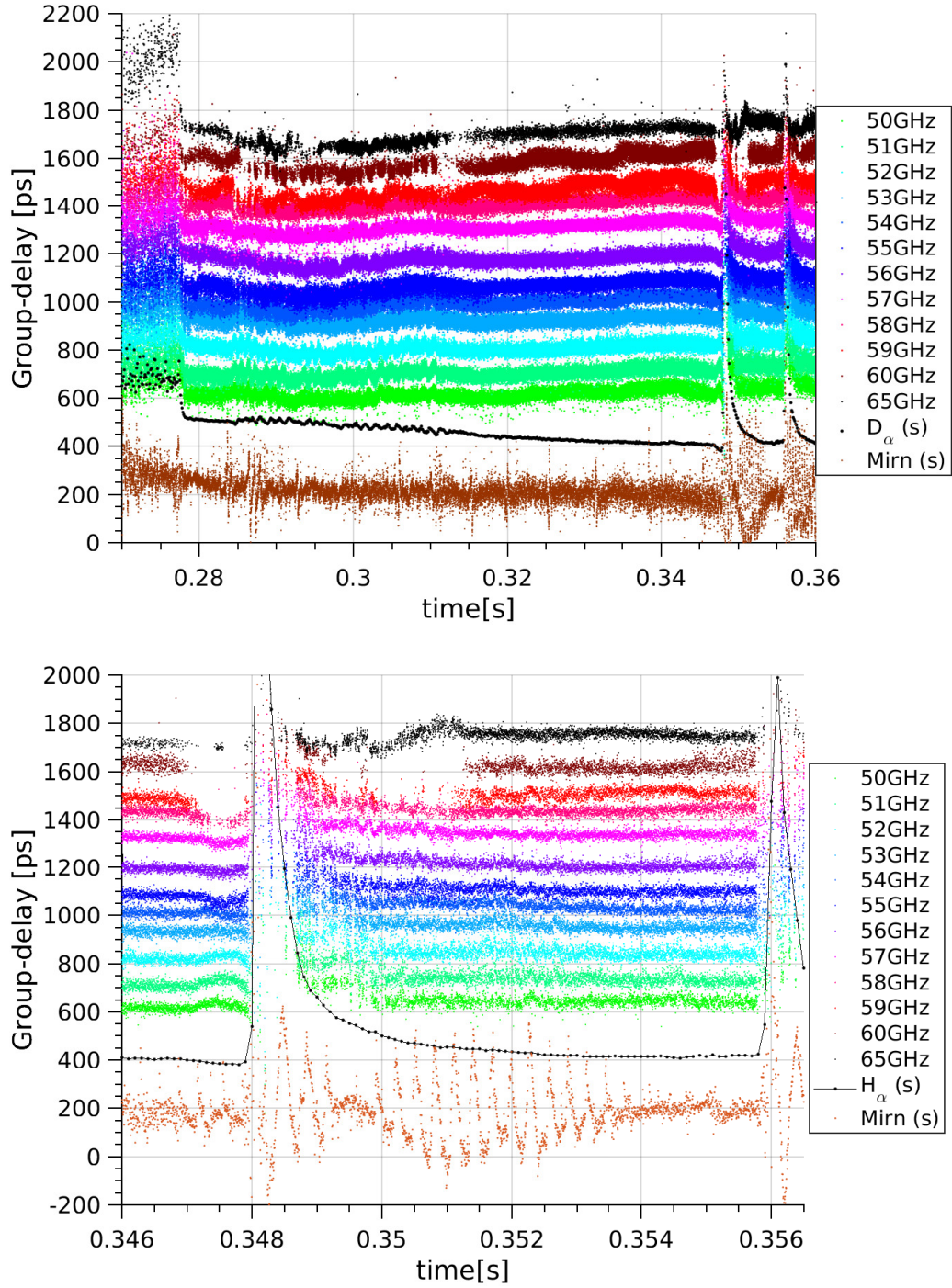
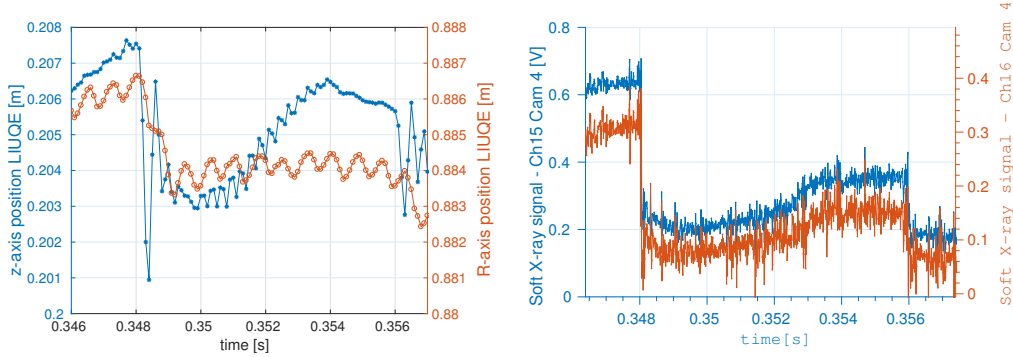


Figure 5-14: SPR data in X-mode polarization before ELM in shot 60929. Frequencies 50-60GHz are being reflected from ρ_{ψ} 0.995-0.982 with $k_{\perp} < 30\text{m}^{-1}$. Pulse return rates are above 97% for all frequencies inside the period 0.32-0.34 for example. Group-delays for each frequency have been arbitrarily shifted vertically to more clearly show their individual time evolution.

position change in-between ELMs since no macroscopic motion is observed in the $\rho_\psi = 0.984\text{--}0.995$ sampled here. During the ELM event, since no pulse width is available, SPR group-delay values cannot be trusted to provide unambiguous information. However, LIUQE suggests a vertical motion of 6mm during the ELM event.

Soft X-ray (sensitive to Bremsstrahlung radiation $\propto n_e^2 T_e^{-1/2}$) camera data from channels that view the plasma nearly horizontally are shown in figure 5-15b. The traces show clear signs of the ELM releasing stored energy and possibly inducing a vertical oscillation but do not show signs of the fast oscillations seen in the Mirnov coil and the LIUQE reconstruction. This data suggests that the oscillation is of a magnetic quality and does not correspond to a real vertical displacement: both SPR and soft x-ray data do not show this oscillation.



(a) LIUQE estimation of the vertical (z) and horizontal (r) plasma axis position between ELMs during shot 60929 (b) Soft X-ray channels 15 and 16 from camera 4 located in the upper lateral port looking nearly horizontal at the 60929 plasma.

Figure 5-15: Additional information regarding the inter-ELM magnetics oscillation seen above: (a) LIUQE vertical and radial position estimates. (b) soft X-ray signals from horizontal view lines.

The power spectra of SPR channels above were analyzed using the interpolation method outlined in section 5.3.3 on page 128 since the hit percentage is found above 90% during the H-mode phase before the first ELM at 0.356 above in figure 5-14. Figure 5-16 on the next page shows the PSD estimate of all frequencies including the first L-mode period where the effective Nyquist frequency is reduced due to lower pulse return rates. Almost all frequencies show a frequency signature or ‘mode’ with a discrete set of frequencies around 100kHz 10-20ms before the ELM crash at 0.348s. The ‘mode’

seems strongest at frequency 59GHz which is also one of the frequencies that features increased pulse return loss 1ms before the ELM crash in the bottom figure 5-14. Figure 5-17 shows a temporal snap of the group-delay PSD of frequency 59GHz during a quieter period and immediately before losing signal 1ms before the ELM crash. The snap shows the ELM precursor mode featuring discrete frequencies around 100kHz separated by about 19-22kHz. This ~ 20 kHz separation is the same across all frequencies and is seen more clearly in frequencies 55 and 57GHz, for instance. Not all frequencies show the signature with the same strength. This can be due to the different output powers and receiver sensitivities of each frequency, which lead to the fluctuations in timing precision shown in 5-5 on page 121.

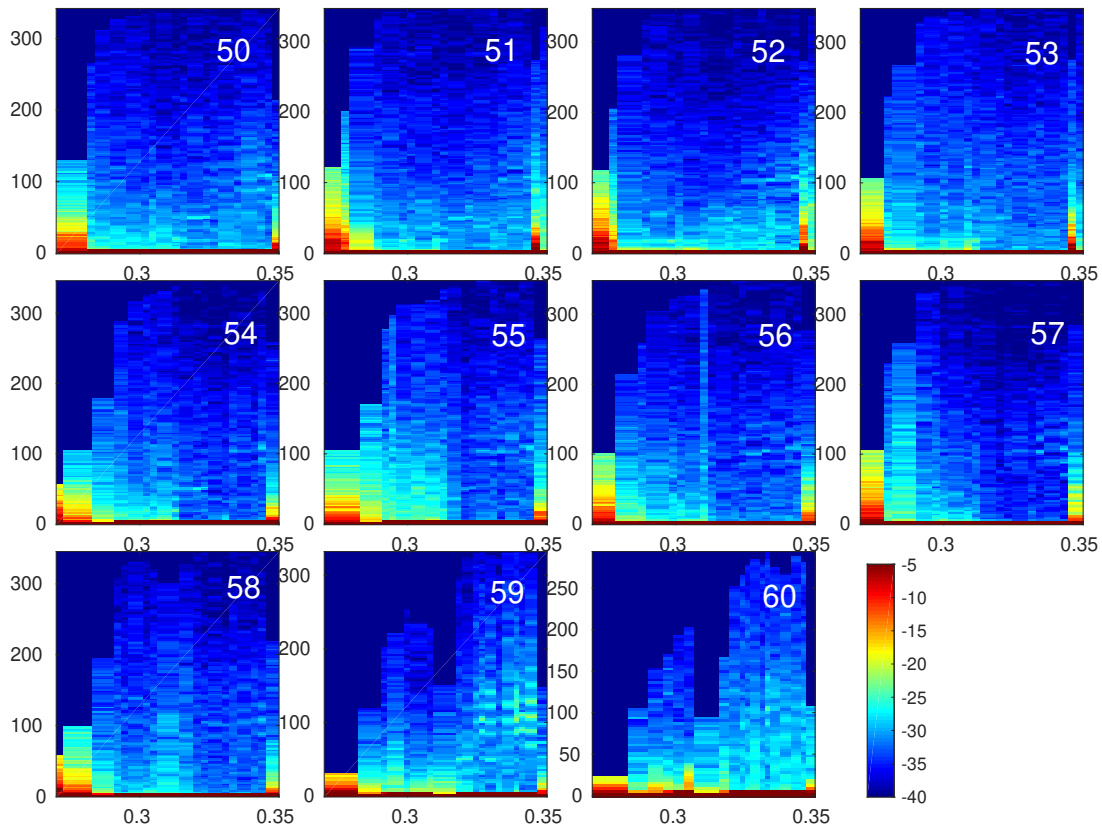


Figure 5-16: PSD of SPR data during ELM-free period of shot 60929 leading to the first ELM at 0.348. Interpolation Welch method and 6ms temporal windows are used.

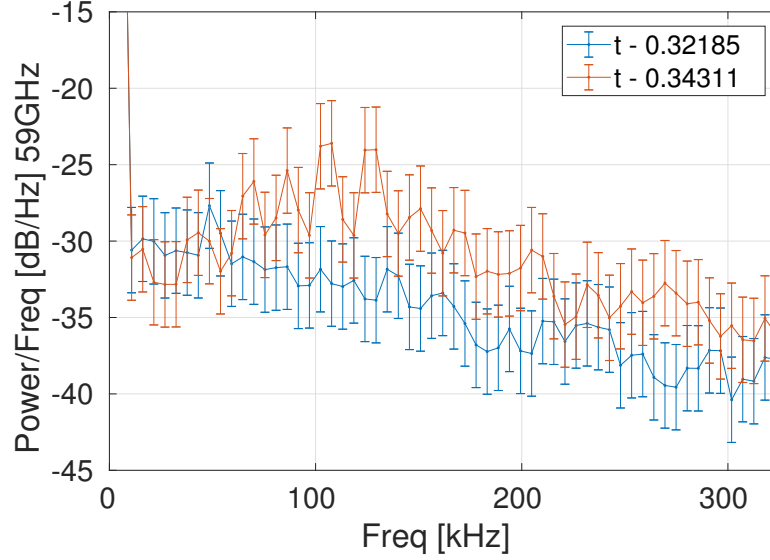


Figure 5-17: PSD of X-mode SPR group-delay data for frequency 59GHz at two instants between the ELM-free period leading to an ELM at 0.348.

O-mode polarization - ρ_{ψ} 0.97-0.955

In shot 62744, frequencies 50-61GHz, 63, 66, and 67GHz were used to sample the plasma in the O-mode polarization. Shot 62744 features the same plasma shape ($\delta_{\text{top}} 0.20-0.25$) but slightly lower average density at 6.5×10^{19} at the first ELM event vs 8×10^{19} for 60929 above. Figure 5-18 shows the SPR raw data through the L-H transition and through the first two ELMs. Note that, again, the SPR group-delay data have been artificially shifted to allow better visibility of individual frequencies. In the case of O-mode, the V-band frequencies are reflected deeper in the plasma. Using the TS measurement at 0.75s, output frequencies from 51 to 61GHz are estimated to cover the range ρ_{ψ} 0.967-0.955 with $k_{\perp} < 15 \text{ m}^{-1}$. Frequencies 63, 66, and 67GHz are included to observe deeper cutoff layers at ρ_{ψ} 0.952, 0.9372, 0.88 albeit with poorer alignment k_{\perp} 18, 35, and 88 m^{-1} , respectively. Pulse return rates for frequencies 51-59 GHz are above 95% in average, while 60, 61, and 63GHz are about 70% average. 66 and 67GHz are shown for completion but feature pulse return rates of only ~20%.

It is interesting to note that the H_{α} signal shows a transition to H-mode before the O-mode SPR lowest frequency of 51GHz (in this case) shows signs of such transition. This

is because of the higher densities sampled by the O-mode polarization. This fact also explains why the L-H transition in this case consists of a continuous transition which takes $\sim 40\text{ms}$ to reach frequency 61GHz . It is interesting to note also that the first two frequencies (51 and 52GHz) feature bifurcations between two group-delay values spaced by about $80\text{-}100\text{ps}$, which is beyond the SD of H-mode SPR data of 23ps (see section 5.3.2). These bifurcations are indicated by yellow opaque ellipses with a red border in top of figure 5-18. These bifurcations indicates either rapid motion of the cut-off layer between two seemingly discrete values or possibly repeated discrete pulse dispersion. Since the SPC-150Nx does not measure pulse width, the physical reason behind this bifurcation cannot be unequivocally determined. It is at these very bifurcations that the PSD of these two frequencies show increased broadband fluctuations as shown in figure 5-20 further discussed below.

Another interesting observation that is not very clear in figure 5-18, due to the artificial spacing between frequencies, is that $100\mu\text{s}$ before the ELM occurs all frequencies seem to all move away from the antenna and gather towards a narrower group-delay difference between each other. Figure 5-19 shows the raw data without artificial separation focused at the onset of the ELM to better illustrate this observation. Frequency 67GHz , which is being reflected beyond the pedestal, suddenly joins the rest of the frequencies right before the ELM. Such gathering of group delays is indicative of a steeper density profile, which could be triggering the non-linear ELM instability. Note also that, as in the case of figure 5-14, the H_α signal dips about 1ms before the ELM crash. In this case we observe, similarly, a change to the group delays in frequencies $55\text{-}58\text{GHz}$ (in both figures 5-18 and 5-19) but not nearly as pronounced as in the X-mode case in figure 5-14. The Mirnov coil is also seen to oscillate strongly without an accompanying SPR or H_α oscillation during and after the ELM.

Figure 5-20 shows the PSD of this data for all frequencies except 66 and 67GHz which feature poor pulse return rates. We find an increase in broad-band fluctuations under 150kHz observed when the bifurcations are seen in the raw data of frequencies 51 and 52GHz in figure 5-18. We may remark as well that these broad-band fluctuations are observed in the two channels closest in ρ_ψ ($51\text{GHz}=0.972$ and $52\text{GHz}=0.971$) to those

where data was being right before the ELM (frequencies above 59GHz $\rho_\psi > 0.989$) in the X-mode data above. Figure 5-21 shows temporal snapshots of frequency 51GHz showing the PSD details at three different times: when there are no bifurcations (quiet time $t=0.699s$), when the bifurcations begin at $t\sim 0.71$ and before the ELM onset at $t\sim 0.74$. These snaps show that the broad-band signature seen in the O-mode polarization is not as well defined in the X-mode case. There is, however, a clear increase in broadband fluctuations under 150kHz in frequencies 51 and 52GHz in contrast to spectra from frequencies 53GHz. This indicates that the observed inter ELM fluctuations are not present further inside than $\rho_\psi < 0.97$. In comparing the power over frequency (y-axis) of PSD snaps in figure 5-21 with those in 5-17 on page 148, assuming a relationship between the modes in X-mode above and the increase in broadband fluctuations in OM, it can be argued that these inter-ELM fluctuations may be stronger inside $\rho_\psi 0.971 - 0.989$ than $\rho_\psi 0.989 - 0.995$.

The analysis above has focused on the first ELM occurrence which featured a strong quasi-coherent mode/broad-band fluctuations in both polarizations together with marked changes to the cutoff locations before the ELM crash. It is worth noting that the above observations are not always present in between ELMs. Ensemble averaging techniques can be used to extract common trends. Such analysis is left for future work.

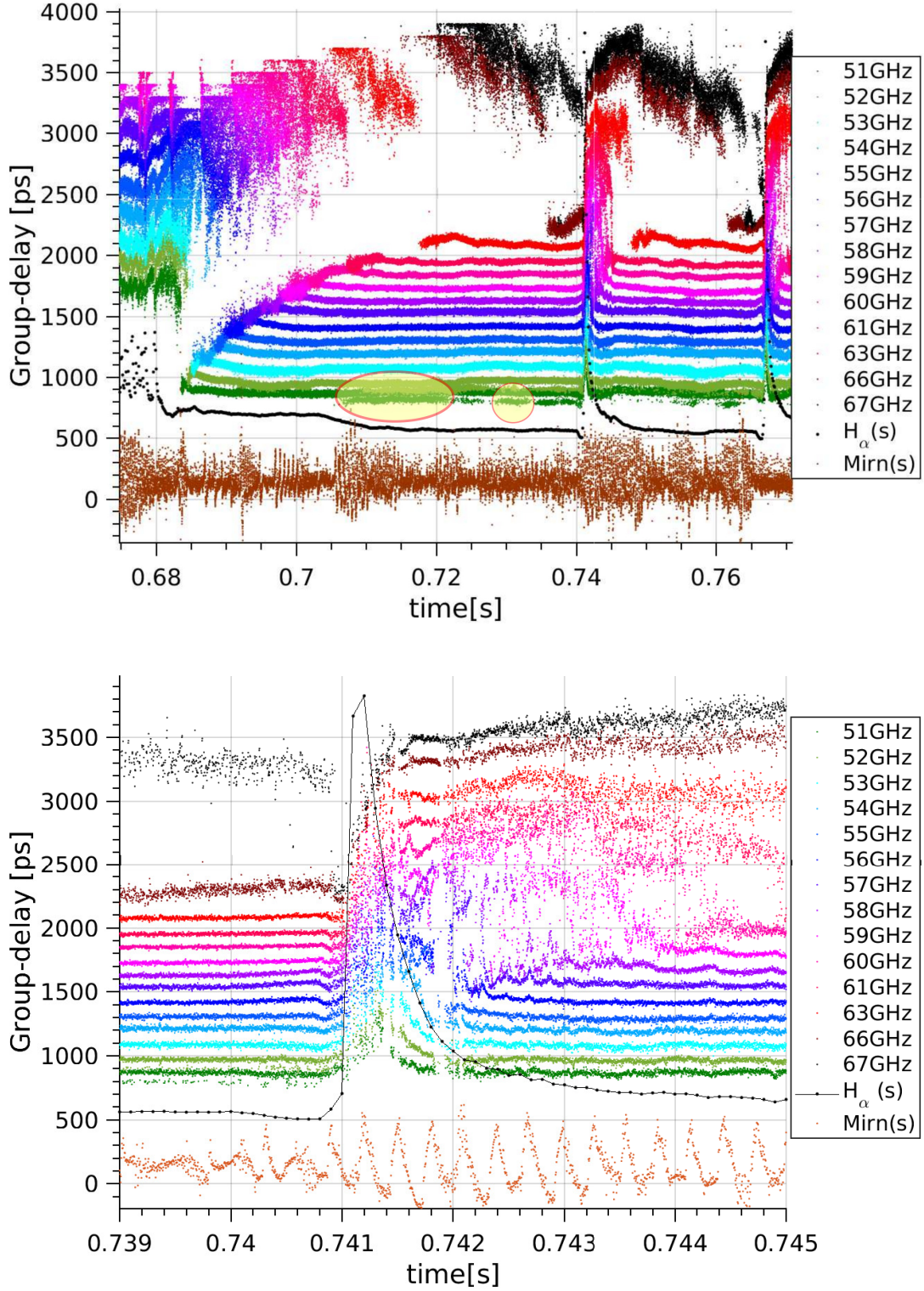


Figure 5-18: SPR data in O-mode polarization before the first ELM in shot 62744. Frequencies 51-61GHz are being reflected from ρ_{ψ} 0.97-0.955 with $k_{\perp} < 15 \text{ m}^{-1}$. Pulse return rates are above 95% for 51-59GHz, 65% for 60-63GHz, and 20% for 66 and 67GHz. Group-delays for each frequency have been arbitrarily shifted vertically to more clearly show their individual time evolution.

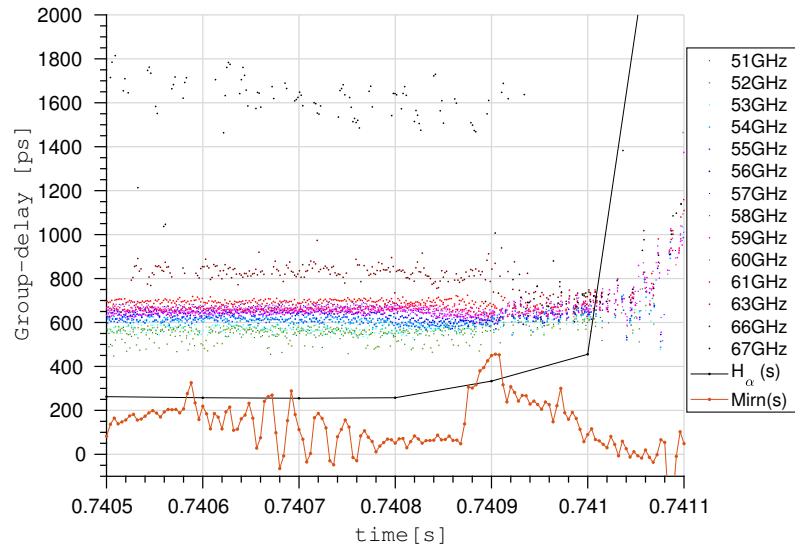


Figure 5-19: Zoomed-in O-mode ELM SPR data showing the sharp density gradient 100 μ s preceding an ELM crash.

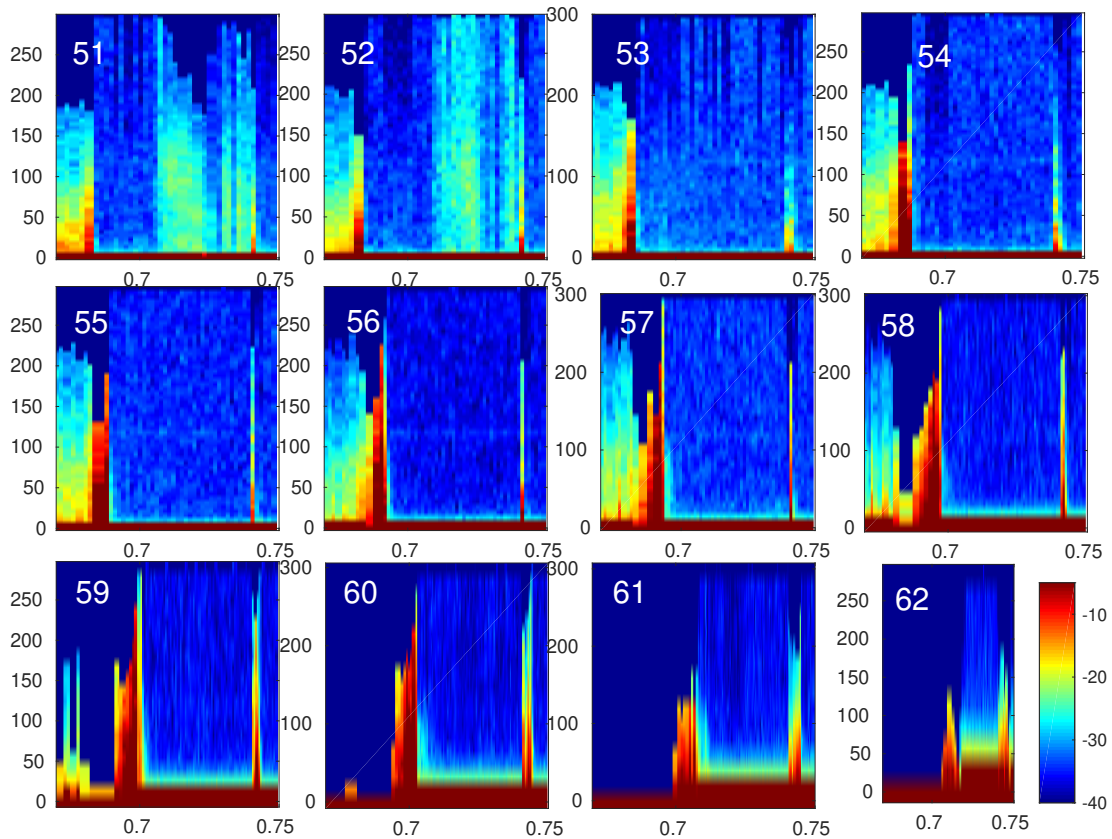


Figure 5-20: PSD of SPR data during ELM-free period of shot 62744 leading to the first ELM at 0.74. Interpolation Welch method and 6ms temporal windows are used.

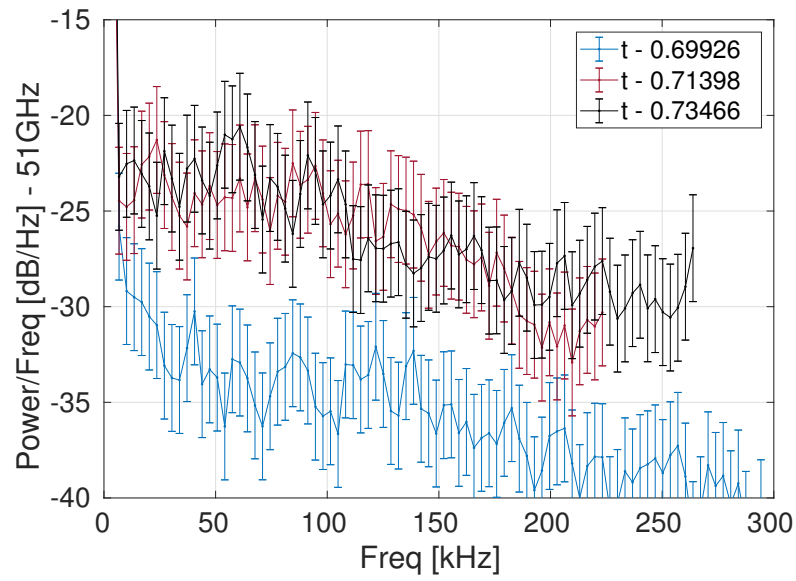


Figure 5-21: PSD snap of O-mode SPR group-delay data for frequency 51GHz at two instants between the ELM-free period leading to an ELM at 0.74s.

5.4 Summary and future perspectives

<i>Criteria</i>	Trad SPR	USPR	AWG-SPR
Range Resolution	1ns pulse = 15cm	6ops = 0.9cm	0.7ns pulse = 11cm
Spurious Reflections	Time-domain filtering	Time-domain filtering	Time-domain filtering
Range Precision	7ops = 1cm	8ops = 2.4cm	17ps = 2.5mm
Spatial Sampling	Fixed Ch# 4GHz gap [126]	Fixed Ch# 1-2GHz gap [137]	Flexible Ch # 1GHz gaps
Temporal Sampling	0.5μs/10pt. prof 0.05μs PRR[130]	10ns/6pt. prof 10μs PRR[134]	2.5μs/20pt. prof 0.12 μs PRR
Effects of Turbulence	Skewed τ_g [145] $\Delta\tau_g = 300ps$ [126] $\Delta\tau_g = 150ps$ [145] Dispersion?	Resilient up to dn/n 40% [143]	$\Delta\tau_g = 100ps$ L-m 30ps H-m Dispersion L-m Δ width = 50ps

Table 5.5: Comparing pulsed-wave reflectometry techniques with the newly developed AWG-driven SPR system. PRR refers to pulse repetition rate.

Table 4.2 is now updated with the results presented above on TCV's AWG-driven short pulse reflectometer. As shown in table 5.5, previous limitations regarding the fixed spatial sampling of heterodyne SPR systems have been overcome by using a variable frequency pulse source that also provides a synced local-oscillator: the M8195A AWG. A broadband pulse reflectometer has been thus conceived. The timing hardware range precision has been improved by a factor of 4. Unfortunately, the current hardware configuration fixes the pulse bandwidth in hardware leading to a fixed range precision. However, the flexibility regarding frequency output allows for an effective arbitrary smoothing bandwidth where subsequent pulses can sample arbitrarily small steps in frequency, at the expense of temporal resolution.

Another fundamental contribution made by the direct sampling technique has been the confirmation that, even in strongly turbulent L-mode plasmas, pulse dispersion is not a show-stopper for short pulse reflectometry as has been argued in the past [118]. The pulse width changes from a 10ps SD over the band against a mirror to a 70ps SD inside the plasma. Yet, adding half of this SD to the timing system's precision, still allows every

pulse to sample the location of the cutoff with sub-cm range precision. The contribution of this source of error to the resulting density profiles as seen in figure 5-11 is not very large.

The direct sampling approach promises an exciting future for the diagnostic. SPC has recently purchased a fast sampling system from Guzik (ADP7104 10-bit 32GSa/s) with a memory of up to 64GBytes. This sampling system, featuring a 10GHz analog bandwidth, will allow direct sampling of the mixer output from the Rx module for over 1.5 seconds. Digital analysis of this data should then allow measurements of phase and possibly Doppler shifts in addition to the group-delay, amplitude, and width demonstrated here. Also, the direct sampling approach has the potential to allow the consideration of reflected pulses of smaller amplitude through advanced analysis routines.

Phase measurements at arbitrary pulse carrier separations have the potential to allow measurements of the density fluctuation correlation length as suggested theoretically by Cohen et al. [143]. Laviron et al. [59] also suggested a hybrid AM-pulse radar technique where differential phase measurements are made at the pulse repetition rate. Such system would overcome the CWAM challenges of interpreting multiple reflections with the automatic time discrimination of pulsed-wave systems. It can also provide a separate measurement of the group-delay with a higher SNR through the use of a narrower filtering pass-band [59].

If the IF pulse is directly measured, changes to its IF frequency become possible. This will allow the application of short pulse reflectometry in the Doppler back-scattering (DBS) configuration addressed in chapter 3 with a continuous-wave system. A pulsed DBS system has the potential of providing density profiles *and* poloidal rotation velocities simultaneously which would remove the fundamental reliance of DBS on background TS profiles [89, sec.9]. Such a system would obtain both the velocity and position of scattering location simultaneously.

Without a hardware IF filter in the receiver, full measurement of the mixer output will allow the output pulse width to change at will, potentially during a shot. This will allow pulse dispersion studies [131] that as presented in section 4.3 have the potential to measure the local density profile slope. Furthermore, varying the pulse bandwidth

would completely remove the smoothing bandwidth limitation of short pulse reflectometry techniques. Lastly, a direct digital sampling system should allow an increase of the current 8.33MHz pulse repetition frequencies by interleaving pulses. Assuming a safe distance of 10ns between pulses, interleaving should allow for pulse repetition rates of up to 100MHz, enhancing the temporal resolution of a 20 point profile down to 0.2 μ s.

Profile reconstruction methods presented here use the Abel inversion for O-mode and the Bottolier-Curtet method for X-mode. The latter assumes a linear refractive index shape in each integration step, which can lead to inaccurate profile inversions. More adequate functional representations of the refractive index have been recently introduced by Morales et al. [62] and Shelukhin et al. [61] which have the potential to improve the accuracy of the recovered profile.

5.5 Conclusions

This chapter has described the technical details and first data of a newly developed broadband short (ns-scale) pulse reflectometer on the TCV tokamak. The instrument can access both equilibrium density profiles and density fluctuation information with sub-cm spatial resolution and micro-second time resolution. The output polarization freedom allows coverage of 3-7 and 0.8-4 10^{19} m^{-3} densities in O and X-mode, respectively. Short pulses in the V-band have been produced by using a fast AWG and x6 varactor multipliers. The group-delay of these pulses has been measured down to 17ps resolution using both analog and direct sampling techniques against a mirror including 10dB power variations. Direct sampling has allowed measurements of pulse width variations showing that while dispersion does occur, in average, pulse widths increase only by 4%. The scatter of measured pulse widths motivates an increase in the analog-timing group-delay uncertainty from 17 to 40ps, which decreases the vacuum group-delay range precision from 2.5 to 6mm. A competitive time resolution has been achieved with pulse repetition rates of up to 8.33MHz, leading to 20-point profiles with a temporal resolution of only a factor of two lower than the fastest CWFm reflectometers.

Pulses reflected from highly turbulent L-mode plasmas shows group-delay fluctua-

tions in the order of 100ps (1.5cm in vacuum). Temporal resolution can be sacrificed in order to reduce this group-delay standard-deviation and easily recover sub-cm range precision, thus providing unique flexibility in the temporal resolution reconstruction of density profiles. Micro-second resolution profiles have been demonstrated, effectively increasing the temporal resolution of edge density measurements in TCV by a factor of 10^3 . Furthermore, previous limitations of SPR systems [118] regarding spatial sampling and smoothing bandwidths have been fundamentally removed in this implementation. The 2GHz IF filter fixes the pulse bandwidth in hardware. However, the flexibility regarding pulse carrier frequency should allow for an effective arbitrary smoothing bandwidth where subsequent pulses can sample arbitrarily small steps in frequency. Integer steps have been demonstrated.

Appendix A

Diagnostic launcher antenna system

Both the DBS and SPR diagnostics use a quasi-optical launcher antenna inherited from TCV's second-harmonic electron cyclotron resonance heating (ECRH) antennas [164]. This section briefly describes the signal path, launcher antenna, and safety systems in place as of the writing on this manuscript in late April 2019. Figure A-1 shows a 3D drawing of the physical location of the DBS/SPR electronics in the north-west cabinet of the TCV hall and how these are connected to the diagnostic launcher in the upper lateral sector 1 of the tokamak. The signal travels through a coupling quasi-optical telescope, 6.2 meters of circular over-sized waveguide, one regular miter bend, two polarizer miter-bends, and a vacuum window to arrive at the launcher antenna. Each of these steps is presented below.

A.1 Signal path

Figure A-2 shows a zoomed-in sketch of the path seen in figure A-1.

A.1.1 Thomas Keating quasi-optical coupling telescope

Firstly, the WR-15 rectangular waveguide output from the VDI module is connected via a waveguide 90° twist (681V/385 from Mi-Wave) and 90° H-plane bend (670V/385) -not shown above- to a WR-15 corrugated Gaussian horn antenna [165] manufactured by Thomas Keating (TK) Ltd. This horn antenna efficiently (98% [166][pg.170]) transforms

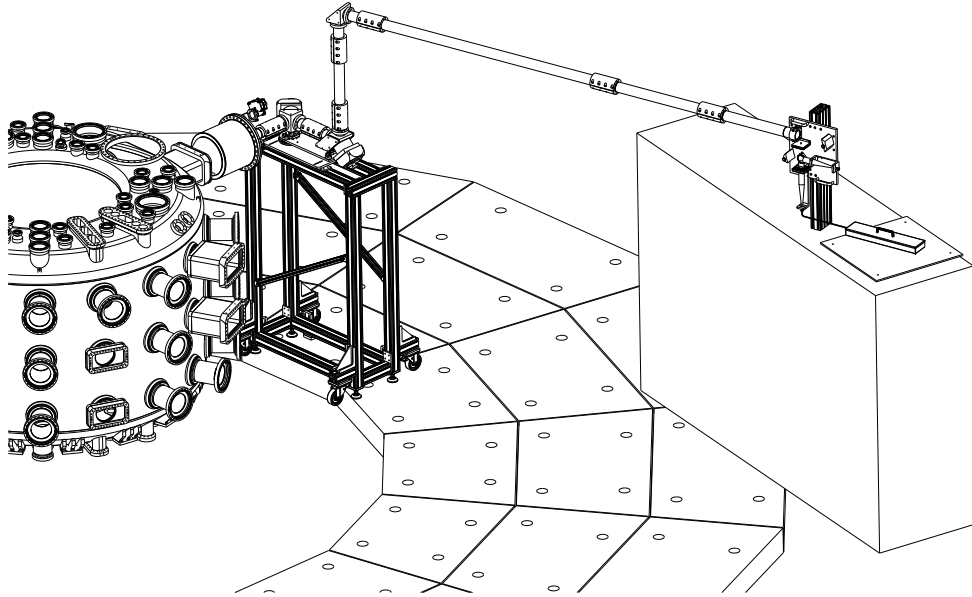


Figure A-1: 3D schematic of the physical location of reflectometry hardware with respect to the launcher antenna and the TCV tokamak

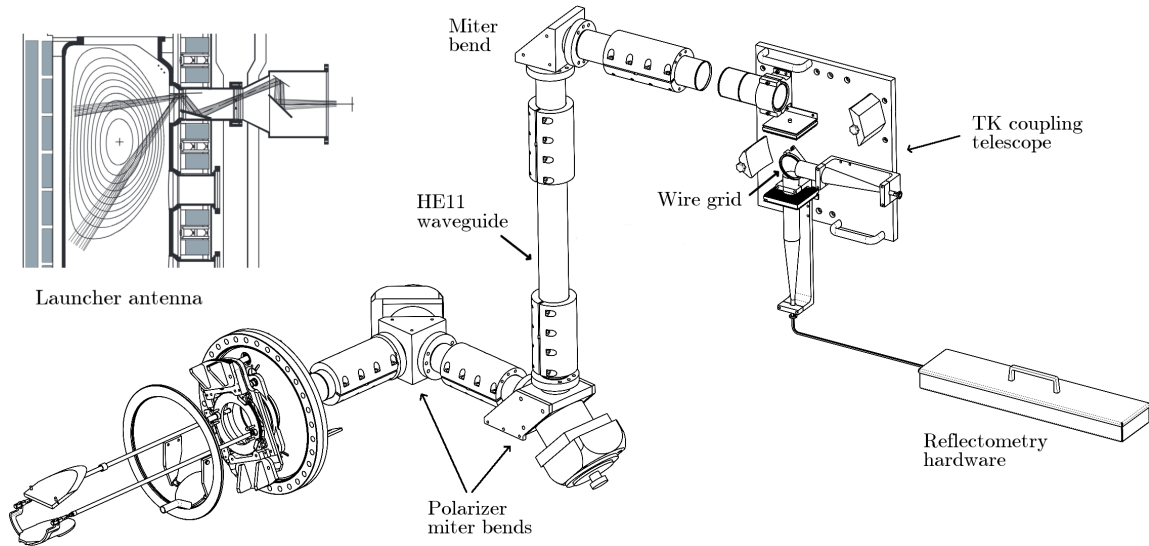


Figure A-2: Zoomed-in view of waveguide path from the reflectometry hardware to quasi-optical launcher antenna. A horizontal 4-meter HE_{11} waveguide section has been shortened for clarity and is shown as a gap above.

the fundamental TE_{10} mode into a free space fundamental TEM_{00} Gaussian beam. This beam is launched into a quasioptical mm-wave coupling telescope manufactured also by TK shown in detail in figure A-3. Using broad-band focusing mirrors, this device ef-

ficiently couples the free space Gaussian beam output from the Gaussian horn into a 63.5mm-diameter circular oversized corrugated waveguide shown in the top-left corner of figure A-2). As seen in figure A-3, the telescope allows two different perpendicular polarizations to be launched and/or received to/from the HE-11 waveguide: a horizontal polarization coming from the bottom horn and a vertical polarization coming from the side horn. This is achieved using a wire-grid polarizer which reflects incident horizontal polarizations. The horizontal polarization (bottom horn) is currently used for reflectometry diagnostics, while the vertical polarization (horizontal horn, following the ELVA safety element in figure A-3) is currently used by Correlation ECE diagnostics [167].

The original documentation of the TK coupling telescope shows W-band horns in all inputs. Yet, since both focusing mirrors are separated by the sum of their focal lengths, its design allows broadband operation in other quasi-optical bands. Using Gaussian-beam q-parameter formalism [49, p. 185], it can be shown that frequencies down to 35GHz may be propagated through the mirrors without clipping. Because of this and given that the same manufacturer custom-built the V-band corrugated Gaussian horn for this very telescope assembly, it can be safely assumed that the TK coupling telescope effectively couples V-band frequencies.

From 2014 until June 2018, the rectangular WR-15 waveguide from the reflectometry hardware was instead tapered to WR-19 (U band) and coupled through U-band twists and bends into a smooth-walled U-band Gaussian horn antenna courtesy of Forschungszentrum Jülich. This solution was abandoned since over-moding was observed during VNA measurements above 70GHz. Also, the outgoing Gaussian beam width and radius of curvature were not optimized for ideal coupling with the TK telescope. Lastly, the smooth-walled Gaussian horn antenna has a smaller power conversion efficiency at 89% and lacks the pattern symmetry and polarization purity of the corrugated horn [166][pg. 170-175]. Insertion losses of the U-band coupling components, the smooth-walled Gaussian horn, and the coupling telescope were measured to be 1.0 ± 0.3 dB using time-domain-gated VNA measurements.

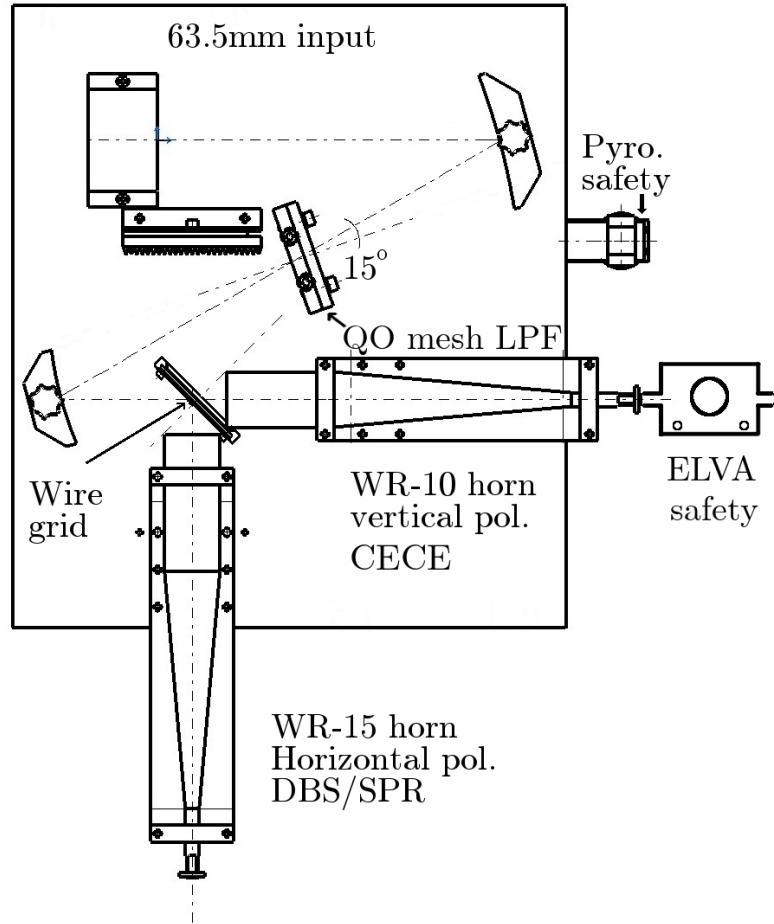


Figure A-3: Thomas Keating Ltd coupling telescope allowing two separate linear polarizations to be launched/received to/from the plasma simultaneously. Created by Tibor Tersztianszky.

A.1.2 HE_{11} waveguide and miter-bend

Once the signal from the Gaussian horns is coupled to the HE_{11} waveguide, it travels 6.2 meters through 3 miter bends to arrive at the launcher antenna. This $HE_{1,1}$ waveguide was manufactured by the Magnetic Fusion Energy division of General Atomics (MFE-GA). It is widely used in TCV to transport gyrotron power because of its extremely low losses. The GA website shows that the 63.5mm waveguide featuring corrugations of period 0.66mm, width 0.46mm, and depth 0.41mm can achieve an attenuation of only 0.1dB over 10 meters for 50GHz [168]. By comparison, the conductive losses of a copper (fundamental $TE_{1,0}$) rectangular waveguide at 19.4dB over 10 meters ([103, p. 119]). The 63.5mm waveguide can be operated down to 40GHz with relative low losses and up to

225GHz without Bragg reflections [168].

The name HE_{11} refers to a transverse electromagnetic mode solution to wave propagation in cylindrical coordinates. This solution is azimuthally symmetric and varies with radius as the zeroth-order Bessel function [166, p. 168]. It couples efficiently at open ended waveguide to a Gaussian beam with beam waist radius of about two thirds of the circular waveguide radius ($w=0.6435a$). The straightness of the HE_{11} E-field lines seen in figure 2 of [169] show that there is virtually no cross-polarization, which is of great importance in the current application coupling multiple orthogonal polarizations of similar frequency simultaneously.

According to the manufacturer's website [168], the 90° miter-bend that brings the $HE_{1,1}$ waveguide towards the fast polarizers may introduce mode conversion losses. These vary approximately as the ratio of the wavelength to the waveguide diameter, raised to the power of 1.5. For 50GHz and the 63.5mm diameter, these losses amount to 1.63% (-0.07dB). Theoretical losses through the HE_{11} waveguide and miter bend should then add up to only about 0.14dB.

A.1.3 Polarizer miter bends

The next step in the signal path is a pair of polarizing miter bends. These are used to optimize the polarization of the Gaussian beam that arrives at the plasma LCFS to ensure optimal coupling to either O or X-mode. These miter bends were also manufactured by MFE-GA. They consist of rectangular grooved gratings fabricated on HE_{11} waveguide miter bends mirrors [170]. Two such grooved mirrors with different groove depths can be used to generate a wide range of output polarizations when fed an input linear polarization. The fundamental WR-15 rectangular waveguide output is linearly polarized and should be maintained by both the TK coupling telescope mirrors and the HE_{11} waveguide. Thus, a linear polarization is fed to the first polarizer miter bend mirror.

Figure A-2 shows that the waveguide inputs to both polarizer miter bends are at 90° to each other, resulting in a 45° incident beam angle on the grooved mirror. A simple physical picture of the process can be sketched [170] by considering a beam incident at a 45° angle to a horizontal grating. If the distance between the grooves is less than half a

wavelength, the parallel component will be reflected (as in a waveguide cutoff), while the perpendicular component propagates to the bottom of the grooves before reflection. The depth of the grooves then controls the amount of E_{\parallel}/E_{\perp} relative phase shift. Assuming a linear input polarization, a linear polarization rotator can thus be conceived by using groove depths of $\lambda/4$ (180°) and an elliptical (or circular) polarizer with groove depths of $\lambda/8$. Changing the angle of the grooved mirrors about the reflection plane can lead to complex reflection polarizations well described by grating plane wave theory. Further details can be found in [170, 171].

These polarizers use direct-drive servomotors to control the rotation of the grooved mirrors about the axis normal to their surface. Rotary servos from Bayside Motion Group (R150D) are driven by Parker Automation Gemini GV6-U6E motor drivers. The GV6 drivers feature advanced motion and sequencing capabilities and can be programmed via RS-232. The miter bend mirrors can be moved by up to 60° in ~ 0.1 s with a resolution of 0.01° . Polarization can be changed during the shot, as demonstrated in section 3.3. These polarizers have been used in TCV for oblique ECE applications; further technical details can be found in Silva et al. [172]. There are two working approaches to operating the polarizer miter bend angles. The simplest approach consists of using its dedicated Vdraw GUI interface. This interface uses a set of Python classes to send commands to the serial port of a BRIX GB-BSi3H-6100 computer connected to the Gemini driver units. This Vdraw GUI window allows initialization, homing, individual command queries, and programming static polarizer angles held throughout the shot.

This functionality was inspired by a more complete MATLABTM GUI [172] that requires a remote-desktop connection to the BRIX computer. This interface allows independent control of both polarizer angles in three separate modes: static, feedforward, and feedback. The *feedforward* mode plays a given preprogrammed angle waveform after receiving a trigger. This mode of operation allowed the polarization rotation measurements in section 3.3. The *feedback* mode rotates the polarizer angles as a function of an external analog input voltage, which can be changed in real-time during the shot. Currently only the static and feed-forward modes have been tested during a TCV shot. The miter bend mirror angle values during a shot are routinely recorded and stored in TCV's

MDSPlus database by directly sampling an analog output available from the Gemini motor drivers at 20kHz using CAMAC digitizers.

During plasma operation, the ideal polarizer miter bend angles for the best possible transmission of a particular frequency and linear polarization in the telescope to a target arbitrary elliptical polarization in the plasma must be calculated. The first step is to calculate the required polarization (α and β) at the plasma LCFS based on the expected plasma conditions through the LIUQE magnetic reconstruction of a similar shot. This is achieved by using the ECH control routine (ECHCS) [173] which allows an accurate computation of the ideal polarization α and β for coupling either the O or X mode as a function of frequency. The second step is to calculate the best polarizer miter bend angles based on the required plasma polarization and upon which linear polarization at the TK coupling telescope is being used (either reflectometry or ECE). The ECPOL [115] suite is used for this purpose. Coupling efficiencies calculated show that although the HE₁₁ waveguide and fast polarizers have been designed for 82.7GHz, V-band frequencies can still be coupled to either O or X mode with >90% power transmission. The Vdraw GUI interface includes a wrapper function that allows the polarizer angles to be optimized for individual as well as multiple frequencies.

The DBS diagnostic benefits particularly from the freedom of output ellipticity since for optimal perpendicular incidence to the main B-field, a small toroidal angle needs to be introduced - usually between 5 and 12 degrees. This toroidal angle requires a non-zero ellipticity (β) to match the curvature of the plasma edge, which can be a function of output frequency. The SPR diagnostic uses a zero toroidal angle that results in small elliptical polarization angles $\beta < 2^\circ$. These polarizers and computational tools allow both reflectometry diagnostics to routinely couple to either O or X modes in a rich variety of plasma shapes and locations, which is a powerful and unique capability.

A.1.4 Vacuum window

A vacuum window acts as a vacuum seal at the interface between the launcher and the elliptical polarizer output. The window is mounted in a CF100 flange of ~150mm diameter. The thickness was measured to be 7.53 ± 0.14 mm. Because of the changing refractive

index and finite width of the window, it acts as a Fabry-Perot interferometer with varying amounts of absorption and reflection over the V-band. Unfortunately, these changing S parameters also affect the group delay ($\partial\phi/\partial\omega$) of transmitted pulses by as much as 30ps, which is beyond the 17ps SPR requirement. Fortunately, the excellent experimental facilities available for mm-wave measurements at SPC allowed the careful quantification of this effect as seen in figure A-4.

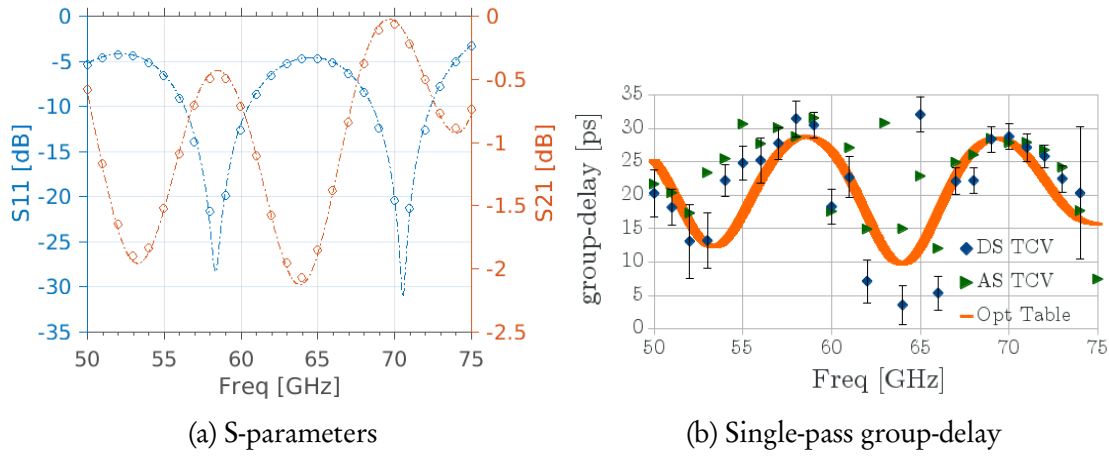


Figure A-4: Transmission, reflection and group-delay variations over the V-band.

A TK quasioptical measurement table presented in detail here [174] was used together with a Keysight VNA N5224A and the VDI WR-15 extension modules to measure the network properties. Transmission (S_{21}) and reflection (S_{11}) coefficients results are shown in figure A-4a. The formal definition of these parameters can be found in [175]. The discrete circles in the figure result from integrating a 1GHz Gaussian function around each individual frequency point and indicate that pulse reflection coefficients are not necessarily those of the carrier frequency.

The heterodyne quasioptical measurements included phase changes over frequency, which allows determination of the group delay changes over the V-band. As seen in figure A-4b, the group delay through the vacuum window is not constant and must be taken into consideration when interpreting pulse-reflectometry data. Peak changes can reach 20ps in a single pass, which can result in up to 40ps round-trip differences. Figure A-4b shows the quasioptical table results as well as measurements with the direct (DS) and analog sampling (AS) pulse timing techniques discussed in section 5.2. These mea-

measurements were done in-situ during a vacuum opening of TCV with a mirror installed inside the vessel facing the launcher antenna. Although the agreement is not very good inside frequencies 60-65GHz (which may be due to signal-to-noise limitations in frequencies 60, 61, and 65GHz as addressed in section 5.2), the agreement elsewhere is within error bars. This agreement amongst all techniques indicates that the effect is real and provides confidence in the correction applied to SPR group-delay data.

The refractive index of the vacuum window material can be estimated to be [176] $N = \frac{c}{2\Delta f \cdot w}$ where w is the width of the window measured to be 7.53 ± 0.14 mm. Using the Δf seen in the sharp S_{11} drops in figure A-4a, the refractive index can be approximated as $N = 1.63 \pm 0.03$. The material was identified as quartz by technical personnel, although the refractive index corresponds more to Rexolite based on [177].

A.2 Quasi-optical launcher antenna

The antenna used by SPR/DBS diagnostics is identical to TCV's X2 ECRH launchers explained in detail here [164]. It is a quasi-optical, telescopic, steerable antenna designed to couple high power (MW) 82.7GHz gyrotron power into the highly variable TCV plasmas. It allows steering of the beam over two degrees of freedom: $550 \pm 0.2^\circ$ in the poloidal direction (see top-left sketch in figure A-2) and $360 \pm 1^\circ$ in the toroidal direction. The poloidal angle can be swept through its entire range during a shot within 500ms. The toroidal angle can only be changed between shots. Figure A-5 shows a 3D drawing of the launcher. It shows the vacuum window and the mouth of the HE_{11} waveguide leading to the elliptical polarizer miter bend. The figure also highlights the motors responsible for poloidal θ and toroidal ϕ motion.

The quasioptical launcher antenna has been designed to maintain the input polarization at its highly steerable output but has been optimized for 82.7GHz. Assuming a Gaussian beam output from the HE_{11} waveguide, Gaussian complex beam parameter formalism was used to compute the power coupling of V-band beams passing through all 4 mirrors of the launcher. It was found that at the lowest frequency (where the largest beam width expansion should occur), 94.7% of the input power is transmitted through

the launcher.

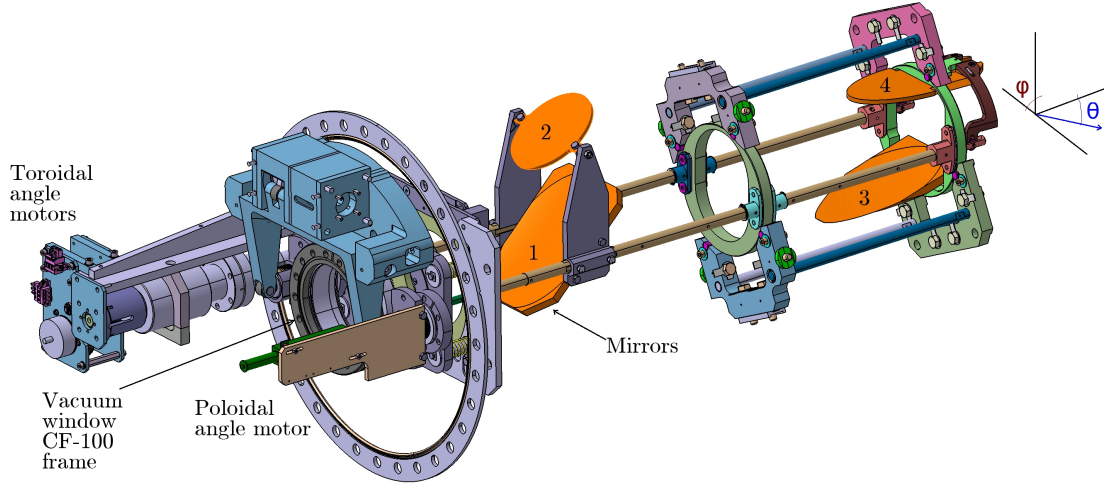


Figure A-5: 3D schematic of the diagnostic launcher. Inspired from [178] and created by Tibor Tersztyanszky

Figure A-6 focuses on the internal telescopic design of the launcher. This 2D sketch includes the optical dimensions of an 82.7GHz beam. It can be seen that mirrors 1 and 3 are focusing while 2 and 4 are flat. Focal length and mirror dimensions can be found in the source code of PrefGeom, which was validated against this drawing. Figure A-6 shows that mirror 4 is responsible for the poloidal angle motion. The latter was chosen flat to ensure the output beam characteristics do not change with poloidal angle. Lastly, figure A-6 shows via an arrow that the Gaussian beam focal point is found in close proximity to the fourth mirror. The quasioptical design of the launcher was aimed at having this focal point outside the plasma's LCFS for X₂ frequencies in order to facilitate the analysis of beam propagation via ray-tracing codes. Since ray-tracing codes evolve each ray independently from each other, it is imperative to start the calculation after the beam's focal point to avoid an unphysical crossing of rays. In the case of a 50GHz beam, the beam focal point has also been found outside the plasma LCFS in all shots analyzed to-date.

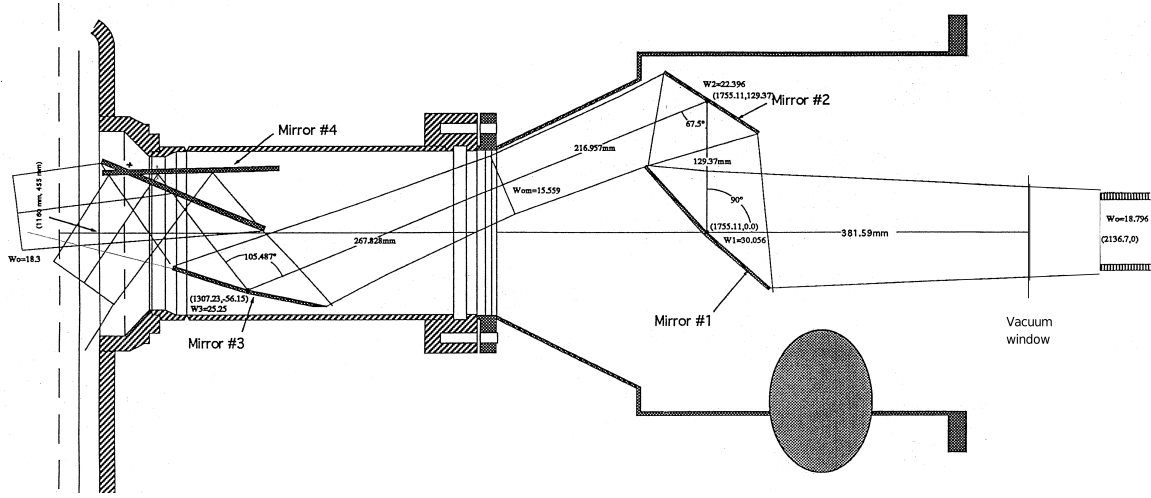


Figure A-6: 2D schematic of the quasioptical design of the diagnostic/ECRH-X₂ launcher. Taken from [178].

A.3 Protection from ECH stray power

TCV is well-known for its high ECRH power density [173]. At its peak, 2.8MW of 82.7GHz second harmonic (X₂) and 1.3MW of 118GHz third harmonic (X₃) have been available for heating and current drive (the total power will be increased further in 2019). The diagnostic launcher is located in an upper lateral port at the same toroidal location as a vertical X₃ port, through which up to 1.3MW of power can be injected. While the vertical X₃ launchers cannot launch directly into the diagnostic port, the broadband nature of the 63.5mm circular corrugated waveguide makes stray X₃ ECH power an imminent danger to the diagnostic. Furthermore, two 500kW X₂ launchers are located in a toroidally adjacent location, only about 40cm toroidally from the diagnostic launcher port, and this power could easily enter the diagnostic launcher after one reflection from the inside wall.

The damage threshold of the V-band VDI transceiver at the core of the DBS diagnostic (section 3.1) is 100mW. The damage threshold of the VDI receiver module of the SPR diagnostic (section 5.1) is even lower at 1mW. Thus, about nine order of magnitude attenuation (90dBm) is required in the worse case scenario to safely operate these reflectometers; 94dBm for X₂ and 91dBm for X₃ to be precise. Fortunately, no damage to DBS or SPR components has been encountered to-date.

The first protection systems are found at the vacuum window. In TCV, all ports featuring a vacuum window are furnished with a pyroelectric detector, and this window features a WR-10 Schottky diode, in addition. These sensors respond to large mm-wave power fluxes which can rapidly increase the window temperature and induce cracking, leading to vacuum leaks. Signals from both these sensors are connected to the TCV emergency interlock system which can rapidly shut off gyrotron power when required.

In addition to these generic protection systems, specialized mm-wave hardware has been installed to provide attenuations of -76dB against X₂ and -110dB X₃ frequencies. Firstly, a quasioptical QMC-K1798 mesh low pass filter from TK provides -26dB rejection at X₂ and over -40dB for X₃ frequencies (-3dB point at 76GHz). It is installed half-way between the two mirrors of the telescope as shown in figure A-3. This filter consists of active metal layers embedded in polypropylene and reflects blocked power. It has been installed at a 15° angle to the normal upon recommendation by Richard Wyld from TK. The angle was chosen so that reflected power is aimed away from the top mirror. As seen in figure A-3, a pyroelectric detector has been placed directly observing the reflected power. This detector is sensitive to both gyrotron power and a drastic increase in the mesh-filter temperature (IR blackbody radiation). The signal from the detector is also connected to the TCV safety interlock system. This quasioptical mesh filter acts as a first line of defense, since it tolerates relatively large amounts of power before serious damage occurs.

Secondly, a V-band waveguide low-pass filter with a -3dB point at 76GHz manufactured by SAGE millimeter (SWF-75379340-15-L1) provides -50dB protection against X₂ and -70dB against X₃ with only about 1.5dB IL. According to the manufacturer, the cavity design allows power inputs of up to 100W (50dBm) before arcing occurs. Unfortunately, if input powers do exceed this threshold, the damaged filter detunes and allows the high-power radiation through.

In order to avoid such circumstances, a third line of defense exists: a fast waveguide safety detector manufactured by ELVA-1 (FPS-10/83) implemented in the vertical polarization telescope line (see horn in the right-hand side of figure A-3). This device consists of a WR-10 fast PIN diode switch in series with a 10dB directional coupler. The coupler

directs 10% of the input power towards a zero-bias WR-10 Schottky diode detector that controls the status of the WR-10 PIN switch. When the input power exceeds a certain selectable threshold between 5mW and 1W, the PIN diode switch is engaged to induce a -40dB attenuation over the entire W-band to protect circuitry downstream with a 8ns response time. Also, when the threshold is exceeded, an active-low TTL output signal is triggered. This TTL output is connected to the gyrotron safety interlock system in TCV via the DBS-diagnostic *slave* module. This safety detector was also found to be sensitive to X₃ radiation by tests performed using the WR-6.5 VDI extension modules and a PNA.

This safety detector is routinely configured to alert the interlock system when powers exceeding 1W are measured at the WR-10 Gaussian horn line. Although, the SAGE WR-15 could theoretically withstand 100W before arcing, no destructive testing has been performed to check this assumption. Personal email communications with Al Hislop from Pacific Millimeter have highlighted that strip-line filters (used in ECE waveguide notch-filter filters connected directly downstream from the WR-10 horn) are at risk of arcing with powers exceeding 4W and melting at 75W. Thus a 1W safety trip should ensure no permanent damage occurs to waveguide filters. According to Hislop, when arcing occurs in strip-line notch-filters these are detuned: its notch frequency changes or its depth decreases, which allows the high power mm-wave power to reach downstream components. Furthermore, 1W at the WR-10 Gaussian horn output corresponds to about 400W of X₂ or 10kW of X₃ power received at the quasi-optical filter, which are already unacceptably large amounts of power received in the diagnostic launcher line. At 1W settings, a safety trip is rarely observed in practice.

Unfortunately, the safety system architecture described above limits the SNR of ECE systems above the -3dB point of the quasioptical filter at 76GHz. When both ECE and reflectometry diagnostics must be operated simultaneously, the quasi-optical filter needs to be removed. The ELVA-safety switch then becomes the first line of defense. In these cases, reflectometry hardware can be protected from X₃ frequencies by an additional WR-15 waveguide strip-line low-pass filter from Pacific Microwave (MOD 80LPF S/N 010). It features IL under 1dB over the V-band, a -3dB point at 86.35GHz and -60dB

rejection at X_3 frequencies. Fortunately, Pacific's strip-line low-pass filter technology allows a fuse-like operation: when arcing or melting occurs, the damaged filter introduces high insertion losses ($>60\text{dB}$) that protect downstream hardware. Using both the Pacific and SAGE waveguide filters provides -50dB and -130dB attenuation against X_2 and X_3 frequencies, respectively.

Acknowledgements

I would firstly like to thank my two supervisors without whom this work would not have been possible. Thank you both for accepting me as your student and for your unwavering moral and technical support. Stefano, words fail me at expressing the deep gratitude, respect, and admiration I have for you. You are an outstanding scientist and human being. It has been a pleasure and an honor working with you. Thank you for always finding the time to carefully answer my questions and look over my papers. Thank you for your open door, your smile, and your relentless commitment to excellence. Thanks for rocking through my hideous 60-page diagnostic proposal in first year and for still believing in me and this project. Laurie, do you happen to have an old Russian IF amp, unmounted from a tank, with less than 1.1dB NF a voltage controlled attenuator over ethernet? I am sure you have that in your office somewhere! Thank you for all your help unraveling the myriad of microwave challenges found along the way. Thank you for your honesty. Thank you for supporting the orchestration of my monopoly over the diagnostic launcher and for protecting me from distractions. You had my back, and I appreciated that. Thanks also for sharing your passion for biking with me.

I would like to express my gratitude to Dr. Fasoli for the opportunity of doing a PhD at SPC. Thank you for enabling me to explore my passion for hardware and innovation by allowing my initial thesis topic change. Thank you to Holger Remeirides and Basil Duval for their guidance as well as their patience and understanding on my thesis choice. Thank you to my thesis committee members: Pascale Hennequin, Terry Rhodes, and Antoine Merle for reading the final draft and improving the ultimate quality of this work with your insights. This work relied heavily on the world-class expertise and experience of the ECH group at SPC. Thank you Stefano Alberti for granting me unrestricted use of

the WR-15 VDI modules, the LeCroy scope, and the PNA - truly state-of-the-art mmw hardware. This thesis would have been impossible without these tools. I appreciated also our technical discussions and your inspiring insights. Thanks also go to Tim Goodman for setting up the diagnostic launcher system. It is one of the most flexible and lossless antenna systems in the world. You laid significant ground work both in hardware and software to enable reflectometry to happen at TCV. Thank you also to Miguel, Pierre, PF, and Matthieu, and the wonderful TCV team for all your technical and logistical help. Vladislav Scheslavskiy from H&B is thankfully acknowledged for prompt feedback and helpful discussions on the performance parameters of the SPC-150Nx module. I would also like to thank Jeffrey Hesler and Steven Durant from VDI for prompt feedback and helpful discussions regarding the performance parameters of the 'VDI heads'. Thanks for shipping the modules back so quickly! Thank you Cedric for insightful discussions regarding SOL density profiles. Thanks Claudio for collecting valuable CXRS data. Thanks goes also to the engineers at Millitech, Jared Greenberg and Chris Euvrard, with whom I exchanged many useful ideas on the conception of SPR. Thanks finally to the administrative staff at SPC: Christian, Tushi, Edith, and Roxanne.

A heartfelt thank you goes also to all my fellow PhD students at SPC. Hamish, bro, your friendship was a beacon of compassion and kindness in this often murky waters. I will miss our jams and our long discussions. Your bad humor, nihilism, and that slight buzz in my right ear will stay with me forever. Thanks to all my fellow musicians too! The Sausage, NTM, Vibrations, The Overworked: Fede, Mirko, Wayne, Guillermo, Semih, Alberto, Jean. You brought many colors to my life and helped nourish my soul through the most unforgiving of trials. Thank you Arthur and Eric for making the Musical such a force of nature. Thank you Vulfpeck, Tom Misch, Deep Purple, The Eagles, Mr. Big, U2, ... how could anybody regard life as anything but wonderful after listening to your epic jams. Thank you, thank you Mengdi! Thanks for sharing your time, experiences, and your daily smile with me. Thanks for taking care of my plants and for all the amazing tea you brought us from your travels. Thanks to Raph, Josefine, Paola, Davide, Hugo, Matthieu, Umar, Tran, Francesco, and all the lovely people I am forgetting for making these 4 years such a lovely experience. Thanks Andre for your

kindness and for sharing your passion for biking. Thanks Master Sifu Karne di Kane for mixing tapes and autogaining all-night-long.

I would like to dedicate this thesis work to my parents. Gracias por todo lo que me han dado y este regalo de la vida. Soy muy afortunado de ser su hijo. Sin ustedes no habria podido llegar hasta aquí. A papi Pedro, gracias por tus consejos, tu perspectiva, y por siempre estar allí por nosotros. Gracias por liderar la 'Aventura llamada Canada', que aunque no sin momentos duros, me ha permitido trabajar en algo tan bello, estimulante e importante como la fisica de plasmas y la fusion nuclear. Tu fuerza de carácter y tu ejemplo ha brotado en mi un espiritu de lucha y ambición incansables. Gracias mamichita, bajo-bajo, por tu voz cada Domingo dandome alientos, recordandome que soy el positivo, el emprendedor viajero y buscador. Me ayudaste a levantarme siempre, simplemente con tu mensaje optimista y chistoso. La vida es dura, pero es la gente como usted que la hacen tan bella y que valga todas las mil y unas penas. Gracias Prudence por escucharme y compartir vivencias in the hustling of building something new. Ojalá podamos trabajar en algo pronto y compartir mas viajes juntos. Pame, thanks for being there to talk with me, overseas, but present and caring. I deeply appreciated our discussions and your insight in unraveling life's complexities. You are a wonderful human being and sister. Last but most certainly not least, je me permets d'écrire quelques mots en français. Merci à Christian Vez et toute l'équipe Goudimel. C'était un vrai plaisir de partager avec vous les cadeaux de la musique, la foi, et votre tradition Protestante. Merci pour votre accueil et patience. Merci à la famille Vienna-Urfer de m'avoir intégré à votre troupe avec tellement d'amour et convivialité.

Un grand merci surtout à Clara Vienna. Tu es sans doute la meilleure découverte que j'ai pu faire pendant ma thèse. Tu es un vrai coauteur de cette travail, sans toi je ne serais jamais arrivé assez loin sans péter un câble. Tu donnes du sens et direction à ma vie. Merci de me partager le message du Christ. Merci de me forcer à sortir du labo :-P, et pour ta patience envers moi et ma dedication parfois extrême au travail. On est arrivé au bout, ensemble. Merci pour ta vie et ton amour. Je t'aime.

Glossary

ADC	Analog to Digital Converter
AWG	Arbitrary waveform generator
CDF	Constant Fraction Discriminator
(C)ECE	(Correlation) Electron cyclotron emission
ELM	Edge-localized mode
ECRH	Electron cyclotron resonance heating
FIR	Far-infrared interferometer
FWHM	Full width at half max
H&B	Becker and Hickl. Manufacturers of the SPC-150Nx timing module.
IL	Insertion losses
L/H-mode	Low/High confinement regime
mmw	millimeter wave
O/X-mode	Polarization of electromagnetic wave at perpendicular incidence to a magnetised plasma
PNA	A fancy name for a Vector network analyzer

PSD	Power spectral density
RF	Radio frequency
SMA	SubMiniature version A. A type of coaxial RF connector
SNR	Signal to noise ratio
SPC	Swiss Plasma Centre
SPR	Short pulse reflectometer
TS	Thomson scattering (diagnostic)
TAC	Time to amplitude converter
TCV	Tokamak à Configuration Variable
TK	Thomas Keating Ltd.
TTL	Transistor-transistor logic
VDI	Virginia Diodes Inc.
X ₂ /X ₃	Second/Third harmonic ECRH

Bibliography

- [1] FOM Institute for Plasma Physics Rijnhuizen. *Energy, Powering Your World*. GmbH, Bavaria-Druck, Munich, Germany, 2005. [1](#)
- [2] BP. BP Statistical Review of World Energy. Technical report, BP Energy Economics, London, England, 2018. [1](#)
- [3] Chris Hope, Paul Gilding, and Jimena Alvarez. Quantifying the Implicit Climate Subsidy Received By Leading Fossil Fuel Companies. *Cambridge Judge Business School*, Working pa(02):1–12, 2015. ISSN 00214922. [2](#)
- [4] Intergovernmental Panel on Climate Change. *Climate Change 2014: Synthesis Report; Chapter Observed Changes and their Causes*. 2014. ISBN 9789291691432. doi: 10.1046/j.1365-2559.2002.1340a.x. [2](#)
- [5] Valérie Masson-Delmotte, Panmao Zhai, Hans-Otto Pörtner, Debra Roberts, Jim Skea, Priyadarshi R Shukla, Anna Pirani, Wilfran Moufouma-Okia, Clotilde Péan, Roz Pidcock, Sarah Connors, J B Robin Matthews, Yang Chen, Xiao Zhou, Melissa I Gomis, Elisabeth Lonnoy, Tom Maycock, Melinda Tignor, and Tim Waterfield. *Global warming of 1.5 degrees C - An IPCC Special Report*. IPCC, Switzerland, 2018. ISBN 9789291691517. doi: 10.1017/CBO9781107415324. [2](#)
- [6] E. Mazzucato. *Electromagnetic waves for thermonuclear fusion research*. World Scientific Publishing Co., 1st edition, 2014. [3](#), [45](#), [47](#), [53](#), [84](#)
- [7] JP Freidberg. *Plasma physics and fusion energy*. Cambridge University Press, The

- Edinburg Building, Cambridge, UK, 2007. ISBN 9780521851077. 3, 7, 8, 10, 15, 17
- [8] Engineering Wiki and Technology History. Mark Oliphant - A biography. URL <https://ethw.org/Mark{ }Oliphant>. 4
- [9] C. Sublette. Nuclear Weapons archive, 2007. URL <http://nuclearweaponarchive.org/Russia/TsarBomba.html>. 4
- [10] J D Lawson. Some Criteria for a Useful Thermonuclear Reactor. *Proceedings of the Physical Society*, 70:6–10, 1957. 4
- [11] John Wesson. *Tokamaks*. Clarendon Press-Oxford, Oxford, 3rd editio edition, 2004. 5, 8, 10, 21, 38
- [12] N. J. Lopes Cardozo, A. G.G. Lange, and G. J. Kramer. Fusion: Expensive and Taking Forever? *Journal of Fusion Energy*, 35(1):94–101, 2016. ISSN 01640313. doi: 10.1007/s10894-015-0012-7. 6
- [13] Vitalii D Shafranov. The initial period in the history of nuclear fusion research at the Kurchatov Institute. *Physics-Uspekhi*, 44(8):835–843, 2001. ISSN 1063-7869. doi: 10.1070/PU2001V044N08ABEH001068. URL <http://stacks.iop.org/1063-7869/44/i=8/a=A13?key=crossref.719505968875b4c998f5b61b3d9b64d5>. 6
- [14] Francis Troyon, R. Gruber, H. Saurenmann, S. Semenzato, and S. Succi. MHD-limits to Plasma Confinement. *Plasma Phys. Contr. Fusion*, 26(1A):209–215, 1984. 9, 16, 17
- [15] L Colas, L Costanzo, and C Desgranges. Hot spot phenomena on Tore Supra ICRF antennas investigated by optical diagnostics. *Nuclear ...*, 1, 2003. URL <http://iopscience.iop.org/0029-5515/43/1/301>. 9
- [16] S. Coda, T. P. Goodman, M. A. Henderson, F. Hofmann, Z. A. Pietrzyk, O. Sauter, S. Alberti, C. Angioni, K. Appert, R. Behn, P. Blanchard, P. Bosshard,

- R. Chavan, A. Degeling, B. P. Duval, D. Fasel, A. Favre, I. Furno, P. Gomez, P. Gorgerat, J. P. Hogge, P. F. Isoz, B. Joye, P. Lavanchy, J. B. Lister, X. Llobet, J. C. Magnin, A. Manini, B. Marlétaz, P. Marmillod, Y. Martin, An Martynov, J. M. Mayor, J. Mlynar, J. M. Moret, P. Nikkola, P. J. Paris, A. Perez, Y. Peysson, R. A. Pitts, A. Pochelon, H. Reimerdes, J. H. Rommers, E. Scavino, A. Sushkov, G. Tonetti, M. Q. Tran, H. Weisen, and A. Zabolotsky. High-power ECH and fully non-inductive operation with ECCD in the TCV tokamak. *Plasma Physics and Controlled Fusion*, 42(12 SUPPL. B):311–321, 2000. ISSN 07413335. doi: 10.1088/0741-3335/42/12B/323. 9, 15, 17
- [17] Johan Willem Oosterbeek. *Towards a self-aiming microwave antenna to stabilise fusion plasmas door*. PhD thesis, University of Utrecht, 2009. 10
- [18] F. Wagner, A. Becoulet, R. Budny, V. Erckmann, and ... On the heating mix of ITER. *Plasma Physics and Controlled Fusion*, 52(12):124044, dec 2010. ISSN 0741-3335. doi: 10.1088/0741-3335/52/12/124044. URL <http://stacks.iop.org/0741-3335/52/i=12/a=124044?key=crossref.4da322579bef3f7e3f454b8f500baccd>. 10, 12
- [19] B.a. Carreras. Progress in anomalous transport research in toroidal magnetic confinement devices. *IEEE Transactions on Plasma Science*, 25(6):1281–1321, 1997. ISSN 00933813. doi: 10.1109/27.650902. URL <http://ieeexplore.ieee.org/lpdocs/epic03/wrapper.htm?arnumber=650902>. 10, 37, 39, 42
- [20] F. Wagner, G. Fussmann, T. Grave, M. Keilhacker, M. Kornherr, K. Lackner, K. McCormick, E. R. MÜller, A. Stäbler, G. Becker, K. Bernhardt, U. Ditte, A. Eberhagen, O. Gehre, J. Gernhardt, G. v. Gierke, E. Glock, O. Gruber, G. Haas, M. Hesse, G. Janeschitz, F. Karger, S. Kissel, O. KLÜber, G. Lisitano, H. M. Mayer, D. Meisel, V. Mertens, H. Murmann, W. Poschenrieder, H. Rapp, H. Röhr, F. Ryter, F. Schneider, G. Siller, P. Smeulders, F. Söldner, E. Speth, K. H. Steuer, Z. Szymanski, and O. Vollmer. Development of an Edge Transport Barrier

- at the H-Mode Transition of ASDEX. *Physical Review Letters*, 53(15):1453–1456, 1984. ISSN 00319007. doi: 10.1103/PhysRevLett.53.1453. [11](#)
- [21] F. Wagner. The physics basis of ITER confinement. *AIP Conference Proceedings*, 1095:31–53, 2009. ISSN 0094243X. doi: 10.1063/1.3097319. [11](#)
- [22] D.G. Whyte, A.E. Hubbard, J.W. Hughes, and ... I-mode: an H-mode energy confinement regime with L-mode particle transport in Alcator C-Mod. *Nuclear Fusion*, 50(10):105005, oct 2010. ISSN 0029-5515. doi: 10.1088/0029-5515/50/10/105005. URL <http://stacks.iop.org/0029-5515/50/i=10/a=105005?key=crossref.76e3332b73592f6e6b157a67f119a92d>. [11](#), [79](#)
- [23] M. E. Austin, A. Marinoni, M. L. Walker, M. W. Brookman, J. S. DeGrassie, A. W. Hyatt, G. R. McKee, C. C. Petty, T. L. Rhodes, S. P. Smith, C. Sung, K. E. Thome, and A. D. Turnbull. Achievement of Reactor-Relevant Performance in Negative Triangularity Shape in the DIII-D Tokamak. *Physical Review Letters*, 122(11):115001, 2019. ISSN 0031-9007. doi: 10.1103/PhysRevLett.122.115001. URL <https://link.aps.org/doi/10.1103/PhysRevLett.122.115001>. [12](#)
- [24] M. Keilhacker, A. Gibson, C. Gormezano, P. J. Lomas, P. R. Thomas, M. L. Watkins, P. Andrew, B. Balet, D. Borba, C. D. Challis, I. Coffey, G. A. Cottrell, H. P.L. De Esch, N. Deliyannis, A. Fasoli, C. W. Gowers, H. Y. Guo, G. T.A. Huysmans, T. T.C. Jones, W. Kerner, R. W.T. König, M. J. Loughlin, A. Maas, F. B. Marcus, M. F.F. Nave, F. G. Rimini, G. J. Sadler, S. E. Sharapov, G. Sips, P. Smeulders, F. X. Söldner, A. Taroni, B. J.D. Tubbing, M. G. Von Hellermann, and D. J. Ward. High fusion performance from deuterium-tritium plasmas in JET. *Nuclear Fusion*, 39(2):209–234, 1999. ISSN 00295515. doi: 10.1088/0029-5515/39/2/306. [12](#)
- [25] Mitsuru Kikuchi. The large tokamak JT-60: a history of the fight to achieve the Japanese fusion research mission. *The European Physical Journal H*, 577:551–577,

2018. ISSN 2102-6459. doi: 10.1140/epjh/e2018-90054-2. URL [{%}0A. 12](https://doi.org/10.1140/epjh/e2018-90054-2)
- [26] Daniel Clery. Panel backs ITER fusion project's new schedule, but balks at cost, 2016. URL <http://www.sciencemag.org/news/2016/04/updated-panel-backs-iter-fusion-project-s-new-schedule-balks-cost>. 13
- [27] Alberto Loarte. The ITER Research. In *FuseNet PhDevent*, Saint-Paul-les-Durance, 2018. 13
- [28] P.B. Snyder, R.J. Groebner, J.W. Hughes, T.H. Osborne, M. Beurskens, a.W. Leonard, H.R. Wilson, and X.Q. Xu. A first-principles predictive model of the pedestal height and width: development, testing and ITER optimization with the EPED model. *Nuclear Fusion*, 51(10):103016, oct 2011. ISSN 0029-5515. doi: 10.1088/0029-5515/51/10/103016. URL <http://stacks.iop.org/0029-5515/51/i=10/a=103016?key=crossref.334289a0972991b200871ad1b82fa95c>. 13, 143
- [29] U A Sheikh, M Dunne, L Frassinetti, P Blanchard, B P Duval, B Labit, A Merle, O Sauter, C Theiler, and C Tsui. Pedestal structure and energy confinement studies on TCV. *Plasma Physics and Controlled Fusion*, 61(1):014002, 2019. ISSN 0741-3335. doi: 10.1088/1361-6587/aae7bd. URL <http://stacks.iop.org/0741-3335/61/i=1/a=014002?key=crossref.2de9d13e138d0f2e61ccfdd4f7c06402>. 13
- [30] A. Merle, O. Sauter, and S. Yu Medvedev. Pedestal properties of H-modes with negative triangularity using the EPED-CH model. *Plasma Physics and Controlled Fusion*, 59(10), 2017. ISSN 13616587. doi: 10.1088/1361-6587/aa7aco. 13, 17
- [31] B Labit, H D E Olivera, R Maurizio, A Merle, P Molina, and U Sheikh. Plasma shape and fueling dependence on the small ELMs regime in TCV and AUG. In

- 27th IAEA Fusion Energy Conference, Gandhinagar, India, October 22-27th, pages 1-8, 2018. [13](#), [143](#)
- [32] Alexander N. Karpushov, René Chavan, Stefano Coda, Vladimir I. Davydenko, Frédéric Dolizy, Aleksandr N. Dranitchnikov, Basil P. Duval, Alexander A. Ivanov, Damien Fasel, Ambrogio Fasoli, Vyacheslav V. Kolmogorov, Pierre Lavanchy, Xavier Llobet, Blaise Marlétaz, Philippe Marmillod, Yves Martin, Antoine Merle, Albert Perez, Olivier Sauter, Ugo Siravo, Igor V. Shikhovtsev, Aleksey V. Sorokin, and Matthieu Toussaint. Neutral beam heating on the TCV tokamak. *Fusion Engineering and Design*, 123:468-472, 2017. ISSN 09203796. doi: 10.1016/j.fusengdes.2017.02.076. URL <https://doi.org/10.1016/j.fusengdes.2017.02.076>. [15](#), [18](#)
- [33] S Coda, E Asp, E Fable, T P Goodman, O Sauter, V S Udintsev, R Behn, M A Henderson, A Marinoni, G P Turri, C Zucca, and the TCV team. The physics of electron internal transport barriers in the TCV tokamak. *Nuclear Fusion*, 47(7): 714-720, 2007. ISSN 0029-5515. doi: 10.1088/0029-5515/47/7/023. [15](#), [17](#), [26](#)
- [34] F. Hofmann, O. Sauter, H. Reimerdes, I. Furno, and A. Pochelon. Experimental and theoretical stability limits of highly elongated tokamak plasmas. *Physical Review Letters*, 81(14):2918-2921, 1998. ISSN 10797114. doi: 10.1103/PhysRevLett.81.2918. [15](#), [16](#)
- [35] H. Reimerdes, I. Furno, F. Hofmann, An Martynov, A. Pochelon, and O. Sauter. Sawtooth behaviour in highly elongated TCV plasmas. *Plasma Physics and Controlled Fusion*, 48(11):1621-1632, 2006. ISSN 07413335. doi: 10.1088/0741-3335/48/11/004. [16](#)
- [36] Y Camenen, a Pochelon, R Behn, a Bottino, a Bortolon, S Coda, a Karpushov, O Sauter, G Zhuang, and the Tcv Team. Impact of plasma triangularity and collisionality on electron heat transport in TCV L-mode plasmas. *Nuclear Fusion*, 47: 510-516, 2007. ISSN 0029-5515. doi: 10.1088/0029-5515/47/7/002. [16](#)

- [37] A. Marinoni, S. Brunner, Y. Camenen, S. Coda, J. P. Graves, X. Lapillonne, A. Pochelon, O. Sauter, and L. Villard. The effect of plasma triangularity on turbulent transport: modeling TCV experiments by linear and non-linear gyrokinetic simulations. *Plasma Physics and Controlled Fusion*, 51(5):055016, 2009. ISSN 0741-3335. doi: 10.1088/0741-3335/51/5/055016. 16
- [38] M. Fontana, L. Porte, S. Coda, and O. Sauter. The effect of triangularity on fluctuations in a tokamak plasma. *Nuclear Fusion*, 58(2), 2018. ISSN 17414326. doi: 10.1088/1741-4326/aa98f4. 16
- [39] Zhouji Huang and Stefano Coda. Dependence of density fluctuations on shape and collisionality in positive- and negative-triangularity tokamak plasmas. *Plasma Physics and Controlled Fusion*, 61(1), 2019. ISSN 13616587. doi: 10.1088/1361-6587/aadb59. 16, 17
- [40] D D Ryutov, R H Cohen, T D Rognlien, and M V Umansky. A snowflake divertor: a possible solution to the power exhaust problem for tokamaks. *Plasma Physics and Controlled Fusion*, 54(12):124050, dec 2012. ISSN 0741-3335. doi: 10.1088/0741-3335/54/12/124050. URL <http://stacks.iop.org/0741-3335/54/i=12/a=124050?key=crossref.a7eacbb00a486fd2363245995abf09ea>. 17
- [41] F Piras, S Coda, B P Duval, B Labit, J Marki, S Yu Medvedev, J. M. Moret, A Pitzschke, and O Sauter. "Snowflake" H mode in a tokamak plasma. *Physical Review Letters*, 105(15):3–6, 2010. ISSN 00319007. doi: 10.1103/PhysRevLett.105.155003. 17
- [42] Silvano Gnesin. *Electron Cyclotron Heating and Suprathermal Electron Dynamics in the TCV Tokamak*. Phd thesis, Ecole Polytechnique Federale de Lausanne, 2011. 17
- [43] E. Mazzucato. Microwave reflectometry for magnetically confined plasmas. *Review of Scientific Instruments*, 69(6):2201, 1998. ISSN 00346748. doi: 10.1063/1.

1149121. URL <http://scitation.aip.org/content/aip/journal/rsi/69/6/10.1063/1.1149121>. 20, 23, 43, 81, 82, 83, 88, 95
- [44] Andreas Pitzschke. *Pedestal Characteristics and MHD Stability of H-Mode Plasmas in TCV*. Phd thesis, Ecole Polytechnique Federale de Lausanne, 2011. 20, 65
- [45] S Barry. *The extension of the FIR interferometer of TCV to a polarimeter and measurements of the Faraday rotation caused by the poloidal magnetic field*. PhD thesis, National University of Ireland, Cork, 1999. 20
- [46] L. W. Owen, T. Uckan, P. K. Mioduszewski, and A. Pospieszczyk. H α measurements and modeling of plasma confinement in TEXTOR with the ALT-II pump limiter. *Journal of Nuclear Materials*, 176-177(C):803–809, 1990. ISSN 00223115. doi: 10.1016/0022-3115(90)90147-F. 21
- [47] H. Zohm. Edge localized modes (ELMs). *Plasma Physics and Controlled Fusion*, 38(2):105–128, 1996. ISSN 07413335. doi: 10.1088/0741-3335/38/2/001. 22, 143
- [48] O. Sauter, S. Brunner, D. Kim, G. Merlo, R. Behn, Y. Camenen, S. Coda, B. P. Duval, L. Federspiel, T. P. Goodman, A. Karpushov, a. Merle, and Tcv Team. On the non-stiffness of edge transport in L-mode tokamak plasma(s). *Physics of Plasmas*, 21(5):055906, may 2014. ISSN 1070-664X. doi: 10.1063/1.4876612. URL <http://scitation.aip.org/content/aip/journal/pop/21/5/10.1063/1.4876612>. 22
- [49] H J Hartfuss and Thomas Geist. *Fusion Plasma Diagnostics with mm-Waves - An Introduction*. Wiley-VCH - Physics Textbooks, 2013. 23, 25, 26, 27, 29, 43, 57, 96, 138, 161
- [50] Ambrogio Fasoli. *Plasma Physics II Kinetic theory of plasmas*. 2011. 23
- [51] Francis Chen. *Introduction to plasma physics and controlled fusion*. Plenum Press, New York, first edition, 1984. ISBN 1475704615. 23

- [52] V.L. Ginzburg. *Propagation of Electromagnetic Waves in Plasma*. Gordon & Breach Science Publishers Ltd, 1961. 28
- [53] A. Zabolotsky and H. Weisen. Density profile peaking in the presence of ECRH heating in TCV. *Plasma Physics and Controlled Fusion*, 48(3):369–383, 2006. ISSN 07413335. doi: 10.1088/0741-3335/48/3/003. 30
- [54] William Elmore and Mark Heald. *Physics of Waves*. McGraw-Hill Inc., New York, NY, first edit edition, 1969. 31, 32, 58
- [55] E. Poli, A. G. Peeters, and G. V. Pereverzev. TORBEAM, a beam tracing code for electron-cyclotron waves in tokamak plasmas. *Computer Physics Communications*, 2001. ISSN 00104655. doi: 10.1016/S0010-4655(01)00146-1. 32
- [56] I.H. Hutchinson. *Principles of Plasma Diagnostics*. Cambridge University Press, New York, 2nd edition, 2002. 33, 136
- [57] P. Varela, M. E. Manso, A. Silva, J. Fernandes, and F. Silva. Initialization of plasma density profiles from reflectometry. *Review of Scientific Instruments*, 66(10):4937–4942, 1995. ISSN 00346748. doi: 10.1063/1.1146178. 34, 136, 138
- [58] N. Vianello, C. Tsui, C. Theiler, S. Allan, J. Boedo, B. Labit, H. Reimerdes, K. Verhaegh, W. A.J. Vijvers, N. Walkden, S. Costea, J. Kovacic, C. Ionita, V. Naulin, A. H. Nielsen, J. Juul Rasmussen, B. Schneider, R. Schrittwieser, M. Spolaore, D. Carralero, J. Madsen, B. Lipschultz, and F. Militello. Modification of SOL profiles and fluctuations with line-average density and divertor flux expansion in TCV. *Nuclear Fusion*, 57(11), 2017. ISSN 17414326. doi: 10.1088/1741-4326/aa7db3. 34, 37, 58, 136, 138, 140
- [59] C Laviron and AJH Donné. Reflectometry techniques for density profile measurements on fusion plasmas. *Plasma Physics and Controlled Fusion*, 38(7), 1996. URL <http://iopscience.iop.org/0741-3335/38/7/002>. 34, 81, 85, 86, 88, 89, 95, 97, 101, 102, 105, 155

- [60] H. Bottollier-Curtet and G. Ichtschenko. Microwave reflectometry with the extraordinary mode on tokamaks: Determination of the electron density profile of Petula-B. *Review of Scientific Instruments*, 58(4):539–546, 1987. ISSN 00346748. doi: 10.1063/1.1139266. 34, 35, 139
- [61] D. A. Shelukhin, V. A. Vershkov, G. F. Subbotin, D. V. Sarychev, A. A. Petrov, V. G. Petrov, M. M. Sokolov, and G. B. Igonkina. Measurements of electron density profile by frequency modulated continuous wave reflectometer in the T-10 tokamak using high magnetic field side probing and extraordinary mode lower cutoff. *Review of Scientific Instruments*, 89(9), 2018. ISSN 10897623. doi: 10.1063/1.5039151. 34, 156
- [62] R. B. Morales, S. Hacquin, S. Heuraux, and R. Sabot. New density profile reconstruction methods in X-mode reflectometry. *Review of Scientific Instruments*, 88(4), 2017. ISSN 10897623. doi: 10.1063/1.4979513. 34, 156
- [63] Cornwall Lau, Greg Hanson, John Wilgen, Yijun Lin, and Steve Wukitch. Scrape-off layer reflectometer for Alcator C-Mod. *Review of Scientific Instruments*, 81(10):1–4, 2010. ISSN 00346748. doi: 10.1063/1.3491225. 36
- [64] Richard Schubert. *Randschichtreflektometrie hochfrequenzgeheizter Plasmen an ASDEX*. PhD thesis, Technical University Munich, 1991. 36
- [65] H. Tennekes and J.L. Lumley. *A First Course in Turbulence*. The Massachusetts Institute of Technology, Cambridge, MA, 1972. ISBN 0262200198. 37
- [66] ME Manso, P Varela, and I Nunes. Reflectometry in conventional and advanced plasma scenarios on ASDEX Upgrade and perspectives for ITER. *Plasma physics and ...*, 73, 2001. URL <http://iopscience.iop.org/0741-3335/43/12A/306>. 38, 46, 105, 128
- [67] M Kong, Blanken T., F. Felici, Galperti C., Maljaars E., Sauter O., Vu T., Carpanese F., Merle A., J.-M. Moret, F Pesamosca, E Poli, M Reich, and A A

- Teplukhina. Control of NTMs and integrated multi-actuator plasma control on TCV. *Nuclear Fusion*, Accepted, 2019. 38
- [68] Gabriele Merlo. *Flux-tube and global grid-based gyrokinetic simulations of plasma microturbulence and comparisons with experimental TCV measurements PAR*. Phd thesis, Ecole Polytechnique Federale de Lausanne, 2016. 38, 39
- [69] W. Horton. Drift waves and transport. *Reviews of Modern Physics*, 71(3):735–778, 1999. ISSN 0034-6861. doi: 10.1103/RevModPhys.71.735. 39, 41
- [70] Hugo Arnichand. *Identification of trapped electron modes in frequency fluctuation spectra of fusion plasmas Doctoral thesis Identification of Trapped Electron Modes in Frequency Fluctuation Spectra of fusion plasmas*. PhD thesis, Aix Marseille Université; Ugent; CEA Cadarache; Forschungszentrum Jülich, 2015. 39
- [71] C. Bourdelle, X. Garbet, R. Singh, and L. Schmitz. New glance at resistive ballooning modes at the edge of tokamak plasmas. *Plasma Physics and Controlled Fusion*, 54(11), 2012. ISSN 07413335. doi: 10.1088/0741-3335/54/11/115003. 39
- [72] Thibaut Vernay. *Collisions in Global Gyrokinetic Simulations of Tokamak Plasmas using the Delta-f Particle-In-Cell Approach: Neoclassical Physics and Turbulent Transport*. PhD thesis, Ecole Polytechnique Federale de Lausanne, 2013. 40, 41
- [73] Jiquan Li and Y Kishimoto. Role of collisionless trapped electron mode in tokamak plasmas with electron internal transport barrier. *Plasma Physics and Controlled Fusion*, 44(5A):A479–A485, 2002. ISSN 07413335. doi: 10.1088/0741-3335/44/5A/353. URL <http://stacks.iop.org/0741-3335/44/i=5A/a=353?key=crossref.5eeaeb9b105e0a560b7e92186886bcfe>. 40
- [74] N Bretz. One dimensional modeling of the wavelength sensitivity, localization and correlation in reflectometry measurements of plasma fluctuations. *Phys. Fluids B*, 4(8):2414–2422, 1992. ISSN 08998221. doi: 10.1063/1.860210. 41, 45, 103
- [75] P H Diamond, S-I Itoh, K Itoh, and T S Hahm. Zonal flows in plasma—A review. *Plasma Physics and Controlled Fusion*, 47(5):R35–

- R161, may 2005. ISSN 0741-3335. doi: 10.1088/0741-3335/47/5/R01. URL <http://stacks.iop.org/0741-3335/47/i=5/a=R01?key=crossref.a4dceee0ba00403ce427a135a3569ce5>. 42, 130
- [76] G D Conway, B Scott, J Schirmer, M Reich, A Kendl, and the Asdex Upgrade Team. Direct measurement of zonal flows and geodesic acoustic mode oscillations in ASDEX Upgrade using Doppler reflectometry. *Plasma Physics and Controlled Fusion*, 47(8):1165–1185, 2005. ISSN 0741-3335. doi: 10.1088/0741-3335/47/8/003. 42
- [77] C.A. de Meijere, S. Coda, Z. Huang, L. Vermare, T. Vernay, V. Vuille, S. Brunner, J. Dominski, P. Hennequin, A. Krämer-Flecken, G. Merlo, L. Porte, and L. Villard. Complete multi-field characterization of the geodesic acoustic mode in the TCV tokamak. *Plasma Phys. Contr. Fusion*, 56(7):072001, 2014. ISSN 13616587. doi: 10.1088/0741-3335/56/7/072001. 42, 51
- [78] Zhouji Huang, Stefano Coda, Gabriele Merlo, Stephan Brunner, Laurent Villard, Benoit Labit, and Christian Theiler. Experimental observations of modes with geodesic acoustic character from the core to the edge in the TCV tokamak. *Plasma Physics and Controlled Fusion*, 60(3):034007, 2018. ISSN 0741-3335. doi: 10.1088/1361-6587/aaa71d. 42
- [79] E Mazzucato and R Nazikian. Microwave reflectometry for the study of density fluctuations in tokamak plasmas. *Plasma Physics and Controlled Fusion*, 33(3):261–274, 1991. ISSN 0741-3335. doi: 10.1088/0741-3335/33/3/009. URL <http://stacks.iop.org/0741-3335/33/i=3/a=009?key=crossref.eedabb360cb1da6710de1580903e0d46>. 44
- [80] E Holzhauer and M Hirsch. Theoretical and experimental investigation of the phase-runaway in microwave reflectometry. *Plasma physics and ...*, 1869, 1998. URL <http://iopscience.iop.org/0741-3335/40/11/004>. 45, 105
- [81] G. D. Conway. Scattering of reflectometer signals from rippled surfaces. *Review of Scientific Instruments*, 64(10):2782–2788, 1993. ISSN 00346748. doi: 10.1063/1.

1144417. URL <http://scitation.aip.org/content/aip/journal/rsi/64/10/10.1063/1.1144417>. 45, 83, 102, 122, 123
- [82] G D Conway, L Schott, and A Hirose. Comparison of reflectometer fluctuation measurements from experiment and two-dimensional numerical simulation. *Review of Scientific Instruments*, 67(11):3861, 1996. ISSN 00346748. doi: 10.1063/1.1147287. URL <http://scitation.aip.org/content/aip/journal/rsi/67/11/10.1063/1.1147287>. 45
- [83] D Carralero, P Manz, G Birkenmeier, M Brix, M Groth, H W Müller, U Stroth, N Vianello, E Wolfrum, Asdex Upgrade, J E T Contributors, and Eurofusion M S T Team. Experimental Validation of a Filament Transport Model in Turbulent Magnetized Plasmas. *Physical Review Letters*, 215002(November):1–5, 2015. doi: 10.1103/PhysRevLett.115.215002. 45
- [84] G D Conway. Effects of reflectometer asymmetries on fluctuation measurements. *Plasma Physics and Controlled Fusion*, 41(1):65–92, 1999. ISSN 0741-3335. doi: 10.1088/0741-3335/41/1/005. URL <http://stacks.iop.org/0741-3335/41/i=1/a=005?key=crossref.293a908ed5b880187c2a713f4ac9c65e>. 46
- [85] L.G. Bruskin, A. Mase, and Tamano T. Two-dimensional microwave scattering by fluctuations of plasma density and magnetic field. *Plasma Phys. Contr. Fusion*, 37: 255–269, 1995. 46
- [86] E. Mazzucato. Small-scale density fluctuations in the adiabatic toroidal compressor. *Physical Review Letters*, 1976. ISSN 00319007. doi: 10.1103/PhysRevLett.36. 792. 46
- [87] M. Hirsch, E. Holzhauer, J. Baldzuhn, and B. Kurzan. Doppler reflectometry for the investigation of propagating density perturbations. *Rev. Sci. Instrum.*, 72(1):324, 2001. ISSN 00346748. doi: 10.1063/1.1308998. URL <http://scitation.aip.org/content/aip/journal/rsi/72/1/10.1063/1.1308998>. 46, 69, 80

- [88] C Honoré, P Hennequin, A Truc, and A Quéméneur. Quasi-optical Gaussian beam tracing to evaluate Doppler backscattering conditions. *Nuclear Fusion*, 46(9):S809–S815, 2006. ISSN 0029-5515. doi: 10.1088/0029-5515/46/9/S16. URL <http://stacks.iop.org/0029-5515/46/i=9/a=S16?key=crossref.1c36b0f3b15464d5f440c3073cee0681>. 47, 59
- [89] G D Conway, J Schirmer, S Kluge, W Suttrop, E Holzhauser, and the Asdex Upgrade Team. Plasma rotation profile measurements using Doppler reflectometry. *Plasma Phys. Contr. Fusion*, 46(6):951–970, jun 2004. ISSN 0741-3335. doi: 10.1088/0741-3335/46/6/003. URL <http://stacks.iop.org/0741-3335/46/i=6/a=003?key=crossref.bc56d3ab826fb70cbd11ae3bdd7445a1>. 47, 48, 51, 69, 155
- [90] E Z Gusakov and A Yu Popov. Non-linear theory of fluctuation reflectometry. *Plasma Phys. Contr. Fusion*, 44:2327–2337, 2002. ISSN 07413335. doi: 10.1088/0741-3335/44/11/303. 48
- [91] E Blanco and T Estrada. Study of Doppler reflectometry capability to determine the perpendicular velocity and the k-spectrum of the density fluctuations using a 2D full-wave code. *Plasma Physics and Controlled Fusion*, 50(9):095011, sep 2008. ISSN 0741-3335. doi: 10.1088/0741-3335/50/9/095011. URL <http://stacks.iop.org/0741-3335/50/i=9/a=095011?key=crossref.6f3c473b3ab9ffe73a01d2be7ff4c5ae>. 48
- [92] C Lechte, G D Conway, T Görler, and C Tröster-Schmid. X mode Doppler reflectometry k -spectral measurements in ASDEX Upgrade: experiments and simulations. *Plasma Physics and Controlled Fusion*, 59(7):075006, 2017. ISSN 0741-3335. doi: 10.1088/1361-6587/aa6fe7. URL <http://stacks.iop.org/0741-3335/59/i=7/a=075006?key=crossref.027409da289f3e3798f8159cff3247ad>. 48, 78
- [93] P. Hennequin, C. Honoré, A. Truc, A. Quéméneur, N. Lemoine, J. M. Chareau, and R. Sabot. Doppier backscattering system for measuring fluctuations and their

- perpendicular velocity on Tore Supra. *Rev. Sci. Instrum.*, 75(10 II):3881–3883, 2004. ISSN 00346748. doi: 10.1063/1.1787920. 48, 51
- [94] T. Happel, T. Estrada, E. Blanco, V. Tribaldos, A. Cappa, and A. Bustos. Doppler reflectometer system in the stellarator TJ-II. *Rev. Sci. Instrum.*, 80(7), 2009. ISSN 00346748. doi: 10.1063/1.3160106. 48, 61
- [95] J C Hillesheim, W a Peebles, T L Rhodes, L Schmitz, T a Carter, P-a Gourdain, and G Wang. A multichannel, frequency-modulated, tunable Doppler backscattering and reflectometry system. *Rev. Sci. Instrum.*, 80(8):083507, 2009. ISSN 1089-7623. doi: 10.1063/1.3205449. URL <http://www.ncbi.nlm.nih.gov/pubmed/19725655>. 48, 51, 61
- [96] J. C. Hillesheim, N. A. Crocker, W. A. Peebles, H. Meyer, A. Meakins, A. R. Field, D. Dunai, M. Carr, and N. Hawkes. Doppler backscattering for spherical tokamaks and measurement of high-k density fluctuation wavenumber spectrum in MAST. *Nuclear Fusion*, 55(7), 2015. ISSN 17414326. doi: 10.1088/0029-5515/55/7/073024. 48
- [97] M Hirsch and E Holzhauer. Doppler reflectometry with optimized temporal resolution for the measurement of turbulence and its propagation velocity. *Plasma Physics and Controlled Fusion*, 46:593–609, 2004. ISSN 0741-3335. doi: 10.1088/0741-3335/46/4/002. 49
- [98] Fochi A. Conway, G.D., Lechte C. Assessment of Doppler reflectometry accuracy using full-wave codes with comparison to beam-tracing and analytic expressions. In *12th International Reflectometry Workshop*, volume 2015, pages 1–14, 2015. 49, 57
- [99] National Instruments. Field Wiring and Noise Considerations for Analog Signals, 2016. URL <http://www.ni.com/white-paper/3344/en/{#}toc5>. 54
- [100] J Schirmer, G D Conway, H Zohm, W Suttrop, E Holzhauer, and Asdex Upgrade Team. Radial Correlation Doppler Reflectometry on ASDEX Upgrade. In *7th In-*

- ternational Reflectometry Workshop (IRW7) for fusion plasma diagnostics*, Garching, 2005. Max-Planck-Institut für Plasmaphysik. 54, 56
- [101] W. A. Peebles, T. L. Rhodes, J. C. Hillesheim, L. Zeng, and C. Wannberg. A novel, multichannel, comb-frequency Doppler backscatter system. *Review of Scientific Instruments*, 81(10), 2010. ISSN 00346748. doi: 10.1063/1.3464266. 54, 56, 57
- [102] R. Soga, T. Tokuzawa, K. Y. Watanabe, K. Tanaka, I. Yamada, S. Inagaki, and N. Kasuya. Developments of frequency comb microwave reflectometer for the interchange mode observations in LHD plasma. *Journal of Instrumentation*, 11(2), 2016. ISSN 17480221. doi: 10.1088/1748-0221/11/02/C02009. 54, 56
- [103] David M. Pozar. *Microwave Engineering*. Addison-Wesley Publishing Company Inc., Reading, Massachusetts, 1993. 55, 82, 93, 162
- [104] F Hofmann and G Tonetti. Tokamak equilibrium reconstruction using Faraday rotation measurements. *Nucl. Fusion*, 28, 1988. ISSN 0029-5515. doi: 10.1088/0029-5515/28/10/014. URL <http://iopscience.iop.org/0029-5515/28/10/014>. 58
- [105] Cedric Tsui. Private communication, 2019. 58
- [106] O. E. Garcia, J. Horacek, R. A. Pitts, A. H. Nielsen, W. Fundamenski, V. Naulin, and J. Juul Rasmussen. Fluctuations and transport in the TCV scrape-off layer. *Nuclear Fusion*, 47(7):667–676, 2007. ISSN 00295515. doi: 10.1088/0029-5515/47/7/017. 58, 136
- [107] J. M. Moret. A software package to manipulate space dependencies and geometry in magnetic confinement fusion. *Review of Scientific Instruments*, 76(7), 2005. ISSN 00346748. doi: 10.1063/1.1946608. 58
- [108] G. D. Conway, E. Poli, T. Happel, and the ASDEX Upgrade Team. Interaction of Mean and Oscillating Plasma Flows Across Confinement Mode Transitions. *Plasma and Fusion Research*, 5:S2005–S2005, 2010. ISSN 1880-6821. doi: 10.1585/

- pfr.5.S2005. URL <http://www.jspf.or.jp/PFR/PFR{ }articles/pfr2010S2/pfr2010{ }05-S2005.html{ }0Ahttp://joi.jlc.jst.go.jp/JST.JSTAGE/pfr/5.S2005?from=CrossRef>. 59
- [109] P. D. Welch. The Use of Fast Fourier Transform for the Estimation of Power Spectra: A Method Based on Time Averaging Over Short, Modified Periodograms. *IEEE Transactions on Audio and Electroacoustics*, 15(2):70–73, 1967. ISSN 00189278. doi: 10.1109/TAU.1967.1161901. 61, 62
- [110] J. S. Bendat and Piersol A. G. *Random Data: Analysis and Measurement Procedures*. John Wiley and Sons, Inc., New York, NY, first edition, 1971. 61
- [111] W.S. Cleveland. Robust Locally Weighted Regression and Smoothing Scatterplots. *Journal of the American Statistical Association*, 74(368), 1979. 62
- [112] Adelchi Azzalini. *The Skew-Normal and Related Families*. Cambridge University Press, first edition, 2013. ISBN 9781107029279. 63, 64
- [113] Giorgia Dellaferrera. Covariance analysis and error measurement characterization of Tokamak equilibrium reconstruction. Technical report, Swiss Plasma Centre. Ecole Polytechnique Federale de Lausanne, Lausanne, Switzerland, 2018. 66, 75, 138
- [114] Claudio Marini. *Poloidal CX visible light plasma rotation diagnostics in TCV*. Phd thesis, Ecole Polytechnique Federale de Lausanne, 2017. URL <https://tinyurl.com/ya8qwu7m>. 69
- [115] Federico Felici. ECPOL : equations and Matlab tools for EC wave reflection and polarization calculations. Technical report, LRP 01/2012, Swiss Plasma Centre, EPFL, Lausanne, Switzerland, 2012. 71, 72, 73, 165
- [116] Max Born and Emil Wolf. *Principles of Optics*. Cambridge University Press, Cambridge, UK, 7th edition, 1999. 71

- [117] A. E. White, W. A. Peebles, T. L. Rhodes, C. H. Holland, G. Wang, L. Schmitz, T. A. Carter, J. C. Hillesheim, E. J. Doyle, L. Zeng, G. R. McKee, G. M. Staebler, R. E. Waltz, J. C. Deboo, C. C. Petty, and K. H. Burrell. Measurements of the cross-phase angle between density and electron temperature fluctuations and comparison with gyrokinetic simulations. *Physics of Plasmas*, 17(5), 2010. ISSN 1070664X. doi: 10.1063/1.3323084. 79
- [118] EJ Doyle, KW Kim, and JH Lee. Reflectometry applications to ITER. *Diagnostics for Experimental Thermonuclear Fusion Reactors*, pages 117–132, 1996. URL <http://link.springer.com/chapter/10.1007/978-1-4613-0369-5{ }12>. 81, 86, 91, 95, 96, 97, 98, 99, 100, 102, 105, 110, 154, 157
- [119] P Varela, M.E Manso, a Silva, the Cfn Team, and the Asdex Upgrade Team. Review of data processing techniques for density profile evaluation from broadband FM-CW reflectometry on ASDEX Upgrade. *Nuclear Fusion*, 46(9):S693–S707, sep 2006. ISSN 0029-5515. doi: 10.1088/0029-5515/46/9/S05. URL <http://stacks.iop.org/0029-5515/46/i=9/a=S05?key=crossref.ad84a6a5a6b1a3760bec0a26fddc76db>. 85, 106
- [120] K. W. Kim, E. J. Doyle, T. L. Rhodes, W. a. Peebles, C. L. Rettig, and N. C. Luhmann, Jr. Development of a fast solid-state high-resolution density profile reflectometer system on the DIII-D tokamak. *Review of Scientific Instruments*, 68(1):466, 1997. ISSN 00346748. doi: 10.1063/1.1147607. URL <http://scitation.aip.org/content/aip/journal/rsi/68/1/10.1063/1.1147607>. 85
- [121] F. Clairet, C. Bottereau, A. Medvedeva, D. Molina, G. D. Conway, A. Silva, and U. Stroth. 1 ÎJ S Broadband Frequency Sweeping Reflectometry for Plasma Density and Fluctuation Profile Measurements. *Review of Scientific Instruments*, 88(11), 2017. ISSN 10897623. doi: 10.1063/1.4991789. 85, 86, 102, 105, 107, 109, 111, 115

- [122] Jean-Claude Giacalone, Roland Sabot, Frédéric Clairet, Christine Bottereau, and Diego Molina. Measurement of the density of magnetized fusion plasma using microwave reflectometry. *International Journal of Microwave and Wireless Technologies*, 1(06):505, jan 2010. ISSN 1759-0787. doi: 10.1017/S175907870999078X. URL http://www.journals.cambridge.org/abstract/{_}S175907870999078X. 86
- [123] Amanda Eileen Hubbard. Measurement of electron density on JET by microwave reflectometry. 1987. 86, 107
- [124] E. De La Luna, J. Sanchez, V. Zhuravlev, I. García-Cortés, G. R. Hanson, J. B. Wilgen, J. H. Harris, J. Dunlap, R. Kaita, B. Leblanc, G. R. Tynan, L. Schmitz, and L. Blush. First results with amplitude modulation reflectometry on the PBX-M tokamak. *Review of Scientific Instruments*, 66(1):403–405, 1995. ISSN 00346748. doi: 10.1063/1.1146540. 87, 88, 100, 102, 106, 107
- [125] M. Hirsch, H.-J. Hartfuss, T. Geist, and E. de la Luna. Amplitude modulated heterodyne reflectometer for density profile and density fluctuation profile measurements at W7-AS. *Review of Scientific Instruments*, 67(5):1807, 1996. ISSN 00346748. doi: 10.1063/1.1146978. URL <http://link.aip.org/link/RSINAK/v67/i5/p1807/s1{&}Agg=doi>. 87, 88, 100, 107
- [126] S. H. Heijnen. *Pulsed Radar Reflectometry - A new approach to measure electron densities in thermonuclear plasmas*. PhD thesis, Utrecht University, 1995. 88, 89, 90, 91, 97, 98, 99, 104, 108, 110, 127, 154
- [127] V F Shevchenko, A. A. Petrov, and V G Petrov. Pulse radar reflectometry for fusion plasma diagnostics. *International Journal of Infrared and Millimeter Waves*, 14(9):1755–1768, 1993. ISSN 0195-9271. doi: 10.1007/BF02101330. 89, 104, 110
- [128] T. Tokuzawa, K. Kawahata, R. O. Pavlichenko, K. Tanaka, and a. Ejiri. Pulsed radar reflectometry on the LHD. *Review of Scientific Instruments*, 72(1):328, 2001. ISSN 00346748. doi: 10.1063/1.1326900. URL <http://scitation.aip.org/content/aip/journal/rsi/72/1/10.1063/1.1326900>. 89, 108

- [129] Walsh M.J. Shevchenko V. F. First results from the small tight aspect ratio tokamak multifrequency pulse radar reflectometer. *Review of Scientific Instruments*, 68(5):2040–2045, 1997. doi: 10.1063/1.1148075. 90, 99
- [130] J. C. van Gorkom, M. J. van de Pol, and a. J. H. Donné. The ten-channel pulsed radar reflectometer at the TEXTOR-94 tokamak. *Review of Scientific Instruments*, 72(1):336, 2001. ISSN 00346748. doi: 10.1063/1.1316747. URL <http://scitation.aip.org/content/aip/journal/rsi/72/1/10.1063/1.1316747>. 90, 99, 102, 108, 154
- [131] N Bretz, S Coda, P H Diamond, S-I Itoh, K Itoh, T S Hahm, S Haquin, S Heuraux, I Boucher, C Fanack, G Leclert, W. Horton, Keilhacker, C Laviron, J H Donne, M E Manso, J Sanchez, A. Marinoni, S Coda, R Chavan, G Pochon, Young-Su Roh, F. Wagner, and Christian Theiler. Drift. *Plasma Physics and Controlled Fusion*, 22(3):20–26, dec 1999. ISSN 0741-3335. doi: 10.1088/0741-3335/49/12B/S01. URL http://stacks.iop.org/0741-3335/49/i=12B/a=S01?key=crossref.4b1659cd2933e3e40b713717cd852006http://infoscience.epfl.ch/record/202710/files/iaea{__}14.pdf. 92, 155
- [132] C. W. Domier, E. Chung, E. J. Doyle, H.-X. L. Liu, a. Lapidus, N. C. Luhmann, W. a. Peebles, X.-H. Qin, T. L. Rhodes, and L. Sjogren. Development of technology and techniques for reflectometry. *Review of Scientific Instruments*, 63(10):4666, 1992. ISSN 00346748. doi: 10.1063/1.1143657. URL <http://scitation.aip.org/content/aip/journal/rsi/63/10/10.1063/1.1143657>. 92
- [133] S Kubota, T Onuma, and M Katoh. Initial measurements from an ultrashort-pulse reflectometer on GAMMA 10. *Japanese journal of...*, 202:0–4, 1999. URL <http://iopscience.iop.org/1347-4065/38/2B/L202>. 92
- [134] T Tokuzawa, T Kaneba, K Kawahata, K Tanaka, S Sakakibara, S Inagaki,

- N Tamura, and Y Nagayama. Microwave Reflectometer for Density Profile and Fluctuation Measurements on LHD. In *31st EPS Conference on Plasma Physics*, volume 28, pages 2–5, London, 2004. European Physical Society. 92, 94, 154
- [135] Takahiro Kaneba, Tokuzawa Tokihiko, Okamoto Atsushi, and Yoshimura Shinji. Application of Ultrashort-Pulse Reflectometer to a HYPER-I Device Plasma. *Journal of Plasma Fusion Research*, 6:417–420, 2004. 92, 93
- [136] Young-Su Roh. Study on the Chirped Waveform of the USPR Pulse using the Impulse Response of a Waveguide. *Journal of the Korean Institute of Illuminating and Electrical Installation Engineers*, 24(3):20–26, 2010. ISSN 1229-4691. doi: 10.5207/JIEIE.2010.24.3.020. 93
- [137] Y. Roh, C. W. Domier, and N. C. Luhmann. Ultrashort pulse reflectometry for electron density profile measurements on SSPX. *Review of Scientific Instruments*, 72(1):332, 2001. ISSN 00346748. doi: 10.1063/1.1308999. URL <http://scitation.aip.org/content/aip/journal/rsi/72/1/10.1063/1.1308999>. 93, 99, 108, 154
- [138] Simon Kingsley and Shaun Quegan. *Understanding RADAR Systems*. McGraw-Hill Book Company. London, 1992. 95, 97
- [139] R Sabot, a Sirinelli, J.-M Chareau, and J.-C Giacalone. A dual source D-band reflectometer for density profile and fluctuations measurements in Tore-Supra. *Nuclear Fusion*, 46(9):S685–S692, sep 2006. ISSN 0029-5515. doi: 10.1088/0029-5515/46/9/S04. URL <http://stacks.iop.org/0029-5515/46/i=9/a=S04?key=crossref.52b2e1413fe39e5f968d6a7727e087e9>. 95, 96
- [140] G. Wang, L. Zeng, E. J. Doyle, T. L. Rhodes, and W. a. Peebles. Improved reflectometer electron density profile measurements on DIII-D. *Review of Scientific Instruments*, 74(3):1525, 2003. ISSN 00346748. doi: 10.1063/1.1527251. URL <http://scitation.aip.org/content/aip/journal/rsi/74/3/10.1063/1.1527251>. 96

- [141] Merrill Skolnik. *Introduction to RADAR systems*. McGraw-Hill Book Company. London, internatio edition, 1981. ISBN 0070579091. 97, 101
- [142] T. Tokuzawa, K. Kawahata, K. Tanaka, and the Lhd Experimental Group. Electron density profile measurement using Ka -band microwave impulse radar reflectometer on LHD. *Nuclear Fusion*, 46(9): S670–S676, sep 2006. ISSN 0029-5515. doi: 10.1088/0029-5515/46/9/S02. URL <http://stacks.iop.org/0029-5515/46/i=9/a=S02?key=crossref.163917597807eaf2d18d21a2d1675e93>. 99, 102
- [143] Bruce I. Cohen, Thomas B. Kaiser, and John C. Garrison. One- and two-dimensional simulations of ultra-short-pulse reflectometry. *Review of Scientific Instruments*, 68(2):1238–1243, 1997. ISSN 00346748. doi: 10.1063/1.1147896. 104, 105, 108, 110, 111, 154, 155
- [144] Vladimir F. Shevchenko. Effect of Density Fluctuations on the Pulse Reflectometry of a Tokamak Plasma. *Plasma Physics Reports*, 23(2):151–157, 1996. ISSN 1063780X. 104, 111, 127
- [145] Vladimir F. Shevchenko. Status and Prospects of Pulse Radar Reflectometry on the START tokamak. *Diagnostics for Experimental Thermonuclear Fusion Reactors*, 2, 1998. 104, 105, 127, 154
- [146] E. J. Doyle, T. Lehecka, N. C. Luhmann, and W. A. Peebles. X-mode broadband reflectometric density profile measurements on DIII-D. *Review of Scientific Instruments*, 61(10):2896–2898, 1990. ISSN 00346748. doi: 10.1063/1.1141971. 105
- [147] Zhouji Huang. *Experimental study of plasma turbulence in the TCV tokamak*. Phd thesis, Ecole Polytechnique Federale de Lausanne, 2017. 105
- [148] T. Tokuzawa, K. Kawahata, K. Tanaka, Y. Nagayama, LHD Experimental Group, T. Kaneba, and a. Ejiri. X-mode pulsed radar reflectometer for density fluctuation measurements on LHD. *Review of Scientific Instruments*, 74(3):1506, 2003. ISSN

00346748. doi: 10.1063/1.1537880. URL <http://scitation.aip.org/content/aip/journal/rsi/74/3/10.1063/1.1537880>. 110, 111
- [149] AJH Donné, SH Heijnen, and CAJ Hugenholtz. Pulsed radar reflectometry and prospects for fluctuation measurements. *Fusion engineering and design*, 35:73–80, 1997. URL <http://www.sciencedirect.com/science/article/pii/S0920379696006710>. 110, 124
- [150] S. Hacquin, S. Heuraux, M. Colin, and G. Leclert. Use of dispersive effects for density profile reconstruction from pulse radar reflectometry measurements alone. *Plasma Physics and Controlled Fusion*, 42(3):347–358, 2000. ISSN 07413335. doi: 10.1088/0741-3335/42/3/311. 110, 124
- [151] S. Hacquin, S. Heuraux, M. Colin, and G. Leclert. Fast computations of wave propagation in an inhomogeneous plasma by a pulse compression method. *Journal of Computational Physics*, 174(1):1–11, 2001. ISSN 00219991. doi: 10.1006/jcph.2001.6867. 111
- [152] D.R. Bolton, Cruickshank P.A.S., D.A. Robertson, and G.M. Smith. Sub-nanosecond coherent pulse generation at millimetre-wave frequencies. *Electronic Letters*, 43(6), 2007. ISSN 19758359. doi: 10.1049/el. 111
- [153] P. Molina Cabrera, S. Coda, L. Porte, N. Offeddu, P. Lavanchy, M. Silva, and M. Toussaint. V-band Doppler backscattering diagnostic in the TCV tokamak. *Review of Scientific Instruments*, 89(8), 2018. ISSN 10897623. doi: 10.1063/1.5007433. 112, 116, 136, 138
- [154] Wolfgang Becker. The bh TCSPC Handbook. Technical Report 7th edition, Becker and Hickl GmbH., Berlin, 2010. URL <http://www.becker-hickl.de/handbook.htm>. 115, 120
- [155] Caen. Time Measurements with CAEN Waveform Digitizers. Technical report, CAEN, Viareggio, 2015. 119

- [156] C Fanack, I Boucher, F Clairet, S Heuraux, G Leclert, and X L Zou. Ordinary-mode reflectometry: modification of the scattering and cut-off responses due to the shape of localized density fluctuations. *Plasma Physics and Controlled Fusion*, 38(11):1915–1930, 1999. ISSN 0741-3335. doi: 10.1088/0741-3335/38/11/004. [127](#)
- [157] N. R. Lomb. Least-squares frequency analysis of unequally spaced data. *Astrophysics and Space Science*, 39(2):447–462, 1976. ISSN 0004640X. doi: 10.1007/BF00648343. [129](#)
- [158] J.-M. Moret, F. Buhlmann, and G. Tonetti. Fast single loop diamagnetic measurements on the TCV tokamak. *Review of Scientific Instruments*, 74(11):4634–4643, 2003. ISSN 0034-6748. doi: 10.1063/1.1614856. [130](#)
- [159] A. Klein, H. Carfantan, D. Testa, A. Fasoli, and J. Snipes. A sparsity-based method for the analysis of magnetic fluctuations in unevenly-spaced Mirnov coils. *Plasma Physics and Controlled Fusion*, 50(12):1–17, 2008. ISSN 07413335. doi: 10.1088/0741-3335/50/12/125005. [130](#)
- [160] D. Testa, A. Corne, G. Farine, C. Jacq, T. Maeder, and Matthieu Toussaint. 3D, LTCC-type, high-frequency magnetic sensors for the TCV Tokamak. *Fusion Engineering and Design*, 96-97(2):989–992, 2015. ISSN 09203796. doi: 10.1016/j.fusengdes.2015.05.065. [130](#)
- [161] C. A. De Meijere, S. Coda, Z. Huang, L. Vermare, T. Vernay, V. Vuille, S. Brunner, J. Dominski, P. Hennequin, A. Krämer-Flecken, G. Merlo, L. Porte, and L. Villard. Complete multi-field characterization of the geodesic acoustic mode in the TCV tokamak. *Plasma Physics and Controlled Fusion*, 56(7), 2014. ISSN 13616587. doi: 10.1088/0741-3335/56/7/072001. [131](#)
- [162] A. Diallo, J. W. Hughes, M. Greenwald, B. Labombard, E. Davis, S. G. Baek, C. Theiler, P. Snyder, J. Canik, J. Walk, T. Golfinopoulos, J. Terry, M. Churchill, A. Hubbard, M. Porkolab, L. Delgado-Aparicio, M. L. Reinke, and A. White. Observation of edge instability limiting the pedestal growth in Tokamak plas-

- mas. *Physical Review Letters*, 112(11):1–5, 2014. ISSN 00319007. doi: 10.1103/PhysRevLett.112.115001. 143
- [163] C J Ham, S C Cowley, and G Brochard. Nonlinear Stability and Saturation of Ballooning Modes in Tokamaks. *Physical Review Letters*, 116, 23500(June):1–5, 2016. doi: 10.1103/PhysRevLett.116.235001. 143
- [164] T P Goodman, S Alberti, M A Henderson, A Pochelon, M Q Tran, Ecole Polytechnique, and Federale De Lausanne. Design and installation of the electron cyclotron wave system for the TCV tokamak. In *Symposium on fusion technology SOFT*, pages 19–22, Lisbon (Portugal), 1996. 159, 167
- [165] R. J. Wylde. Millimetre-wave Gaussian beam-mode optics and corrugated feed horns. *IEE Proceedings, Part H - Microwaves, Optics and Antennas*, 131(pt.H, no. 4):258–262, 1984. 159
- [166] Paul F. Goldsmith. *Quasioptical Systems: Gaussian Beam Quasioptical Propagation and Applications*. Institute of Electrical and Electronics Engineers, Inc., New York, 1998. ISBN 0780310179. 159, 161, 163
- [167] M. Fontana, L. Porte, and P. Molina Cabrera. Correlation electron cyclotron emission diagnostic in TCV. *Review of Scientific Instruments*, 88(8), 2017. ISSN 10897623. doi: 10.1063/1.4997075. 161
- [168] James Anderson and J. Doane. General Atomics Microwave Technologies: Straight Corrugated Waveguides, 2019. URL <http://www.ga.com/straight-corrugated-waveguides>. 162, 163
- [169] J. L. Doane. Mode converters for generating the HE₁₁ (gaussian-like) mode from TE₀₁ in a circular waveguide. Technical Report 1927, Princeton University, Princeton, New Yersey, 1982. 163
- [170] John L. Doane. Grating polarizers in waveguide miter bends. *International Journal of Infrared and Millimeter Waves*, 13(11):1727–1743, 1992. ISSN 01959271. doi: 10.1007/BF01010741. 163, 164

- [171] J. Doane, H. Grunloh, W. Martin, and W. Wu. Polarizer miter bends for high-power microwave transmission: Ohmic loss and cooling. *Fusion Engineering and Design*, 102:99–107, 2016. ISSN 09203796. doi: 10.1016/j.fusengdes.2015.11.017. URL <http://dx.doi.org/10.1016/j.fusengdes.2015.11.017>. 164
- [172] M. Silva, T. Goodman, F. Felici, and L. Porte. Fast polarizers installation for ECRH and ECE in TCV. *Fusion Engineering and Design*, 86(6-8):1256–1259, 2011. ISSN 09203796. doi: 10.1016/j.fusengdes.2011.01.043. 164
- [173] T.~P. Goodman and the TCV team. Experience in integrated control of the multi-megawatt electron cyclotron heating system on the TCV tokamak: the first decade. *Nuclear Fusion*, 48(5):054011–+, 2008. ISSN 00295515. doi: 10.1088/0029-5515/48/5/054011. 165, 169
- [174] R.J. Wylde. Agilent VNA Quasi-Optical systems, 2018. URL <http://www.terahertz.co.uk/tk-instruments/products/agilentvna>. 166
- [175] Agilent Technologies. Understanding the Fundamental Principles of Vector Network Analysis. *Application Note 5965-7707E*, page 15, 2012. ISSN 14764660. doi: 10.1086/650463. URL <http://www.agilent.com/>. 166
- [176] Alireza Kazemipour, Martin Hudlíčka, See Khee Yee, Mohammed A. Salhi, Djamel Allal, Thomas Kleine-Ostmann, and Thorsten Schrader. Design and Calibration of a Compact Quasi-Optical System for Material Characterization in Millimeter/Submillimeter Wave Domain. *IEEE Transactions on Instrumentation and Measurement*, 64(6):1438–1445, 2015. ISSN 00189456. doi: 10.1109/TIM.2014.2376115. 167
- [177] JW Lamb. Miscellaneous data on materials for millimetre and submillimetre optics. *International Journal of Infrared and Millimeter Waves*, 1996. URL <http://link.springer.com/article/10.1007/BF02069487>. 167

- [178] R Chavan and J. Magnin. Gyrotrons 82.7 GHz : Réalisation mécanique du mouvement poloidal du miroir # 4 des lanceurs X2. Technical report, Centre de Recherches en Physique de Plasma - EPFL, Lausanne, Switzerland, 1998. [168](#), [169](#)

Pedro A. Molina Cabrera

CONTACT INFORMATION	Rue Haute 23 Grandson, Switzerland, CH1422 Tel: (+41)762 81 5052	Nationalities: Canadian and Ecuadorian Date of Birth: 05 - April - 1987 pedro.molina@epfl.ch								
PROFESSIONAL HIGHLIGHTS	<ul style="list-style-type: none">- Experimental engineering physicist excited about state of the art diagnostics and exploring the links between turbulence and transport in fusion plasmas.- First hand experience with design, implementation, operation, and data analysis of advanced microwave diagnostics in tokamak experiment.- Excellent team-working and communication skills gained through team-work projects and extra-curricular activities in international environments.- Native-like proficiency in English and Spanish. Fluent French.									
TECHNICAL SKILLS	<table><tr><th>Data analysis and Programming</th><th>Hardware</th></tr><tr><td>MATLAB, Python, C Fortran, C++, Java</td><td>VNA measurements, IF stage design integration, and testing</td></tr><tr><th>Plasma diagnostics</th><th>Teaching</th></tr><tr><td>Reflectometry, DBS, ECH stray detectors, Langmuir probes</td><td>Plasma physics laboratories Electromag. and thermodynamics</td></tr></table>		Data analysis and Programming	Hardware	MATLAB, Python, C Fortran, C++, Java	VNA measurements, IF stage design integration, and testing	Plasma diagnostics	Teaching	Reflectometry, DBS, ECH stray detectors, Langmuir probes	Plasma physics laboratories Electromag. and thermodynamics
Data analysis and Programming	Hardware									
MATLAB, Python, C Fortran, C++, Java	VNA measurements, IF stage design integration, and testing									
Plasma diagnostics	Teaching									
Reflectometry, DBS, ECH stray detectors, Langmuir probes	Plasma physics laboratories Electromag. and thermodynamics									
EDUCATION	<p>PhD. in Tokamak Physics Sep 2014-Present <i>Swiss Plasma Centre - EPFL, Lausanne, Switzerland.</i></p> <ul style="list-style-type: none">- Thesis: Tokamak plasma edge studies by microwave short-pulse reflectometry and backscattering. <p>MSc. Nuclear Fusion Science and Engineering Physics (Cum Laude) Sep 2012-14 <i>Joint degree offered by Ghent, Complutense, Carlos III, Nancy, and Stuttgart universities.</i></p> <ul style="list-style-type: none">- Thesis: Modeling capacitively coupled plasmas for impedance matching studies in the ALINE device. <p>MSc. Space Studies (Cum Laude) Sep 2010-11 <i>International Space University, Strasbourg, France</i></p> <ul style="list-style-type: none">- Thesis: Pulsed Plasma Thrusters, a global review and experiments. <p>BSc. Eng. Engineering Physics (First Class Honours) Sep 2006-10 <i>Queen's University, Kingston, ON, Canada</i></p> <ul style="list-style-type: none">- Final year project: Design of a constellation of nanosatellites to monitor magnetic environment at the second Lagrangian point.									
PROFESSIONAL EXPERIENCE	<p>Diagnostic development and exploitation Sep 2014-Present <i>Swiss Plasma Centre - TCV tokamak unit, Lausanne, Switzerland</i></p> <ul style="list-style-type: none">• Design, development, testing, and initial exploitation of innovative V-band fast AWG-driven short pulse reflectometer to access equilibrium density profiles and fluctuations.• Design, development, testing, and initial exploitation of sweepable V-band Doppler backscattering diagnostic to measure density fluctuations' rotation velocities and energy spectra. <p>Junior Software and Controls Engineer Mar-Sep 2012 <i>Bionik Laboratories Inc., Toronto, ON, Canada</i></p> <ul style="list-style-type: none">• Designed and implemented control algorithms to mimic human walking pattern with 4-BLDC motors using Atmega-2560 MCU and external motor-driver chips.• Designed and implemented GUI control-pannel for exo-skeleton legs using C# and OpenGL.									

Teacher assistant: Physics laboratories

Sept 2014-Present

Faculty of Basic Sciences - EPFL, Lausanne, Switzerland

- Supervised cold plasma laboratory experimental course for 3rd year bachelor physics students: basic plasma properties and diagnostics (langmuir probes and basic spectroscopy).
- Repaired experiment set-up in 1981 to measure dispersion relation and Landau damping of ion acoustic waves
- Awarded special recognition by faculty of physics in Fall 2017 term for special involvement in Plasma speaker experiment.

INTERNSHIP
EXPERIENCE**Graduate Research Assistant**

Jun-Sep 2011

*Space Transportation Group , Prof. Georg Herdrich**Institute of Space Systems, University of Stuttgart, Germany*

- Assimilated hundreds of PPT publications unveiling important performance characteristics published in international conference.
- Familiar with characterization and utilization of high-voltage circuits for ceramic spark-plug ignition of Pulsed Plasma Thrusters (PPT).

Undergraduate Summer Research Assistant - Government funded

May-Sep 2010

*Space Physics Group, Prof. Jean-Marc Noël**Department of Physics, Royal Military College, Canada*

- Designed and constructed prototype of highly-sensitive 3-axial search-coil spacemagnetometer to fly aboard CIMON Cubesat mission within 4 month internship.
- Configured pre-amp stage and flight-processor (in C and Assembly language) to measure magnetic field values from prototype magnetometer for calibration purposes

Undergraduate Summer Research Assistant - Government funded

May-Sep 2009

*Balloon Astrophysics Group, Prof. Barth Netterfield**Department of Physics, University of Toronto, Canada*

- Wrote software routines in C within Linux environment to track azimuth with on-board magnetometers.
- Manufactured electrical connectors and mechanical mounts for attitude-control system of stratospheric balloon-borne IR telescope.

Research Assistant

May-Sep 2008

*Nuclear Materials Research Group, Prof. Rick Holt**Mechanical and Materials Engineering, Queen's University, Canada*

- Programmed LabView VIs for data-acquisition and motion-control of four nuclear-materials experiments involving laser dilatometer, servo and stepper motors, and large hydraulic rigs.
- Translated large experiment code from object-oriented Visual Basic to LabView improving controllability and performance.

PART-TIME
EXPERIENCE**Teacher Assistant: APSC 142 - Introduction to 'C'**

Jan-Apr 2008,09,10

Department of Electrical Engineering, Queen's University, Kingston, ON

- Assisted groups of 10-15 students learning 'C' using Lego-Robots during weekly laboratory sessions.
- Gained unique understanding of programming styles/concepts and enforced good programming practices.
- Punctually marked quizzes and term projects.

VOLUNTEER
EXPERIENCE**Engineering Design Team Leader**

Jan 2008 - 2010

Queen's Space Engineering Team, Queen's University, Kingston, ON

- Programmed Arduino-nano board in C and assembly to relay GPS, thermometer, and altitude data to ground-station using on-board radio.
- Revived and led space engineering design team of 15-students to compete in the AAS-AIAA CanSat games. Led team through NASA-supervised PDR, CDR, and PFR phases, producing high-quality documentation. Ranked second out of fifteen international teams in first year in the competition.

Robotics Engineering Art Project

May 2009 - 2010

Departments of Fine Arts and Mechanical Engineering, Queen's University

- Programmed motion sensors to dictate movement of silicon sculptures in engineering-art project displayed in the City of Kingston art-gallery.
- Designed and built power circuits and general wiring for 15 servomotors and 7 motion sensors to connect with single-board PC.
- Applied engineering skills and artistic creativity to successfully collaborate with individuals of different backgrounds.

PUBLICATIONS

P. Molina Cabrera, S. Coda, L. Porte, A. Smolders. *V-band short pulse reflectometer diagnostic in the TCV tokamak*. Review of Scientific Instruments, Submitted Feb. 2019. Currently at second round of reviews.

P. Molina Cabrera, S. Coda, L. Porte, N. Offeddu, P. Lavanchy, M. Silva, and M. Toussaint. *V-band Doppler backscattering diagnostic in the TCV tokamak*. Review of Scientific Instruments, 89(8), 2018. ISSN 10897623. doi: 10.1063/1.5007433. 132, 149

M. Fontana, L. Porte and P. Molina Cabrera., *Correlation electron cyclotron emission diagnostic in TCV* published in Review Of Scientific Instruments, vol. 88, num. 8, p. 083506, 2017

CONFERENCE PUBLICATIONS

P. Molina Cabrera, S. Coda, L. Porte, A. Smolders., *Pulse Reflectometer and Doppler back-scattering diagnostics in the TCV Tokamak*. 45th Conference on Plasma Physics. European Physical Society, Prague, Czech Republic, July 2-6, 2018. P1.1015.

Molina Cabrera P., Herdrich G., Lau M., Schoenher T., *Pulsed Plasma Thrusters: A global review and long awaited classification*. 32nd International Electric Propulsion Conference, Wiesbaden, Germany, 11-15 September 2011.

Molina Cabrera P., Tolyarenko N., *Benefits, Drawbacks, and Main Challenges of the VASIMR engine*. 32nd International Electric Propulsion Conference, Wiesbaden, Germany, 11-15 September 2011.

CONFERENCE CONTRIBUTIONS

Oral: *Reflectometry diagnostics in TCV* was presented at the 14th International Reflectometry Workshop at the Swiss Plasma Center of the Ecole Polytechnique Fédérale de Lausanne, May 22-24th 2019, Switzerland.

Poster: *Reflectometry diagnostics in TCV* was presented at the 45th Conference on Plasma Physics. European Physical Society, Prague, Czech Republic, July 2-6, 2018.

Poster: *Reflectometry diagnostics in TCV* was presented at the 59th Annual Meeting of the APS Division of Plasma Physics, October 23 - 27, 2017, Milwaukee, WI, US.

Poster: *Measuring electron density profiles and fluctuations in the pedestal of the TCV tokamak with innovative U-band arbitrary short pulse reflectometer* was presented in the 21st Topical Conference on High-temperature Plasma Diagnostics, June 5-9th 2016, Madison, WI, US.

Oral: *Microwave reflectometry in TCV* was presented at the Joint Annual Meeting of the Swiss and Austrian societies, September 1 - 4, 2015, Vienna, Austria.

AWARDS

Prime Speciale - Faculty of Basic Sciences- EPFL Oct 2017

Awarded by the Dean of the faculty of physics in the basis of exceptional service in the role of teacher assistant for the 3rd year bachelors laboratory course.

Best Film award - Jury of Exposure Science Film Hackaton - UNIL/EPFL Nov 2017

Exposure science film hackaton: Teams of four individuals create a short science film in just 3 days with the help of expert mentors and inspiring seminars. Film Sun in a Box created by *Sons of the Sun* team won best film by jury and second best film by audience vote.

EM Fusion Cat.A Scholarship - Erasmus Mundus Fusion Consortium 2012-Present

Awarded by European Commission EACEA in the basis of academic performance and potential to succeed in EM Fusion master program.

CFISU Masters Scholarship - International Space University 2010-2011

Awarded by the Canadian Foudation for the International Space University in the basis of academic performance and potential to succed in master program.

CANSAT competition 2nd place ranking - Engineering Society, Queen's University June 2010

Awarded to Queen's Space Engineering Team for performance at the AAS/AIAA 6th CanSat Competition in Amarillo Texas.

Dean's Scholar Award - Applied Science, Queen's University 2006-2010

Awarded in the basis of academic performance.

Millenium Scholarship - Canada Millenium Scholarhip Foundation 2008

Awarded in the basis of academic performance, service to the community, leadership, and interest in innovation.

Cameron Applied Science Award - Applied Science, Queen's University 2008

Awarded to engineering students involved in non-traditional fields such as Engineering-Art through the Robotics project.

EXTRA-CURRICULAR ACTIVITIES

Music: Piano, guitar, and singing for over 10 years. Member of progressive rock(Vibrations), folkloric (Causanacunchi) bands and community choirs (Lep's Go, Goudimel).

Martial Arts: Capoeira (1yr), Vo Vietnam (2yrs), Choy Lee Fut (1yr), Haidong Gumdo (Black Belt - 4yrs), Aikido (2 yrs), Tai-Chi (1yr)

Astronomy: Royal Astronomical Society Member. Awarded 'Explore the Universe' certificate.

RC Model Aircraft: Electric and gas powered RC aircraft enthusiast.

